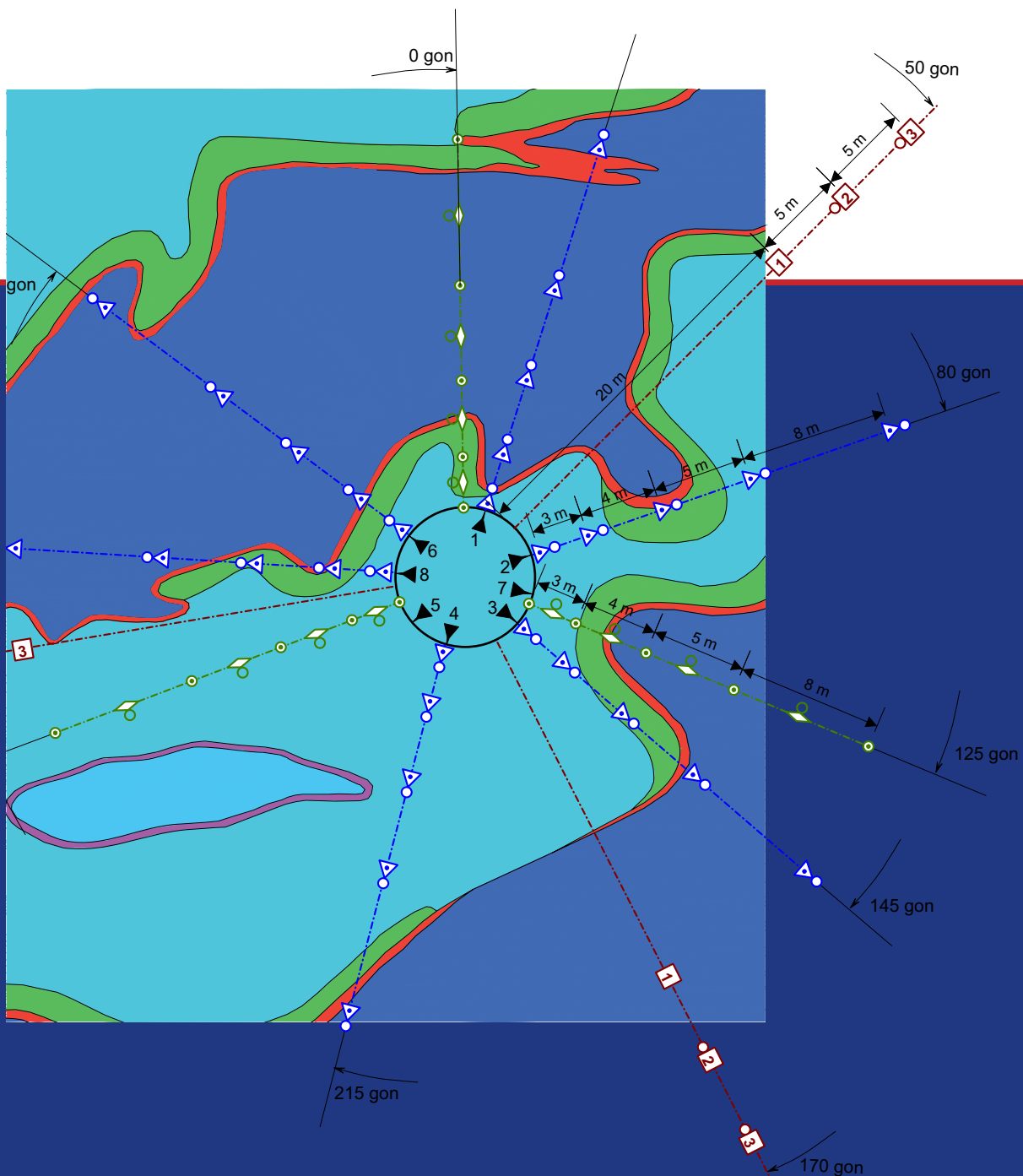


Description of the Gorleben site
Part 4:

Geotechnical exploration of the Gorleben salt dome



Description of the Gorleben site
Part 4:
Geotechnical exploration
of the Gorleben salt dome

Description of the Gorleben site
Part 4:

Geotechnical exploration of the Gorleben salt dome



German edition:

Standortbeschreibung Gorleben Teil 4
Geotechnische Erkundung des Salzstocks Gorleben

ISBN 978-3-510-95988-4

More information/Purchase: <http://www.schweizerbart.de>

© Bundesanstalt für Geowissenschaften und Rohstoffe (BGR)
Geozentrum Hannover
Stilleweg 2
30655 Hannover
Germany

www.bgr.bund.de

ISBN 978-3-9814108-0-8

Foreword

Research has been carried out since 1979 on the Gorleben salt dome, located in the rural district of Lüchow-Dannenberg in Lower Saxony, to investigate its suitability as a geologic repository for radioactive waste. The investigation programme consists of geological, mining engineering, and geotechnical exploration from the surface and underground, as well as analysing and evaluating all of the aspects necessary to competently assess its suitability and long-term safety. The Gorleben site was investigated in detail for a period of more than 20 years to understand the internal structure of the salt dome, the overburden and the adjoining rock. First results of this exploration were published in interim reports in 1983, 1990 and 1995. The findings published in these reports substantiated the potential suitability of the salt dome as a geologic repository for radioactive waste.

The investigation work at the Gorleben site was suspended as a consequence of the agreement reached on 14 June 2000 between the German government and the power supply industry. This moratorium applied for a period of at least three years, but a maximum of ten years. Nevertheless the German government issued a statement on Gorleben which confirmed that the previous findings from its investigation did not contradict the site's potential suitability.

It is now possible after the termination of the surface exploration programme, and for the purpose of documenting the results of the extensive underground exploration, to present the findings of the geoscientific investigations of the Gorleben site in an overall report. The first part presents the hydrogeology of the overburden. The second part presents the results of the geological and structural geological exploration of the overburden and the adjoining rock, and the third part covers the results of the exploration of the salt dome itself. These findings are supplemented in the present fourth part by the description of the geotechnical investigations.

This compilation of data, and the presentation of the technical evaluation of the geoscientific exploration results serve both to document the investigations and to bring more objectivity into the contentious public and political debate concerning the Gorleben site.



(Volkmar Bräuer)

- Repository Project Manager -

Abstract

This report describes and presents the results of the geotechnical investigations, carried out as part of the underground exploration programme up to the beginning of the moratorium on 1 October 2000.

Parameters to characterise the rock mass and the site were determined by the geotechnical investigations in the form of in-situ measurements and laboratory tests. The data determined form reference data sets for the description of the thermal, mechanical and hydraulic rock properties, which are used to elaborate conceptual models and to conduct model calculations. They are the input parameters for model calculations and are used to draw inferences on the stability of the underground workings, and to assess the integrity of the salt barrier, as well as the long-term safety of a geologic repository in the salt formation. Although the exploration of the salt dome has not yet been completed, the investigations overall allow the conclusion that none of the geoscientific findings contradict the suitability of the Gorleben salt dome for the construction and operation of a geologic repository.

Table of contents		Page
1	Introduction	11
2	Geotechnical investigations at Gorleben	12
3	Description of the investigation area	14
4	Seismological evaluation of the Gorleben site	17
4.1	Gorleben seismometer network	17
4.2	Results of the seismometer measurements	19
5	Temperature field in the exploration area	21
5.1	Salt dome geothermy	21
5.2	Thermo-physical laboratory investigations	23
5.3	In-situ temperature field measurements	24
5.3.1	Temperature measurement locations	24
5.3.2	Measured changes in temperature	26
5.3.2.1	Deep boreholes	26
5.3.2.2	Boreholes in the exploration area	27
5.3.3	Determining the initial three-dimensional temperature field	29
6	Geomechanical in-situ measurements	34
6.1	Measuring methods	35
6.1.1	Rock stress measurements	35
6.1.2	Determining the load-deformation behaviour	39
6.1.3	Rock mass deformation measurements	41
6.1.4	Temperature measurements	46
6.2	Measurement locations	46
6.3	Results of the in-situ measurements	52
6.3.1	Shafts 1 and 2	52
6.3.1.1	Temperature developments	52
6.3.1.2	Determination of primary stress	54
6.3.1.3	Measurement of long-term stress changes	57
6.3.1.4	Dilatometer measurements	59
6.3.1.5	Deformation measurements	59
6.3.2	Exploration level	70
6.3.2.1	Temperature development	70
6.3.2.2	Determination of primary stress	72
6.3.2.3	Measurement of long-term stress changes	74
6.3.2.4	Deformation measurements	76

7	Rock-hydraulic investigations	83
7.1	Permeability measurements	83
7.1.1	Methodology	84
7.1.2	Investigations in exploration boreholes	85
7.1.2.1	Exploration area 1 (EB1)	86
7.1.2.2	Infrastructure area	86
7.1.3	Investigations in short boreholes	87
7.2	Estimating the volumes of isolated occurrences of fluids	88
7.2.1	Formulation and calculation of the material balance equation	88
7.2.2	Necessary measurements	91
7.2.2.1	Stabilised pressure measurements	92
7.2.2.2	Outflow measurements	93
7.2.3	Size of the penetrated isolated occurrences of fluid	94
7.2.3.1	Occurrences in the Zechstein 3	94
7.2.3.2	Occurrences at the Zechstein 3 / Zechstein 2 boundary	96
7.2.3.3	Occurrences in Zechstein 2	96
8	Characterisation of the mechanical properties	97
8.1	Laboratory investigations on mechanical behaviour	97
8.1.1	Investigation methods	98
8.1.2	Sample material	104
8.1.3	Test results	106
8.1.3.1	Density	106
8.1.3.2	Rock-dynamic parameters	107
8.1.3.3	Elastic deformation behaviour	110
8.1.3.4	Tensile strength (Brazilian test)	115
8.1.3.5	Uniaxial and triaxial compressive strengths	115
8.1.3.6	Post-failure strength	118
8.1.3.7	Failure strain	119
8.1.3.8	Creep behaviour	120
8.2	Material laws governing thermo-mechanical behaviour	124
8.3	Identification of homogenous zones	127
9	Model calculations	131
9.1	Thermal and mechanical rock mass parameters	132
9.2	Interpretation of the deformation measurements	134
9.3	Thermally induced fissures in shaft 1	140
9.4	Northern cross-measure drift in the exploration area	146
9.5	Evaluation of the overcoring tests	151
10	Summary	155

References	162
Abbreviations	170
List of tables	171
List of figures	172
List of appendices	176

1 Introduction

The Federal Institute for Geosciences and Natural Resources (BGR), as the German government's central authority for geoscientific issues, works on the geoscientific aspects of the exploration of the Gorleben site as part of the repository measures of the Federal Ministry for the Environment, Nature Conservation and Nuclear Safety (BMU) and the Federal Office for Radiation Protection (BfS). All of the investigation findings resulting from the surface and underground geological exploration activities are evaluated by BGR, presented in reports and diagrams, and used for model calculations. The results of the exploration and the safety analysis form the basis for the site assessment and the evaluation of the integrity of the salt barrier, as well as the subsequent approval procedures conducted pursuant to the Atomic Energy Act.

In accordance with the agreement reached between the German government and the energy companies on 14 June 2000, work on the Gorleben site was suspended and underground exploration was temporarily put on hold in October 2000. Only part of the planned geotechnical investigations had been carried out by this time. This involved in-situ tests to determine the rock stresses and the load-deformation behaviour of the evaporite in the area around the shafts. When the moratorium began, the investigations on the temperature field in the salt dome and as the mechanical and hydraulic in-situ tests, had to be suspended, as well as the laboratory tests for geomechanical characterisation. In addition, no model calculations have been carried out since 2000. The only activities that continued during the moratorium were seismological monitoring, and deformation and long-term stress measurements within the underground workings – pursued to ensure that a continuous collection exists. Part of the investigation results achieved so far must therefore be seen as preliminary against this background. A final report on the exploration results can only be issued when all the exploration activities have been completed. Nevertheless, the findings presented in this report provide key information for the geotechnical characterisation of the salt dome.

The investigations carried out so far as part of the underground exploration of the Gorleben salt dome were continuously presented in numerous technical and ongoing reports published by BGR, and summarised in detailed final reports at the beginning of the moratorium in October 2000. The reports were handed over to BfS as the authority on whose behalf the investigations were carried out. Because these reports only deal with partial aspects of the underground investigation programme exploring the Gorleben salt dome, this report brings together the current status of the geotechnical exploration work, with the results achieved to date by the in-situ geomechanical, geophysical and mine surveying measurements, as well as the supplementary laboratory tests and model calculations carried out in parallel to the exploration activities.

The results of the hydrogeological exploration in the overburden above the Gorleben salt dome were reported in KLINGE et al. (2007). KÖTHE et al. (2007) presented the geology of the overburden and the adjoining rock of the Gorleben salt dome. The results of the surface and underground geological exploration of the evaporite are reported in BORNEMANN et al. (2008).

2 Geotechnical investigations at Gorleben

The Gorleben salt dome was proposed by the state government of Lower Saxony in 1977 as a possible location for a geologic repository mine for radioactive waste. This prompted the German government to initiate investigations to examine the suitability of the site for the storage of radioactive waste. The aim of these investigations is to verify the safety of the structure, and the operation of the geologic repository, as well as to confirm its long-term safety. This involved the development and implementation of a wide-ranging geotechnical exploration programme at the Gorleben site which was interrupted when the moratorium started.

The geotechnical investigation programme was jointly elaborated by BGR and BfS, and agreed with the Deutsche Gesellschaft zum Bau und Betrieb von Endlagern für Abfallstoffe (DBE – German Company for the Construction and Operation of Waste Repositories) (HUND et al. 1991). The criteria defined for the investigation programme specified the following aspects according to STIER-FRIEDLAND et al. (1997):

- The geoscientific data required for the site-specific safety analysis.
- Satisfying the requirements for seamless documentation of the geoscientific conditions around the site.
- The necessary geoscientific information needed for the detailed mining engineering planning of the underground workings.

To assess the suitability of the Gorleben salt dome as a geologic repository for radioactive waste, and to satisfy the aforementioned criteria, continuous and wide-ranging collection and documentation of the conditions and loads of the rock mass are required. The determination and provision of site-specific parameters and information are also necessary (HÄNSEL & PREUSS 1991 and EILERS & PREUSS 1997).

This was the background against which comprehensive laboratory tests and in-situ measurements were conducted for the thermal, mechanical and hydraulic characterisation of the rock mass as part of the geotechnical exploration programme. The results of these investigations are also an important basis for the model calculations carried out

for the necessary site-specific safety analyses looking at the operational phase and the post-operational phase. In addition, the long-term measurements combined with the simulation results are important aspects for monitoring the stability of the underground workings during the exploration phase and during operations. All of the investigation results, combined with the geological findings, form the basis for assessing the suitability of the Gorleben salt dome as a geologic repository for radioactive waste, as well as for planning a geologic repository mine and for implementing the planning approval procedure (STIER-FRIEDLAND et al. 1997).

To achieve these exploration objectives, the investigation programme includes the following geotechnical investigations (EILERS & PREUSS 1997):

- Geophysical investigations:
 - Assessing the earthquake hazard at the Gorleben site by undertaking seismological measurements.
 - Determining the natural temperature field within the salt dome and changes to the temperature field during the exploration phase and the operational phase.
- Geomechanical/geotechnical in-situ investigations:
 - Determining the primary stress state of the rock mass and the changes over time arising from the mining activities and thermal load.
 - Determining the deformation of the rock mass over time caused by the mining activities and thermal load.
 - Hydraulic characterisation of the salt dome and determining liquid and gas reservoirs.
- Geomechanical laboratory investigations:
 - Determining the thermo-mechanical properties and the material parameters of the encountered rocks, and developing a material model for the realistic description of the thermo-mechanical rock mass behaviour.

Because the geotechnical investigations only enable very localised analysis and assessment of the properties of the rock mass, the determined rock mass parameters have to be extrapolated over large parts of the underground rock mass. Zones in the rock mass with similar properties are therefore grouped together as homogenous zones (EILERS & PREUSS 1997).


3 Description of the investigation area

The Gorleben salt dome is located in the Lüchow-Dannenberg district of Lower Saxony close to the border between Lower Saxony, Mecklenburg-Western Pomerania, Brandenburg and Saxony-Anhalt. The salt dome has a north-east/south-west alignment and is approximately 14 km long and at its maximum 4 km wide. The structure continues to the north-east of the Elbe river in the form of the Rambow salt dome where it extends in narrower form for another 16 km. Top salt is around 250 m below ground level, and the base Zechstein is at a depth of between 3200 m and 3400 m.

The huge majority of the sediments in the Gorleben salt dome consist of Zechstein Series rock salt, with minor amounts of anhydrite, claystone and carnallite. Homogenous, continuous halite zones are primarily found within the Staßfurt-Folge (z2). This salt consists on average of around 95 % halite and 5 % anhydrite. The Leine and Aller-Folge (z3, z4), however, are characterised by more frequent changes in lithology (JARITZ 1993). The stratigraphic sequence exposed in the underground workings extends from Hauptsalz beds in the Staßfurt-Folge (z2HS) to the Anhydritmittelsalz of the Leine-Folge (z3AM). Table 3.1 summarises the stratigraphic sequence exposed in the underground workings. A detailed description of the geology and tectonics of the exposed rocks is found in BORNEMANN et al. (2003) and BORNEMANN et al. (2008).

The Hauptsalz of the Staßfurt-Folge (z2HS) forms the core of a central upright main anticline within the salt dome. The younger sequences in the Leine-Folge (z3) and the Aller-Folge (z4) are primarily found in the peripheral zones of the salt dome. They are also frequently found in the core of the salt dome in narrow deep-reaching synclines, and are overlain in part by the Hauptsalz in the overhangs. The gas exploration well "Gorleben Z1" (1957) drilled in the north-western salt dome flank also penetrated basal, flat-bedded Zechstein rocks from the Werra-Folge (z1) and lower Staßfurt-Folge (z2). These rocks are not found in the salt dome. Appendices 1 and 2 show the 840 m level and a geological section between the two shafts.

Table 3.1: Simplified stratigraphic table of the Zechstein beds around the underground workings in Gorleben, showing the average thicknesses

Area	Division	Group	Formation	Thickness [m]	Symbol		
Infrastructure Area	Zechstein 3	Anhydritmittelsalz		60	z3AM	approx. 170 m	
		Buntes Salz		12	z3BT		
		Bank-/Bändersalz		14	z3BK/BD		
		Orangesalz		50	z3OS		
		Liniensalz		31	z3LS		
Exploration Area 1	Zechstein 3	Basissalz		16	z3BS	approx. 80 m	
		Hauptanhydrit		40 bis 80	z3HA		
		Leine-Karbonat		1,5	z3LK		
		Grauer Salzton		2,5	z3GT		
	boundary Zechstein 2 / Zechstein 3						
	Zechstein 2	Gebänderter Deckanhydrit		1,5	z2DA		
		Decksteinsalz		0,5	z2DS		
		Kaliflöz Staßfurt		0 bis 17	z2SF		
Kieseritische Übergangsschichten			2,5	z2UE			
Zechstein 1	Hangendsalz		10	z1HG	approx. 800 m		
	Hauptsalz		700 bis 800	z1HS			
	Kristallbrockensalz			z1HS3			
	Streifensalz			z1HS2			
	Knäuelsalz			z1HS1			
	Legend 						

Underground exploration began with the start of the work to sink the shafts Gorleben 1 and Gorleben 2. Once the shafts had both been sunk, work then began on connecting the shafts via the main drift at the 840 m level. Breakthrough to join up the two drifts happened on 21 October 1996. The infrastructure rooms were then excavated close to the shafts: these consisted of workshops, operations rooms and store rooms. The underground workings for transport and mine ventilation were excavated at several levels. Exploration area 1 (EB1) was then drifted in the north-west of the infrastructure area and is bounded in a west-east direction by cross-cut 1 West and cross-cut 1 East, as well as in the north-south direction by the northern cross-measure drift and the main drift. Figure 3.1 shows the status of the underground workings excavated in the exploration mine (source: DBE).

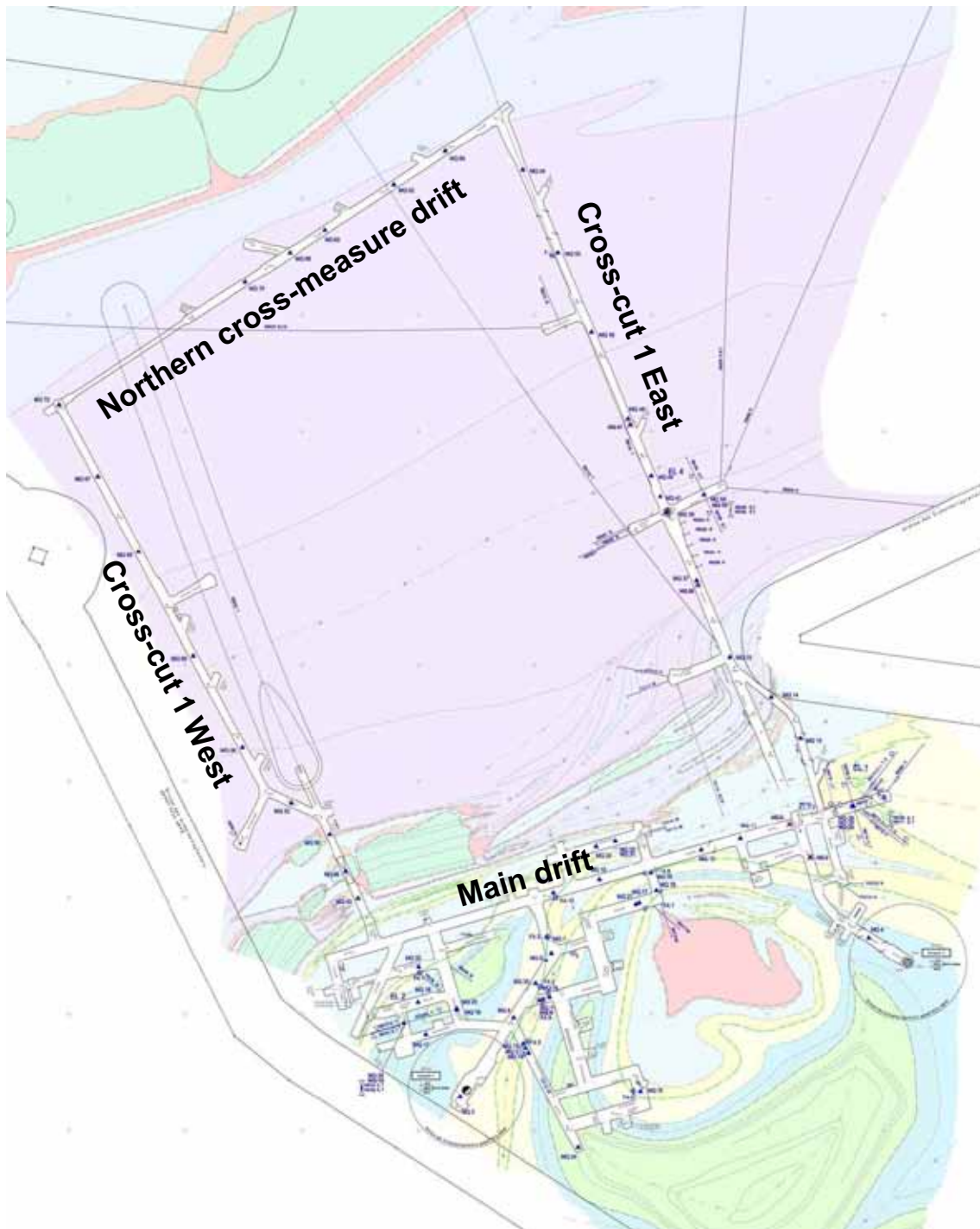


Figure 3.1: Underground workings of the Gorleben exploration mine (source: DBE)

4 Seismological evaluation of the Gorleben site

The earthquake activity in northern Germany is very low compared to seismically active regions such as the Upper Rhine Graben or the Lower Rhine Embayment. Nevertheless, in the last 1200 years a few earthquakes with maximum intensities (12-grade classification of the severity of earthquake ground shaking on the basis of observed effects) of VI (minor damage) have been observed here (LEYDECKER 2007). Within a radius of about 50 km from the Gorleben site, a macroseismically observed earthquake is known to have occurred in the Altmark in 1680 and is classified as intensity IV – V. These earthquakes underline that rare neotectonic events occur in this region.

Prior to setting up the Gorleben seismometer network, the absence of sensitive local seismometer stations meant that no small magnitude (instrumentally determined logarithmic scale of the seismic energy of an earthquake, “Richter scale”) earthquakes could be recorded in the past. The Gorleben seismometer network was set up to monitor local earthquake activity, to identify potential tectonic displacements arising from faulting, and to identify tectonic elements which could potentially jeopardise the stability of the planned geologic repository or weaken its isolation from the biosphere.

4.1 Gorleben seismometer network

The network of seismometer stations around the Gorleben salt dome was developed and installed between 1981 and 1985. Continuous operations began in early 1986 (HENGER et al. 1988). The network consisted originally of six borehole seismometer stations: the three-component station (GOR 1) located in the centre of the network is surrounded by vertical seismometers (GOR 2 to GOR 6) arranged in a pentagon shape with a diameter of approx. 20 km (cf. Figure 4.1). The GOR 4 station was removed in 2003 (KAISER et al. 2004).

The seismometers of the Gorleben seismometer network were installed at a depth of 300 m below ground level in steel-cased boreholes. Dedicated lines transmit the seismometer data to the data centre in Trebel near Gorleben where they are examined automatically to identify seismic events. Identified events are stored in digital form. The proper functioning of the network is monitored by BGR in Hanover where the data are retrieved daily automatically and analysed interactively on-screen.

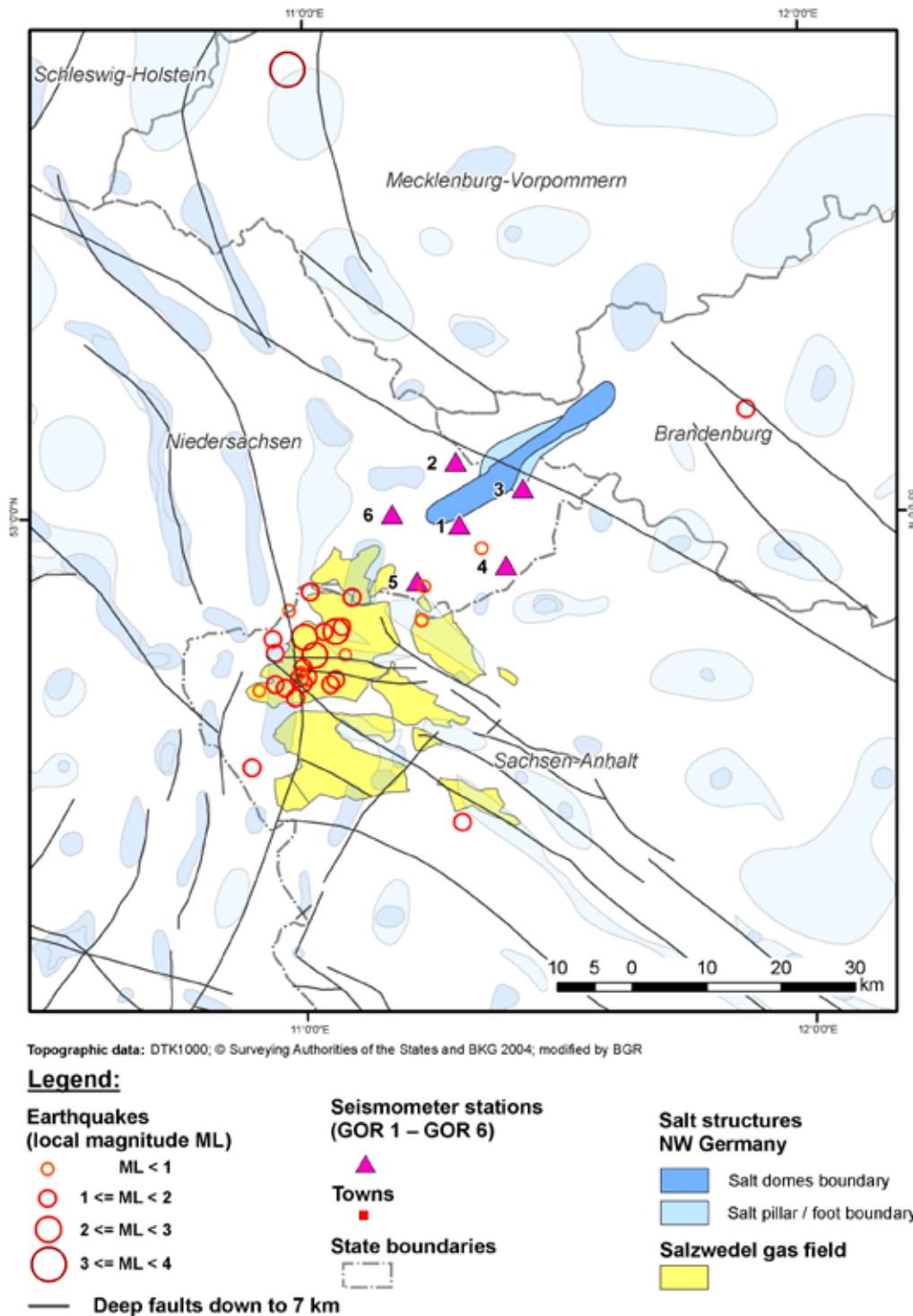


Figure 4.1: Seismometer station network around Gorleben and the epicentres of the seismic events (excluding blasting events) recorded and localised by this station network within a radius of approx. 50 km from the Gorleben site.

Sources: Deep faults to 7 km depth (JUNG et al. 2002); salt structures NW Germany (BALDSCHUHN et al. 1996), with additions/corrections by BGR; gas field: State Authority for Mining, Energy and Geology, Hanover, and Gaz de France Production Exploration Deutschland GmbH.

Because the seismometers are located 300 m below the surface, the seismograms show both direct seismic waves and those reflected from the ground surface (total travel time approx. 0.31 s). This interference has an effect on the amplitudes as well as the frequencies of the seismograms. This effect on the signals is tolerable because installing the seismometers at a significant depth below the ground surface reduces ground noise so considerably compared to surface locations that even micro-earthquakes of very small magnitude can be detected.

4.2 Results of the seismometer measurements

Continuous seismic monitoring of the Gorleben area began in February 1986. In addition to teleseismic and regional earthquakes, a large number of local seismic events have been detected since then. Most of these events are associated with blasting, primarily in Brandenburg, Lower Saxony and Saxony-Anhalt. The earthquakes recorded and localised up to the end of 2007 by the Gorleben seismometer network in a radius of approx. 100 km are listed in Table 4.1 and shown in Figure 4.1 (KAISER & SCHLOTE 2008).

The strongest earthquake within a radius of 100 km took place at a distance of approx. 65 km with its epicentre near Zarrentin on 19/05/2000. This was a tectonic earthquake with a focal depth of 17 km and a magnitude of $ML = 3.4$ (GRÜNTAL et al. 2007).

The minor number of earthquakes observed so far within a radius of approx. 50 km from the Gorleben site are concentrated in the area to the west of Salzwedel (Saxony-Anhalt). The strongest earthquake with a magnitude of $ML = 2.6$ took place on 21/12/1984. The magnitudes of the other quakes were between $ML = 0.0$ and $ML = 2.1$. All of the epicentres are located within a gas field from which large volumes of natural gas were being produced, and are concentrated in the Salzwedel-Peckensen part of the gas field (Figure 4.1). The gas production volumes were reduced considerably in the period after German reunification, leading to a decline in the already fairly minor earthquake activity. It can therefore be concluded that all of the earthquakes observed in this area to date were induced by the gas production activity.

Not a single earthquake was detected in the immediate vicinity of the Gorleben salt dome over the whole monitoring period (December 1984, February 1986 to December 2007). The detection threshold around the seismometer network is approx. $ML = 0.5$.

In combination with the historical findings, the results of the seismic monitoring of the Gorleben salt dome indicate that the selected site lies in a seismically quiet area. "Seismically quiet" in the monitored area not only refers to stronger earthquakes with macroseismic effects, but also microseismic activity.

Table 4.1: Earthquakes within a radius of approx. 100 km from the Gorleben site detected by the Gorleben seismometer network

Date	Location	Coordinates in degrees		Origin time GMT	Mag ML	Dist in km
		Latitude N	Longitude E			
21/12/84	SW Salzwedel	52.835	11.018	00:33:45.5	2.6	32
09/03/86	SW Salzwedel	52.815	10.988	20:52:26.7	0.9	29
26/03/88	SW Salzwedel	52.806	11.059	07:13:25.7	1.4	27
28/04/88	SW Salzwedel	52.784	10.979	01:37:07.3	1.4	32
25/07/88	NW Salzwedel	52.912	11.009	00:26:10.3	1.6	22
02/03/89	SW Salzwedel	52.793	10.907	00:47:17.9	1.0	35
21/09/89	SW Salzwedel	52.802	10.994	20:19:01.7	1.3	30
13/11/90	SW Salzwedel	52.809	11.003	02:25:37.2	1.1	29
05/10/91	WNW Salzwedel	52.869	11.072	19:07:00.9	1.4	21
03/06/92	SW Salzwedel	52.808	10.987	13:00:35.3	1.0	30
28/07/92	SW Salzwedel	52.800	11.048	15:37:21.7	1.1	28
28/07/92	W Salzwedel	52.854	10.934	16:56:30.0	1.5	29
26/10/92	NW Salzwedel	52.905	11.092	21:00:03.7	1.7	17
11/12/92	E Klötze	52.633	11.308	16:40:26.8	1.8	40
21/07/93	W Salzwedel	52.857	10.997	04:22:37.8	2.1	26
22/07/93	SW Salzwedel	52.800	10.939	03:12:35.1	1.9	33
21/10/93	W Salzwedel	52.863	11.036	01:26:58.8	1.0	23
02/11/93	W Salzwedel	52.889	10.967	17:13:16.8	0.9	26
18/03/94	W Salzwedel	52.835	11.078	00:24:13.7	0.6	22
04/05/94	SW Salzwedel	52.700	10.892	05:41:05.7	1.3	43
16/07/95	W Salzwedel	52.838	10.939	16:51:12.0	1.4	30
20/01/97	W Salzwedel	52.796	10.958	06:01:55.0	1.3	32
18/03/99	SW Salzwedel	52.863	11.060	01:48:50.4	2.0	23
19/05/00	Zarrentin SW Schwerin	53.540	10.970	19:22:41.5	3.4	65
10/12/00	Wistedt SW Salzwedel	52.820	10.993	17:37:13.4	1.1	28
13/05/01	4.5 km ENE Salzwedel	52.876	11.230	06:02:48.5	0.6	14
05/06/01	5.5 km NE Perleberg	53.125	11.883	03:10:21.8	1.0	41
06/02/03	Dangenstorf	52.917	11.236	03:40:41.2	-0.2	10
11/02/03	4.5 km ENE Salzwedel	52.877	11.230	05:43:29.2	0.0	14
03/07/04	4.3 km SE Trebel	52.962	11.351	19:53:15.9	0.4	4

ML = local magnitude (logarithmic scale for the seismic energy of an earthquake, Richter scale)

From a seismological point of view at least, this means that there are no indications of any recent fault displacements close to the salt dome. Tectonic movements which could have the potential to jeopardise the stability of the exploration mine, or even the occurrence of faulting processes which could extend directly into the exploration area, have not been identified on the basis of the measurement results. Together with the detailed information on the geological-tectonic development, this further verifies the positive conclusions on the long-term safety of the site from a seismological point of view.

5 Temperature field in the exploration area

Determining the original unaffected rock mass temperature field within Exploration area 1 is important for the characterisation of the whole salt dome with regard to its suitability as a geologic repository for radioactive waste. The natural temperature field refers to the natural geothermal state existing in the area of investigation prior to the start of all investigation and mining work, and therefore acts as the reference field for all of the subsequent temporal and spatial changes in temperature caused by the construction and operation of the underground workings. The temperature measurement methods and the results are presented in detail in GRISSEMANN & CZORA (2003).

5.1 Salt dome geothermy

The natural geothermal field in the salt dome is determined by the terrestrial heat flow rising up from below, as well as the thermal conductivity properties and the structure of the geological layers. Because the thermal conductivities of evaporites are approximately twice as high as in the surrounding sedimentary horizons, heat rising towards the earth's surface is concentrated in evaporites. Therefore the heat flow densities in the centre of the salt dome, as well as in the overlying overburden, are much higher than in the adjoining rock.

Geothermal modelling by DELISLE (1980) represents the first findings on the temperature field in the Gorleben salt dome. The selected parameters are based on standard and empirical values for salt domes and evaporites. The results of this modelling were verified by temperature measurements undertaken in deep boreholes which penetrated the salt dome as part of the preliminary geoscientific exploration (KOPIETZ 1983, ALBRECHT et al. 1991), and by high-resolution underground temperature measurements recorded in the geological exploration boreholes drilled at EB1 (GRISSEMANN & CZORA 2003).

Figure 5.1 shows the calculated typical thermal flow lines (dashed) and the orthogonally aligned isotherms in a schematic cross section of the Gorleben salt dome (DELISLE 1980).

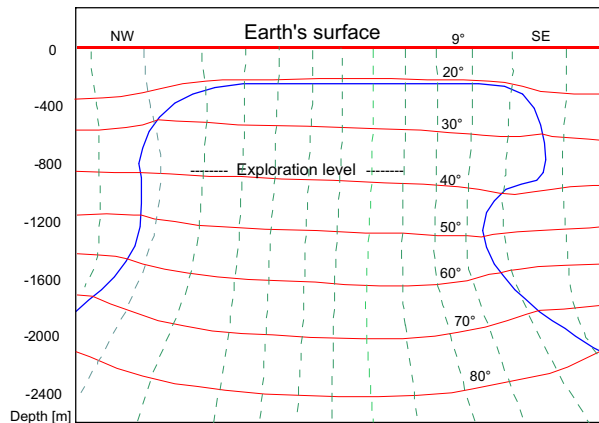


Figure 5.1: Geothermal field in the Gorleben salt dome based on a 2D modelling (DELISLE 1980)

The isotherms, which run uniformly parallel to the ground surface a large distance away from the salt dome, dip down in the root zone of the salt dome. The opposite occurs in the uppermost parts of the salt dome, and in the overburden in particular, where the isotherms arch upwards. The asymmetry of the salt dome flanks is reflected in the asymmetry of the temperature field, whereby in the central area the isotherms dip gently from north-west to south-east.

The modelling indicates that a temperature of approx. 38 °C could be expected at the exploration level (840 m below ground level) the temperature at this depth in the salt dome is thus around 5 °C higher than calculated using the average continental geothermal gradient of around 3 K per 100 m (cf. Chapter 5.3).

Natural vertical heat flow in the central part of the salt dome as predicted by the modelling is approx. 110 mW/m² to 120 mW/m², i.e. around twice as high as the regional average value of approx. 50 mW/m² to 60 mW/m² (HÄNEL 1998).

Sinking the shafts and drifting the underground workings in the exploration area, as well as the associated intense ventilation of the drifts, initially resulted in the rapid cooling down of the rock mass in the perimeters of the drifts, and the development of a cool halo around each drift, which extended within a few years to several tens of metres into the adjoining rock (KAPPELMEYER & HÄNEL 1974). The temperatures recorded during geotechnical investigations directly on the drift perimeters or in shallow boreholes drilled from the drifts are therefore generally much lower than the original rock temperature and vary temporally as well as spatially (cf. Chapter 6.3). This distortion of the natural temperature field means that these temperature measurements cannot be used as a reference level for the evaluation of past and future temperature changes. This can only be done with

the temperatures extrapolated from the measured values. The following describes how the initial temperature field is determined from the measured temperatures.

5.2 Thermo-physical laboratory investigations

Laboratory investigations to determine the petrophysical and rock-mechanical properties are an important part of rock characterisation. This analysis was carried out alongside the in-situ investigations on rock samples from representative locations as part of the exploration work at the Gorleben site. The material parameters determined in this way were used to interpret the geophysical and rock-mechanical measurements, and are an important factor in the thermal characterisation of the salt dome (GRISSEMANN & CZORA 2003). They also provide the input parameters for model calculations.

The investigations were carried out over the whole period of the underground exploration of the Gorleben salt dome so far from 1996 to 2000 and were summarised in EISENBURGER & GRISSEMANN (2003). Tests were carried out on over 150 salt samples in total, and the analysis was carried out in laboratories at BGR as well as external laboratories, sometimes using different methods and processes – this was done to avoid any technical measurement and methodological errors.

The thermo-physical laboratory tests revealed that the analysed salt rocks only have very low porosities. The measured values for the Gorleben samples were between 0 % and 1.6 %.

The thermal conductivities were determined for a range of temperature and pressure conditions. Temperatures between 0 °C and 200 °C, and pressures between 0 MPa and 20 MPa were selected for the tests. Measurements revealed that the thermal conductivity of halite decreases with rising temperatures. At 20 °C it is approx. 5.5 W/(m·K) but only approx. 3.5 W/(m·K) at 200 °C. Conversely, the thermal conductivity rises with increasing pressures. By approx. 5 MPa, microfractures heal up – these microfractures are probably not formation-specific, but artefacts of the mechanical processing of the samples. The only exceptions were a few carnallitite samples which showed only very low thermal conductivities.

The thermal expansion coefficient was determined dynamically at a heating rate of 5 K/min over a temperature range from approx. 20 °C to 290 °C. The linear thermal expansion coefficient was calculated from the axial deformation of cylindrical specimens due to temperature changes. The average linear thermal expansion coefficient in halite is $\alpha = 3.7 \cdot 10^{-5} \text{ K}^{-1}$. The lowest value was $\alpha = 3.5 \cdot 10^{-5} \text{ K}^{-1}$. and the highest $\alpha = 3.9 \cdot 10^{-5} \text{ K}^{-1}$. The measured values deviate slightly from the standard values which

indicate an average linear expansion coefficient of $\alpha = 4.0 \cdot 10^{-5} \text{ K}^{-1}$ for temperatures of 20 °C to 100 °C. The difference is attributed to natural material inhomogeneities in the specimens. The carnallitic samples have a linear expansion coefficient of $\alpha = 3.3 \cdot 10^{-5} \text{ K}^{-1}$ at temperatures of 20 °C to 100 °C.

Because the specimens expand when heated, a differentiation is made between the specific thermal capacity under constant volume c_v and under constant pressure c_p . In the case of solid bodies, $c_p = c_v$ is assumed because of the very low differences. This parameter has to be taken into consideration when describing transient temperature-dependent processes, i.e. processes which change over time. The specific thermal capacity investigations were carried out at a temperature range between room temperature and 250 °C. An average between $c_p = 0.85 \text{ kJ}/(\text{kg} \cdot \text{K})$ and $c_p = 0.90 \text{ kJ}/(\text{kg} \cdot \text{K})$ was measured for the investigated halite samples within this temperature range, with an average temperature dependency of

$$c_p = 0,847 \text{ kJ}/(\text{kg} \cdot \text{K}) + 0,000274 \cdot T(^{\circ}\text{C}) \quad (5.1)$$

This result matches the standard figures given in the literature.

5.3 *In-situ temperature field measurements*

The high-resolution borehole temperature measurements were carried out with an explosion-proof measurement system (Figure 5.2). The measurement accuracy depends largely on the equalisation times of the temperature sensors to the ambient medium, as well as any temperature differences between the medium filling the borehole (air or salt mud), and the borehole perimeter. Brine-filled boreholes are more suitable in principle than dry boreholes for determining temperatures. Additional correction calculations have to be carried out for air-filled boreholes.

5.3.1 Temperature measurement locations

Temperature measurements were carried out in shaft exploratory boreholes Go 5001 and Go 5002, as well as in the deep borehole Go 1003. For safety reasons, and also for operational reasons, high-resolution geothermal borehole measurements in the underground workings could only be carried out in a few exploration boreholes (Figure 5.3). This reduction in the density of geothermally usable measurement points – particularly in the infrastructure area between the shafts, as well as along the north-west flank – must be taken into consideration when looking at the spatial temperature distribution calculated by interpolation and extrapolation.



Figure 5.2: Temperature measuring apparatus in an ex-proof housing

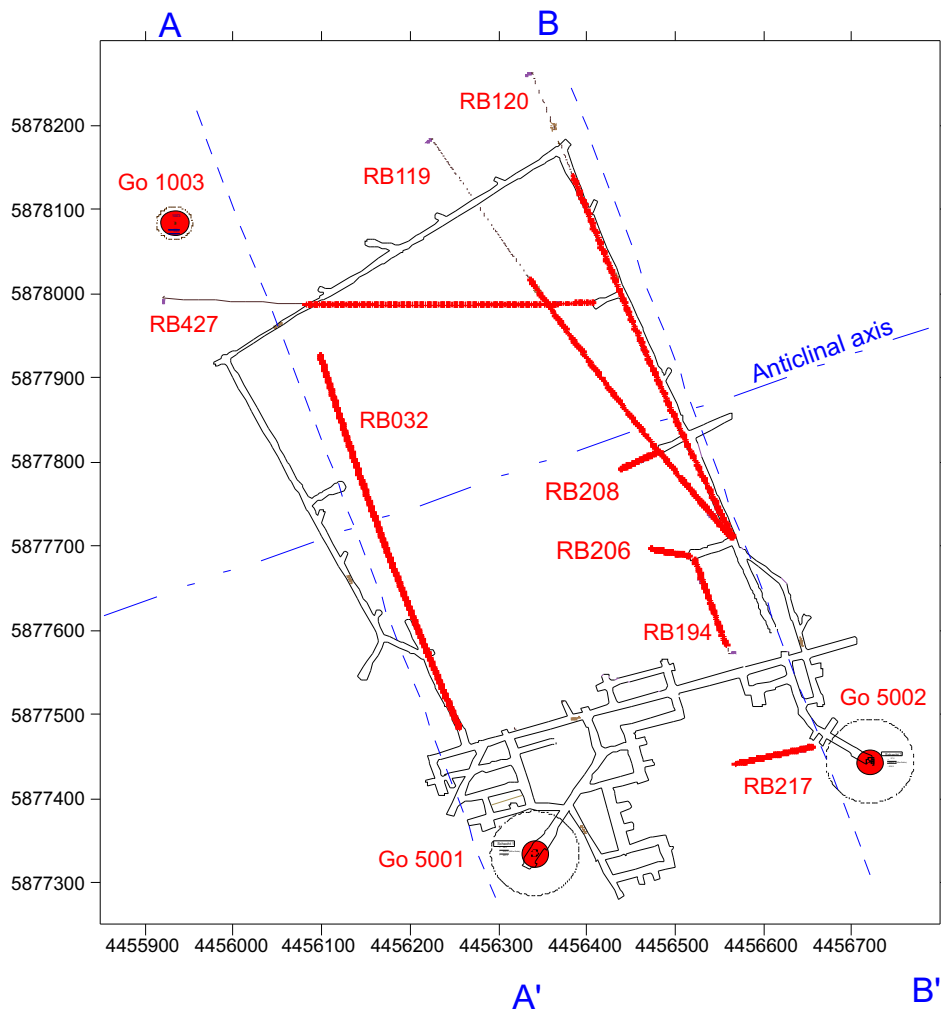


Figure 5.3: Location map of the geothermally-logged boreholes

5.3.2 Measured changes in temperature

5.3.2.1 Deep boreholes

Figure 5.4 shows the complete temperature profile of shaft exploratory borehole Go 5001. This is supplemented in Table 5.1 by a few temperature values determined in the 3 deep boreholes at depths above and below the exploration level. In addition, Table 5.1 also shows the geothermal gradients and the heat flow densities derived from the temperature measurements and based on a thermal conductivity of 5 W/(m·K).

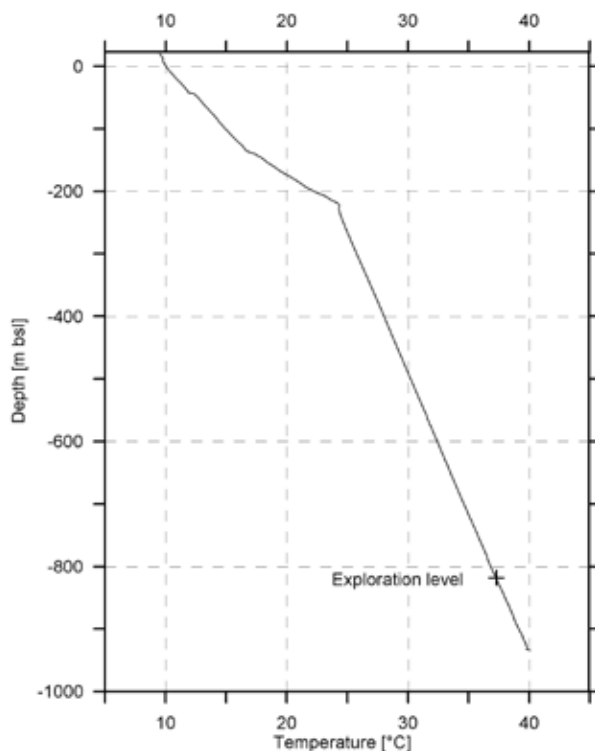


Figure 5.4: Temperature distribution in shaft exploratory borehole Go 5001

An average temperature gradient in a vertical direction of 2.3 K per 100 m is calculated from the measured values in a depth zone between -700 m bsl and -900 m bsl. Assuming a thermal conductivity of 5.0 W/(m·K) for the salt dome, this indicates an average heat flow density of 115 mW/m² and therefore corresponds to the numerical modelling results determined prior to the measurements (DELISLE 1980). The used thermal conductivity value was repeatedly determined in laboratory analysis for halite samples from the Gorleben site at a temperature of 40 °C (EISENBURGER & GRISSEMANN 2003), and can therefore be considered representative.

Table 5.1: Temperature data from deep boreholes Go 1003, Go 5001 and Go 5002 at depths ranging from - 700 m bsl to - 900 m bsl

Depth [m bsl]	Temperature [°C]		
	Go 1003 10/05/1983	Go 5001 28/02/1983	Go 5002 19/01/1983
-700.00	35.58	34.61	34.59
-750.00	36.49	35.74	35.82
-800.00	37.87	36.82	36.94
-816.50	38.22	37.21	37.29
-850.00	38.97	38.01	38.09
-900.00	40.04	39.15	-
Geothermal vertical gradient $\Delta T / \Delta z$ [K/100 m]			
Absolute	2.35	2.29	2.26
Average	2.30		
Heat flow density $k \cdot \Delta T / \Delta z$ [mW/m ²]			
Absolute	117	115	113
Average	115		

In the depth range examined within EB1 (Table 5.1) a horizontal temperature difference of almost 1 °C is indicated between the Go 1003 borehole running close to the north-west margin of the salt dome, and the Go 5001 and Go 5002 shaft exploratory boreholes drilled close to the SE flank.

5.3.2.2 Boreholes in the exploration area

The temperature plot of a borehole filled with brine is shown using borehole RB032 as an example (Figure 5.5). In addition to the drilled depths of the borehole which drops slightly to the NNW, the abscissa shows the stratigraphic names of the horizons penetrated by the borehole.

The brine drilling fluid used to drill the well remained in the borehole when the well had been completed. The borehole was therefore filled with brine to a depth of 35 m. At the brine-free top of the borehole, where the temperature of the air does not correspond to the rock temperature because it is cooled down by the ventilation air in the drift (KAPPELMEYER & HÄNEL, 1974), the temperature climbs rapidly at first from 25.6 °C at the mouth of the borehole, and then more slowly to a value of 35.6 °C immediately above the top of the brine. The temperature jumps by 1.9 °C to 37.5 °C when the probe enters the brine. The temperature then rises only very slowly to the deepest part of the borehole with an average

gradient of 0.4 K per 100 m borehole depth. Because of the ideal thermal coupling between the liquid and the rock mass, as well as the much lower convection and diffusion compared to the air-filled part of the borehole, the measured liquid temperature corresponds to the rock temperature at this location.

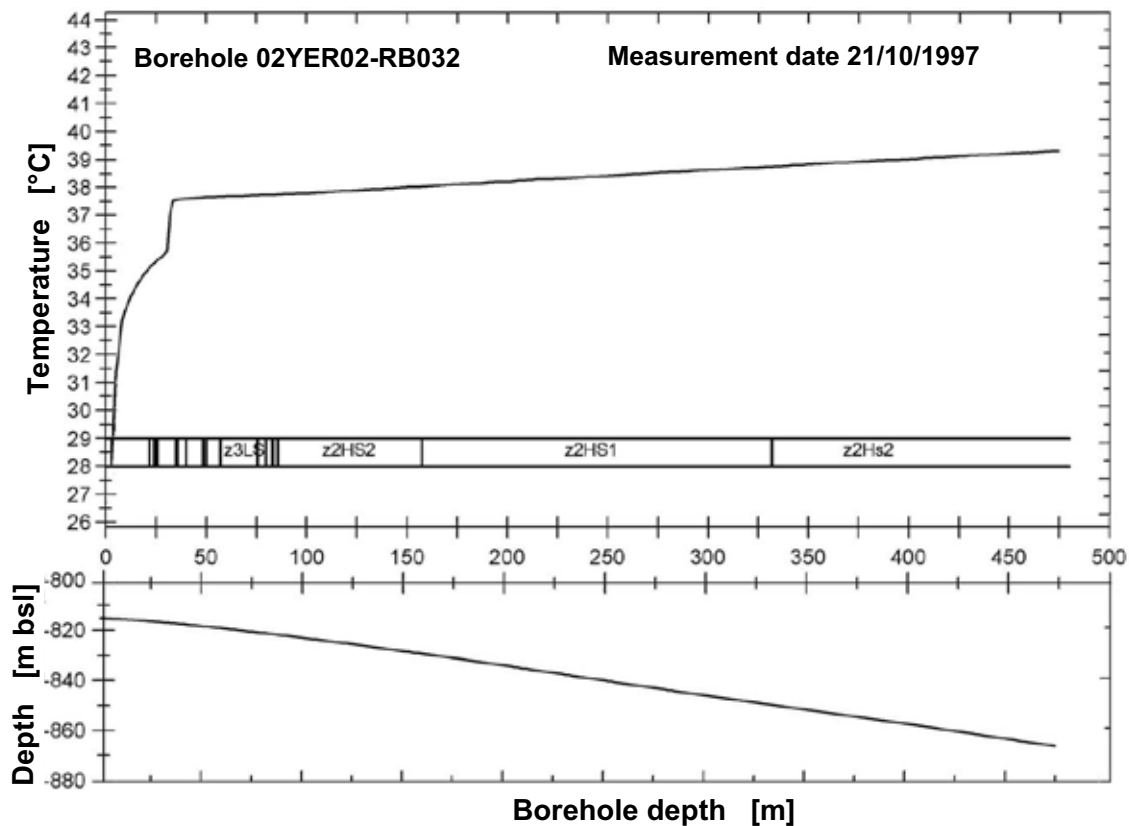


Figure 5.5: Temperature distribution in borehole RB032

The temperature increase of 1.8 K over a depth increase of 49 m in the brine-filled part of the borehole calculates directly to a vertical temperature gradient of 3.6 K per 100 m. However, because this figure is much higher than the average vertical temperature gradient of 2.3 K per 100 m measured in the deep boreholes, it is assumed that there is an additional horizontal temperature gradient, which cannot be determined more accurately until all of the boreholes are considered together (cf. Chapter 5.3.3).

Unlike the measurements in the liquid-filled boreholes, RB032 and RB217, the temperatures in the other boreholes were measured in dry conditions. Figure 5.6 shows a typical temperature distribution in a dry borehole using borehole RB120 as an example. This temperature distribution is characterised by a transition zone of over 100 m between the temperatures influenced by the ventilation air and the unaffected temperature zone. Temperature equalisation in this long transition zone takes place by the convection and diffusion of the borehole air.

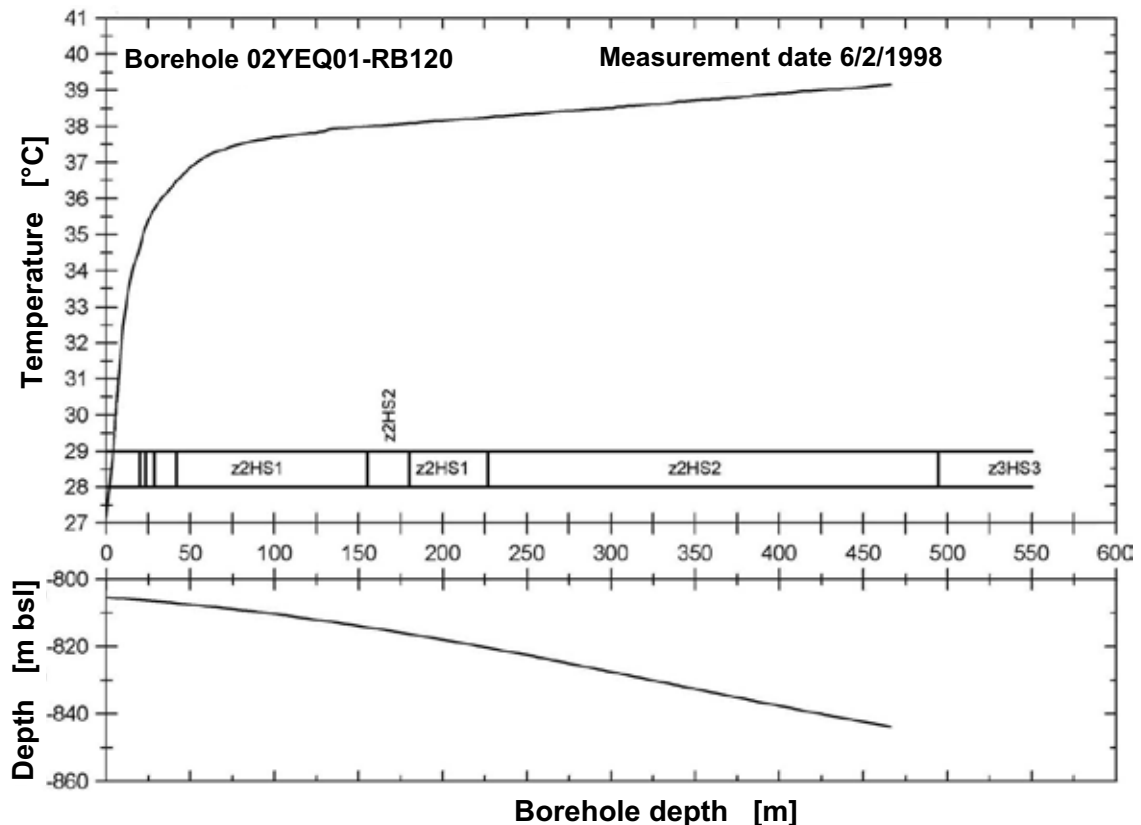


Figure 5.6: Temperature distribution in borehole RB120

5.3.3 Determining the initial three-dimensional temperature field

The natural temperature field can only be determined by using the parts of the borehole temperature distribution where the measured temperature in the borehole medium – air or brine – corresponds as closely as possible to the rock temperature and is not affected by the cooling effect of the ventilation air. The first sections of the measurement plots are therefore ignored when calculating the vertical and horizontal temperature profiles. The temperatures unaffected by the ventilation can be approximated by a linear equation. The affected zones are defined as sections where the measured values deviate from the calculated straight lines by more than 0.08 K.

Figure 5.7 shows the calculated temperature distribution in a vertical section orthogonal to the axis of the salt structure, which was aligned parallel to cross-cut 1 West (section A-A' in Figure 5.3). An isotherm map of the depth section from -750 m to -900 m was prepared by bilinear regression analysis from the temperature measurement data corrected for the influence of the mine ventilation (GRISSEMANN & CZORA 2003). This isotherm map is projected onto the geological section.

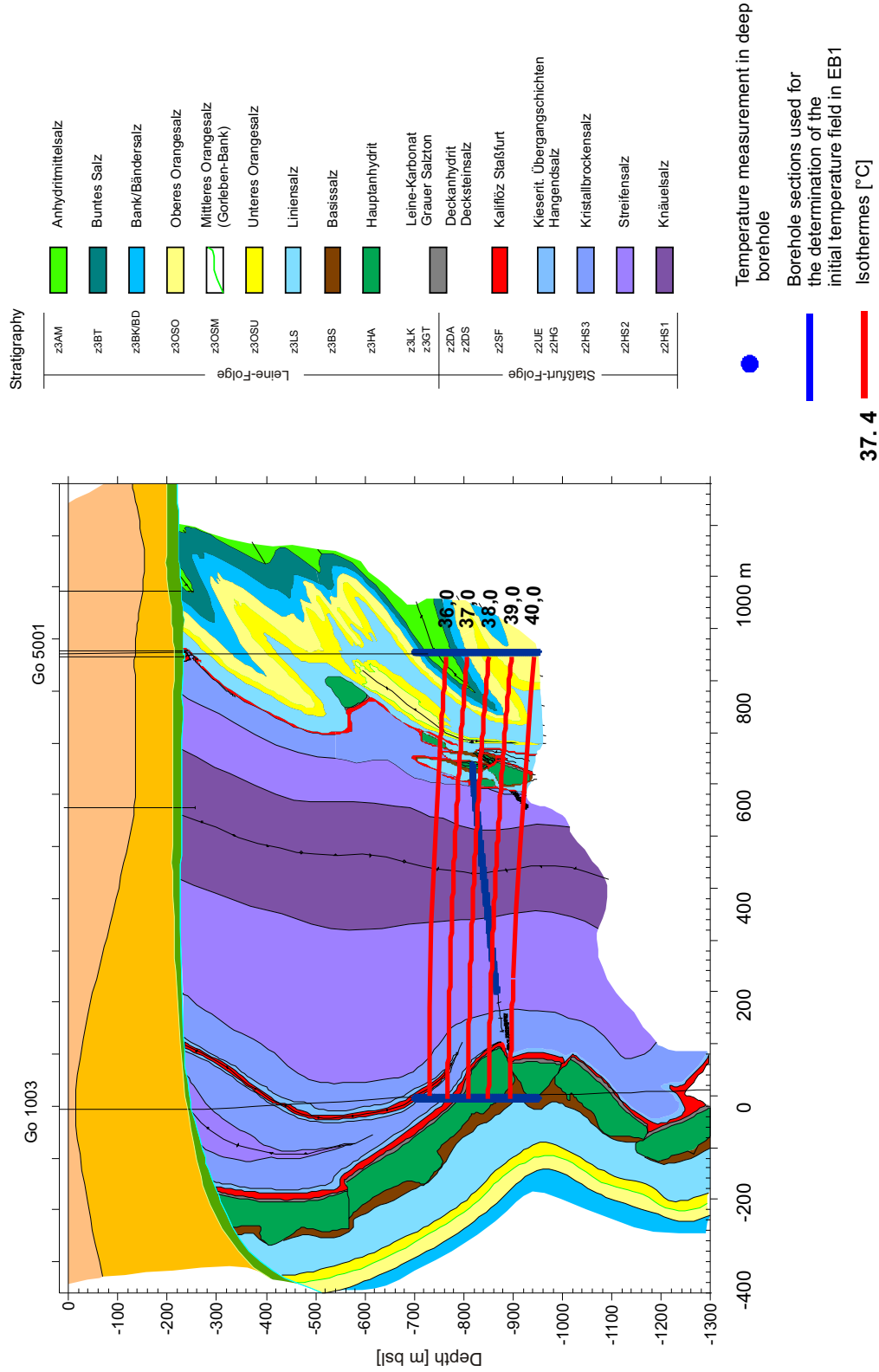


Figure 5.7: Vertical geological cross section A-A' of boreholes Go 1003, RB032 and Go 5001 (from BORNEIMANN et al. 2003) with isotherms of the natural temperature field for the depth zone surrounding the exploration level

According to this, the initial rock temperature at the reference point at the 840 m level is 37.85 °C, and the average geothermal gradient 2.35 K per 100 m. In addition, a curved temperature decline can be identified orthogonal to the axis of the main anticline from NW to SE with a calculated average of 0.114 K per 100 m depth. This is attributed to the asymmetry at the salt dome flanks. The results of the temperature measurements match the temperature field postulated by DELISLE (1980) with the help of numerical modelling (cf. Figure 5.1).

To determine the initial horizontal temperature distribution at the exploration level, temperatures measured in the boreholes at different depths were reduced arithmetically to the depth of the exploration level (-816.5 m bsl, 840 m level). An average vertical gradient of 2.35 K per 100 m was applied (GRISSEMANN & CZORA 2003). The results give rise to the following conclusions:

- The temperatures decrease from NW to SE at the depth of the exploration level. The trend is almost linear at -0.1 K per 100 m in a central zone of +/- 200 m around the axis of the anticline – in other words, in the exploration area EB1 sensu stricto – and further in the direction of the shaft 1. This levels out to the NW in the opposite direction. The temperature measured in the Go 1003 deep borehole is slightly lower than would be expected from the linear extrapolation of the trend in the central EB1.
- The temperatures in boreholes RB120, RB119 and RB194, as well as Go 5002, which can all be combined in cross section B-B' following cross-cut 1 East, is systematically around 0.25 K higher than the temperatures in cross section A-A' (see Figure 5.3). Therefore, there is also a positive component in the temperature gradients in a north-east direction along the anticlinal axis.

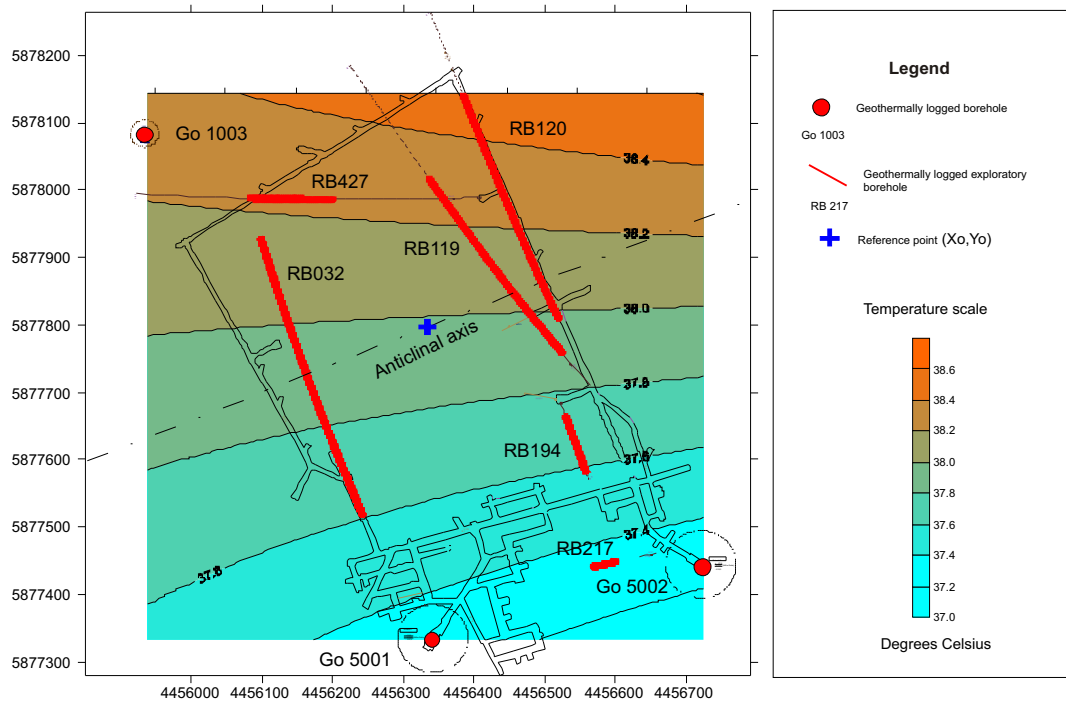


Figure 5.8: Initial temperature field at the depth of the 840 m level

The temperatures reduced to the depth of the 840 m level are all shown in Figure 5.8 summarised within a horizontal isotherm map of the exploration level, and projected into the site plan of the exploration level in Figure 5.9 (BORNEMANN et al. 2003).

The natural initial rock temperature field at EB1, derived from the measurements and interpolated from the trend analysis, can be described by the following parameters according to GRISSEMANN & CZORA (2003):

Average temperature: $T_m = 37.97 \text{ }^\circ\text{C} \pm 0,08 \text{ }^\circ\text{C}$

Horizontal gradient in direction: 394 gon

Vertical geothermal gradient: 2.35 K per 100 m

Horizontal geothermal gradients:

In WE direction -0.0122 K per 100 m

In SN direction +0.151 K per 100 m

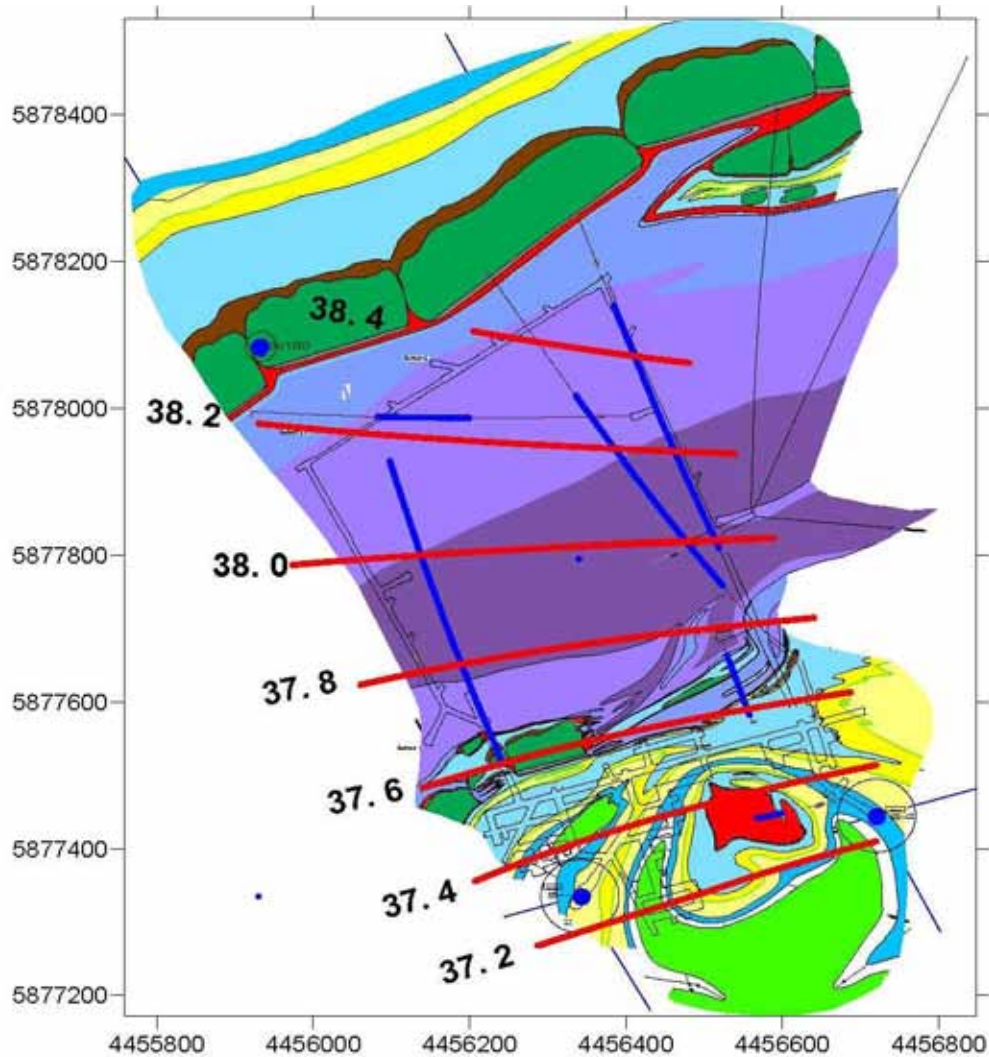


Figure 5.9: Horizontal geological cross section at the 840 m level after BORNEMANN et al. (2003) with natural temperature field isotherms, legend in Figure 5.7

The main temperature distribution gradient of the slightly inhomogeneous field is mainly aligned NNW to N. The original rock temperatures increase by approx. 1.3 K from the southernmost point of the network (south of shaft 1) to the northernmost point where the northern cross-measure drift branches off into cross-cut 1 East. Whilst this temperature increase corresponds to the results of the numerical modelling, it is noticeable that only in the southern part of the investigation area do the isotherms run virtually parallel to the direction of the main anticline as expected, whilst in the northern part there tends to be a local west-east trend. As a general rule, temperature variations of this extent are not unusual in salt domes and have been observed on several occasions (SCHUSTER 1968, GRISSEMANN et al. 2000). Local temperature fluctuations are localised, e.g. at the transition from the Staßfurt-Folge (z2) to the Leine-Folge (z3) in the folded northern flank, because the two members of the sequence – Kaliflöz Staßfurt (z2SF) and Grauer Salzton (z3GT) –

are the only lithologies within the salt dome whose thermal conductivities differ significantly from the main lithological components halite and anhydrite.

The distortions in the temperature field may also be caused, however, by the relative proximity to the northern boundary of the salt dome with the adjoining rock. Variations in the temperature field at this boundary, along strike as well as in the direction of folding, could be due to the folding of the boundary between the Staßfurt-Folge (z2) and the Leine-Folge (z3) and the intense fragmentation of the Hauptanhydrit on the northern flank of the main anticline (see Figure 5.7 and Figure 5.9) – this variation is particularly evident at the depth of the exploration level.

6 Geomechanical in-situ measurements

The geomechanical exploration programme elaborated by BGR and BfS comprises short-term and long-term stress measurements, as well as deformation measurements involving convergence measurements, extensometer measurements, inclinometer measurements and fissurometer measurements. Dilatometer tests were also carried out at selected locations to determine the elastic deformation behaviour of the rock mass. The short-term stress measurements as well as the dilatometer tests were provisionally concluded as a result of the moratorium. Long-term stress measurements and the deformation measurements, however, were continued during the moratorium as monitoring measures.

The short-term stress measurements were carried out to determine the primary stress state within the rock mass. The measurements and the results are presented in highly detailed reports in HEUSERMANN et al. (2003a) and HEUSERMANN et al. (2003c). The long-term stress measurements are used for the continuous observation and documentation of any stress changes that occur in the rock mass during the exploration phase. Large-scale as well as localised rock mass deformations, which can be recorded by deformation measurements, occur as a result of relocation processes in the rock mass initiated by the excavation of underground workings as well as the operation of the exploration mine.

Geomechanical and mine surveying measurements are used as the basis for the continuous documentation of deformation and stress changes, as well as to determine site-specific in-situ parameters to characterise the rock mass. In addition, measurement results also form the basis for elaborating and validating geomechanical models and model calculations as part of the stability analyses and integrity verifications.

The ongoing long-term stress and deformation measurements are conducted by DBE. The scope of the measurements, data processing and data evaluations were defined

by BGR and DBE. The processed measurement data were made available to BGR in reports and on electronic data media until 2000. DBE initially suspended the forwarding of measurement data from the beginning of the moratorium, only making measurement data available again from 2006. The BGR carries out in-depth evaluations, assessments and interpretations of the measurement data looking at geological and mining influences.

6.1 Measuring methods

6.1.1 Rock stress measurements

In-situ stress measurements were carried out using several methods to determine the primary rock stress state as well as long-term stress changes within the salt dome:

- Short-term measurements using the BGR overcoring method
- Short-term measurements using the hydro-frac method
- Long-term measurements using stationary stress monitoring stations

The short-term tests are mainly used to determine the primary rock stresses, whilst the long-term measurements are used to record stress changes.

Overcoring tests using the BGR method

The BGR overcoring method is a stress release method to determine the rock stresses. Methods of this kind measure rock mass deformations initiated by overcoring a pilot borehole. The stresses causing these rock mass deformations can be determined from back calculations of the measured deformations, applying specific material parameters and taking the borehole geometry into consideration.

The overcoring tests using the BGR method first involve drilling a corehole with a diameter of 148 mm down to the intended measuring horizon. A coaxial pilot borehole with a diameter of 46 mm and a length of around 1.0 m is then drilled. The BGR measuring probe is then installed in this borehole and directionally oriented with the help of a setting string. After a short period of waiting, a coring bit with a diameter of 148 mm is then used to overcore the pilot borehole and the installed measuring probe. At the same time, the probe measures the change in diameter of the pilot borehole caused by the releasing of stress by overcoring. The rock core with the pilot hole and the measuring probe are then recovered by pulling the core string. The diagram in Figure 6.1 shows each step of the overcoring test.

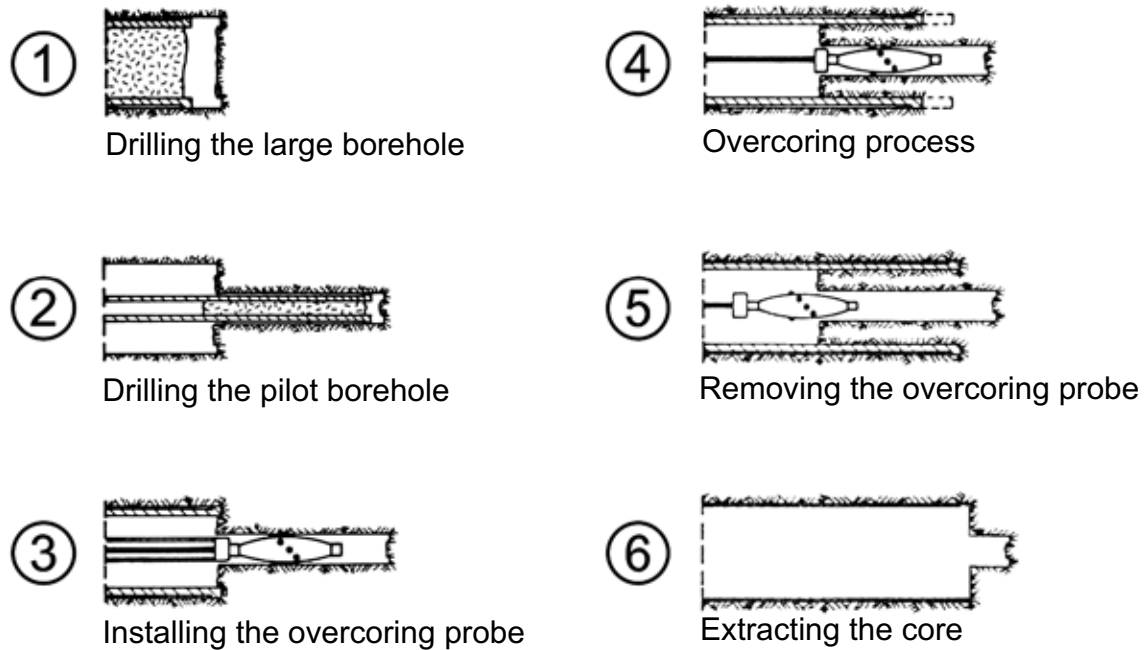


Figure 6.1: Overcoring test principle following the BGR method

The cores with the axial holes are then used for biaxial tests in the BGR laboratory to determine material-specific parameters (Chapters 8.1.1 and 8.1.1.3).

The measuring probe used for the stress release deformations consists of a central body with four inductive displacement transducers mutually offset by 45° which measure the changes in diameter of the pilot borehole (Figure 6.2). The measurement data are continuously transmitted to the measuring unit by the cable connected to the probe. Four pairs of plates are used to fix the probe in the pilot borehole – these are spring-loaded and ensure that the probe sits firmly in the hole.



Figure 6.2: BGR overcoring probe type Mk14 in a rock salt core

When overcoring tests are carried out in brittle rocks, the evaluation of the measurement results can generally be carried out assuming an elastic rock behaviour. Using the BGR overcoring method, this involves calculating a deformation ellipse for each measurement location from the measured diameter changes in the pilot borehole. Applying elasticity theory based on the main axes of these deformation ellipses, the maximum and minimum rock stresses in the measuring plane are calculated using the material parameters from the biaxial tests (Chapter 8.1.1.3).

In addition to the elastic properties, the inelastic properties also have to be taken into consideration in ductile evaporites. Analytical and numerical examinations reveal that the results of overcoring tests in salt are considerably influenced by the stress relaxation caused by creep in the area around the pilot borehole and the associated time-dependent decrease in radial stress (HEUSERMANN 1984 and HEUSERMANN 1995). If this stress decrease is ignored and the evaluation is based only on relations that apply to elastic behaviour, results for the rock stress state will generally be too low in areas affected by higher primary stresses or at greater depths (> 500 m).

Special finite-element calculations were carried out to be able to quantitatively estimate the influence of the lithostatic pressure on the stress release deformation in the overcored pilot borehole in creepable salt (see Chapter 9.5). The calculations aimed to determine a stress-dependent (and therefore also a depth-dependent) evaluation factor κ . The stress values determined using the aforementioned evaluation method have to be multiplied by this factor to derive the actual rock stresses at the location in question.

Hydro-frac method

The hydraulic fracturing method (hydro-frac method for short) is used to determine the primary stresses in boreholes by hydraulically fracturing the rock mass. This is done by sealing off an exploration borehole at the necessary depth using a double packer system, and injecting a liquid (or a gaseous) medium into the interval of the borehole lying between the packers (Figure 6.3). The injection pressure is increased until the rock stress and the tensile strength of the rock mass are exceeded: this causes fracturing of the borehole perimeter and penetration of the injection medium. Further injection enlarges the fracture and causes the fracture front to migrate into the rock mass. The fracture stops spreading when no more liquid is injected. This allows measurement of the pressure (the so-called resting pressure) which is just enough to hold the fracture open. After completely releasing the pressure, a follow-up test is carried out to measure the opening pressure of the artificial fracture. It is assumed that the minimum principal stress in the rock mass corresponds to the resting pressure measured at the test location. This principal stress is aligned normal to the fracture surface.

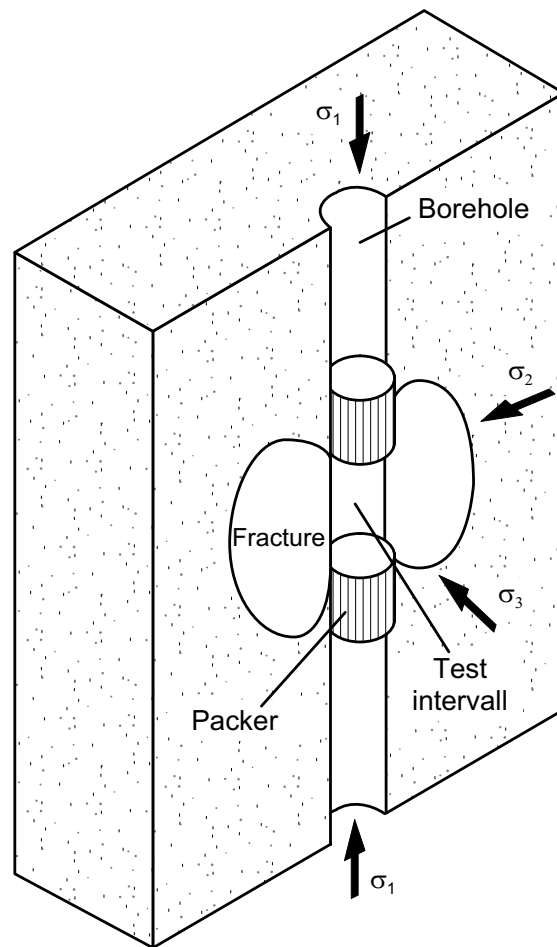


Figure 6.3: Principle of the Rock stress measurements using the hydro-frac method (BRÄUNER 1991)

Because of their many years of experience, K-UTEC, Sondershausen, was selected by DBE to carry out the hydro-frac tests at the Gorleben site.

Long-term stress measurements

The borehole inclusion method using stationary stress monitoring stations built by Glötzl was used for the long-term stress measurements. This method can generally be used to determine stress changes in rock masses. In addition, absolute stresses can be determined in the long term in ductile rock masses.

The monitoring stations installed in measurement boreholes each have four pressure cells with different orientations (Figure 6.4). These four cells allow stress components to be recorded in the plane orthogonal to the borehole axis.

The pressure cells consist of hydraulic valve sensors that work on the hydraulic compensation principle (FRANZ 1958).



Figure 6.4: Stress monitoring stations with Glötzl pressure cells

At least three measuring directions with different orientations are required to determine a stress distribution (stress ellipse), generally assumed to be anisotropic. The four cells in the stress monitoring station are mutually offset by 45° , thus providing simple redundancy in the measurement plane orthogonal to the borehole axis for each station with respect to the number of cells. This allows the clear determination of the anisotropic stress distribution in the measuring plane if present. At least three measurement planes oriented in different directions are required to determine the complete three-dimensional stress state, which means that the stress monitoring stations shown here have to be installed in three measurement boreholes with different spatial orientations.

The cavity between the pressure cells of a monitoring station and the borehole perimeter was filled with a special salt concrete which was investigated in numerous extensive laboratory tests, and has a very similar modulus of elasticity to the adjoining rock salt. With the pressure cells' flat construction, their total stiffness only has a minor influence on the measured stress values (HEUSERMANN & EICKEMEIER 2004). This means that a mechanical correction of the stress changes measured using the borehole monitoring stations can be dispensed with. The measured pressures correspond closely to the stress changes occurring in the rock mass.

6.1.2 Determining the load-deformation behaviour

The material parameters to describe the load-deformation behaviour of rocks (cf. Chapter 8.1.3.3) were determined in laboratory tests. The scale effect has been taken into consideration when extrapolating these material parameters to the properties of the rock mass. The scale effect encompasses all of the influencing factors of the fabric and the mechanical behaviour of the rock mass which are inadequately represented in laboratory tests. Dilato-

meter tests were therefore carried out to determine the location-specific moduli of elasticity of the rock mass.

The BGR dilatometer, type Mk III (Figure 6.5) was used for the borehole dilation tests (PAHL & HEUSERMANN 1991). The BGR dilatometer consists of a main body on which three inductive transducers are arranged at 60° to one another, to measure the changes in diameter of the borehole in radial direction. A high-pressure-resistant hose is fitted over the body of the probe. The transducers lie on special steel plates vulcanised into the hose wall to ensure the measured values are largely unaffected by the deformation of the hose. A measuring cable sends the data to a PC where they are received, saved and presented to allow direct monitoring of the test as it proceeds.



Figure 6.5: BGR dilatometer type Mk III

The procedure for carrying out dilatometer measurements using the BGR method (Figure 6.6) starts with a core hole with a diameter of 148 mm in which a central pilot borehole with a diameter of 86 mm and a length of 2 m is drilled. The dilatometer probe is installed in this pilot borehole using a setting string to ensure that it is oriented to the correct direction and depth. After applying a hydraulic initial pressure of 2 MPa to guarantee the dilatometer lies uniformly along the length of the borehole, the next step is to carry out a reference measurement. This is followed by pressure build-up and pressure release cycles in a range of different load steps with simultaneous recording of the changes in the borehole diameter.

Load steps of 5 MPa, 10 MPa and 15 MPa were selected for the rock salt at the Gorleben site. The stress release steps carried out between each load step lowered the pressure to the initial pressure of 2 MPa. Upon completion of the test and removal of the dilatometer, the test section was overcored and the coring was then continued to lengthen the hole.

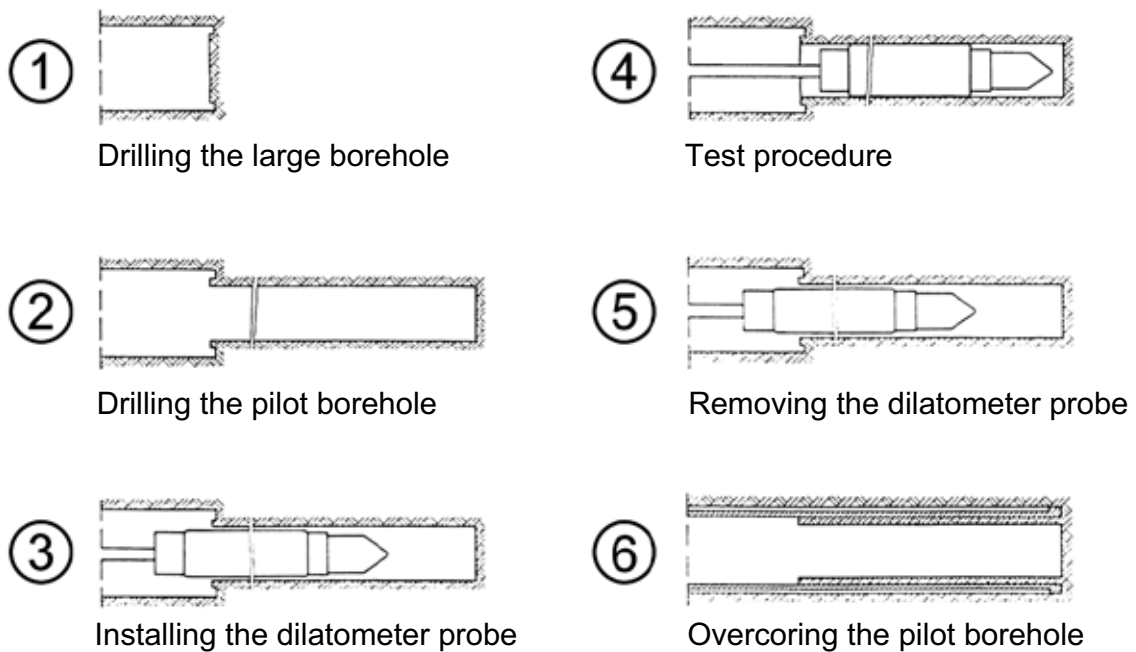


Figure 6.6: Principle of the dilatometer test carried out using a BGR probe

The load deformation curves derived from the dilatometer test are used to determine the modulus of elasticity from the gradient of the secants at the points dividing the stress release branches into three equal sections. The procedure was also used to determine the moduli of elasticity of rocks in laboratory tests (cf. Chapter 8.1.3.3.). The evaluations were carried out using a model consisting of an infinitely long perforated disk in a plane-strain condition under internal load. Assuming an isotropic rock mass behaviour, the modulus of elasticity can be determined after WORCH (1967).

6.1.3 Rock mass deformation measurements

Convergence measurements

Convergence measurements are carried out by using short anchors to permanently mark measuring points (fixed points) on or in the immediate vicinity of the cavity perimeter. The distances between the fixed points (length of the measuring line) are repeatedly measured at regular intervals, and the changes in position determined compared to the first measurement (reference measurement). Positive values of distance changes are classified as divergence (measuring line increases in length), and negative values are classified as convergence (measuring line decreases in length). Figure 6.7 shows the principle behind the convergence measurements.

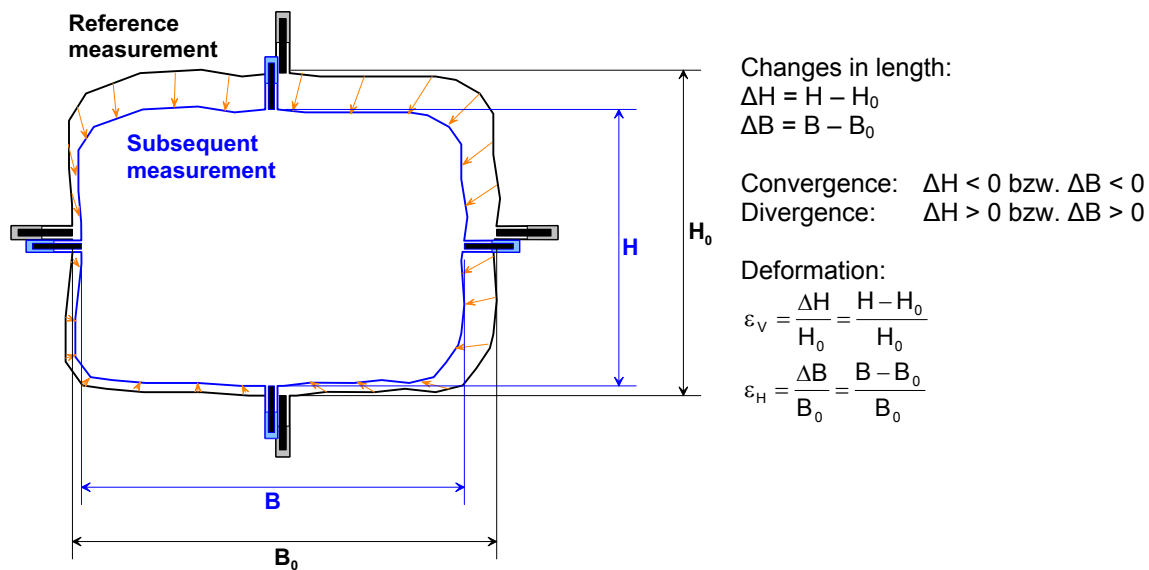


Figure 6.7: Principle behind convergence measurements in a drift

To determine the convergence in the underground workings of the exploration mine, measurement profiles corresponding to the local conditions were installed using at least two measuring lines arranged orthogonal to one another. Three main measuring lines and at least four ancillary measuring lines were set up in each of the convergence measurement profiles of the exploration horizons in the shafts .

The temperatures of the measuring tape used were determined for all of the distance measurements to correct the measured values for the thermal expansion behaviour of the measuring tape. The convergence measuring tools are checked regularly on a test line. The convergence measurement data provided by DBE are temperature-compensated.

Analysis of the measurement results to determine the effects of stratigraphic units, density of excavation and mining activities on the deformation behaviour of the rock mass around the measuring points – also when compared to other deformation measurements – is only feasible when a common basis is used taking into account the different lengths of the convergence measuring lines as well as the different times at which the reference measurements were recorded. Normally, this involves calculating the deformation as a ratio of the measured change in length to the length of the measuring line. Negative deformation indicates convergence, positive values indicate divergence of the measuring line.

To determine the deformation rates, the changes in the calculated deformations over a period of a year are used. This means that seasonal effects are largely eliminated. Deformation is indicated in millimetres per metre (mm/m or per mill); the deformation rates are reported in per mill per year.

When evaluating the convergence measurement data from the Gorleben site, consideration must be given to the fact that no details are available so far on the length of the convergence measuring lines, which means that deformation or deformation rates cannot be determined in this case. The convergence rates are therefore calculated as the change in length of a measuring line over a period of one year. This does at least allow comparison between the convergence measurement data from different measurement profiles.

Extensometer measurements

Extensometers are used to measure changes in distances (displacements) between two or more measuring points along an axis at specified time intervals (DUNNICLIFF 1993). In the case of permanently installed extensometers (e.g. in boreholes), rods (e.g. made of fibre glass) are used and permanently anchored in the rock mass at previously defined positions (measurement points). The displacements of the measurement points (anchor points) are transmitted via these rods to the measuring device and recorded there as changes in distance relative to the extensometer head (reference point). In the case of multiple extensometers, displacements between separate sections of the rock mass along the borehole can be determined by measuring the relative displacement of two anchor points to determine the section displacement (Figure 6.8).

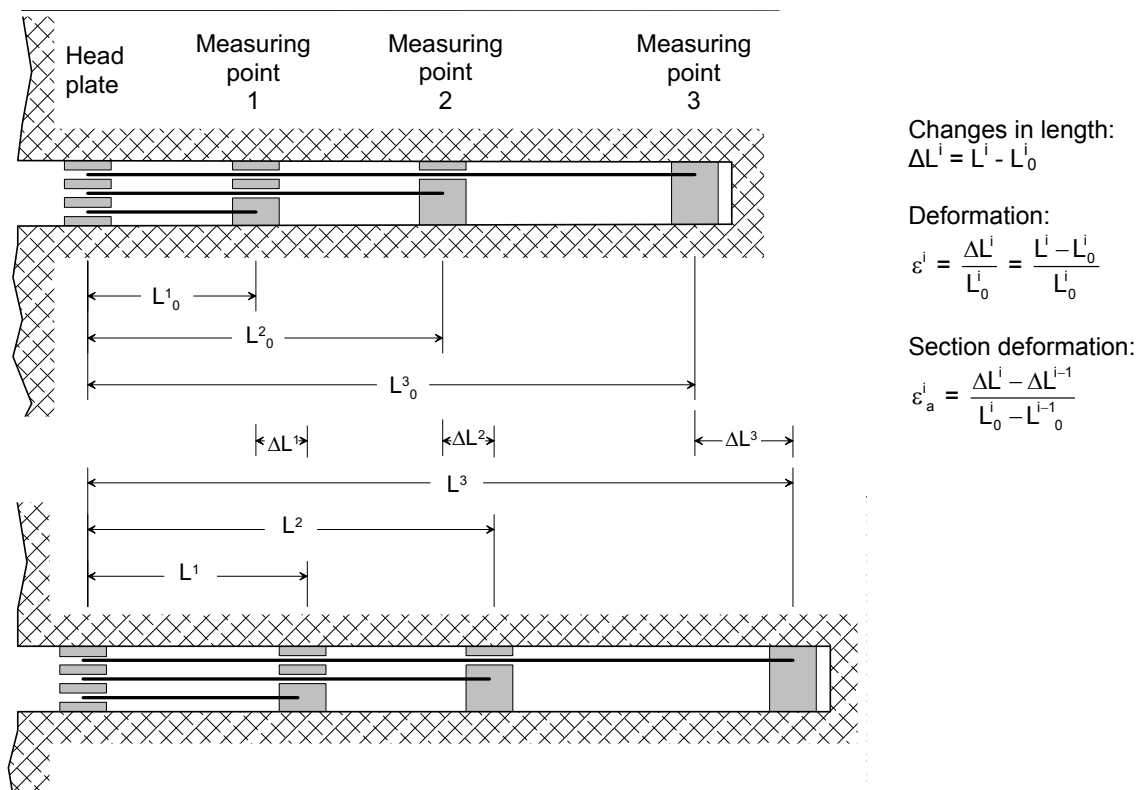


Figure 6.8: Principle behind extensometer measurements using a triple extensometer as an example (after PAUL & GARTUNG 1991).

The displacements of the anchor points relative to the extensometer head are continuously recorded using electrical transducers.

The deformations (in each section) of the measuring lines are determined as a ratio of displacement to the original length of the measuring lines and used for a comparative analysis of the measurement results. Convergence is characterised by negative deformation values, whilst divergence is characterised by positive deformation values. As in the convergence measurements, deformation is measured in millimetres per metre (mm/m or per mill). The calculated deformations are referred to a one-year time interval to determine the deformation rates. The deformation rates are in per mill per year.

Inclinometer measurements

Rock mass deformations which are aligned orthogonal to the axis of the borehole can be recorded with an inclinometer. This makes use of gravity to measure the deviation of the probe from the vertical.

Stationary inclinometer measurements are carried out in Gorleben. This involves dividing up a non-compressible casing into separate measuring lines. The annulus between each section of the casing and the borehole perimeter is completely cemented so that all displacements are transferred directly to the casing. The separate measuring sections are articulated with one another by axially moveable couplings to prevent the displacement of a measuring section being transferred to a neighbouring section (GLÄSS & SCHNIER 1996). Inclinometer probes with a length of one metre in each case are firmly installed in the centre of each measuring section and firmly connected to one another by articulated setting rods. Every inclination measurement borehole is therefore equipped with an inclinometer chain. Figure 6.9 illustrates the principle behind the inclination measurements.

The inclinations of each measuring section are continuously recorded. The measured inclinations are referenced to the length of each inclinometer of one metre and reported in mm/m. Negative values indicate a relative lowering of the measurement profile on the side nearest the mouth of the borehole compared to the side nearest the deepest part of the borehole: this means that the measuring section rises in the direction of the deepest part of the borehole. The positive measured values on the other hand indicate that the measuring section dips down in the direction of the deepest part of the borehole.

The time-dependent changes in the inclination, in other words, the deformation of the rock mass aligned orthogonal to the borehole axis, is determined by comparing the reference measurement with the data from the subsequent measurements.

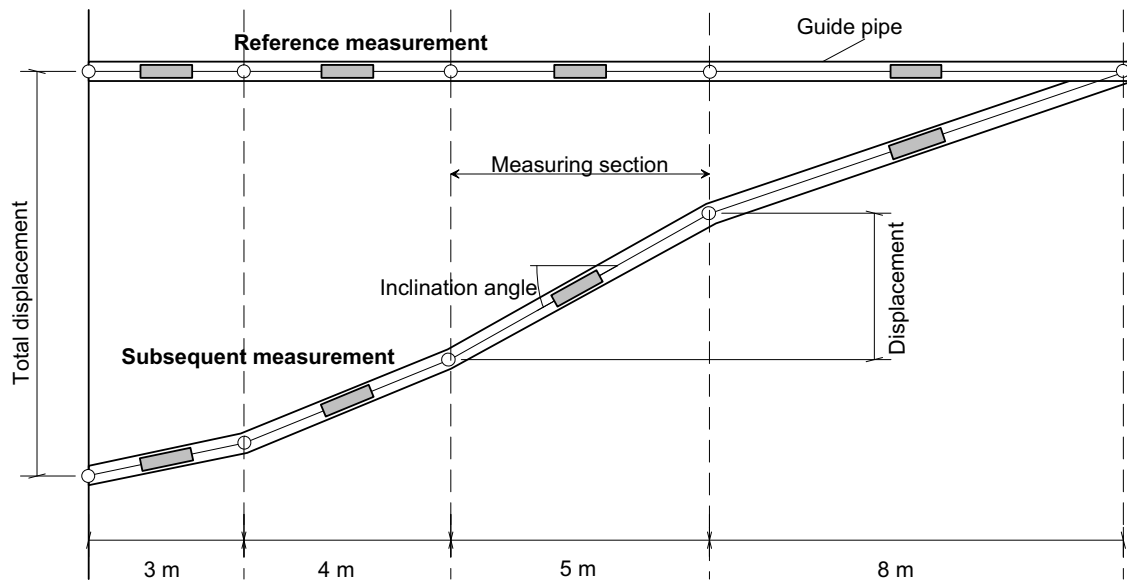


Figure 6.9: Principle behind inclinometer measurements

The inclination values allow the calculation of the vertical displacement of the ends of the measuring section based on the measuring section length. Taking the deepest part of the borehole to be an immovable fixed point for the inclination measurements, the total vertical displacements in the perimeter of the shaft can be determined cumulatively from the vertical displacements of the individual measuring sections.

Fissurometer measurements

Fissurometers allow changes in the apertures of joints and fissures to be measured, i.e. the relative displacement of two blocks with respect to one another can be recorded in three mutually orthogonal directions. They consist of two segments which can move relative to one another (end segment and measuring console), and which are anchored close to the perimeter either side of a joint or fissure in the rock mass. Changes in distance (relative displacement) in three measuring directions are recorded manually with a dial gauge. These changes in distance reveal the relative displacement of the two blocks flanking the joint or fissure. The aperture as well as the relative displacements of the joint or fissure surfaces parallel and orthogonal to the perimeter (width direction and depth direction) are determined. The fissurometer orientation and the measured relative displacements allow the absolute displacements of the blocks bounding the joint or fissure to be calculated, as well as the associated displacement directions. In addition, the subsequent measurements allow the spatial and temporal development to be determined.

6.1.4 Temperature measurements

In addition to the specific stresses or deformations, the temperature is also measured at almost every measuring point of the aforementioned geomechanical and monitoring measurements. These temperatures are used as part of the analysis of the large-scale temperature field in the exploration mine, and its development over time (see Chapter 5), as well as to temperature-correct the stress and deformation measurements in accordance with the sensor-specific temperature dependencies. The deformation measurement results made available by DBE are temperature-corrected.

6.2 *Measurement locations*

The geomechanical measurements are evaluated separately for the following zones:

- **Shaft 1 and shaft 2**
Shaft 1 and shaft 2 are vertical underground workings which were sunk through the overburden using the ground freezing method. With the exception of the drift levels, the shafts are not influenced by any other underground workings. Fresh air is drawn into the underground workings down shaft 1 and the fluctuations in the relative air humidity and the outside temperature can directly be detected in the shaft. Shaft 2 is used amongst other things as upcast ventilation shaft. Changes in the outside weather conditions (temperatures, air humidity) are not detected here. The shafts were sunk in the Zechstein 3 sequence (Leine-Folge) within the salt dome.
- **Infrastructure area and return air level**
The main underground workings of the infrastructure area (workshops, store rooms, etc.) were constructed at the 840 m level. The lower drifts cut at the 880 m level and the 930 m level are also part of the infrastructure area. In addition, the underground workings for the return air level were drifted at the 820 m level. This monitoring zone has a height of 110 m and is characterised by a high density of excavation, particularly at the 840 m level. The underground workings cut through several stratigraphic units (halite) of the Zechstein 3 (Leine-Folge).
- **Exploration area 1 (EB1)**
The EB1 touches the north of the infrastructure area. It is bounded by cross-cut 1 West, the northern cross-measure drift of EB1 and cross-cut 1 East. The underground workings are driven in the Zechstein 2 (Steißfurt-Folge).

Five exploration horizons were set up at different depths in the salt rock areas in each of the shafts:

- Shaft 1:
 - Exploration horizon 1 (EH-350), depth -354.0 m bsl
 - Exploration horizon 2 (EH-450), depth -455.6 m bsl
 - Exploration horizon 3 (EH-550), depth -554.6 m bsl
 - Exploration horizon 4 (EH-650), depth -652.4 m bsl
 - Exploration horizon 5 (EH-720), depth -719.5 m bsl

- Shaft 2:
 - Exploration horizon 1 (EH-370), depth -373.4 m bsl
 - Exploration horizon 2 (EH-450), depth -453.4 m bsl
 - Exploration horizon 3 (EH-570), depth -575.8 m bsl
 - Exploration horizon 4 (EH-670), depth -674.1 m bsl
 - Exploration horizon 5 (EH-760), depth -765.4 m bsl

Each of these exploration horizons comprises a convergence measurement profile, three inclinometer measurement chains, four or six extensometer measurement boreholes and three measurement boreholes equipped with stress monitoring stations. The measurement boreholes are all arranged in different directions with the aim of recording the rock mass deformations and stress changes around the shafts as completely as possible. Figure 6.10 shows the arrangement of the measurement boreholes and the instruments in one of these exploration horizons.

With the exception of the highest exploration horizon of each shaft which has a reduced measurement scope, the arrangement of the measurement boreholes and the measuring instruments (Figure 6.10) is identical in all of the exploration horizons in a shaft. The alignment of the measurements in shaft 1 is rotated by 90° compared to those in shaft 2.

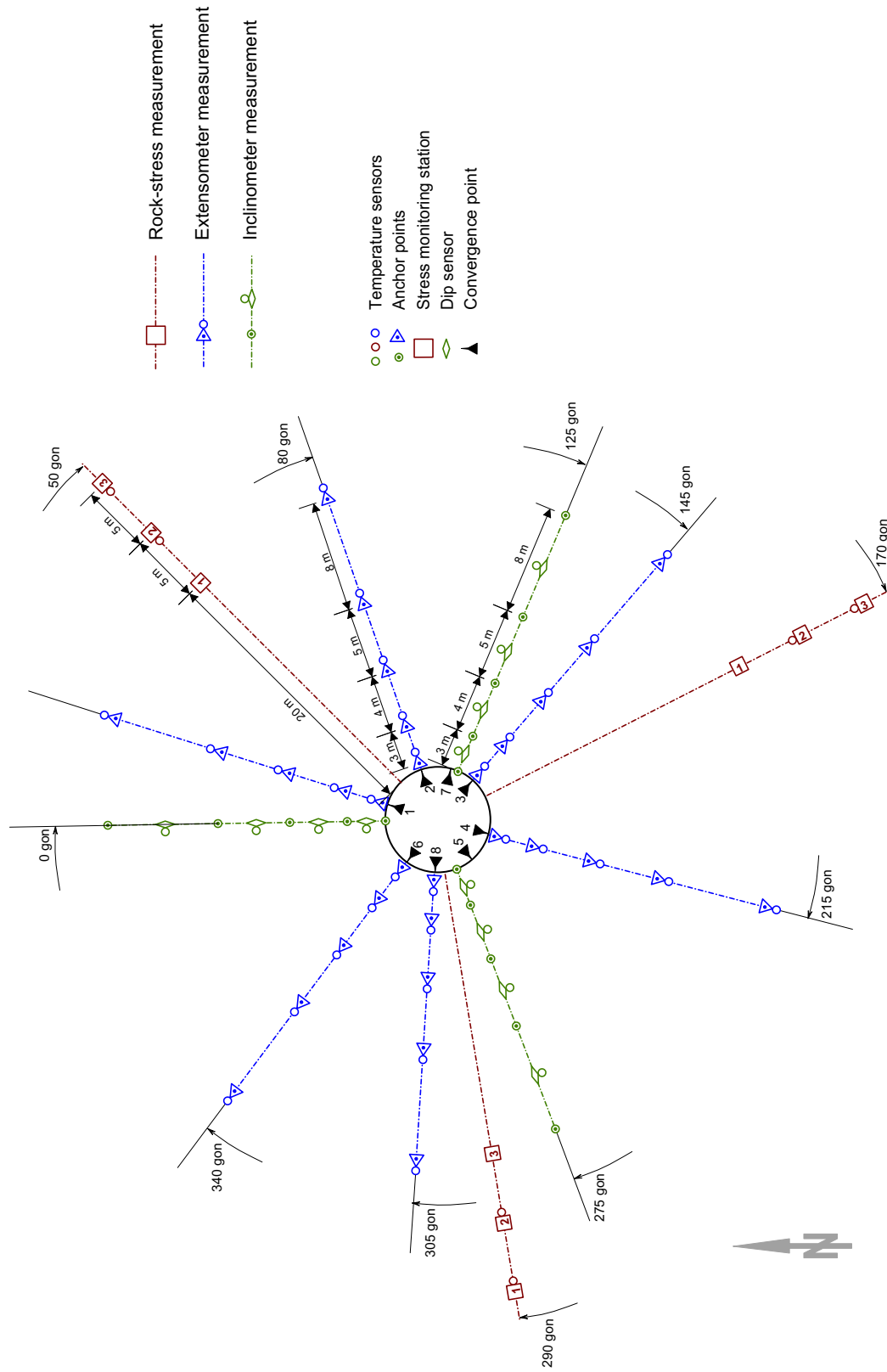


Figure 6.10: Example of the instrumentation installed in an exploration horizon in the shafts (after: DBE)

Dilatometer measurements in the lowest exploration horizons in both shafts were carried out to determine the elastic deformation parameters. The rock stresses around the shafts were determined by overcoring tests using the BGR method (cf. Chapter 6.1.1). Thirty-two overcoring tests in total were carried out in shaft 1 during the drilling of the stress measurement boreholes in exploration horizons EH-450, EH-650 and EH-720. The rock stresses around shaft 2 were determined by a total of 32 overcoring tests in exploration horizons EH-450, EH-570 and EH-760.

Two fissurometers were installed in a western and south-eastern direction in shaft 2 in measurement profile MH-785 to monitor a joint system. This joint system consists of several separate joints. Some of them are partially open, some of them have been healed with recrystallised halite. The joint dip approximately 55 gon to the south-west and are thus orthogonal to the dip of the Oberes Orangesalz beds at this location (z3OSO). The shaft-landing at the 820 m level was driven to the north-west below this joint system (SCHNIER 2003). Two more fissurometers were installed in shaft 2, but no information about depth, direction or measurement alignment is available.

Additional convergence measurement profiles were set up between these exploration horizons so as to create an almost uniform distribution of the convergence measuring points in terms of depth within the shafts. Relatively closely spaced convergence measurement profiles are also installed in the infrastructure area and in EB1. The uniform distribution of the convergence measuring points throughout the underground workings means that the convergence measurements can be considered as a large-scale monitoring technique. It enables the continuous spatial and temporal analysis of the deformation behaviour of the mined portion of the rock mass.

The other measuring techniques, on the other hand, are localised monitoring measurements. Fissurometer measurements are used at the exploration level to monitor the Gorleben Bank, which outcrops exclusively in the underground workings of the infrastructure area, the return air level and the undercuts. Extensometers and stress monitoring stations at the exploration level have been exclusively installed in exploration locations. These exploration locations are localised zones within the underground workings with different exploration objectives:

- Exploration location 1 (EL1) was set up in cross-measure drift 3 east as the eastern extension of the main drift at the 840 m level. The rock mass behaviour of the younger halite beds (Leine-Folge z3) is being investigated here (long-term stress measurements as well as extensometer and convergence measurements) under only slightly disturbed conditions because of the minor influence of the neighbouring underground workings (Figure 6.11). During drilling of the boreholes for

6.3 Results of the in-situ measurements

6.3.1 Shafts 1 and 2

6.3.1.1 Temperature developments

Temperatures have quite an important influence on the measured deformation values and on the detected stress changes. The developments of temperature in the monitored areas are therefore discussed before presenting the measured deformations and stresses. Special ventilation was required during the sinking of shaft 1 and shaft 2. A heating system for the ventilated air was installed to maintain uniform working conditions in the shafts. The influence of the special ventilation on the temperatures in shaft 1 is evident in Figure 6.14 in the relatively constant temperature trends from the start of temperature recording to October 1996 – this example shows the measurement points for the extensometer CG410E at exploration horizon EH-450.

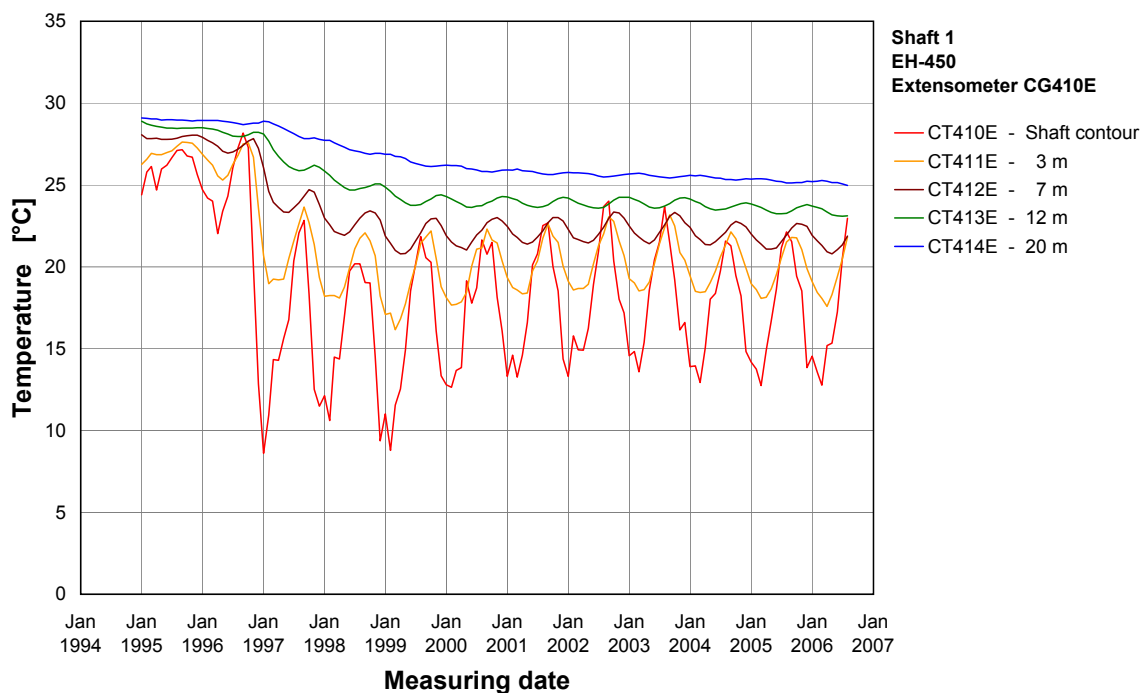


Figure 6.14: Development of temperature at the temperature sensors of extensometer CG410E installed in exploration horizon EH-450 in shaft 1

The special heating system for the ventilation used in shaft 2 was turned off before the setting up of the exploration horizons in shaft 2. The temperatures measured in shaft 2 therefore show seasonal fluctuations up to October 1996 – although the fluctuation of at most 7 °C is relatively low. The temperatures shown in this example were recorded at the measurement points of the extensometer CG420E installed in exploration horizon EH-450 (Figure 6.15).

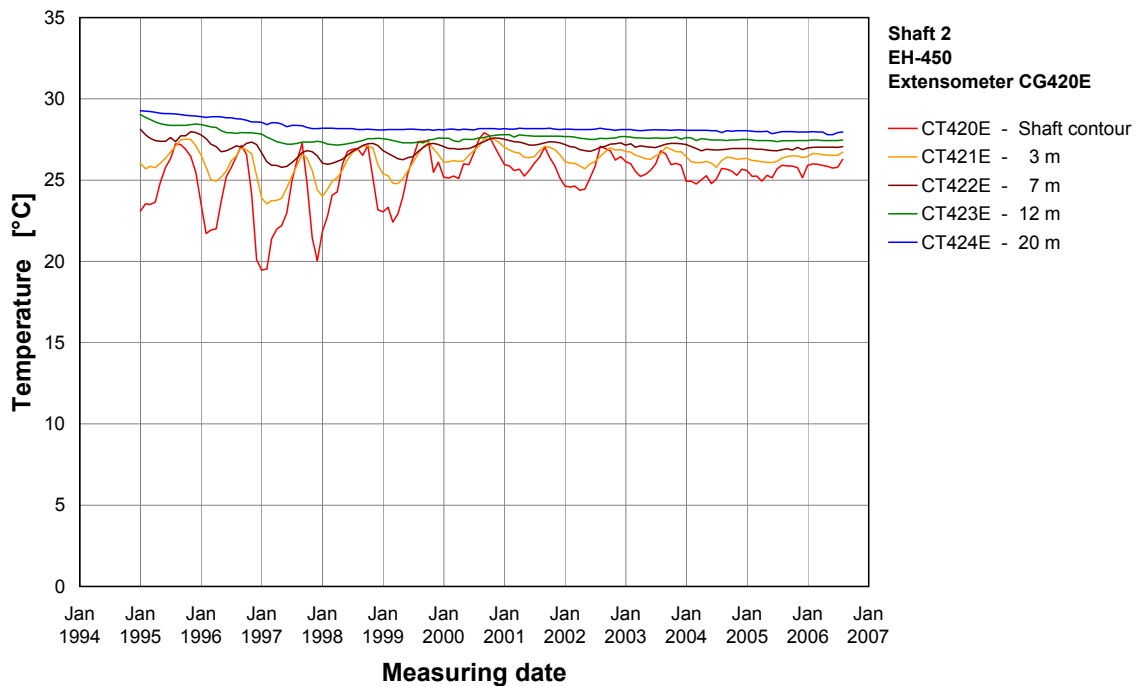


Figure 6.15: Development of temperature at the temperature sensors in extensometer CG420E installed in exploration horizon EH-450 in shaft 2

The ventilation was shifted to circulation ventilation of the underground workings following breakthrough of the main drift between the two shafts in the exploration mine in October 1996. The fresh air is drawn in down the shaft 1, flows through the flat and inclined underground workings to return to the surface via shaft 2. This flow of air transfers temperature changes at the surface into shaft 1. Over the course of a year, this causes the rock mass to warm up during the summer months and cool down during the winter months.

These warming and cooling processes are clearly detectable on the perimeter of shaft 1 by the relatively large fluctuations of the measured rock mass temperatures over the year (Figure 6.14). The seasonal temperature fluctuations decrease with increasing distance from the shaft perimeter. These seasonal temperature changes are no longer detectable at a distance of 20 m from the shaft perimeter. However, a gradual cooling down of the rock mass can be seen since the switch from special ventilation to natural ventilation in 1996. This cooling down of the rock mass is attributable to the relatively low temperature of the ventilation air compared to the relatively high rock temperatures. This difference in temperature transfers heat from the rock mass to the air causing the rock mass to cool down gradually until it reaches a stationary temperature distribution. The temperatures of the shaft perimeter rose on average by 3 °C to 4 °C when the heating system for warming up the ventilation air was installed in the shaft in December 1999.

Similar temperature trends were seen in shaft 2. Establishing through-flow ventilation in October 1996 originally caused a slight decline in the minimum temperatures by around 3 °C in the contour of the shaft. However, once the heating system for the ventilation air was installed in the downcast shaft 1 in December 1999, the minimum rock temperatures rose again by up to 5 °C. The seasonal fluctuations are much lower compared to shaft 1 and do not penetrate as far into the rock mass. This is attributable to the warming of the ventilation air as it flows through the underground workings. In addition to the increased temperature of the ventilation air, there is a smaller difference between the minimum and maximum temperatures of the ventilation air. Thus temperature changes at the surface have only a minor impact on the temperatures of the ventilation air returning to the surface in shaft 2. The warming up of the ventilation air in the mine means that, compared to shaft 1, the difference between the rock temperature and the ventilation air temperature is lower in shaft 2 and consequently the rock mass cools down much more slowly.

6.3.1.2 Determination of primary stress

Overcoring tests (BGR method) were carried out as the measurement boreholes were being drilled in each of the exploration horizons. Figure 6.16 shows the measurement plots from three overcoring tests carried out at various depths in shaft 2. These typical plots all show the characteristic changes which take place in ductile rock salt masses during overcoring tests.

A more or less pronounced reduction in the pilot borehole diameter is initially recorded at the beginning of the overcoring test. The minimum diameter of the pilot borehole is reached when the overcoring process reaches the measurement level of the sensor. An enlargement in the pilot borehole diameter as a result of stress release deformation in the rock core is then observed as the overcoring proceeds. When overcoring has continued for an adequate distance, the stationary phase with no change in the measured values is reached, which reflects complete stress release in the overcored specimen.

A notable feature is the change in the characteristics of the measurement curve with increasing depth: on the one hand, there is a significant increase in the pilot borehole convergence during the first phase of the overcoring process; and on the other hand, the stress release deformations decrease with increasing depth. These effects mean that, with increasing depth, there is a significant drop in the final measured values for changes in borehole diameter after complete stress release. Whilst a major enlargement of the pilot borehole diameter after the overcoring procedure is observed at shallow depths (EH-450), at medium depth (EH-570) the final values are only slightly larger than the reference measurement. At greater depth (EH-760), the final measured diameter change values are actually negative – which means that the overall change is a convergence of the pilot borehole over the whole overcoring procedure.

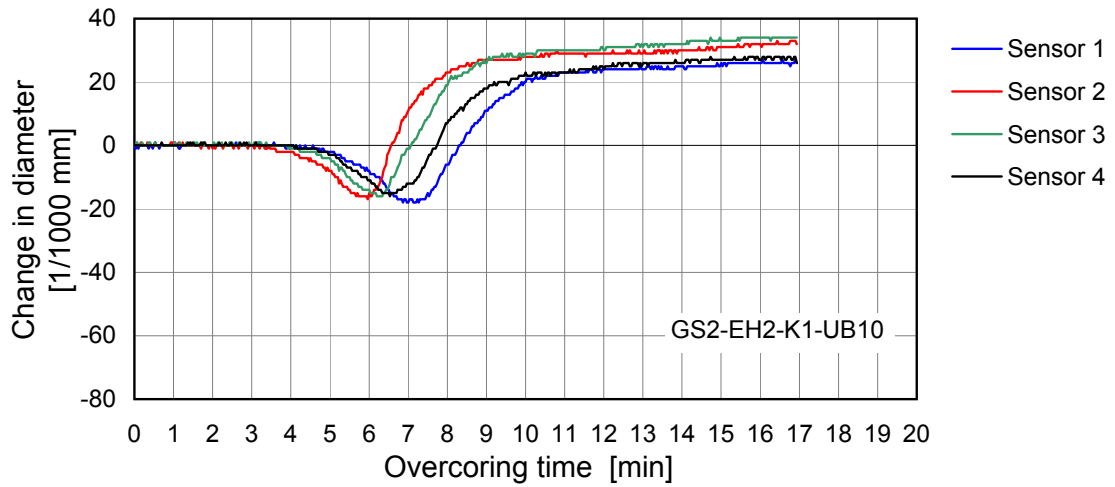
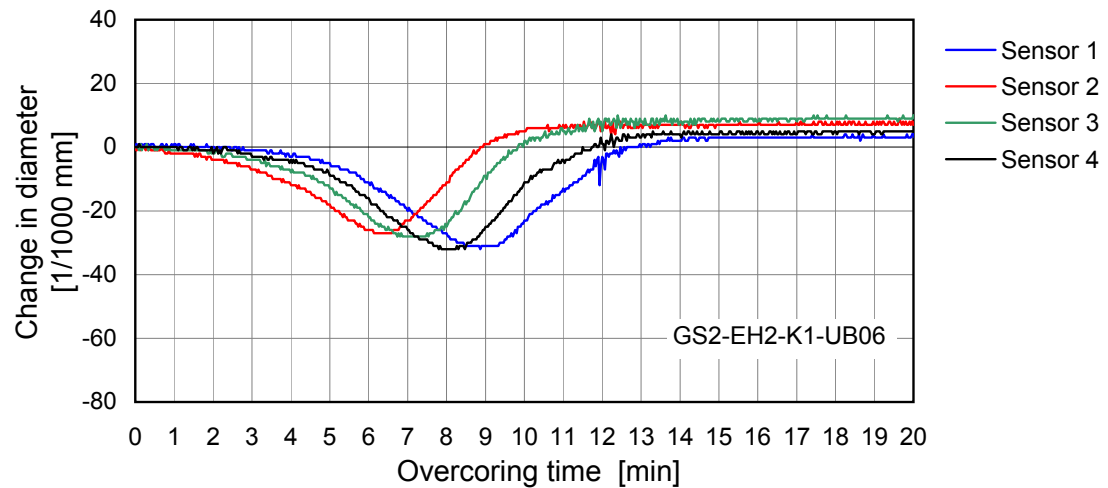
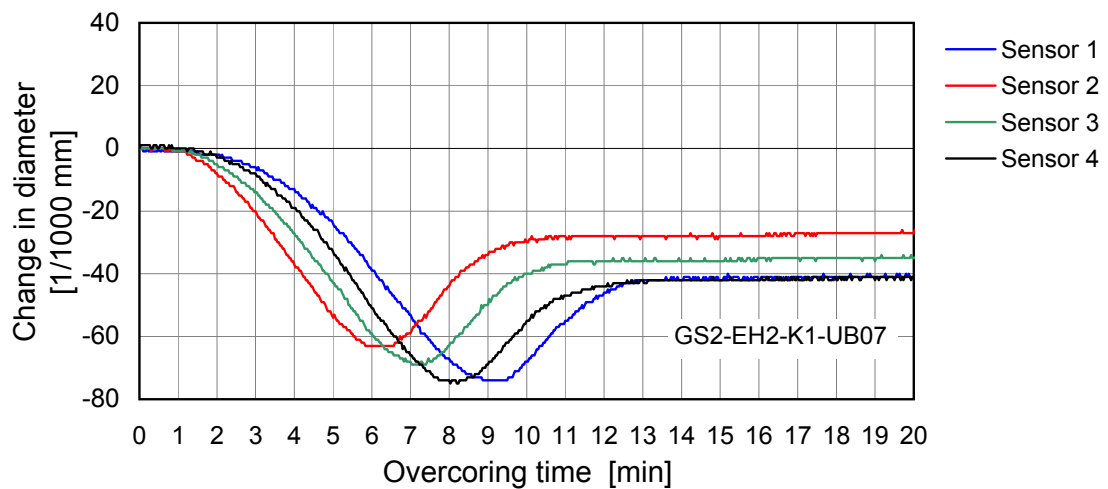
a) Overcoring test at shallow depth (EH-450)

b) Overcoring test at medium depth (EH-570)

c) Overcoring test at great depth (EH-760)


Figure 6.16: Measured changes in diameter of the pilot boreholes during overcoring tests at various depths in shaft 2

This dependency of the observed characteristics of the measurement plots is attributable to the influence of the primary rock stresses and the inelastic material behaviour of rock salt. This involves the initial occurrence of disproportionately large pilot borehole convergence with increasing primary stress caused by temporary relocation stresses acting at the overcoring front. Model calculations of the overcoring procedure taking into consideration the specific material behaviour of rock salt produced very similar plots (HEUSERMANN 1993). The paradox during the stress release phase, that the stress release deformation measured here decreases with increasing primary rock stress, is also attributable to the extremely non-linear inelastic behaviour of rock salt and the associated stress relaxation in the vicinity of the pilot borehole. Model calculations to simulate the overcoring process taking into consideration the high level of non-linear steady-state creep behaviour confirm this effect (cf. Chapter 9.2)

The primary stresses in the rock salt mass determined for shaft 1 and shaft 2 from the overcoring tests are summarised in Figure 6.17 as average values for each of the exploration horizons (HEUSERMANN et al. 2003a).

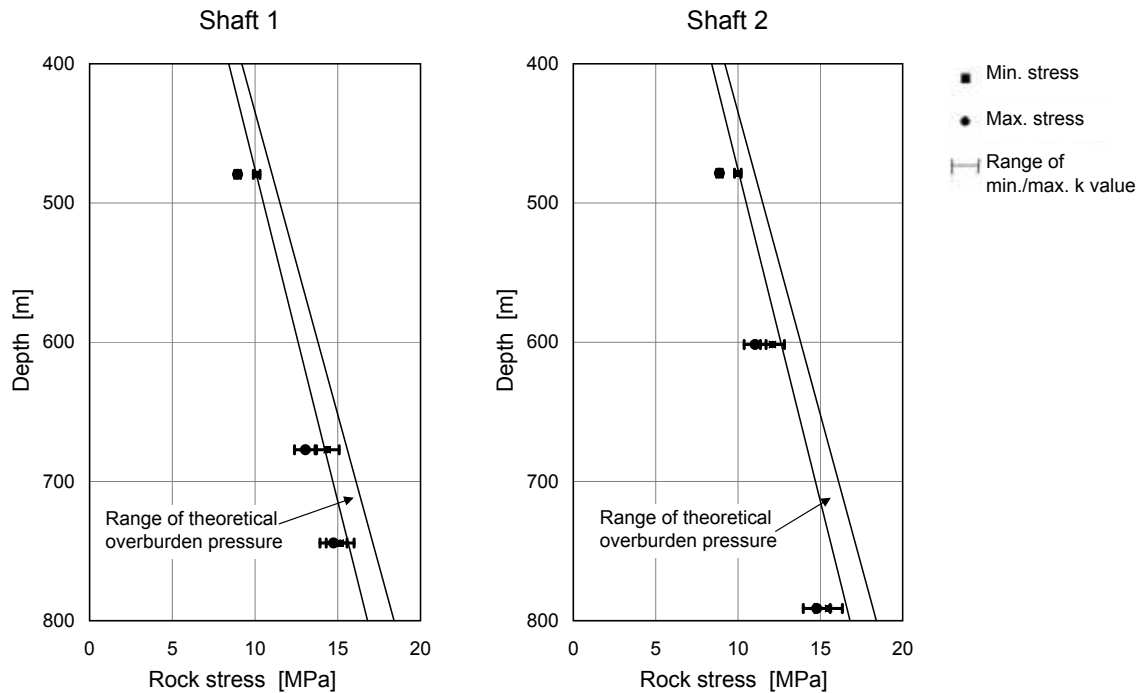


Figure 6.17: Summary of the primary stresses determined by overcoring tests

The maximum and minimum stress components S_1 and S_2 shown in each diagram were only determined for each measurement level orthogonal to the measuring borehole. Based on the overall evaluation of the measurement results generated by boreholes with different orientations, it is valid to approximately equate the stress components S_1 and S_2 with the principal stresses. The figure also shows the range of the calculated stress measurement

values derived from the numerical modelling of the overcoring process (Heusermann et al. 2003b). The upper boundary represents a very ductile material behaviour, the lower boundary less ductile material behaviour.

As shown in Figure 6.17, the minimum and maximum stresses in each exploration horizon differ by only a small amount, which means that it is justified to assume the presence of an isotropic primary stress state. The maximum stresses are generally horizontal, and the minimum stresses vertical. This is attributable to the influence of the shafts with slightly elevated tangential stresses.

The theoretical stress trend derived from the overburden pressure is shown in each diagram for comparison. Uniform densities were assumed here for the rock mass of 2.1 t/m^3 for the lower limit and 2.3 t/m^3 for the upper limit. The measured stress values are slightly lower than the lower boundary. When the influence of the shaft is taken into consideration, this justifies the assumption that the primary stress state increases linearly with depth with the application of a density of 2.1 t/m^3 .

6.3.1.3 Measurement of long-term stress changes

The measurements recorded by the stress monitoring stations in shaft 1 and shaft 2 reveal a great deal of heterogeneity in terms of change over time, scatter and magnitude. In some cases, a gradual increase in stresses over time is identified. Other stress monitoring stations, however, recorded a decrease in measured stresses over time. In other cases, the measurements indicate an increase in stresses in the first few years, then constant or even decreasing values during the subsequent period. Most of the measured stresses lie between 2 MPa to 5 MPa, only a few stresses were higher.

No direct dependencies of the measured stresses on the measurement location, the installation depth of the stress monitoring stations in the boreholes, the depth of the exploration horizon, or the direction of measurement of the pressure sensor were observed on the basis of the available data supplied by the stress monitoring stations. In particular, the minor differences in stress measurement data, which indicate that there is no significant directional dependency of the measured stresses, support the assumption that an isotropic rock stress state exists in the salt dome, as already interpreted from the results of the overcoring tests.

The overall stress measurement data in the shafts indicate seasonality, with local maximum values in spring, and local minimum values in autumn. The temperatures measured at the stress monitoring stations only show a slight decrease in rock mass temperatures over the whole measurement period but with no seasonal fluctuations. However, there is a

clear correlation between the yearly stress changes and the seasonal fluctuations in rock mass temperatures at the perimeters of the shafts. This situation is shown in Figure 6.18, which presents the development of the stress measurement values and the corresponding temperatures in exploration horizon EH-450 in shaft 1 as a typical example. The changes in rock mass temperature at the perimeter of the shaft here (Figure 6.18, CT410E) reflect the changes in temperature of the ventilation air.

This clear dependency of the stress measurement values on the ventilation air temperatures results in much higher stress changes associated with temperature fluctuations in shaft 1, than shown by the results of the long-term stress measurements in shaft 2, because of the higher seasonal temperature fluctuations of the ventilation air in the downcast shaft 1 than in the upcast shaft 2.

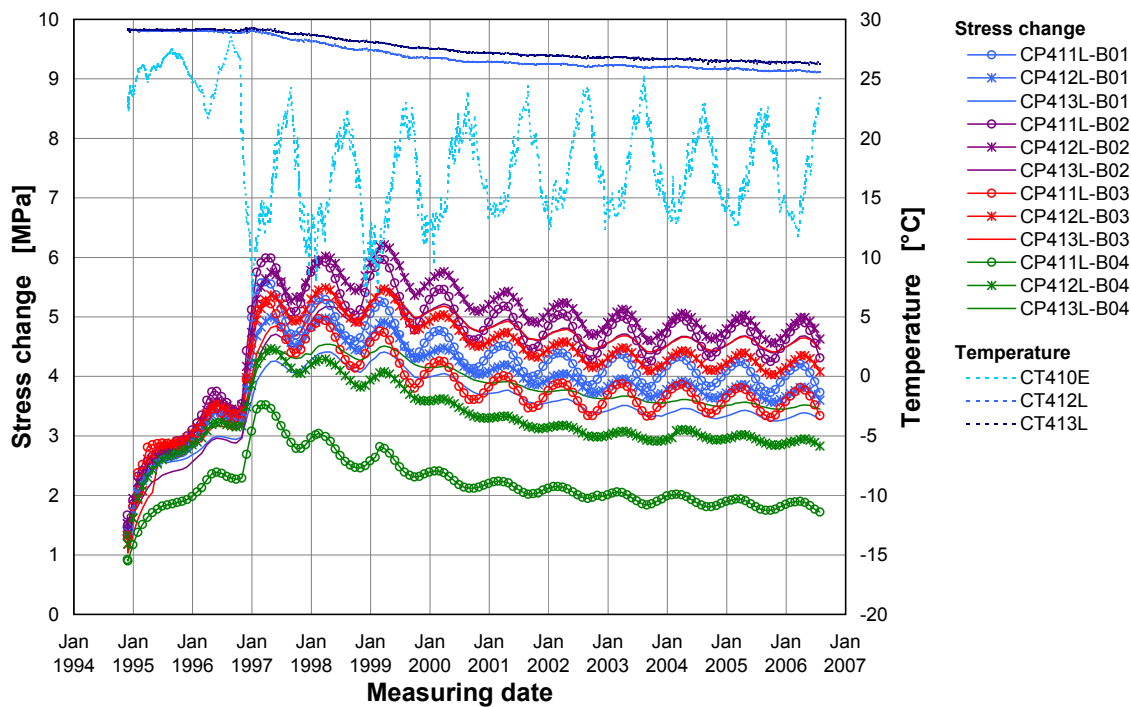


Figure 6.18: Influence of ventilation air temperatures on the measured stress values in exploration horizon EH-450 in shaft 1

These stress fluctuations caused by the changes in temperature of the ventilation air are attributed to thermally induced deformation of the rock exposed at the perimeter of the shaft. Model calculations described in detail in Chapter 9.3 were carried out to clarify this situation.

Because of the relatively small fluctuations in stress of 0.2 MPa to 0.7 MPa versus the comparatively large change in air ventilation temperatures of around 20 °C, no temperature correction of the measured stress values is needed for the long-term analysis of the rock mass stresses.

The decrease in stress after reaching a maximum, which is observed to varying degrees depending on the measurement location, is attributable to the cooling down of the rock mass over a large area. This cooling down gives rise to contraction and therefore to stress release in the rock mass which counteracts the increase in stress caused by creep deformation.

The rock mass cools down relatively quickly after the sinking of the relevant section of the shaft because of the large temperature gradient between the shaft perimeter and the deeper parts of the rock mass. From the time the underground workings are excavated, the cooling slows down more and more as time passes until a stationary temperature distribution is reached and no further cooling down takes place. The stress release will therefore asymptotically approach a final stationary value and thus it can be assumed that the stress will increase again in the long term. A more detailed interpretation is given in Chapter 6.3.2.3.

6.3.1.4 Dilatometer measurements

Two dilatometer measurements were carried out at the lowest exploration levels in each shaft (shaft 1: EH-720, shaft 2: EH-760) to determine the modulus of elasticity of the rock mass. Relatively low average values of 19.8 GPa and 12.9 GPa were recorded in shaft 1. Slightly higher moduli of elasticity of 23.5 GPa and 18.1 GPa were determined in shaft 2.

6.3.1.5 Deformation measurements

The convergence measurement curves in each of the shafts show a qualitative similarity independent of measurement location, and therefore also independent of depth. An example is shown in Figure 6.19 for measurement horizon MH-652. The sketch in Figure 6.19 shows the alignment of the main measurement lines (red) and the ancillary measurement lines (blue) of the convergence measurement stations in shaft 1. The gap in the measurements from the end of 1998 to mid-2001 was due to operational circumstances which prevented manual recording over this period. Other deformation measurements were continued over this period with the use of automatic recording.

Because the convergence measurement stations were installed fairly soon after the excavation of the measurement profiles, the convergence measurement stations initially recorded a significant increase in convergence which was attributed to the continuing work sinking the shafts.

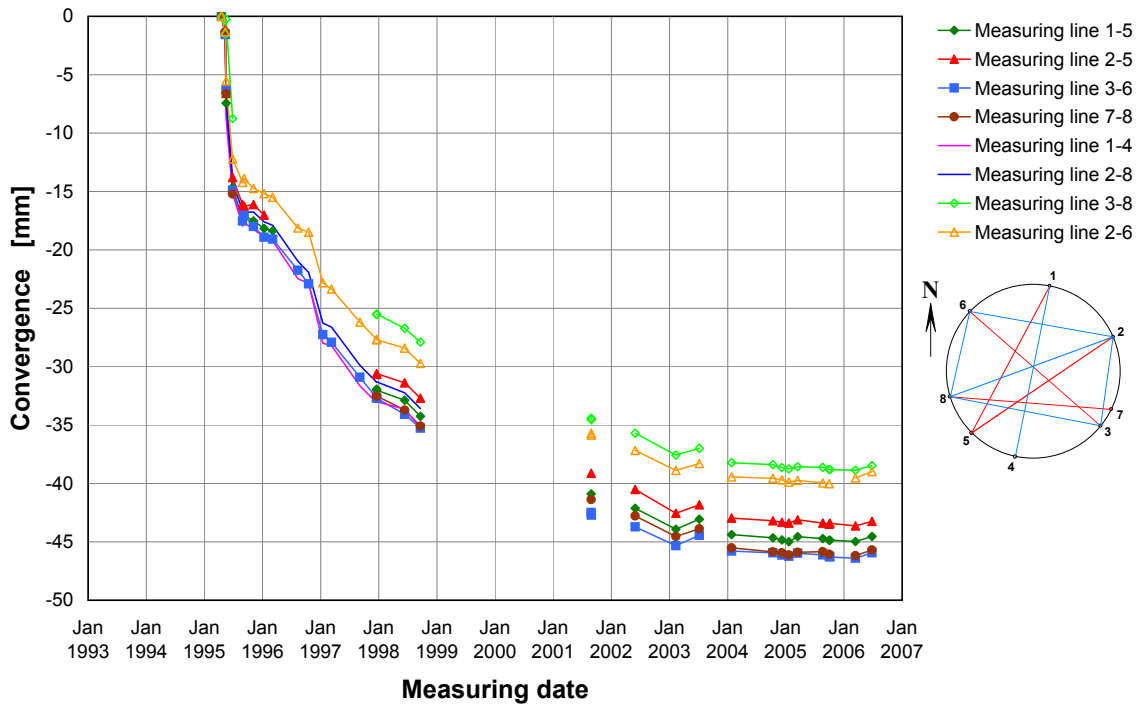


Figure 6.19: Change in convergence at convergence measuring station CG310K at a depth of -652 m bsl in shaft 1

A degressive development in convergence over time is then identified during the subsequent period resulting in almost constant convergence measurement values after a few years. There is, however, a sometimes considerable scatter in the absolute convergence measurement values depending on the measurement location.

Because of the different time periods over which the measurements took place, the period from the beginning of 2003 to the end of 2005 is selected for comparison of the measured convergence rates. This excludes effects associated with excavation and the missing measurements from 1998 to 2001, and enables the deformation behaviour of the rock mass to be analysed with respect to different stratigraphic units. The average convergence rates in the main measuring lines of the convergence measurement profiles in shaft 1 are shown in Figure 6.20 for the period from the beginning of 2003 to the end of 2005.

Extremely low convergence rates were determined in the Oberes Orangesalz to Bank/Bändersalz (z3OSO-BK/BD) in measurement horizon MH-354 – convergence rates which can be ignored when compared to the other measurement horizons. The highest convergence rates were measured in measurement horizon MH-652 in all measurement directions, as well as in horizon MH-554 in direction 1-5. Relatively uniform convergence rates with values of -0.2 mm/a to -0.4 mm/a and greater or lesser degrees of fluctuation, were determined in the convergence measurement profiles in the other horizons from 2003. Figure 6.20 does not reveal any clear increase in convergence rates with depth.

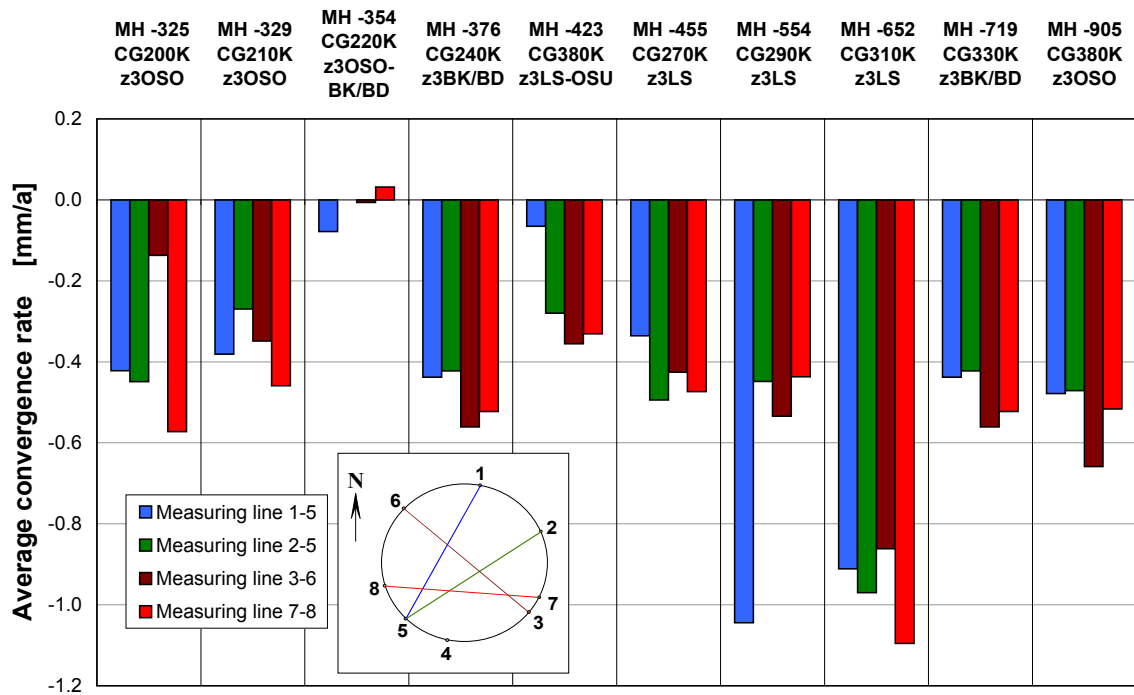


Figure 6.20: Average convergence rates from the beginning of 2003 to the end of 2005 for the main measuring lines of the convergence measurement profiles in shaft 1

There does, however, seem to be a stratigraphic influence because the convergence rates measured in the Liniensalz (measurement horizons MH-554 and MH-652) have higher deformation rates than the measurement results in other stratigraphic units. Nevertheless, no elevated convergence rates were measured in the Liniensalz (z3LS) in MH-455. This measurement can probably be attributed to the position of the Liniensalz in the core of an anticline with underlying Orangesalz (z3OS). In measurement horizon MH-554, Orangesalz is also found higher up in the mine as well as to the south-east and north-west. The convergence measurement profile 1-5, however, with the larger convergence rates, is aligned with the strike of the Liniensalz. This finding would seem to verify the assumption that the Liniensalz beds have a greater deformability. The presence of less deformable Orangesalz would then have the effect of reducing the amount of deformation.

Figure 6.21 shows the calculated convergence rates for the main measuring lines of the convergence measurement profiles installed in shaft 2. The convergence rates are significantly higher in shaft 2, measuring horizon MH-331 where Orangesalz (z3OSO) outcrops. The convergence rates of 1.0 mm/a to 1.5 mm/a are much higher than in the other measurement profiles and also much higher compared to the convergence rates in shaft 1 (cf. Figure 6.20).

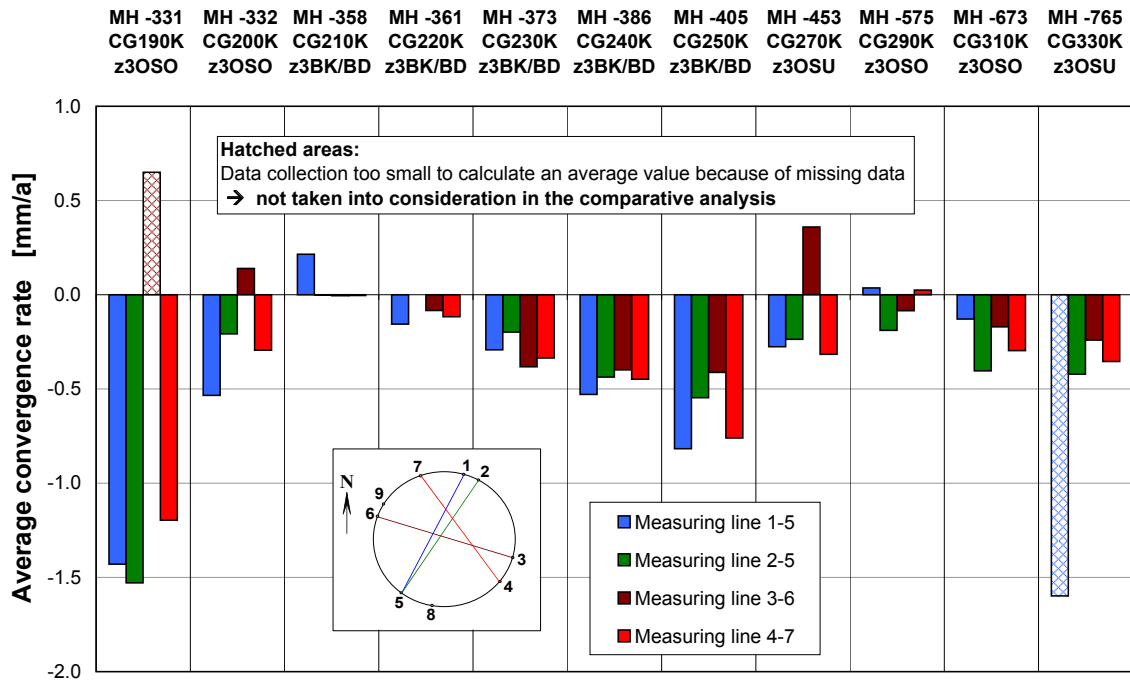


Figure 6.21: Average convergence rates during the period from the beginning of 2003 to the end of 2005 for the main measuring lines of the convergence measurement profiles in shaft 2

Negligible convergence rates were determined in measuring horizon MH-358 where Bank/Bändersalz (z3BK/BD) crops out. The convergence rates determined for the other exploration horizons are in the same range as those in shaft 1. As shown in Figure 6.21, convergence rates in the Bank/Bändersalz appear to be depth-dependent. However, this kind of increase in convergence with depth is not seen in any other parts of shaft 2.

Like the long-term stress measurements, the results of the extensometer and inclinometer measurements in the shafts are also significantly affected by temperatures. Figure 6.22 shows an example of the influence of temperature on extensometer measurements.

Figure 6.22 shows the measured displacements relative to the perimeters of the shaft of each of the measuring points of extensometer CG410E in exploration horizon EH-450 plotted alongside the temperatures recorded at the measuring points. These results show significant seasonal fluctuations in the measured relative displacements which evidently correlate very well with the seasonal fluctuation of the temperatures measured at the perimeter of the shaft (head plate). Although similar measurement results are observed in shaft 2, the range of fluctuations is smaller because of the higher temperature of the ventilation air overall and the smaller temperature fluctuations.

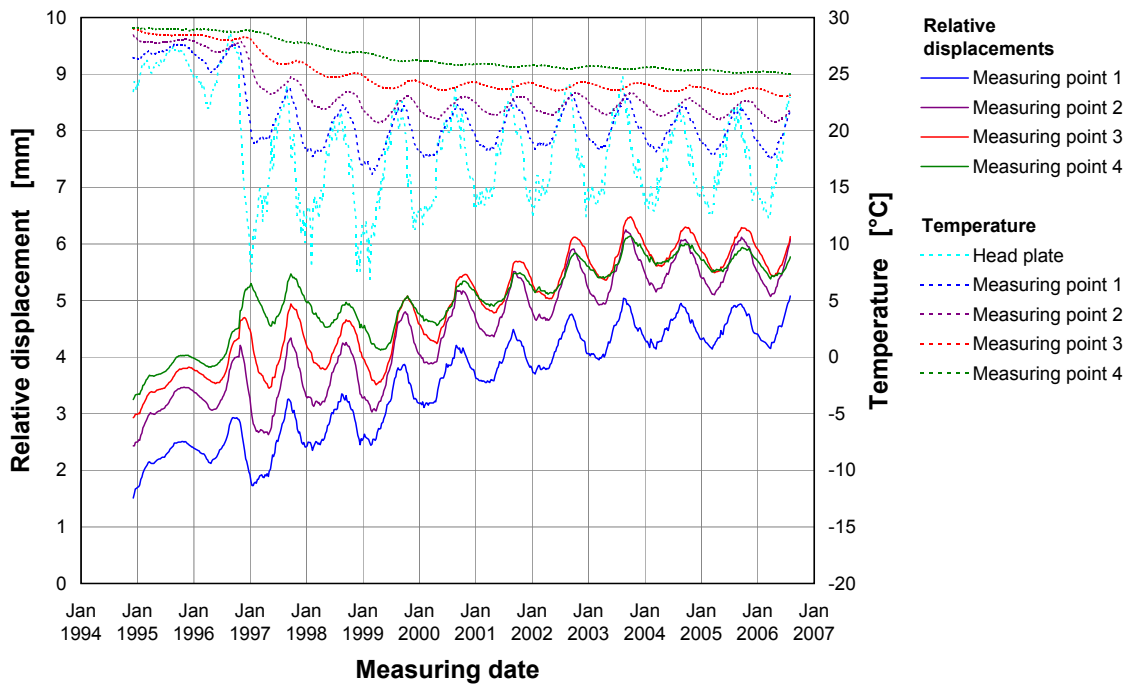


Figure 6.22: Measured relative displacements and temperatures at the CG410E extensometer in exploration horizon EH-450 in shaft 1

This situation has already been discussed and interpreted in Chapter 6.3.1 “Long-term stress measurements”, with a reference to the model calculations on the temperature dependency of the measured stresses and deformations in Chapter 9.3.

Against this background, analysis of the measured deformation and stress changes requires a moving average value of the measurement data calculated for a time period of one year. This enables the long-term trends in the measured values to be determined. The deformation of the sections is calculated based on the average values of the relative displacements. These are not influenced by the seasonal temperature fluctuations as shown in the example given in Figure 6.23 of extensometer CG410E in exploration horizon EH-450 in shaft 1.

This diagram of the section deformations also reveals that the largest deformations are in the rock mass close to the perimeter of the shaft (Section 1: 0.4 – 3 m). Much smaller deformations are measured in the deeper parts of the rock mass. This finding is the same in all of the exploration horizons in the shafts. It can therefore be assumed that the largest deformations in the areas close to the perimeter of the shaft are attributable to loosening up processes arising from the excavation activity during the sinking of the shafts.

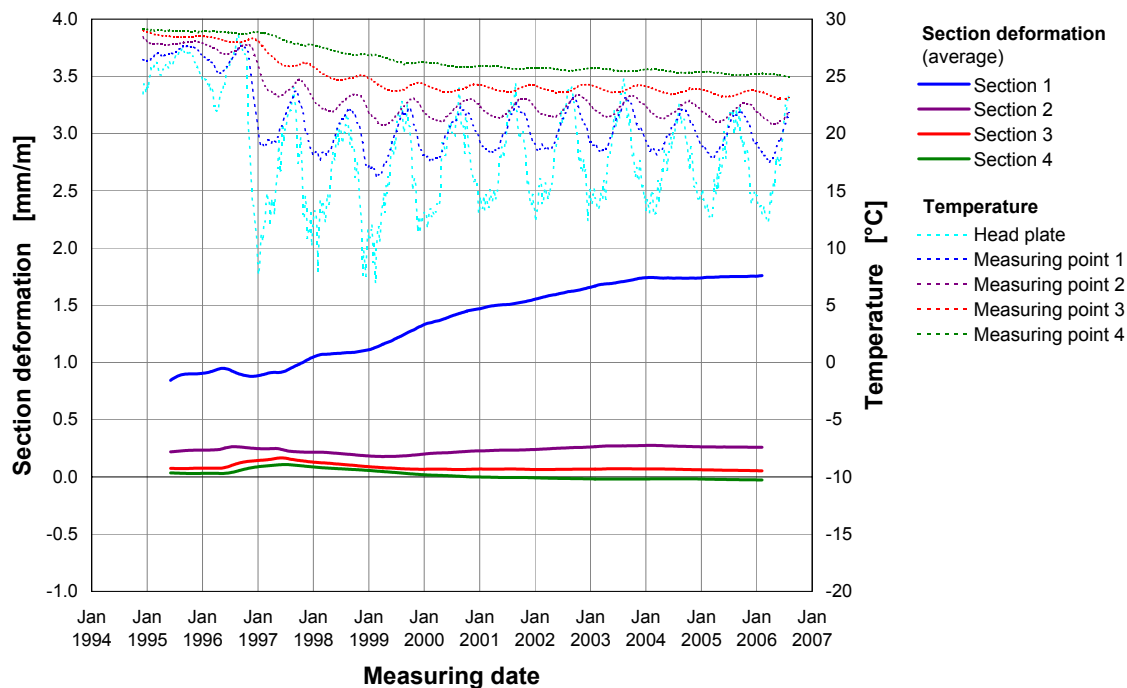


Figure 6.23: Calculated section deformations and measured temperatures at extensometer CG410E in exploration horizon EH-450 in shaft 1

A notable aspect of the results from the extensometer measurements in shaft 1 is the largely constant level of the values of the section deformations from 2004 onwards, seasonal fluctuation having been eliminated – as shown, for example, in the section deformations displayed in Figure 6.23, and also indicated to some extent in the measured relative displacements in Figure 6.22. This finding is also seen in the extensometer measurement results in shaft 2. However, this transition from rising deformation to constant deformation came about earlier at the beginning of 2001. The moratorium means that this finding cannot be attributed to mining activity. And the measured temperature plots show that there was also no change in the mine ventilation (Figures 6.14 and 6.15). A possible cause of this observation may be systematic influences or changes in the pre-evaluation process (e.g. temperature correction). However, no suitable information has been made available so far to evaluate and interpret the measurement data.

Another possible cause could be stress relocations linked to an excavation-damaged zone in the rock mass close to the perimeter of the shaft. In this interpretation, the deformation in the excavation-damaged zone close to the perimeter of the shaft would gradually decrease until a new equilibrium was reached. This interpretation is basically supported by the changes in deformation observed in the extensometer measurements. However, a verifiable interpretation of these deformation data first requires additional analysis by model calculations.

The section deformations measured by the extensometers do not support the existence of a depth-dependency of the rock mass deformations around the shafts. Nevertheless, the section deformations at exploration horizon EH-650 in shaft 1 are much higher compared to the other exploration horizons. Exploration horizon EH-650 in shaft 1 was installed in Leinesalz (z3LS), whilst other stratigraphic units are exposed in the deeper as well as the higher exploration horizons. Like the convergence measurements, the extensometer measurements indicate that the Liniensalz (z3LS) in shaft 1 has a greater deformability than the other stratigraphic units.

By way of contrast, much lower deformations in the extensometer sections close to the shaft perimeter were observed in exploration horizon EH-370 in shaft 2 than in the deeper exploration horizons. Caution is advised here because the installation of exploration horizon EH-370 was delayed by two years. But the Bank/Bändersalz of the Leine-Folge (z3BK/BD) seems to be more resistant to deformation and this also has an effect on the results of the deformation measurements.

Much larger deformations of the extensometer sections close to the shaft perimeter are observed in exploration horizon EH-760 in shaft 2. In this case, the fold axis occurring in the vicinity of exploration horizon EH-760 could lead to greater deformation of this section compared to the other exploration horizons.

Because the extensometer heads on the perimeter of the shaft are also part of the convergence measurement profiles, it is also possible to compare the extensometer measurements with the convergence measurements. This comparison looks at a total measuring line in each case consisting of the measuring lines of the extensometers installed diametrically in the exploration horizons and the associated convergence measuring lines. The relative displacement of the two deepest extensometer measuring points is calculated as the sum of the measured convergence and the measured displacement of the extensometer measuring lines. By assuming that the deepest measuring points of the extensometers are anchored in zones unaffected by any radial rock mass deformations, these can be initially considered to be fixed points. This means that there should be no relative displacement of the two deepest extensometer measuring points, and thus the sum of the convergence and displacement of the extensometer measuring lines should be zero. The results of this consideration of the extensometer and convergence measurements in the exploration horizons in shaft 1 is shown in Figure 6.24.

The calculated relative displacements shown in Figure 6.24 reveal that rock mass deformations take place even in the zones measured by the deepest extensometer points located around 20 m from the perimeter of shaft 1.

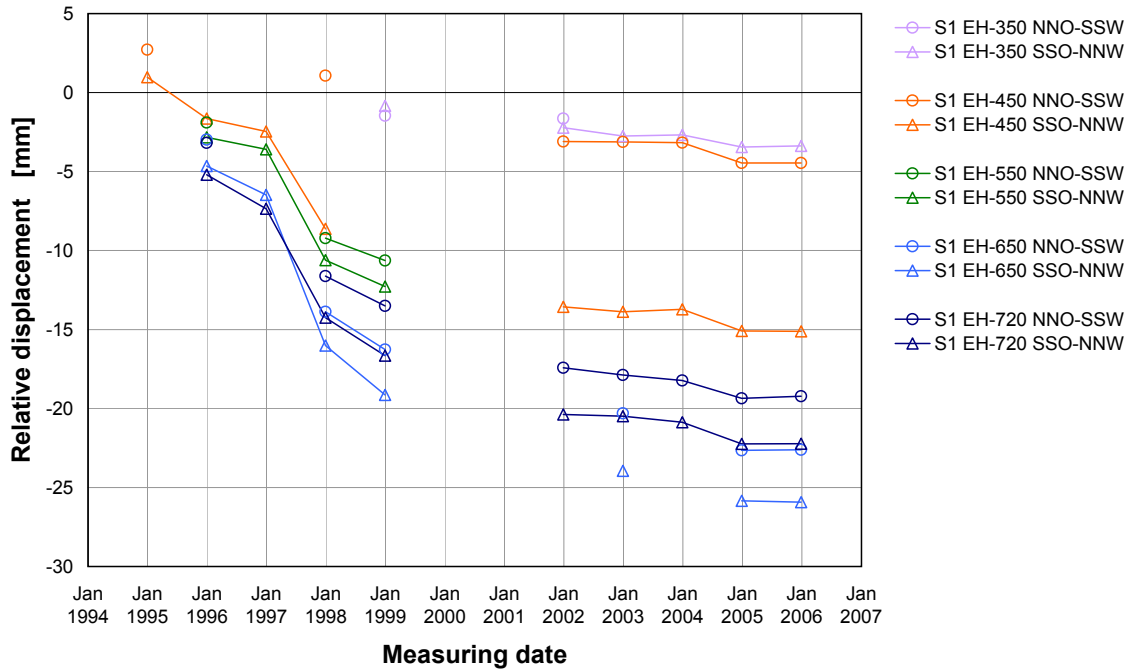


Figure 6.24: Relative displacements at the deepest measuring points of extensometers installed diametrically in the exploration horizons in shaft 1

The negative values for the relative displacement indicate a shortening of the total measuring line. It can therefore be assumed that the rock mass deformations are aligned radially to shaft 1. A general trend of increasing relative displacement with depth can be observed. A similar result is shown by the convergence and extensometer measurements in shaft 2 (Figure 6.25). Rock mass deformations in the deeper-lying rock zones can also be observed here although they are slightly smaller than those seen in shaft 1.

The vertical displacements of the starting points and end points of the individual inclinometer sections are calculated from the inclination changes recorded by the stationary inclinometers. The results of the inclinometer measurements in shaft 1 (Figure 6.26) show that most of the observation points dropped by a maximum of -7 mm from the time the measurements began until the end of 2005. Conversely, the inclinometer boreholes in an east-south-east direction in exploration horizons EH-550 and EH-650, as well as the inclinometer borehole in the west-south-west direction in exploration horizon EH-550, have risen by a maximum of 1 mm over the whole of their lengths or at least in zones close to the shaft. Large rises in the observation points were recorded in the inclinometer borehole in a northerly direction in exploration horizon EH-450. The upward displacement of the perimeter of the shaft here is around 2 mm and initially increases to a maximum value of approximately 3 mm at 7 m from the shaft. The amount of upward displacement then decreases with increasing distance from the shaft until it reaches a value of 0 mm at a distance of 20 m.

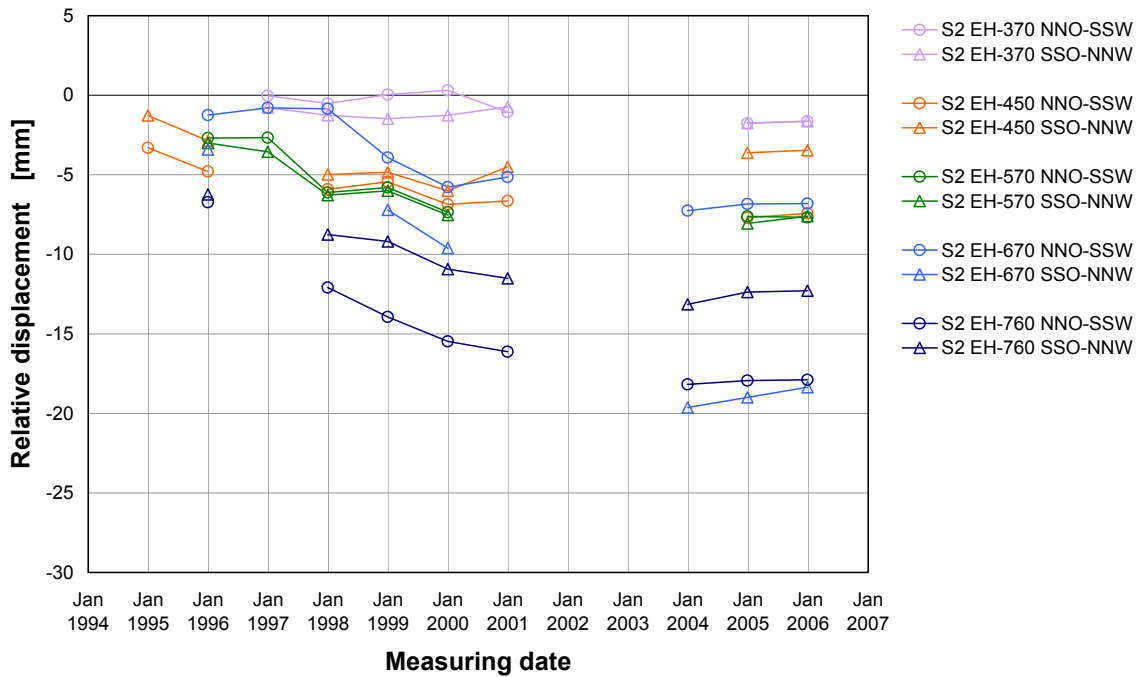


Figure 6.25: Relative displacements of the deepest measuring points of extensometers installed diametrically in the exploration horizons in shaft 2

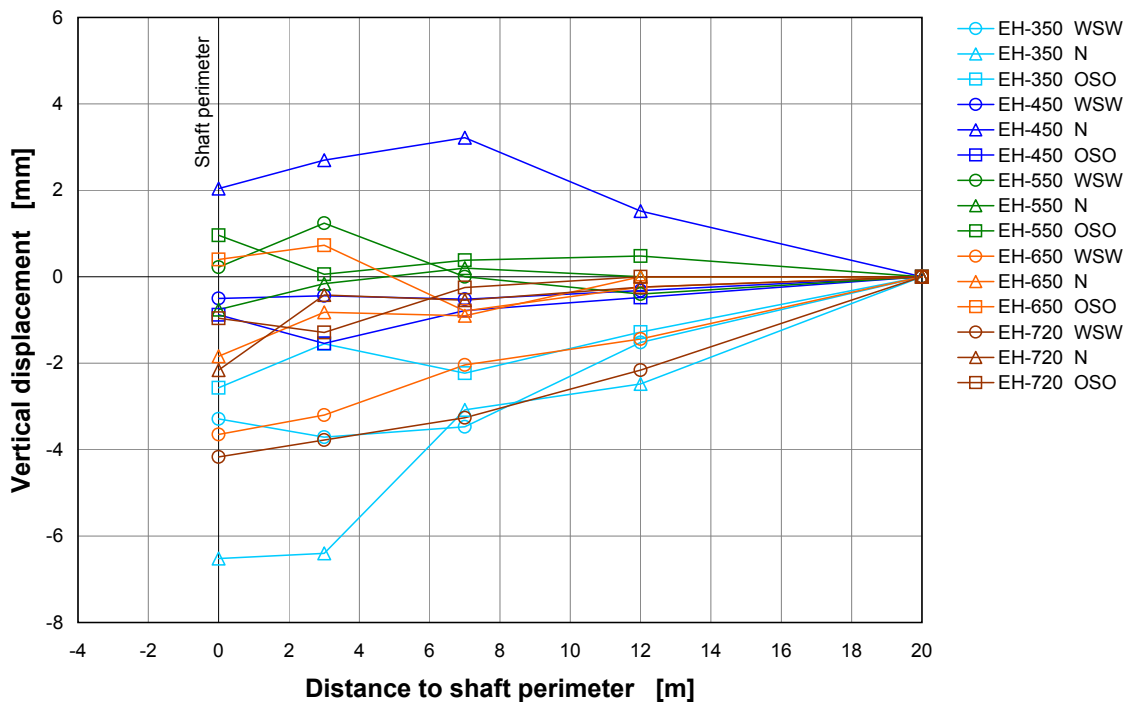


Figure 6.26: Vertical displacements determined from the changes in inclination at the starting points and end points of inclinometer sections in shaft 1

Similar findings are observed in the results of the stationary inclinometer measurements in shaft 2 (Figure 6.27). However, more uplift than subsidence is registered in shaft 2. The maximum subsidence in the zone close to the shaft is around -4 mm, whilst the maximum uplift is around +4 mm.

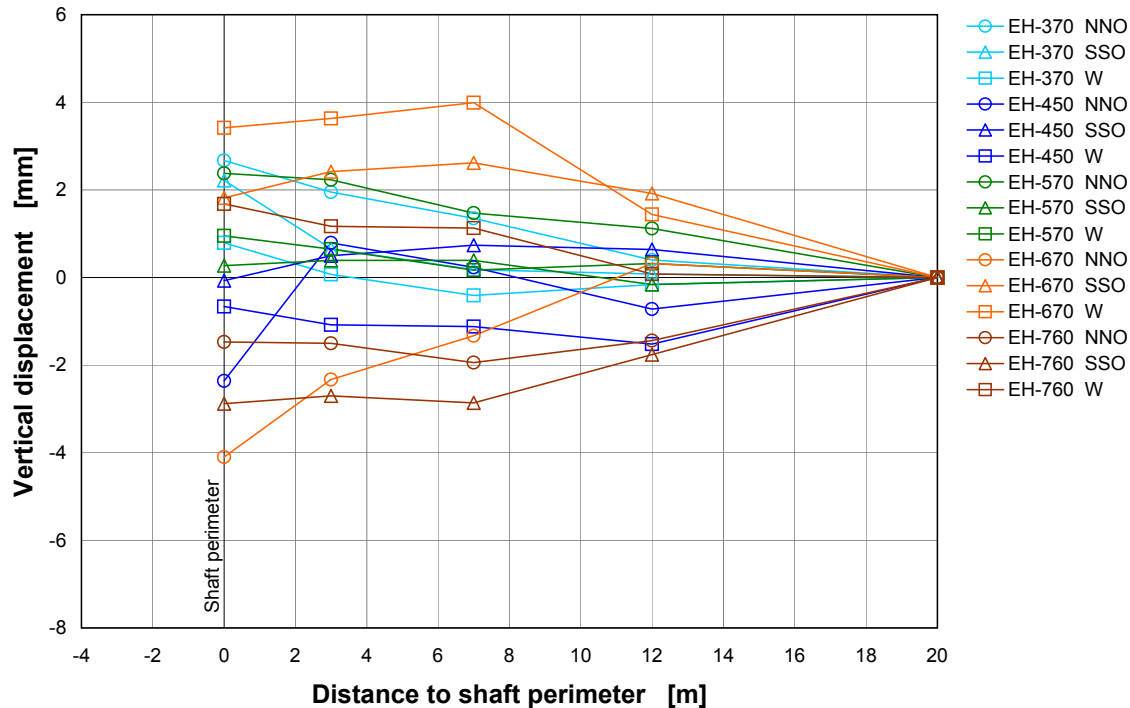


Figure 6.27: Vertical displacements determined from the inclination changes at the starting points and end points of the inclinometer sections in shaft 2

No dependencies on depth or stratigraphy are observed in shaft 1 or shaft 2 for the vertical displacements of the observation points derived from the stationary inclinometer measurements. The results of the inclination change measurements seem to be much more influenced by local variations in the structure of the rock mass or localised relocation processes within the rock mass. It should be noted in this context that the vertical displacements were calculated assuming that no deformation takes place at the deepest points of the inclinometer boreholes located a distance of around 20 m from the shaft perimeter. This assumption only allows conclusions limited to the individual exploration horizon to be drawn and does not take into consideration any large-scale rock mass deformations which could be caused by the drifting of the horizontal underground workings or inclined underground workings, and which may lead to the tilting of the shaft.

The combined analysis of the extensometer and convergence measurements, however, show that rock mass deformations also occur on a large scale in the part of the shaft monitored by measuring instruments. The assumption that no deformation takes place in the deepest parts of the inclinometer boreholes is therefore invalid. This means

that additional measurements are required for a comprehensive analysis of the rock mass deformations around the shafts, recording vertical distance changes between the exploration horizons as well as tilting of the shafts.

Two fissurometers were installed in a south-eastern and western direction to observe a joint system in exploration horizon MH-785 in shaft 2. The measured relative displacements increased initially, but gradually approached almost constant values as shown in Figure 6.28.

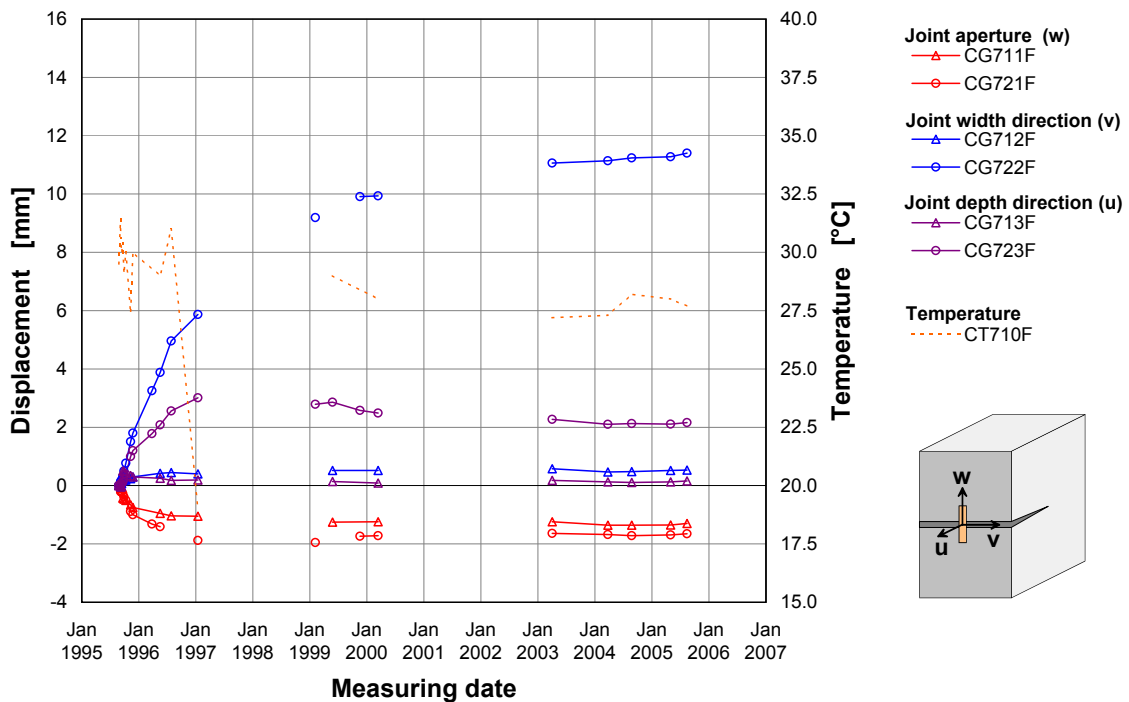


Figure 6.28: Results of the fissurometer measurements in measuring horizon MH-785 in shaft 2

The largest proportion of the total displacement consists of the relative displacement in the joint width direction (at the joint surface parallel to the shaft perimeter) in the south-eastern perimeter (CG710F) and in the joint depth direction (at the joint surface orthogonal to the shaft perimeter) at the western perimeter (CG720F). The measured joint apertures are negative. The measurement results are interpreted as indicating the possible occurrence of displacements in the tilted separating planes aligned towards the centre of the shaft.

6.3.2 Exploration level

6.3.2.1 Temperature development

Figure 6.29 shows as an example the change in temperature over time for the measurement points of three extensometers all installed in the floors of the exploration locations. According to this, the head plate of the extensometer installed at EL2 (the western infrastructure area in the vicinity of shaft 1) has an average annual temperature of 25 °C close to floor level. In EL1 which is located in the eastern exploration area close to upcast shaft 2, a slightly higher average temperature of around 28 °C is measured close to floor level. The average temperatures in EL4, which is located a greater distance from the two shafts, is around 32 °C in the head plate (near floor level) of the extensometer installed at this locality. Seasonal temperature fluctuations are also identifiable at these measurement points and are at their greatest in EL2 at 6 °C to 8 °C. These temperature fluctuations are much lower in EL1 at approximately 3 °C to 5 °C. Temperature fluctuations in EL4 have a maximum of 3 °C and were only observed in the first three years from the start of measurements. The near-floor temperatures were then basically constant. The clear influence of the seasonal temperature changes can be noted in the location-dependent temperature trends on the basis of the observed fluctuations in the measured values and the different average temperatures. This influence decreases with increasing distance to downcast shaft 1.

There are also major differences between the temperature trends in the deeper areas of the rock mass (Figure 6.29). Examples are given for the temperatures of the extensometer measuring points located around 30 m from the floor level. While the rock mass temperature in EL4 only decreased by around 1 °C in the seven years from the time measurements began, the rock mass in EL2 cooled down by approximately 2.5 °C during a six-year measuring period. In EL1 the rock mass temperature decreased by around 11.5 °C since measurements began around eight years previously. These measurement results clearly show the rock mass in EL4 is cooling down much more slowly than in the other exploration locations. This is explained by the rising average temperatures of the perimeters of the underground workings with increasing distance to shaft 1 resulting in a lowering of the temperature differences between the underground workings and the rock mass, and thus reduced heat flows (cf. Chapter 6.3.1.1).

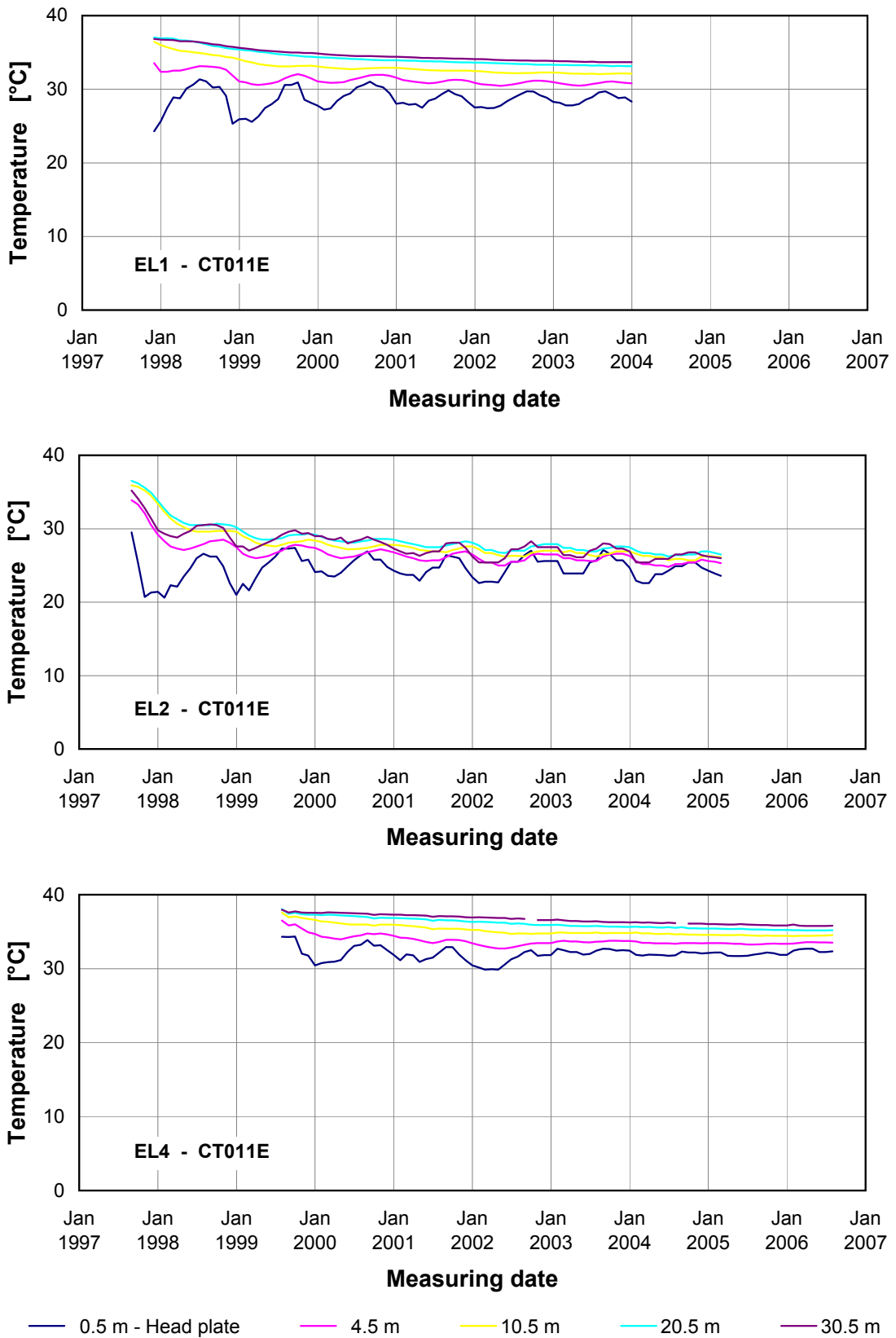


Figure 6.29: Change in temperatures at the measurement points of the floor extensometers installed in the exploration locations

6.3.2.2 Determination of primary stress

Determination the rock stresses at the exploration level is exclusively based on short-term stress measurements in EL1. More than 30 overcoring tests were carried out and evaluated here in a vertical borehole and two inclined boreholes in the floor of the exploration location, and in two horizontal measurement boreholes in the walls of the underground workings.

Figure 6.30 shows an example of the change in diameter over time of the pilot borehole in an overcoring test in EL1. The measurement plots show the characteristic curves for the overcoring tests in ductile rock salt. The significant pilot borehole convergence occurring at the start of overcoring indicates the relatively high rock stresses associated with the great depth of the measurement location at around 840 m.

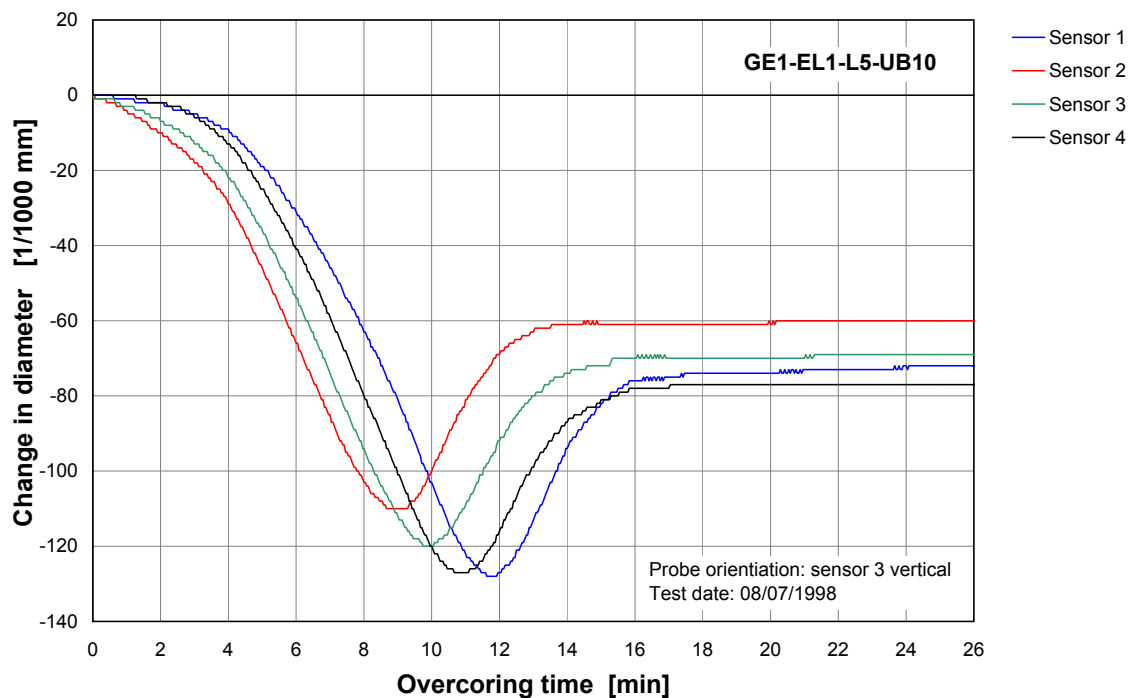


Figure 6.30: Example of an overcoring test in EL1

The overcoring tests indicate that an almost isotropic rock stress is present at exploration location EL1. Most of the measurements show that it is valid to assume a depth-dependent lithostatic primary stress state. A few measurements, however, indicate stress values which are smaller than the theoretical lithostatic pressure. These differences can presumably be explained by the influence of different stratigraphic units at exploration location EL1, and the associated differences in material behaviour – particularly the creep behaviour.

Hydro-frac measurements in horizontal measurement boreholes were also carried out in the walls of the underground workings at EL1 in addition to the overcoring tests (BGR method). The results of the two measuring techniques are compared by comparing the minimum rock stresses determined from the measurements (Figure 6.31). These stresses are derived; on the one hand; from the resting pressures measured in the hydro-frac tests, and on the other hand, from the stress ellipses determined orthogonal to the borehole axis by the overcoring tests. Figure 6.31 shows good correspondence between the results from the two measuring techniques for the measurement boreholes to the south of the exploration location (RB114 and RB118 in Figure 6.11). However, the minimum stresses – particularly in the forward parts of the boreholes with depths of around 20 m – are smaller than the analytically calculated overburden pressure assuming a uniform density of 2.1 t/m³ for the rock mass.

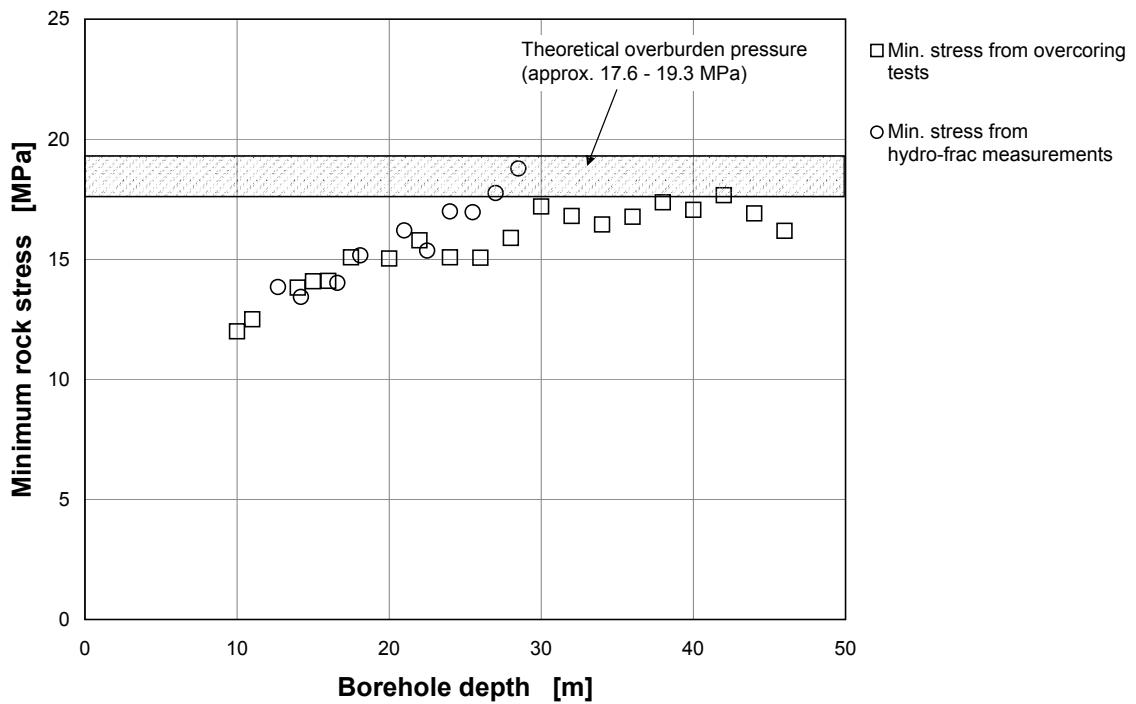


Figure 6.31: Comparison of the minimum stresses derived from the overcoring tests and the hydro-frac measurements

The minimum stresses determined by the hydro-frac tests correspond well with the theoretical overburden pressure in the northern measurement boreholes in EL1 (RB113 and RB265 in Figure 6.11). However, the minimum stresses determined from the overcoring tests at this location are much lower than the overburden pressure.

6.3.2.3 Measurement of long-term stress changes

The long-term stress measurements at the exploration level were also restricted to EL1. Three measurement boreholes were spatially aligned to converge on the same point beneath the exploration location so that the deepest points in the three boreholes are essentially at one point. The monitoring stations installed in these boreholes can be roughly considered to have one shared measuring point. This arrangement and the relative measurement directions of the individual pressure cells make it possible to record the spatial stress state beneath the exploration location. Two more installation boreholes were drilled in the walls of the exploration location in a roughly horizontal alignment (dipping approximately 5°). Stress monitoring stations were installed at the deepest points of both of these boreholes to record the stress components in the plane orthogonal to the borehole axis.

In the floor of the exploration location, there is a good correlation between the measured stress changes in the three measurement boreholes – with the exception of a few pressure cells which probably began to function imperfectly over the course of the measuring period. Figure 6.32 shows, as an example, the trends over time of the measured stress changes in measuring borehole RB116 (cf. Figure 6.11).

The measured stress changes reveal a certain amount of seasonality with a relatively low amplitude of at most 0.1 MPa, which is attributable to the seasonal change in the temperature of the mine ventilation air. The small size of these fluctuations means that no correction of the measured values is required.

The stress change trends over time as measured in the floor of EL1, and shown in Figure 6.32, initially indicate a significant increase in stresses after installation of the stress monitoring stations at the end of 1998, until reaching maximum values between 2.5 MPa and 3 MPa after a few months. The stresses then decrease from this point in time to reach values between 1.8 MPa and 2.2 MPa in the middle of 2006. This stress change over time can be attributed to two counteracting processes taking place in the rock mass.

Firstly, there is the creep of the rock mass, which gradually results in complete friction locking of the stress monitoring stations with the rock mass. Over time, the creep of the rock salt causes the convergence of the measurement borehole and thus a continuous rise in stresses recorded by the pressure cells. This process continues until equilibrium is reached between the rock stresses and the sensor pressure at the measuring location.

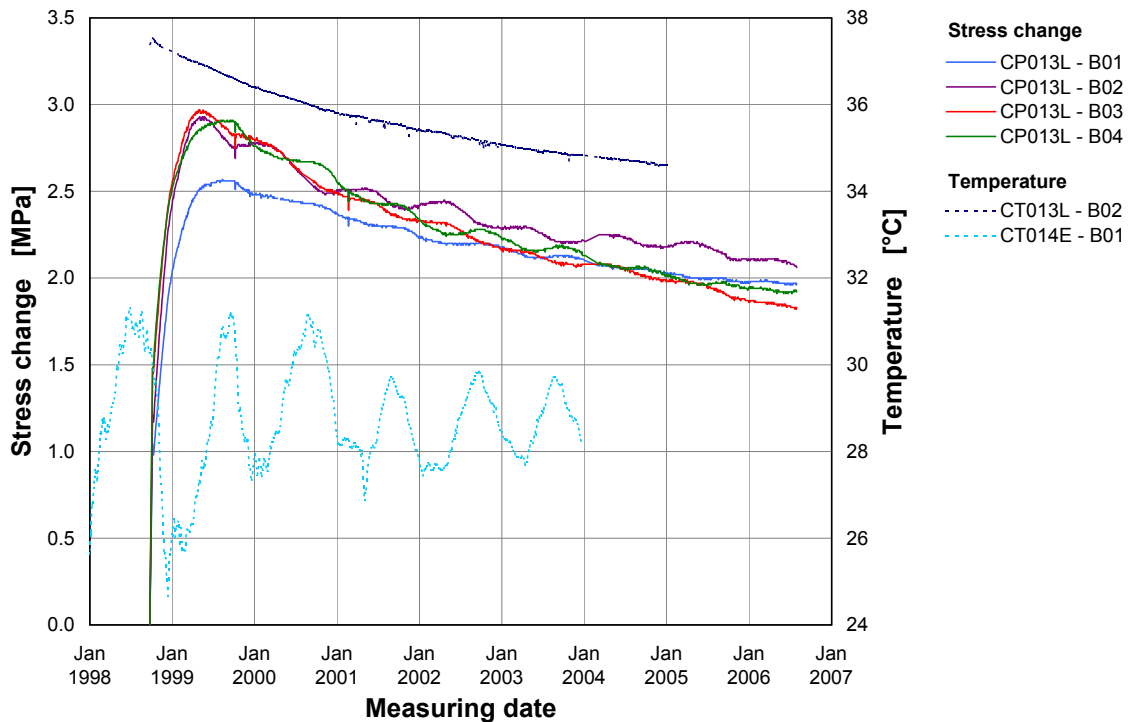


Figure 6.32: Stress changes in the floor of EL1

Secondly, the cooling down of the rock mass caused by the mine ventilation air gives rise to a contraction and thus to stress release which counteracts the stress increase. Because of the temperature gradients, the cooling down at the beginning of the measuring period is relatively large – and therefore also the stress release. Over time from the date of their construction, the cooling down in the underground workings decreases continuously until a stationary temperature distribution is reached. The stress release therefore approaches the stationary end value along an asymptotic curve. This relationship is shown in Figure 6.33 by a qualitative plot of the increase in stress as a result of rock salt creep, of the stress release caused by contraction of the rock mass as a result of cooling down, and of the resulting stress changes over time.

The trends both stress increase and stress release are assumed to be degressive although at different rates of change. This allows the construction of a plot similar to the measured stress change (cf. Figure 6.32) – stress increase up to a local maximum and subsequent stress release. Figure 6.33 also shows that as time passes from the date of excavation, the resulting stress changes can increase again if the stress release has reached a constant end value (stationary temperature field, and no further cooling down) and the creep of the rock mass continues unabated.

This model should be verified by model calculations, but can only be validated by long-term observation of the measured stress values.

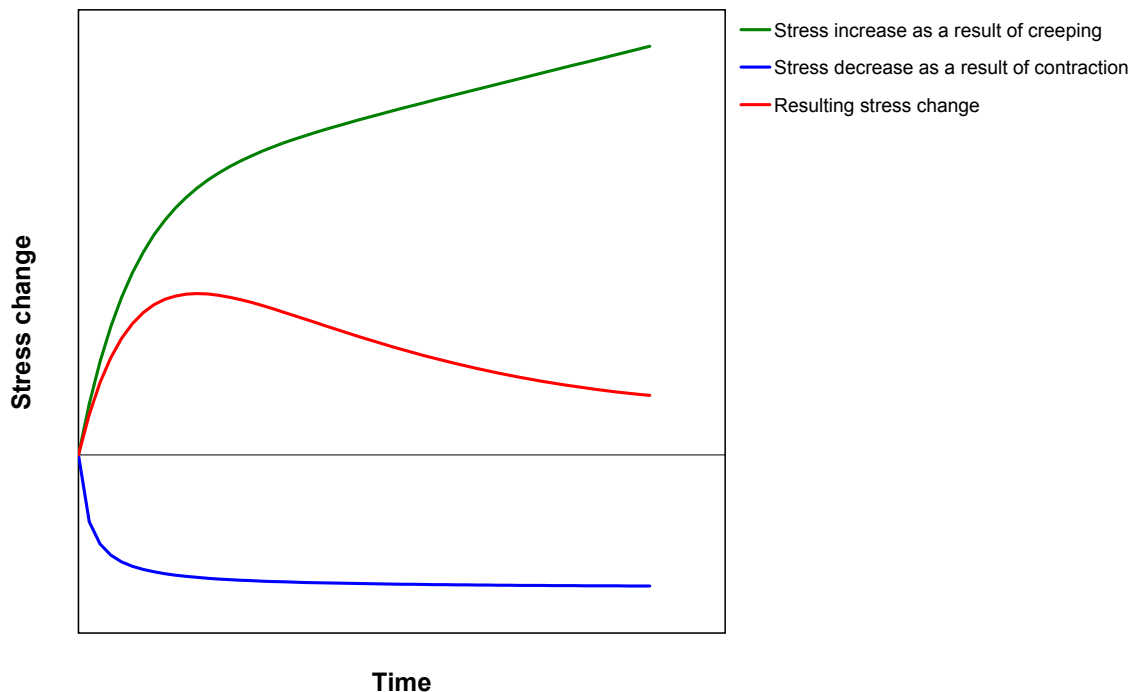


Figure 6.33: Qualitative stress change beneath EL1

The stress monitoring stations in the walls of EL1 reveal a similar development in the change in measured stresses (Figure 6.34) to the stress monitoring stations in the floor. However, the rise in stress at the start of the measurement period is much lower in the walls of EL1, and the maximum stress changes were not reached until 2001 to 2002. In general, it is again assumed here that the counteracting effects of creep-related stress increase and cooling-related stress release are involved. Because of the relatively minor and approximately linear decrease in temperature over time, the plots of the measured stress changes in the walls are flatter than in the floor of EL1.

Figure 6.34 also shows that the stress changes in the stress monitoring station CP015L located to the south of EL1 are higher than the stress changes in the northern wall (CP014L). Overall, stress changes measured in the horizontal boreholes are very low, with maximum values of 4.4 MPa.

6.3.2.4 Deformation measurements

The convergence measurement profiles installed in the exploration area and in the infrastructure zone were able to cover almost all of the stratigraphic units in the Staßfurt-Folge and the Leine-Folge. However, no convergence measurement profiles were installed in areas with exposed Staßfurt potash seams (z2SF) or Hauptanhydrit (z3HA).

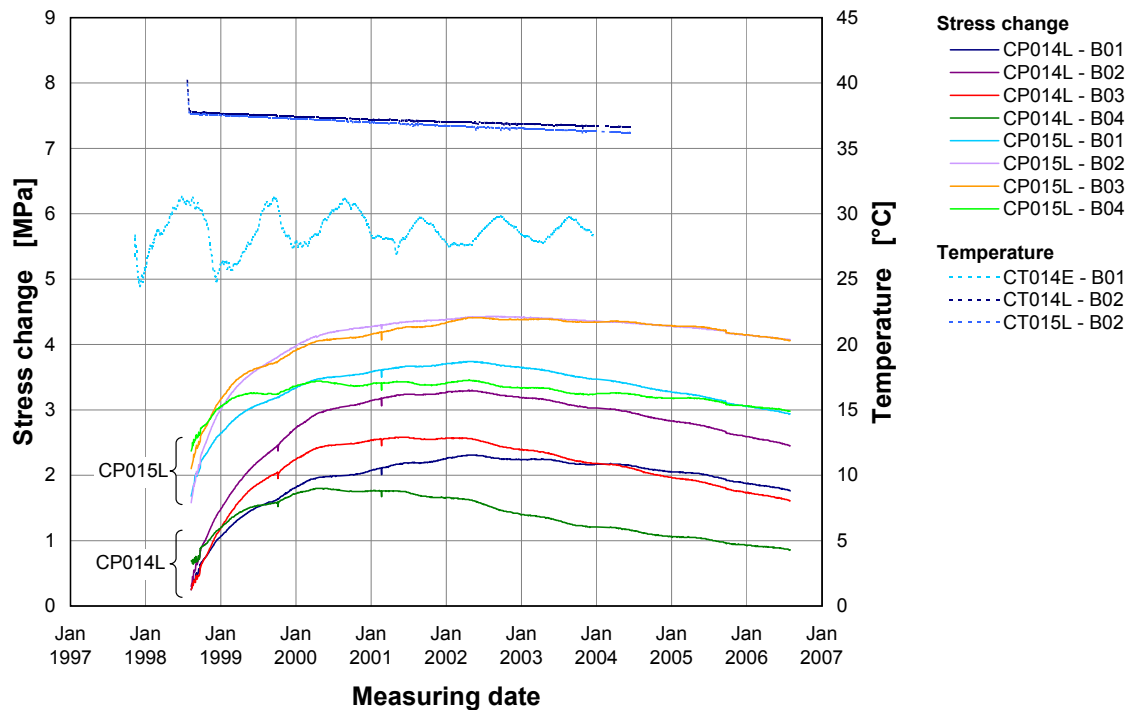


Figure 6.34: Stress changes in the walls of EL1

To compare the convergence measurement results, Figures 6.35 and 6.36 show the deformation rates of the vertical convergence measuring lines as averages for 2003 to 2005. Figure 6.35 shows the results at the exploration area, and Figure 6.36 shows the deformation rates in the infrastructure area.

The highest deformation rates measured in the exploration area are in the measurement profiles with exposed Knäuelsalz in the Staßfurt-Folge (z2HS1). The convergences measured in these zones also produce the highest values. Deformation rates then decrease significantly in the Streifensalz (z2HS2) and the Kristallbrockensalz (z2HS3), and are smallest in the beds of the Leine-Folge (z3). The deformation rates determined for the infrastructure area, and shown in Figure 6.36, should be looked at to analyse the deformation behaviour of the Leine-Folge. In general, there is a decrease in deformation rates from the stratigraphically older Liniensalz (z3LS) to the younger Bank/Bändersalz (z3BK/BD).

The measured convergences in the measurement profiles in exposed Anhydritmittelsalz (z3AM) indicate slightly different behaviour. The deformation rates determined in this youngest unit of the Leine-Folge are larger than those of the geologically older z3BT and z3BK/BD units. The measured deformation properties of the Anhydritmittelsalz are more analogous to those of the Orangesalz (z3OS). The interbedded anhydrite layers probably make the rock easier to deform. The absence of in-situ investigations and laboratory tests

to date mean that this theory can neither be proved nor disproved. Further investigations need to be carried out to unequivocally clarify the influence of the anhydrite layers on the geomechanical behaviour of the Anhydritmittelsalz.

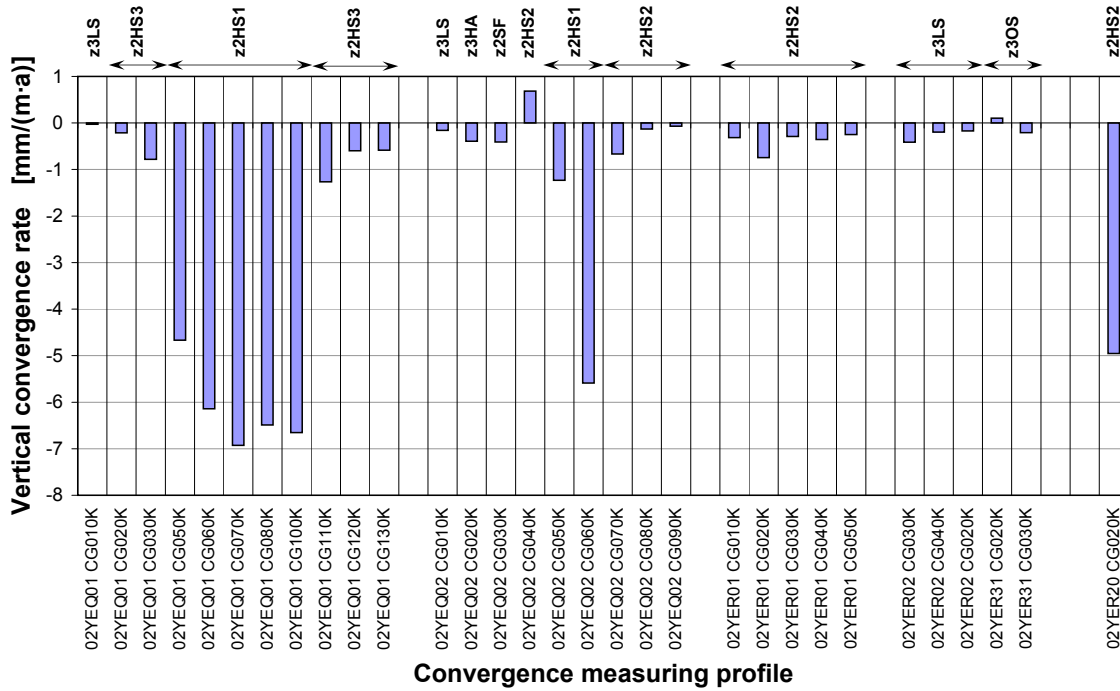


Figure 6.35: Vertical convergence rates in the exploration area drifts

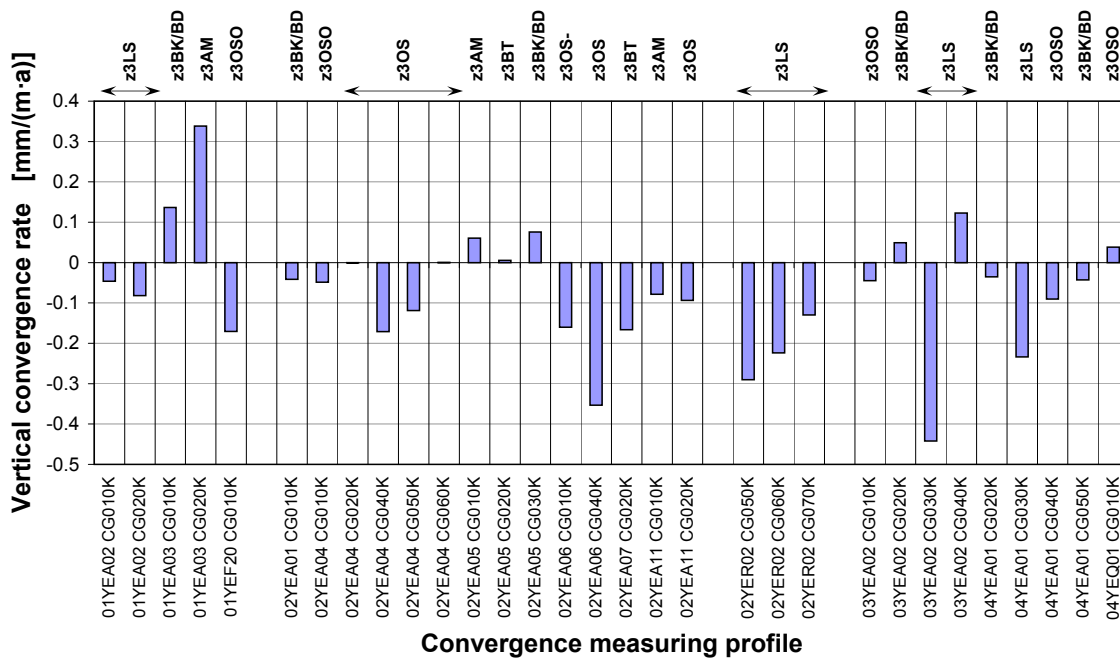


Figure 6.36: Vertical Convergence rates in the infrastructure area drifts

The convergence measurements register changes in the distances between opposing measurement points on the perimeters of underground workings. In the case of the vertical convergence, it is not possible to ascertain what proportion of the convergence is due to subsidence of the roof or rising of the floor. This requires additional measurement data to be collected from underground height measurements to enable the deformation measurements to be completely interpreted. These additional data are collected as part of the mine surveying work carried out in the underground workings.

Extensometer measurements at the exploration level are limited to the exploration locations. The extensometer measurement data are influenced by seasonal fluctuations in the temperature of the ventilation air in EL1 and EL2 in particular. This effect is shown by the examples of measured profile deformations in Figure 6.37. This is why analysis of the long-term deformation trends at each measurement location are based on average deformation calculated for a period of a year (Figure 6.37).

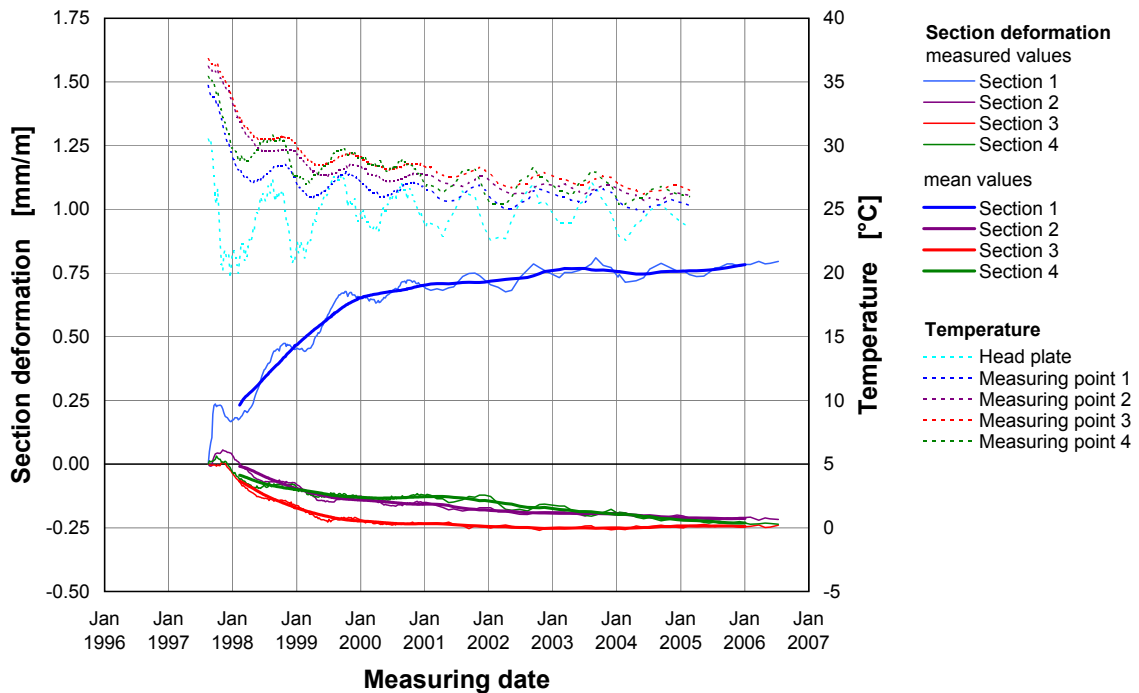


Figure 6.37: Section deformations at extensometer CG011E in EL2

The deformations of the rock mass in EL1 and EL2 are relatively low and largely occur in the zones close to the perimeters of the underground workings. Only very minor deformations are recorded at larger distances to the underground workings. The deformation taking place close to the perimeters of the underground workings is thought to be attributable to excavation damage processes. However, a degressive increase in the deformation close to the sides of the cavities, gradually approaching constant values, has been detected. It therefore appears that a new equilibrium is developing in the region of EL1 and EL2 as time passes from the active excavation of the underground workings.

A comparison of the extensometer measuring results shows that the rock mass deformations occurring in the sections of the roofs and floors in EL1 close to the perimeter are around twice as high as the analogous section deformations in EL2. The deformation of the sections close to the perimeter in the horizontal measuring direction is of the same order of magnitude. EL1 was excavated in Unteres Orangesalz (z3OSO) whilst EL2 was primarily excavated in the younger stratigraphic units of the Leine-Folge. Based on the creep properties of the in-situ rock salts determined by laboratory tests, the deformation in EL1 should actually be larger than in EL2. This, however, is not the case in the deformation in the horizontal direction, but only in the deformation in a vertical direction. The influence of petrography therefore seems to be only of minor importance as for this finding. The causes are therefore thought to have more to do with the degree of excavation because EL1 is only affected to a minor degree by other underground workings, whereas EL2 is influenced by several drifts with both horizontal and vertical cavities.

EL4 excavated in the Hauptsalz (z2HS) highlights the importance of petrography and the creep properties of the in-situ rocks with respect to rock mass deformation. Although the geometrical situation of EL4 is quite similar to EL1. EL4 is affected by much greater deformation than EL1. The convergence measurements confirm the high ductility of the Knäuelsalz in particular (z2HS1), as shown by the measurement results in Figure 6.38 compared to Figure 6.37. The section deformations in EL4 are approximately 30 to 100 times higher than the section deformations determined at other exploration locations. Moreover, the extensometers installed in EL4 measured extensions in all sections for the whole measuring time period.

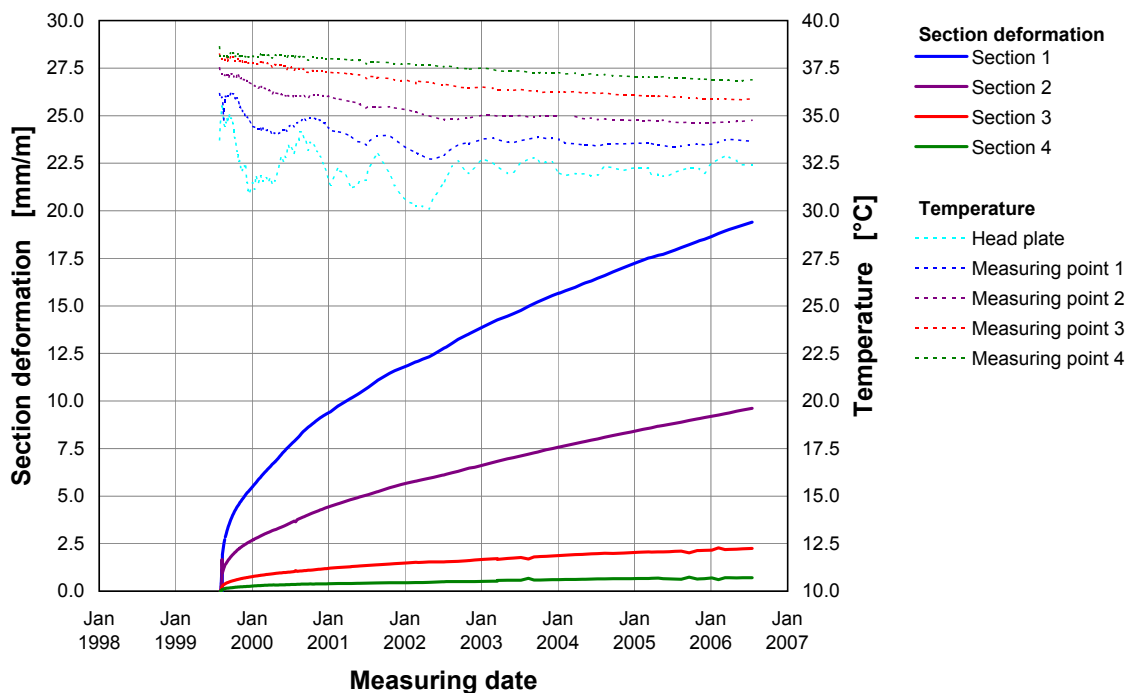


Figure 6.38: Section deformations of extensometer CG104E in EL4

No seasonal fluctuations are seen in the deformation recorded by the extensometer sections in EL4 because the seasonal temperature fluctuations of the ventilation air are much lower compared to the measurement locations close to downcast shaft 1 (cf. Chapter 6.3.2.1). Moreover, the average rock mass temperatures at the perimeters of the drifts are around 7 °C higher, which means that the temperature differences compared to the deeper-lying parts of the rock mass are lower, and cooling down of the rock mass takes place much more slowly.

Degressive increase was still observable until mid-2006 in the deformations of the extensometer sections in EL4. Constant deformation rates, which suggest steady-state creep processes within the rock mass, had still not been reached at this stage, but will probably establish themselves in the next few years.

The deeper rock zones in EL4 (extensometer sections 2 and 3 in Figure 6.38) also indicate a not inconsiderable contribution to the total deformation in the measuring zone. These are even significantly higher than the section deformations in EL2 measured zones close to the perimeters of the excavations. The deformation measured here is therefore only attributable in small part to the excavation-damaged zone, and is mainly caused by the creep deformation of the extremely ductile beds in the Hauptsalz which are present in EL4.

The convergence measurement profiles in the exploration locations are combined with the extensometers installed in the same places. The extensometer heads here are the measurement bolts for the convergence measurements. The combined analysis of the extensometer and convergence measurements reveals that the deepest extensometer measurement points (distance of around 20 m to the perimeters of the drifts) have undergone displacement and must therefore not be considered as fixed points. This deformation of the parts of the rock mass located further from the underground workings makes a not inconsiderable contribution to the drift convergence, particularly in EL4.

This combination of convergence and extensometer measurements is only possible in a few vertical measuring planes in the exploration locations. There is no connection between these measuring planes and the rest of the underground workings or to the other exploration locations. This means no extrapolation is possible on the absolute horizontal or vertical displacements of the measurement locations. The additional mine surveying measurements to determine absolute displacements – such as underground height measurements, network measurements or polygonisation – are therefore considered indispensable.

The fissurometer measurements at the exploration level are exclusively conducted to monitor the deformation of the Gorleben Bank (z3OSM), which is described in

BORNEMANN et al. (2003) as a remarkable horizon consisting largely of anhydrite and with a thickness ranging from several centimetres to a few decimetres. It consists of several zones containing joints and clay layers with displacement zones, and is characterised by different degrees of salt-tectonic deformation. The displacement zones were reactivated by the deformation of the rock salt caused by the drifting of the cavities. The petrography and significance of the Gorleben Bank and the surrounding beds in the geological system are described in detail in BÄUERLE et al. (2000). 21 single fissurometers were installed in total to monitor the Gorleben Bank. In most cases, two single fissurometers are combined into a fissurometer arrangement (FA).

The fissurometer measurements revealed no displacements indicating the opening of the Gorleben Bank. The dominant features are shear deformations in the plane of the Gorleben Bank which are mostly aligned orthogonal to the cavity perimeters and therefore point into the cavities. This finding is shown in Figure 6.39 by the resulting displacement vectors of the individual fissurometer points.

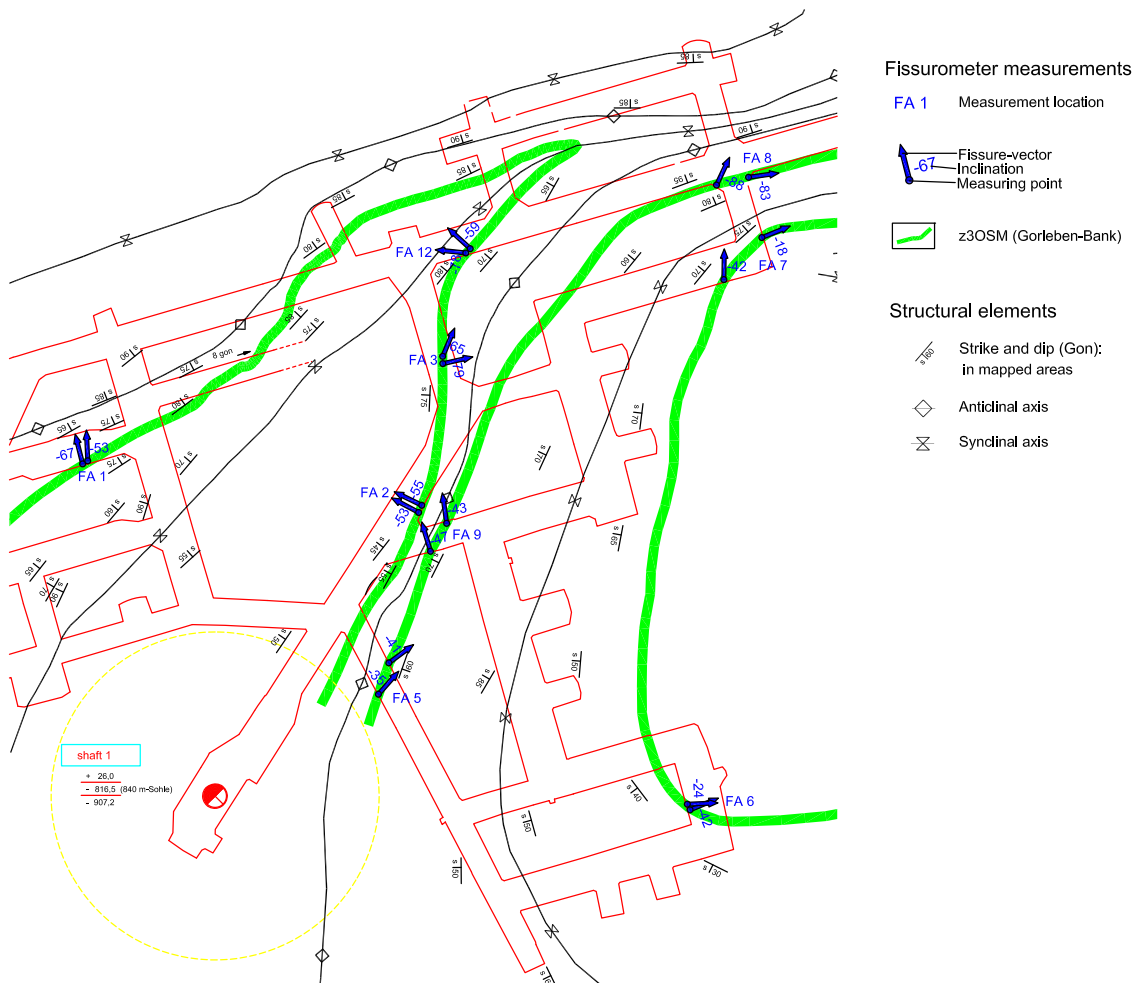


Figure 6.39: Resulting displacement directions of the Gorleben Bank (z3OSM)

One can assume from these results that the measured displacements were initiated by the excavation of the underground workings. The rate of the deformation declines in the long term so that the displacements asymptotically approach a final value whose size is determined by the conditions at each of the measurement locations. This interpretation is supported by the degressive development of the measured displacements.

7 Rock-hydraulic investigations

The hydraulic characterisation of the Gorleben salt dome is carried out using a range of investigation methods to determine the hydraulic properties of the rock salt. The methods which were used and the results are described in detail in a final report (NOWAK & WEBER 2002).

The barrier effect of salt structures is attributable to the almost complete absence of interconnected pore space systems. The connected pores and (micro)joints, which negatively affect the barrier properties of the rock mass are localised and only occur rarely in rock salt. Anhydrite rocks, on the other hand, are frequently jointed. The hydraulic characterisation of the Gorleben salt dome as an overall geological structure therefore has to take into consideration the spatial distribution of tight rock salt, dilatant zones in the rock salt, jointed anhydrite, and isolated occurrences of fluids. Hydraulic borehole tests were carried out in the exploration boreholes for this purpose. Measurements were also carried out in short boreholes which were specifically drilled to test the excavation-damaged zones.

The hydraulic properties of the rock mass are characterised by two parameters: permeability and porosity. This requires the determination of the position and extent of isolated occurrences of fluids, and confirmation of the isolation of the anhydrite from the excavated areas.

7.1 Permeability measurements

Hydraulic borehole tests are carried out to determine the permeability of a rock in a rock formation. The principle behind the different borehole test methods is to inject a test fluid with known viscosity and compressibility into the pore space of the rock to be tested, or to extract it from the rock, and to register the fluid pressure in the borehole in the process. Permeability of the rock can be determined from the change in pressure over time. Pulse tests are particularly good at determining the permeability of tight rocks. This borehole measuring method involves using packers to hydraulically isolate a test interval from the rest of the borehole; establishing a specific (initial) pressure in this interval; and then sealing off the interval. The pressure in the test interval, which is higher than the

pressure in the rock, causes the fluid to flow into the pore space of the rock mass leading to pressure equalisation. Measured changes in pressure over time in the test interval are then used to calculate the permeability.

The test thus determines an upper limit for the permeability of the rock surrounding the tested borehole interval. Figure 7.1 shows, as an example, the processed measurement values of a test and the calculated pressure plots for permeabilities ranging from 10^{-20} m^2 to 10^{-19} m^2 . On the brown curve, the processed measurement values indicate a pressure of $3.66 \cdot 10^5 \text{ Pa}$ after 300,000 seconds (approx. 3.5 days) from the start of the test. If the rock mass had had a higher permeability, for instance of 10^{-19} m^2 (green plot), the pressure at this point in time would already have dropped down to $2.9 \cdot 10^5 \text{ Pa}$. A comparison of the processed measurement values and the calculated pressure plots indicates that the permeability of the rock mass in the test interval is lower than $5 \cdot 10^{-20} \text{ m}^2$ (orange curve).

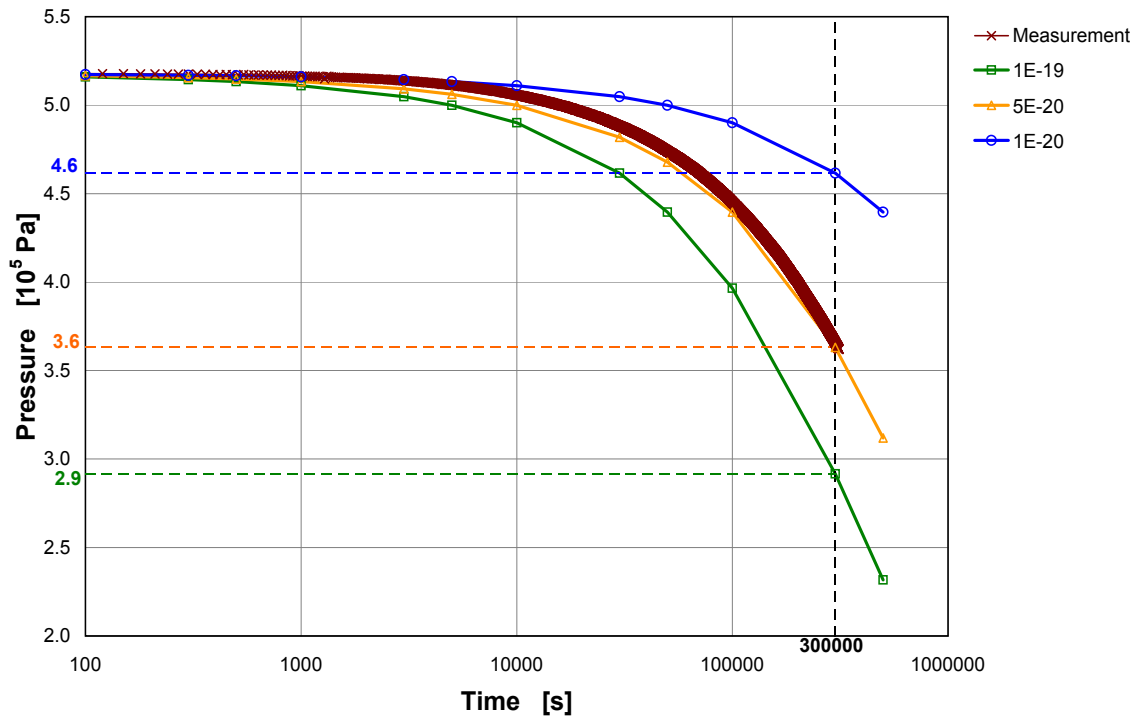


Figure 7.1: Test evaluation example

7.1.1 Methodology

Hydraulic borehole tests with a range of equipment were required to hydraulically characterise the salt barrier at the Gorleben site. These addressed the issues to be studied and provided the various necessary borehole lengths and diameters. The tests were carried out in various stratigraphic units. The measurements carried out in the exploration boreholes served to characterise the rock salt mass, whilst the tests in the short boreholes

were carried out to characterise the excavation-damaged zone around the underground workings.

The first measurements in the exploration boreholes were undertaken with a test apparatus consisting of two hose packers joined together to create a double packer to isolate a test interval of 1 m. The subsequent measurements were carried out with two different sets of test equipment configured for a continuous measurement. Double packers were again used here, but the test interval could be modified up to a length of 10 m using a variable interval string. Figure 7.2 shows the test apparatus used in the Gorleben exploration mine. The technical specifications are described in NOWAK & WEBER (2002).

The sensors in the integrated measuring probe positioned in the interval can measure pressures up to 6 MPa and temperatures between 20 °C and 70 °C from directly within the borehole. An overpressure of around 0.5 MPa is created in the interval after setting the packer.



Figure 7.2: Permeability testing equipment (probe – data station – wireline cable)

A special test apparatus for smaller diameters was used for the short borehole tests: a pneumatically set double packer with a test interval of 0.1 m and single packers were used.

7.1.2 Investigations in exploration boreholes

Hydraulic borehole tests in the halite of the Leine-Folge (z3) and the transition z2/z3 were needed to evaluate the permeability of the rock surrounding the infrastructure area. However, in case the Gorleben salt dome is found to be qualified no disposal of heat-generating radioactive waste is envisaged in these stratigraphic units. Evaluation of the

permeability of the rock mass in Exploration area 1 mainly requires tests in the Hauptsalz incorporating the Kristallbrockensalz (z2HS3), the Streifensalz (z2HS2) and the Knäuelsalz (z2HS1). A disposal of heat-generating radioactive waste will take place in the Hauptsalz in case that the Gorleben salt dome is found to be qualified for this purpose.

7.1.2.1 Exploration area 1 (EB1)

The permeability measurements in EB1 were carried out in one exploration borehole until the start of the moratorium. Pulse tests with magnesium chloride brine were carried out in four test intervals. The new measuring equipment was put into use after these tests had been completed. Pulse tests with nitrogen were then carried out in six test intervals. The pulse pressures in all of the tests were around 0.5 MPa. All of the test intervals were within the Streifensalz (z2HS2).

The upper limits of the rock mass permeability in the borehole intervals tested using magnesium chloride brine lay between $2 \cdot 10^{-20} \text{ m}^2$ and $5 \cdot 10^{-20} \text{ m}^2$. These borehole intervals were then tested again using the new measuring equipment, larger intervals, and nitrogen as the test fluid. These tests found upper limits of rock mass permeability for the tested boreholes of between $2 \cdot 10^{-21} \text{ m}^2$ and $5 \cdot 10^{-22} \text{ m}^2$.

The facies variations in the tested Streifensalz sequence do not have any significant influence on the measured permeabilities. Because of the moratorium on further exploration work, no tests were carried out in the Kristallbrockensalz (z2HS3) or in the Knäuelsalz (z2HS1). Additional investigations are required because the data produced to date are inadequate to characterise the hydraulic properties of all stratigraphic units in EB1.

7.1.2.2 Infrastructure area

Ten hydraulic borehole tests with the first test apparatus were carried out in one exploration borehole in the infrastructure area. The measurements were carried out as pulse tests with initial pressures of around 0.5 MPa, using MgCl_2 brine as the test fluid. Testing was carried out in the rock salts of the Staßfurt and Leine-Folge incorporating the Streifensalz (z2HS2), the Kristallbrockensalz (z2HS3), the Hangendsalz (z2HG), the Kieseritische Übergangsschichten (z2UE), the Kaliflöz Staßfurt (z2SF), the Liniensalz (z3LS) and the Basissalz (z3BS). These tests produced upper limits for the permeability of the rock mass between 10^{-21} m^2 and $5 \cdot 10^{-20} \text{ m}^2$. Hydraulic borehole tests using the new equipment were carried out in another exploration borehole. The tests were carried out as pulse tests with initial pressures of around 0.5 MPa, using nitrogen as the test fluid. Whilst the borehole was being drilled, there was a limited outflow of gas and condensate after drilling through the Gorleben Bank (z3OSM). The next section penetrated by the borehole consisted of

strongly deformed rock in the Unteres Orangesalz (z3OSU) to Liniensalz (z3LS) sequence including numerous joints healed with halite. Four tests were carried out in this zone and produced upper limits of the rock mass permeability of between $5 \cdot 10^{-21} \text{ m}^2$ and 10^{-18} m^2 .

Another test was deliberately targeted at a healed joint partially filled with clear halite and partially by carnallite in the interstitial spaces. The upper permeability limit produced by this test was $5 \cdot 10^{-22} \text{ m}^2$.

Another test, which also produced an upper permeability limit of $5 \cdot 10^{-22} \text{ m}^2$, was carried out in a halite/anhydrite zone interpreted as the end product of the totally altered (pinched out) Kaliflöz Staßfurt (z2SF). The pinched out Kaliflöz Staßfurt (z2SF) is underlain by a Liniensalz (z3LS) syncline with strongly thinned out Basissalz (z3BS) on the flanks. The permeability upper limit determined here was also $5 \cdot 10^{-22} \text{ m}^2$. Another measurement conducted in the transition from z2 to z3 produced a permeability upper limit of $5 \cdot 10^{-19} \text{ m}^2$.

7.1.3 Investigations in short boreholes

Tests were necessary at various locations in short boreholes (length 3 – 4 m) to investigate the influence of different types of salt and geometrical conditions on the permeability of potential excavation-damaged zones. Borehole tests of this nature were carried out at one location in the Oberes Orangesalz (z3OSO) before the start of the moratorium. The three tested boreholes were drilled orthogonal to the perimeter of the cavity along an almost horizontal line with a separation of around one metre. The middle borehole was sealed with a single packer and equipped with apparatus to measure the change in pressure over time. Pulse tests with compressed air were carried out in parallel in the two adjacent boreholes to the right and left. Nine intervals of 0.1 m length were tested with a double packer up to a distance of 1.2 m from the mouth of the borehole.

None of the tests indicated any connections between the boreholes. The permeabilities determined by the tests were in the lower range of values determined at other locations and used for comparison. No significant dilatancy of the rock salt was identified in the measured borehole intervals beyond 0.3 m from the perimeter of the cavity. Figure 7.3 shows the permeabilities determined from these tests together with the figures published in STORMONT (1997) for the Waste Isolation Pilot Plant (WIPP) in Carlsbad (New Mexico).

The distance from the cavity perimeter in this diagram is standardised to the effective radius r of the cavity with the cross-sectional area A defined by STORMONT (1997). The values determined for the Gorleben exploration mine thus appear to be small compared to the in-situ measurement results from other locations.

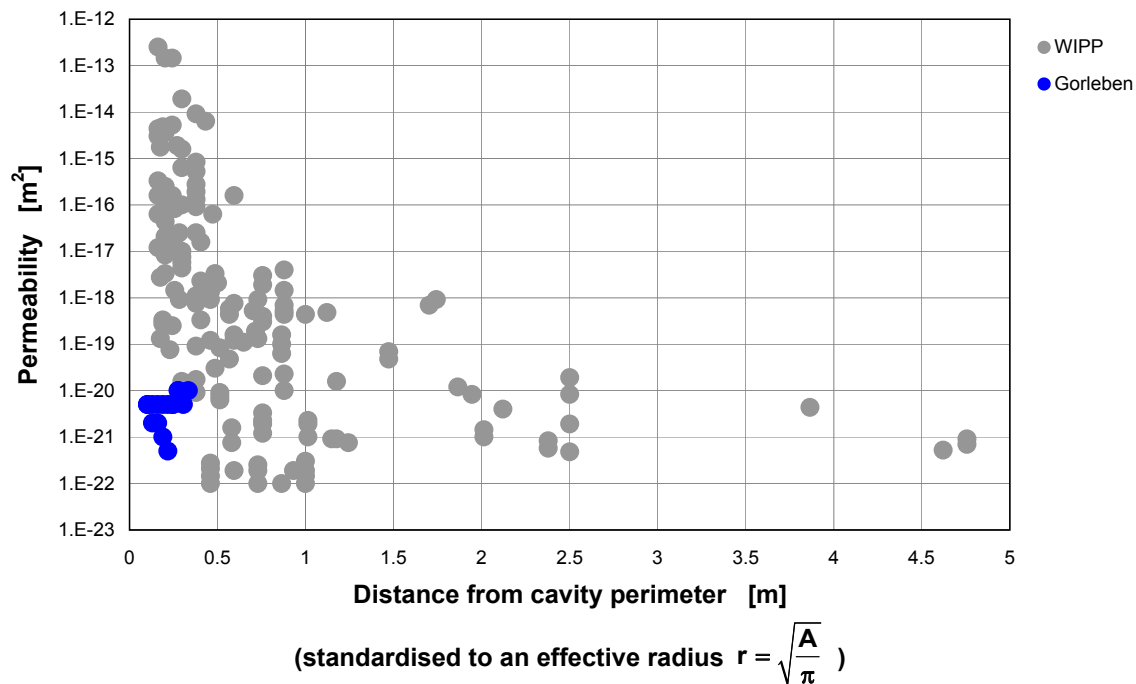


Figure 7.3: Permeability measurements in the excavation-damaged zone in the Gorleben exploration mine and in the WIPP site

7.2 Estimating the volumes of isolated occurrences of fluids

Some exploration boreholes encountered isolated occurrences of fluids in the halite of the Leine-Folge (z3) and the transition z2/z3 outside of the potential disposal areas. Pressure and outflow measurements were carried out in these isolated occurrences of fluids. The data acquired in this way were used in a material balance calculation to determine the total volume of the isolated fluids (gas and brine) in terms of a range between a minimum and a maximum existing volume.

7.2.1 Formulation and calculation of the material balance equation

The principle behind material balance calculations is that the withdrawal of a volume of fluid from an isolated occurrence causes a drop in the pressure of a magnitude dependent on the properties of the fluids and on the fluid volume. The volume of the isolated occurrence of fluids can be calculated by measuring the decline in pressure within this occurrence caused by the withdrawal of fluid. The formulation of the material balance and calculation of the volume of the isolated occurrence of fluid are discussed in detail in NOWAK & WEBER (2002).

When an isolated occurrence of fluids was encountered by a borehole, at least two outflow measurements were carried out, each with a prior and subsequent stabilised pressure measurement. Figure 7.4 shows an example of the measurement procedure in an exploration borehole which encountered gas and brine.

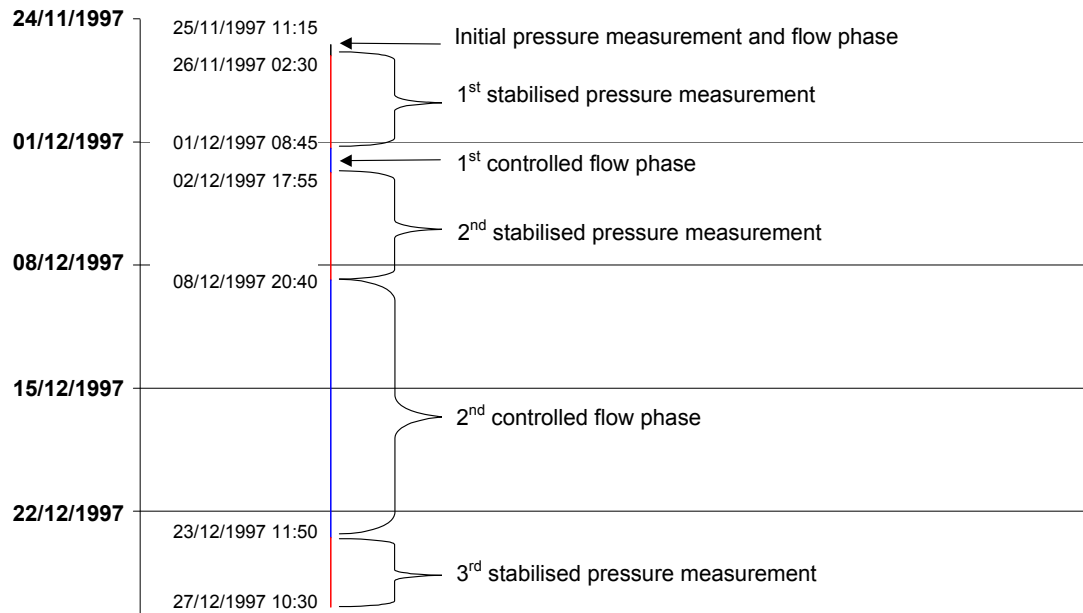


Figure 7.4: Example of the measurement procedure carried out in an exploration borehole

The volume of fluids encountered by the exploration borehole is determined by first putting the outflow and pressure data from the first outflow measurement into the material balance equation. An initial gas/brine ratio m is estimated and used to calculate the initial total volume of fluids.

The gas/brine ratio at the start of the second flow phase is derived from the initial gas/brine ratio, the initial brine volume and the volume of brine produced during the first flow phase. The total volume of fluids is then calculated again with the outflow and pressure data from the second flow phase. The result is considered to be accurate if the fluid volumes calculated for the first and second flow phases match, and the following ancillary conditions are satisfied:

- Ratio m must be larger or equal to zero ($m \geq 0$)
- The calculated initial brine volume in the occurrence of fluids (under standard conditions) must be larger than the total brine outflow volume ($V_{Li} > \Sigma V_{Lp}$)
- The given change in initial brine volume under standard conditions during a flow phase must be equal to the brine volume produced during this flow phase ($\Delta V_{Li} = V_{Lp}$)

In the material balance calculation, the measured pressure and outflow data are varied within ranges reflecting the measuring accuracy, and the gas/brine ratio m is set to the values which yield the minimum and maximum possible total volume of fluids.

The maximum value for the volume of the occurrence of fluids is arrived at when the occurrence of fluids contains no (free) gas phase before being opened up by drilling, in other words, all of the gas is initially dissolved and does not escape until the pressure in the reservoir drops ($m = 0$). Based on a dataset from an exploration borehole, Table 7.1 summarises, as an example, the ancillary conditions and the total volume of fluids calculated from the pressure and outflow measurements. The ancillary conditions highlighted with a grey background are those for the maximum value. The equation system in this case has solutions for a total volume of fluids up to around 2500 m³.

Table 7.1: Material balance for the maximum value in an exploration borehole

		Max.	AC	Min.	V_{Res} [m ³]	V_{LB_L} [m ³]	V_L [m ³]	V_{GB_G} [m ³]	m [-]
p_0 [MPa]	18.00	18.50	$\geq p_0$ [MPa] \geq	18.00	2538.7	2538.7	2545.0	0.0	0.000
$V_{Gp,0}$ [m ³]	0.62	0.62	$\geq V_{Gp,0}$ [m ³] \geq	0.52					
$V_{Lp,0}$ [m ³]	32.39	32.39	$\geq V_{Lp,0}$ [m ³] \geq	32.39	2538.7	2510.7	2512.6	28.0	0.011
p_1 [MPa]	5.80	9.89	$\geq p_1$ [MPa] \geq	5.10					
$V_{Gp,1}$ [m ³]	1192.0	1192.0	$\geq V_{Gp,1}$ [m ³] \geq	344.5	2538.7	2455.3	2455.7	83.5	0.034
$V_{Lp,1}$ [m ³]	56.91	56.91	$\geq V_{Lp,1}$ [m ³] \geq	56.91					
p_2 [MPa]	1.52	1.52	$\geq p_2$ [MPa] \geq	0.90	2538.7	2435.0	2435.3	103.7	0.043
$V_{Gp,2}$ [m ³]	374.07	552.00	$\geq V_{Gp,2}$ [m ³] \geq	346.70					
$V_{Lp,2}$ [m ³]	20.45	20.45	$\geq V_{Lp,2}$ [m ³] \geq	20.45	2538.7	2435.0	2435.3	103.7	0.043
p_3 [MPa]	0.97	0.97	$\geq p_3$ [MPa] \geq	0.63					
$V_{Gp,3}$ [m ³]	661.29	948.20	$\geq V_{Gp,3}$ [m ³] \geq	629.8	2538.7	2435.0	2435.3	103.7	0.043
$V_{Lp,3}$ [m ³]	44.74	44.74	$\geq V_{Lp,3}$ [m ³] \geq	44.74					
p_4 [MPa]	0.32	0.37	$\geq p_4$ [MPa] \geq	0.31	2538.7 (mean value)				

The minimum volume for the same dataset is obtained when the largest possible volume is occupied by free gas in the occurrence of fluids before being opened up by drilling. For the dataset shown above, an initial minimum volume of 193 m³ brine under standard conditions must be assumed. Table 7.2 summarises the ancillary conditions and the total volume of fluids calculated from the pressure and outflow measurements. The constraining ancillary conditions for the minimum value are shown in each case highlighted by a grey background. The minimum value for the total volume of fluids is around 200 m³.

According to these maximum and minimum value, the total volume of fluids in this occurrence penetrated by the exploration borehole is between 200 m³ and 2500 m³.

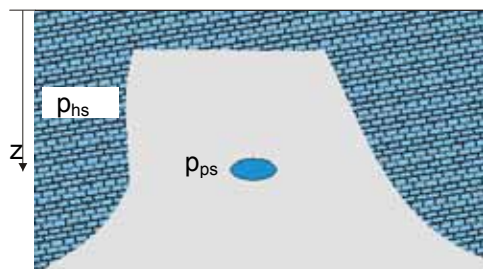
Table 7.2: Material balance for the minimum value in an exploration borehole

		Max.	AC	Min.	V_{Res} [m ³]	V_{LB_L} [m ³]	V_L [m ³]	V_{GB_G} [m ³]	m [-]
p_0 [MPa]	18.50	18.50	$\geq p_0$ [MPa] \geq	18.00	203.1	192.5	193.0	10.6	0.055
$V_{Gp,0}$ [m ³]	0.52	0.62	$\geq V_{Gp,0}$ [m ³] \geq	0.52					
$V_{Lp,0}$ [m ³]	32.39	32.39	$\geq V_{Lp,0}$ [m ³] \geq	32.39	203.1	160.5	160.6	42.6	0.266
p_1 [MPa]	5.10	9.89	$\geq p_1$ [MPa] \geq	5.10					
$V_{Gp,1}$ [m ³]	791.13	1192.0	$\geq V_{Gp,1}$ [m ³] \geq	344.5	203.1	103.7	103.7	99.5	0.959
$V_{Lp,1}$ [m ³]	56.91	56.91	$\geq V_{Lp,1}$ [m ³] \geq	56.91					
p_2 [MPa]	1.50	1.52	$\geq p_2$ [MPa] \geq	0.90	203.1	83.2	83.3	119.9	1.440
$V_{Gp,2}$ [m ³]	346.70	552.00	$\geq V_{Gp,2}$ [m ³] \geq	346.70					
$V_{Lp,2}$ [m ³]	20.45	20.45	$\geq V_{Lp,2}$ [m ³] \geq	20.45	203.1	203.1	203.1	203.1	203.1
p_3 [MPa]	0.97	0.97	$\geq p_3$ [MPa] \geq	0.63					
$V_{Gp,3}$ [m ³]	629.80	948.20	$\geq V_{Gp,3}$ [m ³] \geq	629.8	203.1	83.2	83.3	119.9	1.440
$V_{Lp,3}$ [m ³]	44.74	44.74	$\geq V_{Lp,3}$ [m ³] \geq	44.74					
p_4 [MPa]	0.33	0.37	$\geq p_4$ [MPa] \geq	0.31	203.1 (mean value)				

7.2.2 Necessary measurements

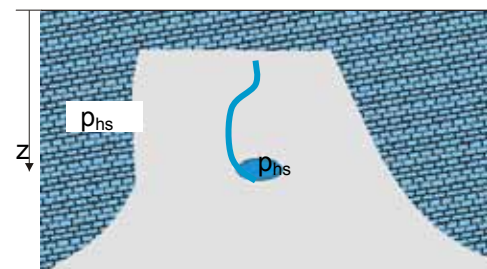
It is not uncommon for salt domes to contain isolated occurrences of fluids. If a borehole penetrates such an occurrence, the measurement of the initial pressure alone can verify that the occurrence of fluids is isolated and no connection to an aquifer outside the salt dome exists. Figure 7.5 shows the two possible cases: an isolated occurrence of fluids and a non-isolated occurrence of fluids.

Isolated occurrence of fluids



Petrostatic pressure $p_{ps}(z)$:
 $p_{ps}(840 \text{ m}) = \rho_g \cdot g \cdot z \approx 18.5 \text{ MPa}$

Non-isolated occurrence of fluids



Hydrostatic pressure $p_{hs}(z)$:
 $p_{hs}(840 \text{ m}) = \rho_L \cdot g \cdot z \approx 11 \text{ MPa}$

Figure 7.5: Isolated and non-isolated occurrence of fluids

In isolated occurrence of fluids, the creep capacity of the ductile rock salt means that over long periods of time, the pressure in the occurrence of fluids will be the same as in the surrounding rock mass. The pressure in an isolated occurrence of fluids is therefore the same as the petrostatic pressure. If an aquifer outside of the salt structure has a pressure of 11 MPa, it is not possible for the pressure in a non-isolated occurrence of fluids at the same depth to have a higher pressure. A higher pressure than the hydrostatic pressure therefore verifies the isolation of an occurrence of fluids.

7.2.2.1 Stabilised pressure measurements

Measured pressures and outflow volumes are used to determine the volume of an occurrence of fluids by means of a material balance calculation. This requires determination of the two unknown parameters: initial gas volume and initial brine volume. Because the material balance for the two unknowns is only based on one conditional equation, it does not produce a unique result. The highest possible degree of accuracy should therefore be aimed at in the stabilised pressure measurements. The Horner graph can be used to extrapolate the measured pressure at the borehole head to the average pressure in the occurrence of fluids. In this approach, the change in pressure is shown against the time function derived from the duration of the pressure build-up phase t and the duration of the preceding flow phase t_{fl} :

$$\ln\left(\frac{t_{fl} + t}{t}\right) \quad (7.1)$$

The longer the pressure build-up, the smaller the time function becomes, and at a value of zero, the sought after pressure in the occurrence of fluids can be read off. Figure 7.6 shows, as an example, the third stabilised pressure measurement in an exploration borehole which encountered an occurrence of fluids, firstly plotted against real time, and secondly as a section of the pressure curve against the Horner time function.

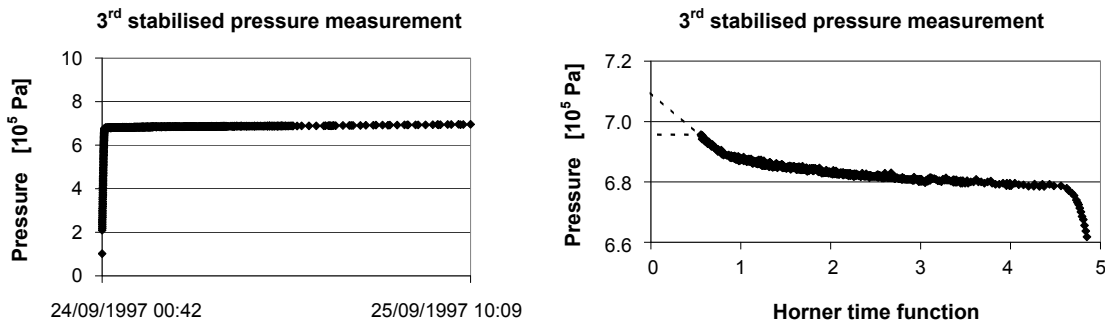


Figure 7.6: Stabilised pressure measurement plot against real time and against the Horner time function

The extrapolation of the Horner graph shows that the sought after average pressure in the occurrence of fluids is around $7.1 \cdot 10^5$ Pa after the prior outflow phases. The last measured pressure can be taken as the minimum value, and in this case it was around $6.95 \cdot 10^5$ Pa. This range in values is applied in the material balance to determine the volume of fluids. The larger the range applied, the larger the range of possible values for the initial gas/brine ratio m . A larger fluid volume is calculated when the pressure change during the flow phase is low.

7.2.2.2 Outflow measurements

The outflow rates from the exploration boreholes which encountered an occurrence of fluids were monitored either continuously or discontinuously. In case of continuous outflow monitoring a separator was used. The separator was used for the interim storage of the outflowing fluids until the brine had been largely degassed and the different phases had separated out. In case of discontinuous outflow monitoring the outflow rates were interpolated such that a lower, a medium and an upper cumulative outflow volume could be derived.

Figure 7.7 shows, as an example, the measured brine outflow rates in an exploration borehole and the cumulative brine volumes during the flow phases calculated from these measurements.

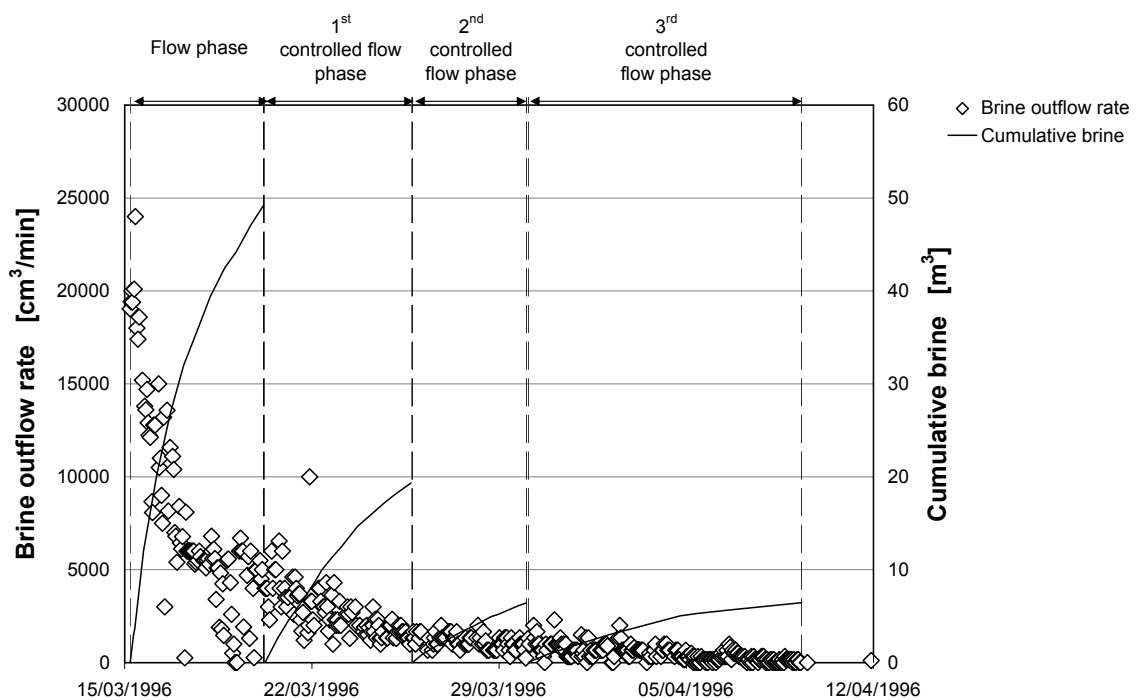


Figure 7.7: Brine outflow rates and cumulative brine outflow in an exploration borehole

The trend of the outflow rate between two measurements in an open borehole must be interpolated to determine the cumulative volume of fluid produced during the flow phase. The medium cumulative volume is derived when the rate of the preceding measurement is assumed for the first half of the time period between these measurements, and the rate of the following measurement is assumed for the rate during the second half of the time period between the measurements. An upper estimate of the cumulative volume can be calculated when the higher flow rate from the neighbouring measurements is applied for the unmonitored time periods – a lower estimate can be calculated by applying the respective lower values. The range derived from the upper and lower estimates was taken

into consideration in the material balance to determine the possible total fluid volume in the occurrence. The larger the range of the values for the outflowing volumes, the larger the range of values for the calculated initial gas/brine ratio.

7.2.3 Size of the penetrated isolated occurrences of fluid

Investigations to determine the occurrence of fluids in the Gorleben salt dome were carried out based on the above theoretical and methodological principles. The stratigraphic horizons in which occurrences of fluids were encountered were also evaluated. This analysis only looked at the beds in Zechstein 2 and Zechstein 3 up to Anhydritmittelsalz (z3AM), because the younger Zechstein horizons were not penetrated during the underground exploration.

7.2.3.1 Occurrences in the Zechstein 3

Occurrences of fluids in Zechstein 3 are only expected in beds which primarily consist of anhydrite and where reservoirs related to joints and strata can form. However, a disposal of heat-generating radioactive waste in Zechstein 3 in case the Gorleben salt dome is found to be qualified is not envisaged anyway, though occurrences of fluid are expected only in specific horizons.

This involves the following stratigraphic units:

- The anhydrite beds 1, 7 and 9 in the Anhydritmittelsalz (z3AM)
- The Gorleben Bank (Mittleres Orangesalz, z3OSM)
- The Hauptanhydrit (z3HA) with accompanying beds: Gebänderter Deckanhydrit (z2GA) to Leine Karbonat (z3LK)

Anhydritmittel (anhydrite beds) 1, 7 and 9 consist of anhydrite layers with thicknesses of about 0.2 to 2.3 m. Taking into consideration that these beds are not continuous but have been strongly boudinised by salt tectonics – in other words, sheared into separate blocks a few metres long with no connection to one another – the isolated occurrences of fluids here can only be in the order of a few litres.

The Gorleben Bank largely consists of a tightly bedded anhydrite layer. Occurrences of fluids are associated with the Gorleben Bank itself, and with secondary healed joints and crystallisation zones in the immediate surroundings. In the explored part of the salt dome, primary-sedimentary fluctuations with thicknesses varying from 3.5 cm to 70 cm within a very short distance were identified in the Gorleben Bank. The clay layer is a zone of

weakness regarding the mechanical behaviour. The bedded sequence was torn apart by the folding tectonics within the Gorleben Bank. This created a zone of displacement which always runs parallel to the bedding of the Gorleben Bank. During the formation of the salt dome, joints opened in the zone of displacement when the bedded anhydrite layer exceeds a thickness of around 6 cm. These limited joints within the zone of displacement became traps as well as a storage medium for brines and gases. The displacement zone acted as a migration path for fluids, also allowing brines and gases to be distributed within the immediate surroundings of joints. This zone of displacement does not create a migration path perpendicular to the Gorleben Bank. When the total thickness of the Gorleben Bank is only a few centimetres, there is either no zone of displacement, or it is only a few millimetres thick (BÄUERLE 2000). The size of the occurrences of fluids can be in the range of a few cubic centimetres. It is possible for the separate occurrences of fluids to be connected to one another via the slickensides in the bedding-parallel faults in the Gorleben Bank.

Brines and gases can be stored in the joints which cut the anhydrite blocks within the Hauptanhydrit sequence. The joints are mostly healed by secondary halite and secondary carnallite. Figure 7.8 shows as an example a core with healed joints from the Hauptanhydrit.



Figure 7.8: Core with healed joints in the Hauptanhydrit

The healing of the joints was not complete. Druse-filled cavities measuring a few centimetres in size have been discovered locally in these joints within the Hauptanhydrit. Only a few open joints several millimetres wide have been observed. In three exploration boreholes inflows from isolated occurrences of fluid occurred. The data from these inflows were analysed in the material balance equation discussed above. Sizes ranging from 100 m³ to several thousand cubic metres were calculated. This range is consistent with the geological model of the encountered isolated blocks of Hauptanhydrit. However, the maximum amount of brine that was produced from one exploration borehole was actually 165.7 m³ which is clearly below the maximum size that was derived for the corresponding occurrence of fluid.

7.2.3.2 Occurrences at the Zechstein 3 / Zechstein 2 boundary

Occurrences of fluids at the z2/z3 boundary are possible if the Hauptanhydrit has become squeezed out by salt-tectonic deformation and the Kaliflöz Staßfurt has either been thickened by stacking or significantly thinned out. Occurrences with two different appearances can be differentiated here:

- Druse-like cavity fillings largely healed by secondary halite and secondary carnallite: the fluids occupy the unhealed interstitial spaces between the crystals. Such druse-like cavity fillings have sizes of max. approx. 1 m³. There is no connection between isolated occurrences. The volume of brines and gases released during drilling is in the order of a few litres.
- Strong deformation of the Unteres Orangesalz and Liniensalz bedding sequence from the Gorleben Bank (Mittleres Orangesalz) up to the boundary between Zechstein 3 and Zechstein 2: this sedimentary sequence is faulted. Its joints and faults are largely healed by secondary clear coarse-crystalline halite (crystals up to 10 cm in size). Secondary carnallite occurs as a subordinate mineral in the interstitial spaces. The brines and gases are stored in the unhealed interstitial spaces between the coarse crystalline halite crystals. The total extent of hydraulically communicating zones within the mentioned stratigraphic units is well over 10 m. Isolated occurrences of fluids were encountered in two exploration boreholes. The inflows were analysed using the material balance equation to determine the total volume of fluids. Sizes ranging from 100 m³ to several thousand cubic metres at maximum were calculated. However, the maximum amount of brine that was produced from the z2/z3 boundary to one exploration borehole was actually 23.7 m³ which is clearly below the calculated maximum size that was calculated for the corresponding occurrence of fluids.

7.2.3.3 Occurrences in Zechstein 2

The Hauptsalz of the Staßfurt-Folge (z2) is a “salt-tectonic breccia”. In case the Gorleben salt dome is found to be qualified the disposal of heat-generating waste is envisaged within the Hauptsalz of the Staßfurt-Folge. No occurrences of fluids such as seen in Zechstein 3 or at the z2/z3 boundary were encountered in the Hauptsalz of the Staßfurt-Folge (z2). The Hauptsalz can be classified as a “salt-tectonic breccia” because the former fabric of the Hauptsalz has become thoroughly mixed and homogenised by repeated fracturing and healing of the halite during diapiric salt uplift (approx. 2 km – 5 km laterally and 3 km vertically). Any brines and gases of sedimentary and diagenetic origin originally present within the Hauptsalz, as well as any metamorphism brines which may have been present, were squeezed out as a result of this mixing to either finish up in the top salt or in

anhydrite-joint reservoirs within the Leine-Folge, such as in the Hauptanhydrit. This is why large occurrences of fluids are not expected to be encountered during the underground exploration of the Hauptsalz in the Gorleben salt dome – this conclusion was confirmed by several exploration boreholes.

8 Characterisation of the mechanical properties

Laboratory tests have to be carried out to characterise the mechanical material behaviour of the rocks by determining the location-specific material parameters. The material parameters can be used as the basis to define the zones at the site with the same material properties and classify them as geomechanically homogenous zones.

These homogenous zones and their material properties are taken into consideration in the elaboration of the site-specific geomechanical model which forms the basis for the development of the numerical models. These numerical models are then used to realistically simulate the load-bearing behaviour of the exploration mine and the geological barriers, as well as to determine the temporal and spatial stress changes affecting the overall structure (LANGER & HEUSERMANN 2001, HEUSERMANN 2001).

The investigations and findings presented here are based exclusively on the rocks encountered in the underground workings within the salt dome. In addition, numerous laboratory tests on the compaction behaviour of crushed salt were carried out, as described in detail in STÜHRENBURG & ZHANG (1998), STÜHRENBURG (2002), and STÜHRENBURG (2004). Although these investigations provide no information on how to characterise the host rock and are therefore not described here. They make a major contribution to the science behind the backfilling and sealing measures used in underground cavities.

8.1 *Laboratory investigations on mechanical behaviour*

Comprehensive laboratory tests were carried out on rock specimens to determine the mechanical behaviour of the stratigraphic units encountered in the exploration mine. This involved determining the deformation and strength properties on the basis of uniaxial and triaxial pressure tests, as well as Brazilian tests. Uniaxial and triaxial long-term tests on cylindrical specimens, as well as real triaxial tests on cubic specimens were carried out to ascertain the long-term deformation behaviour, which is characterised influenced by the marked creep behaviour of rock salt and possibly by dilatant deformation processes. In addition, deformation parameters for the evaluation and interpretation of the overcoring tests to determine the rock stresses were determined in biaxial tests.

8.1.1 Investigation methods

Ultrasonic measurements

Ultrasonic measurements on rock specimens were conducted prior to every strength test to determine the rock-dynamic parameters and to assess the sample quality. This involved determining the velocities of the longitudinal ultrasonic waves (v_p) and the transverse ultrasonic waves (v_s) both parallel and orthogonal (lateral) to the longitudinal axis of the usually cylindrical specimens. The ultrasonic velocities can be used to identify anisotropies associated with the layering and/or crystal alignment. No or not measurable ultrasonic velocities indicate a loose grain fabric, which may be an artefact of drilling or transport processes. The ultrasonic velocities v_p and v_s , as well as the density of each specimen, were used to calculate the dynamic material parameters (modulus of elasticity E_{dyn} and Poisson's ratio ν_{dyn}).

Brazilian tests

In the Brazilian tests, tensile stresses are generated which act orthogonal to the stress plane by applying diametrically opposed line loads to a cylindrical rock specimen. The load is raised until the rock specimen splits. The tensile strength is determined from the maximum load when the specimen fractures, taking into consideration the geometry of the specimen. This analysis must take into consideration fabric anisotropies associated with layering or crystal alignment, and the specimens have to be oriented accordingly to the plane along which the forces are applied (GARTUNG 1985 and DGGT 2008).

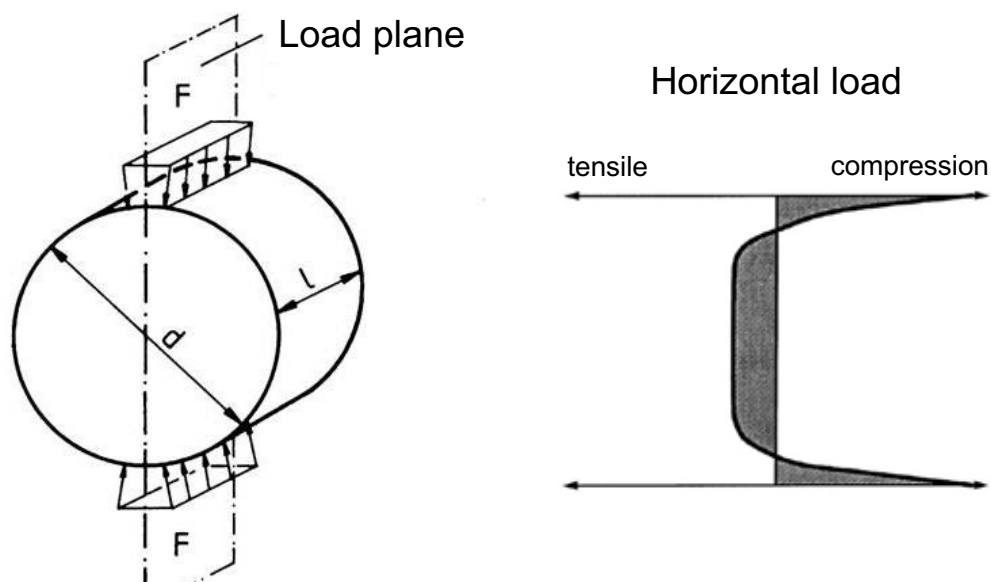


Figure 8.1: Sketch of the principle behind a Brazilian test (GARTUNG 1985 and DGGT 2008)

Strength tests

The mechanical strength tests are carried out on servo-hydraulic and computer-controlled test machines operated by BGR which comply with accuracy class 1 pursuant to DIN 51223. Figure 8.2 diagrammatically shows the general layout of a triaxial test apparatus – with a triaxial pressure cell according to the Kármán principle. Design and technical details are reported by HESSER & SCHNIER (2002).

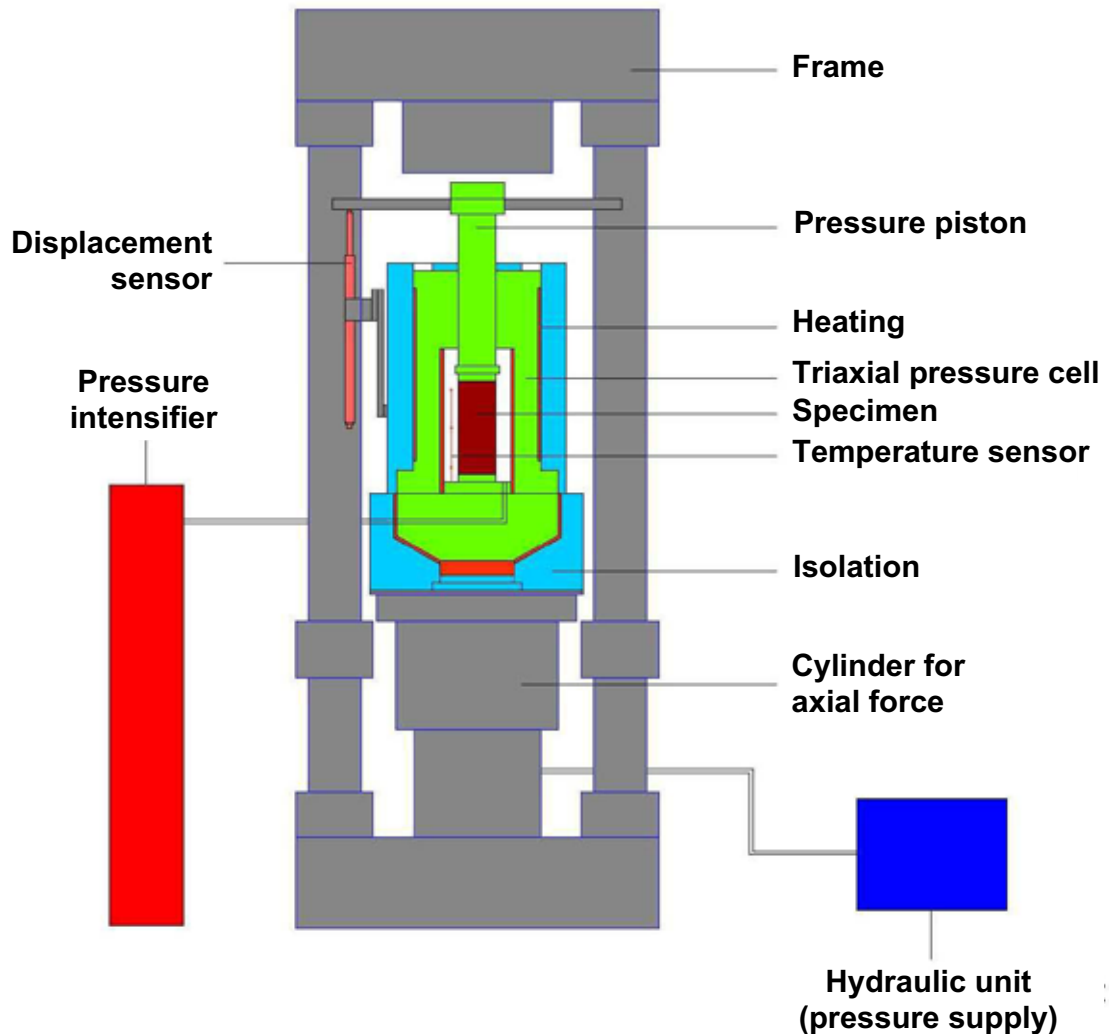


Figure 8.2: Structure of a triaxial test apparatus for mechanical strength investigations

In the uniaxial pressure tests, the specimens were positioned directly between the upper and lower steel plates. In the triaxial tests, a hydraulic supporting pressure (confining pressure) is applied to the outer surface of the specimen in a triaxial pressure cell, where the specimen is protected against the oil in the pressure cell by a rubber jacket.

During strain rate controlled testing, the axial load is increasing until the rock specimen fractures in both the uniaxial tests as well as the triaxial strength tests. In the triaxial tests the straining is continued even after the specimen fails, to determine the post-failure strength.

Unloading and reloading cycles are carried out prior to the failure of the specimen to determine the modulus of elasticity and the Poisson's ratio. Detailed descriptions of the uniaxial and triaxial strength tests are given in HESSER & SCHNIER (2002).

During testing, the axial loads applied to the test specimens are continuously measured, as are the supporting pressure (confining pressure), and the axial deformation. Careful calibration must be carried out to enable the measurements to comply with accuracy class 1 (deviation < 1 % from the final value).

In uniaxial strength tests, the transverse (i.e. radial) expansion of a specimen is determined with a spring clamp, developed by BGR for large circumference expansion.

Contrary to recommendations number 1 and number 2 of the working group "Rock testing technology" of the Deutsche Gesellschaft für Geotechnik e.V. (DGGT) after RISSLER (1979) and MUTSCHLER (2004), determination of the failure strengths was performed taking into consideration the existing cross-sectional surface area of the specimen and the maximum force when the fracture occurred (Figure 8.3).

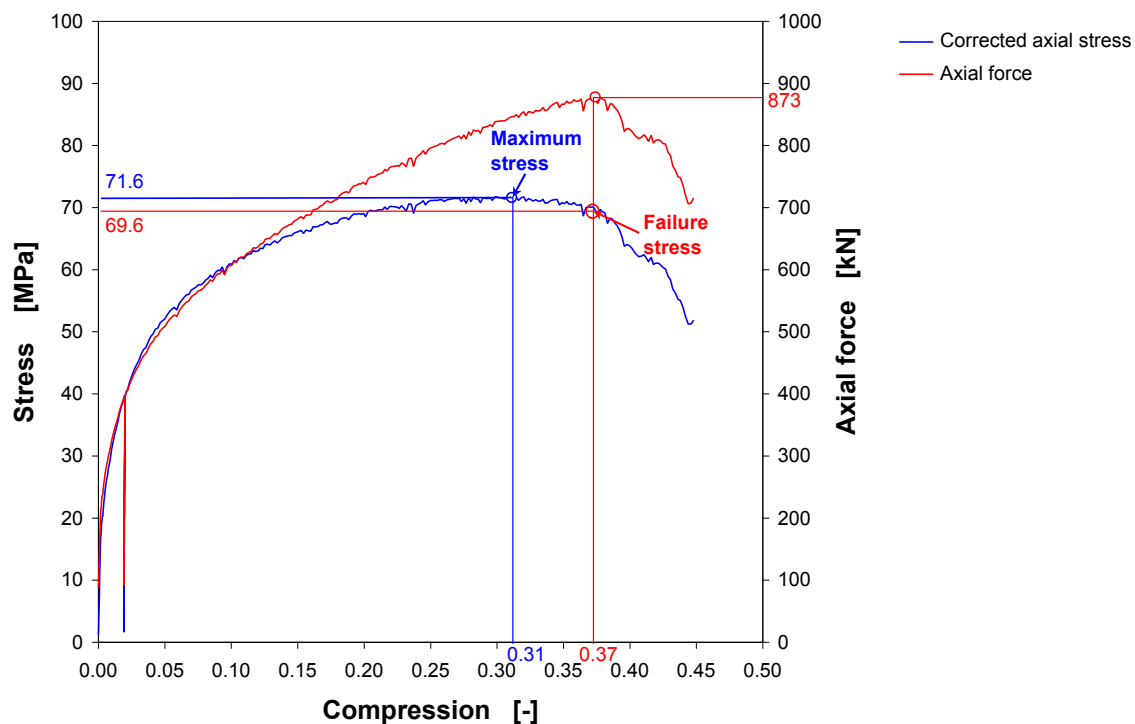


Figure 8.3: Determining the failure stresses in uniaxial and triaxial strength tests

The procedure is based on laboratory findings which revealed that in tests with larger compressions, a further increase in the applied force takes place after the maximum stress is reached until the actual failure occurs. The associated differences to the conventional measurement of failure stress, including failure strain, can be up to a few per cent, depending on the confining pressure. The failure strain quantifies the axial specimen deformation at the point of failure.

Creep tests

Creep – inelastic, time-dependent fractureless deformation – is a key aspect in the characterisation of the mechanical behaviour of rock salt. It should be noted that rock salts are characterised by complex mechanical behaviour. They react in a brittle way to rapid deformation but in a largely ductile way to slow deformation.

To determine the long-term deformation behaviour of the evaporite beds encountered during the exploration of the Gorleben salt dome, the creep behaviour of more than 300 specimens was analysed between 1982 and 2002. This comprised multi-stage creep tests with more than 600 sub tests under uniaxial and triaxial loads, followed by their evaluation.

Uniaxial creep tests were carried out in BGR's creep test apparatus at room temperature (approx. 22 °C) and a relative humidity of 45 % ± 5 %. In the tests carried out in the triaxial test cells, temperatures of up to approx. 150 °C could be applied to simulate thermally-induced near field processes. The tests were usually carried out at temperatures of up to 50 °C.

The creep tests were carried out as compression tests in which the axial load on the cylindrical specimen is larger than the confining pressure ($\sigma_1 > \sigma_3$). The confining pressure σ_3 was in most cases equivalent to the petrostatic pressure at the exploration level (σ_3 : 15 MPa – 20 MPa).

During the tests, the specimens were first brought up to the initial test stress by raising the load by approx. 1 MPa/min. This stress was then kept constant until a constant creep rate developed over a long period of time. The stress was then raised by one load level, increasing the pressure by 1 MPa/min. Each part of the test with constant stress and temperature conditions is referred to below as a sub-test.

The steady-state creep rate for each sub-test was determined to quantify the creep behaviour. Steady-state creep exists as soon as the deformation rate has converged to an almost constant level. It is therefore determined at the end of a sub-test from the relevant deformation-time diagram.

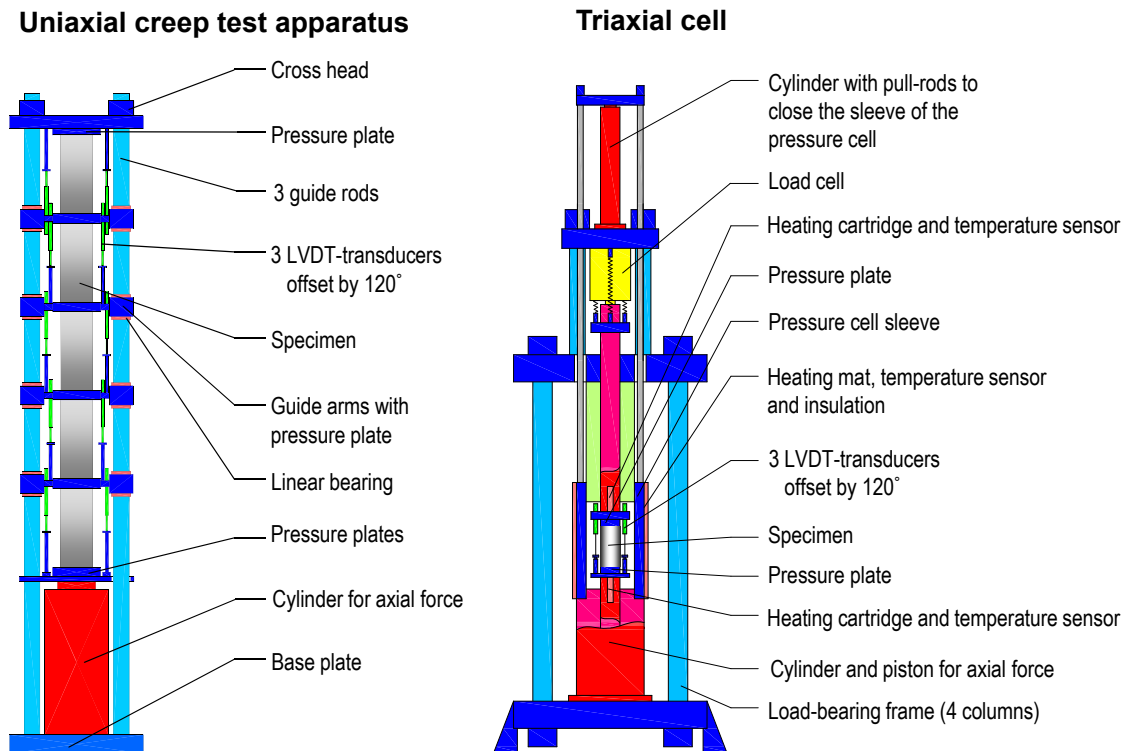


Figure 8.4: Uniaxial and triaxial creep test apparatus

It should be noted that the true steady-state creep rate can be lower. This was revealed by creep tests carried out with specimens consisting of a less ductile rock salt over a much longer duration (PLISCHKE & HUNSCHE 2002).

Creep classes are derived from the calculated creep rates. These classes are based on the creep laws used by BGR (HUNSCHE & SCHULZE 1994). In the case of the uniaxial tests carried out at room temperature, the creep classes are assigned on the basis of the BGRa creep law (PLISCHKE & HUNSCHE 2002) according to equation (8.1) in chapter 8.2. The creep law BGRb on which equation (8.2) is based is used for tests with higher temperatures (i.e. above approx. 30 °C) and for triaxial tests, because humidity induced creep is suppressed under these conditions. The creep classes characterise different creep capacities which are taken into consideration in creep laws BGRa and BGRb by the pre-factor V . A pre-factor value of 1 is used in the BGRa and BGRb creep laws for creep class 5. Creep class 5 therefore defines creep behaviour complying with “standard creep”. Table 8.1 shows the creep classes and the associated pre-factors.

Table 8.1: Pre-factors associated with the creep classes

Creep class K	-1	0	1	2	3	4	5	6	7	8	9
Pre-factor V	1/64	1/32	1/16	1/8	1/4	1/2	1	2	4	8	16

Biaxial tests

The modulus of elasticity of the rock in the investigation zone is needed to evaluate and interpret the overcoring tests used to determine the rock stresses (see Chapters 6.1.1 and 6.3.1.2). To determine the modulus of elasticity, loading and unloading tests were carried out in the cylindrical cores extracted after the overcoring tests. BGR uses a special laboratory apparatus (Robertson cell) for the biaxial tests involved, as shown in Figure 8.5.

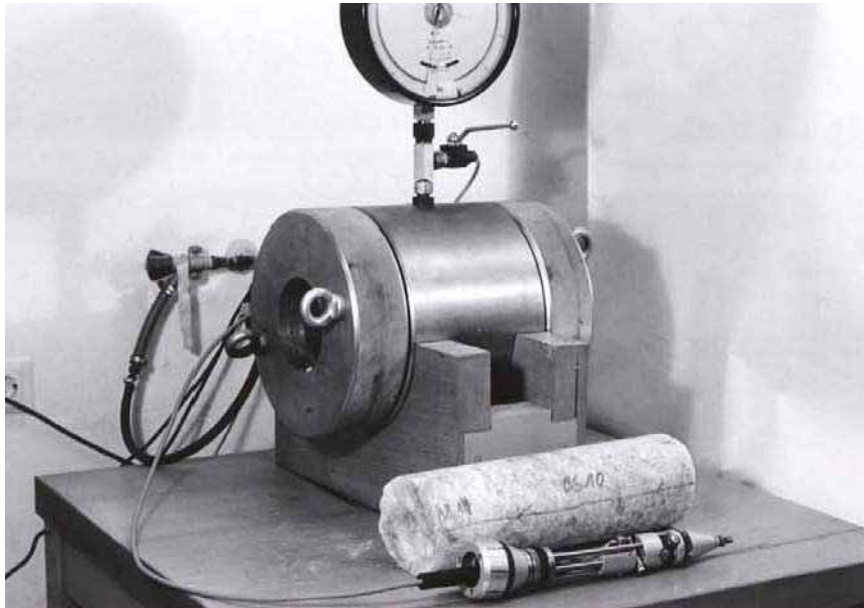


Figure 8.5: Laboratory test apparatus for carrying out biaxial tests on hollow cylindrical specimens

In these biaxial tests, a radially-acting, axial-symmetrical hydraulic pressure is applied to the outer surface of the hollow cylindrical core. The changes in diameter of the centric hole inside the core are measured during several loading and unloading cycles.

Loading was usually at pressures of 5.0 MPa, 7.5 MPa and 10.0 MPa for cores from the shafts, and at 9.0 MPa, 12.0 MPa and 15.0 MPa for cores from the exploration level. In selected cases, an additional higher loading level was applied which corresponds to the theoretical overburden pressure at the depth the samples were taken from.

A measuring system developed by BGR with four sensors each offset by 45° in a clockwise direction was used to continually record the diameter changes in the centric internal borehole.

The laboratory measurements are presented and evaluated in load-deformation diagrams. The gradient of the secant running through the starting point and end point of a unloading branch is used as a measure of the modulus of elasticity. This procedure deviates from

the general method of determining the modulus of elasticity from the secants of the points dividing a unloading branch into three equal sections, but makes sense because of the complete stress release of the overcored specimen which takes place during the overcoring tests, and the special use of the moduli of elasticity determined in this way for the evaluation of the overcoring tests. This evaluation results in lower values of the moduli of elasticity in comparison to the general method.

To convert the measured values into a modulus of elasticity, use is made of the model of a hollow cylinder in a planar stress state (axial stress $\sigma_3 = 0$) under an external radial load after WORCH (1967). Poisson's ratio is not used to determine the modulus of elasticity because of the biaxial stress applied to the specimen in this case, which does not involve the application of any axially acting load.

The modulus of elasticity determined for each core is then assigned to each overcoring test and used as an input parameter to calculate the primary stresses at each measurement location (cf. Chapters 6.1.1 and 6.3.1.2).

8.1.2 Sample material

The stratigraphic units from the Hauptsalz of Zechstein 2 to the Anhydritmittelsalz of Zechstein 3 were encountered in the salt dome during the sinking of the shafts and the drifting of the exploration level. The structure of the Gorleben salt dome, its internal structure, and the geological and mineralogical properties of each stratigraphic unit are described in detail in BORNEMANN et al. (2003). The stratigraphic sub-division of the Zechstein evaporite (Appendix 1) is mainly based on the petrographic composition of the evaporites and the nature of the fabric. Homogenous zones with identical mechanical properties were differentiated to characterise the rock-mechanical properties (cf. Chapter 8.3).

Several cores for geomechanical tests were taken in each exposed stratigraphic unit during the sinking of the shafts and the drifting of the underground workings – particularly when drilling the measurement boreholes in the exploration horizons in the shafts and in the exploration locations at the exploration level. The sampling locations are tied to the spatial position of the underground workings and the boreholes, and are therefore heterogeneously distributed – they do not therefore satisfy geo-statistical criteria in the sense of a uniformly distributed sampling mesh. The sampling locations were defined by the geological mapping results and therefore the specimens can be considered to be representative samples of the geological layers forming the salt dome. A detailed description of the petrography and the fabric was made for each specimen prior to undertaking the laboratory tests.

Only Zechstein 3 (Leine-Folge) beds were exposed in shafts 1 and 2. Cores from the Oberes and Unteres Orangesalz (z3OSO and z3OSU) as well as the Bank/Bändersalz (z3BK/BD) were selected for the laboratory tests from the measurement boreholes in both shafts. In addition to these, samples from the Liniensalz (z3LS) and the Anhydritmittelsalz (z3AM) from shaft 1 were selected for laboratory testing.

Almost 500 specimens in total were analysed from the measurement boreholes in shafts 1 and 2, and from exploration boreholes Go 5001 and Go 5002. More than half of the samples underwent uniaxial and triaxial strength testing. More than 140 samples were used for long-term creep behaviour tests. Two samples were analysed to determine the dilatant deformation processes. Deformation parameters to evaluate the overcoring tests were determined for more than 60 specimens.

At the exploration level, samples were collected and analysed from the following beds in the Zechstein 2 (Staßfurt-Folge, z2) the units Knäuelsalz (z2HS1), Streifensalz (z2HS2), Kristallbrockensalz (z2HS3) and Kaliflöz Staßfurt (z2SF); in the Zechstein 3 (z3) the units Liniensalz (z3LS), Unteres and Oberes Orangesalz (z3OSU, z3OSO), Bank/Bändersalz (z3BK/BD), Bunttes Salz (z3BT) and Anhydritmittelsalz (z3AM).

The Knäuelsalz is the oldest stratigraphic unit in the evaporite beds exposed at the site, and the Anhydritmittelsalz is the youngest unit. Specimens from the Kaliflöz Staßfurt were primarily collected from the Hartsalzfacies (z2SF_ki).

Almost 400 specimens were analysed from the exploration level.

The uniaxial and triaxial strength properties were determined on more than 150 samples. Characterising the creep behaviour also involved testing of more than 150 specimens from the exploration level. The deformation parameters for the overcoring tests were determined on 28 specimens.

With the exception of a few samples consisting of sylvinitic Hartsalz, most of the samples from the shafts and the exploration level consisted of rock salt from the stratigraphic units encountered at the sampling locations with varying quantities of mineral impurities.

8.1.3 Test results

8.1.3.1 Density

The dimensions and masses of each sample were determined as part of the preparatory work carried out on the specimens prior to laboratory testing. The densities were determined from the volumes calculated from the dimensions. Figure 8.6 shows the average rock density of each stratigraphic unit in the shafts and at the exploration level.

The density of individual samples varied between 2.11 g/cm^3 and 2.29 g/cm^3 . The specific gravity of pure halite is 2.17 g/cm^3 .

Higher densities are caused by the presence of other constituents, in particular anhydrite, sometimes also kieserite, as seen in the Hauptsalz as well as partially also in the Anhydritmittelsalz. The lower densities can be caused by the presence of accessory minerals, consisting of e.g. carnallite or sylvite, or by gas inclusions. Lower densities can also be caused artificially by deconsolidation of the fabric as a result of stressing during sample extraction or transport of the rock samples (cf. Chapter 8.1.3.2).

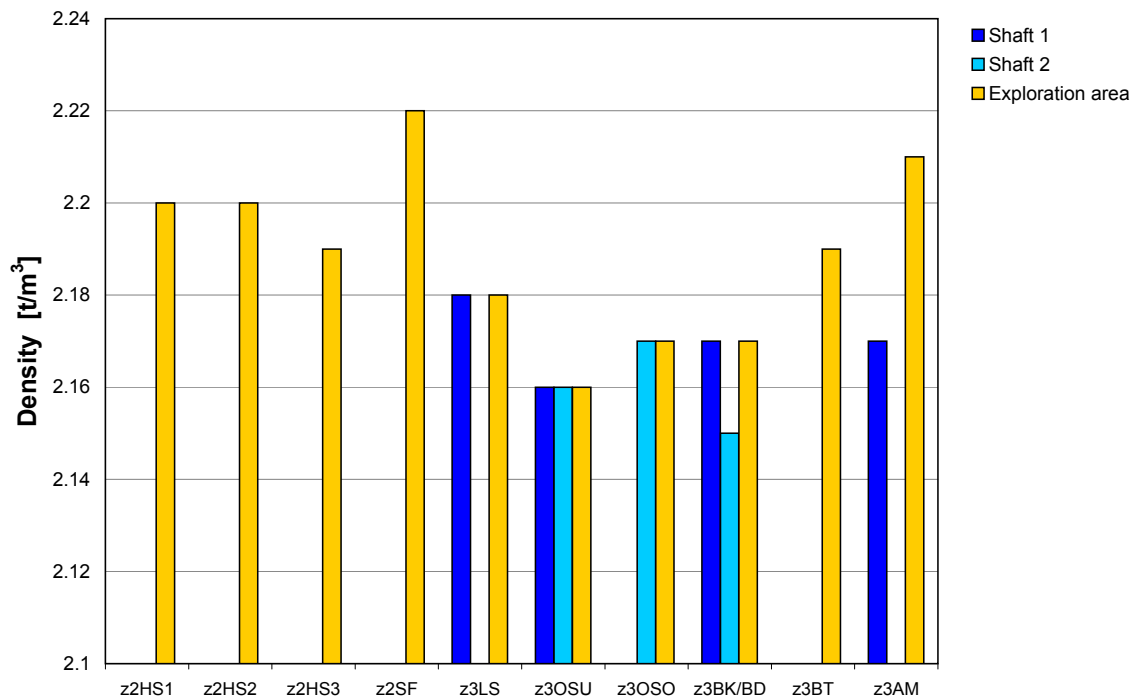


Figure 8.6: Average densities of the investigated rock specimens from different stratigraphic units in shaft 1, shaft 2, and the exploration area

8.1.3.2 Rock-dynamic parameters

The average velocities of the longitudinal P-waves (v_p) and the transverse S-waves (v_s) determined in the longitudinal axes of the specimens in the ultrasonic analysis are summarised in Figure 8.7.

The examination of the individual samples revealed the presence of deconsolidation in the samples from the Unteres Orangesalz (z3OSU), which is also detectable in the samples from the exploration level by the low P-wave velocities and absence of S-waves. No primary geological causes are known to explain this phenomenon. The petrographic composition and the rock fabric of individual stratigraphic units could favour secondary deconsolidation as a result of drifting or sampling. During drilling it was observed that the drilling process (speed, pressure, bit type) has a critical influence on the quality of the cores and therefore also on the specimens. The presence of deconsolidation of this kind meant that only a few ultrasonic measurements could be successfully carried out on specimens from the Unteres Orangesalz (z3OSU) from shaft 2. In other stratigraphic units such as the Liniensalz, damage and foreign mineral inclusions were less noticeable. Low P-wave velocities in the Hartsalz of the Kaliflöz Staßfurt are explained by refraction of the ultrasonic waves at the many mineral boundaries in the samples.

Figure 8.8 shows the average values of the dynamic modulus of elasticity and the Poisson's ratio for the investigated samples per stratigraphic unit. Because of the minor differences, the results of the two ultrasonic displacement directions (parallel and orthogonal to the longitudinal axis) have been combined. The differences in the dynamic elasticity parameters of the stratigraphic units between the locations is low – only the values of the Unteres Orangesalz in shaft 2 and the exploration level were slightly smaller than in the other locations. The scatter in z3AM is, however, higher because of the fluctuating petrographic composition.

Relatively uniform dynamic moduli of elasticity between 34 GPa and 38 GPa were determined for the samples from the Zechstein 2 on the basis of the ultrasonic measurements. However, significant fluctuations in some cases from 30 GPa to 40 GPa were determined for samples from Zechstein 3. This is attributable to the sampling locations. The dynamic Poisson's ratio has a relatively uniform value of between 0.2 and 0.3 for all of the stratigraphic units.

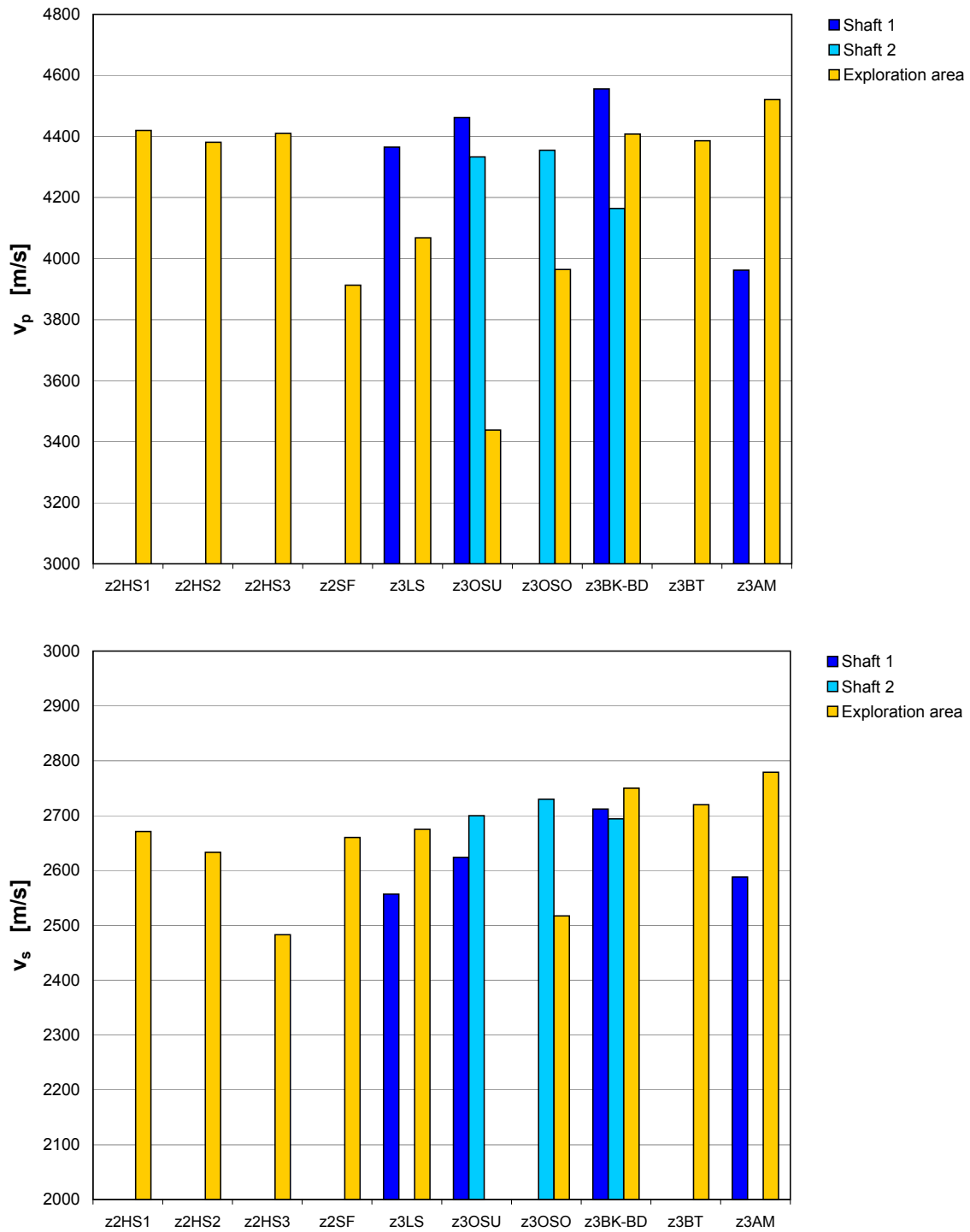


Figure 8.7: Average ultrasonic wave velocities of the specimens from the shafts and the exploration area

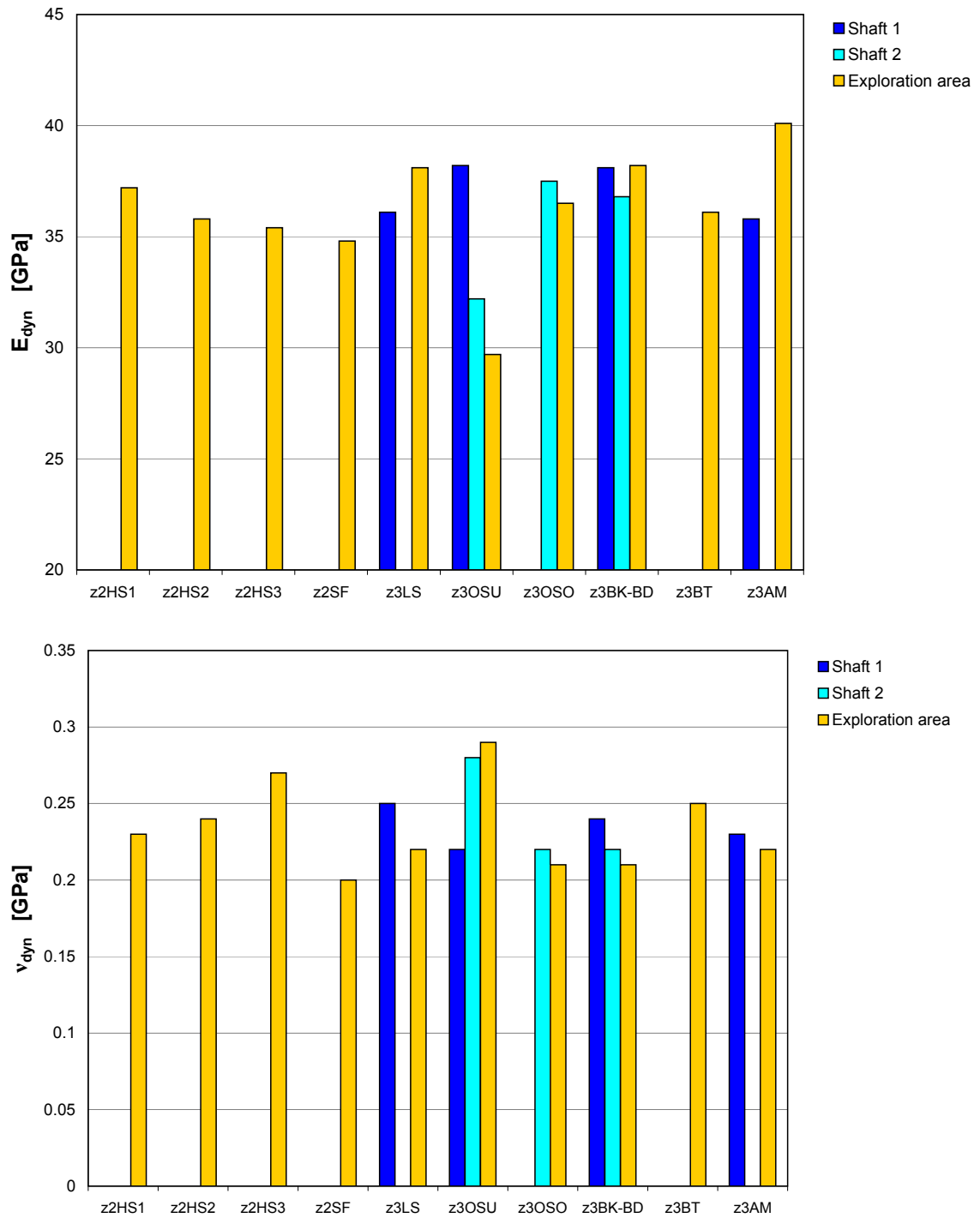


Figure 8.8: Dynamic moduli of elasticity E_{dyn} and dynamic Poisson's ratios v_{dyn} of the investigated stratigraphic units

8.1.3.3 Elastic deformation behaviour

The elastic deformation behaviour is described by the modulus of elasticity and Poisson's ratio. In addition to the relevant dynamic parameters (cf. Chapter 8.1.3.2), the static elastic material parameters were determined in the short-term tests from the unloading and reloading cycles before failure occurs. They were determined as secant moduli at the points dividing the unloading branch into three equal sections in the stress-strain diagram. The static modulus of elasticity was determined from the uniaxial and triaxial pressure tests. For reasons associated with the apparatus, the static Poisson's ratio could only be determined from uniaxial tests with transverse expansion measurements.

Figure 8.9, presenting the test results for specimens from the exploration area, shows a difference with respect to the static moduli of elasticity of around 10 GPa when comparing the uniaxial and the triaxial test results. This verifies that even minor triaxial confining pressures are sufficient to close micro-fractures and pores in the specimens and to stabilise the specimens against the deformation of internal parting planes. Tests with only 0.2 MPa confining pressure produced static moduli of elasticity which lay between those of uniaxial tests and triaxial tests with an confining pressure higher than 1 MPa. In the short-term deformation tests, there was no pre-compaction of the samples as undertaken for the creep tests.

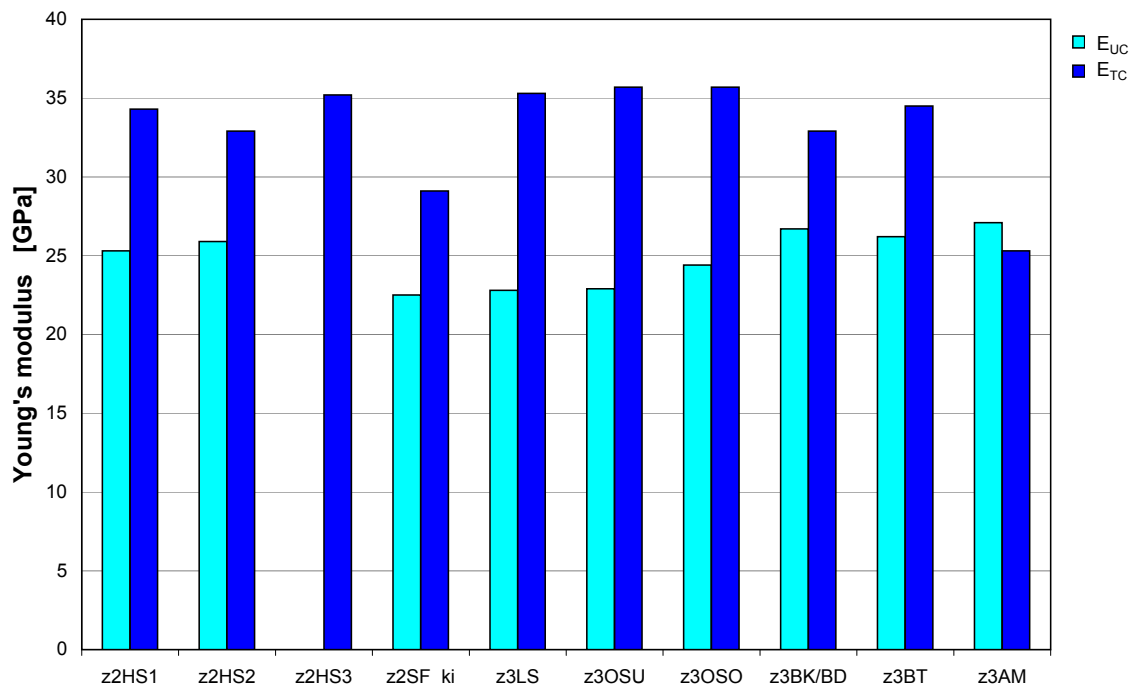


Figure 8.9: Average static moduli of elasticity of the exploration level for uniaxial stresses E_{UC} and triaxial stresses E_{TC}

Relatively uniform static moduli of elasticity of 33 GPa to 36 GPa under triaxial stress, and between 23 GPa and 27 GPa under uniaxial stress, were obtained with the exception of samples from the Anhydritmittelsalz (z3AM) and the Hartsalz of the Kaliflöz Staßfurt (z2SF). The static moduli of elasticity for the Hartsalz are slightly lower than those of rock salt, particularly under triaxial stress. The Anhydritmittelsalz has average static moduli of elasticity of around 25 GPa to 27 GPa under uniaxial as well as triaxial stress. No significant dependency on load boundary conditions is identifiable.

The static moduli of elasticity of the specimens from the shafts lie in a comparable range of 20.7 GPa to 27.3 GPa under uniaxial stress, and of 30.7 GPa to 35.2 GPa under triaxial stress. The test series for z2BK/BD and z3OSU in shaft 2 tend to have lower values. No dependency on the temperature or the load boundary conditions was identified in the triaxial tests on the specimens from the shafts or from the exploration level.

Static Poisson's ratios of 0.25 to 0.32 were determined for all specimens from all the locations in all the stratigraphic units.

A comparison of the results reveals that static moduli of elasticity determined from the triaxial short-term tests correspond closely with the dynamic moduli of elasticity. The same goes for the Poisson's ratios determined during testing.

Determination of the modulus of elasticity from the overcored specimens

The location-specific determination of material parameters for elastic deformation behaviour is required to evaluate the overcoring tests to determine the rock stresses (see Chapters 6.1.1 and 6.3.1.2). Loading and unloading tests in a biaxial stress state were therefore carried out on the hollow cylindrical cores extracted after the field tests.

The modulus of elasticity was determined in biaxial tests, as part of the rock stress determination in the shafts, on 35 overcoring specimens from shaft 1 and 32 specimens from shaft 2. Figure 8.10 shows, as an example, the load-deformation diagrams for a specimen from shaft 2 (EH-570). For all four measurement directions, the specimen load is plotted as a radially acting confining pressure against the change in interior diameter. Changes in diameters determined in various measurement directions produced similar plots and verify the isotropic deformation behaviour of the rock salt.

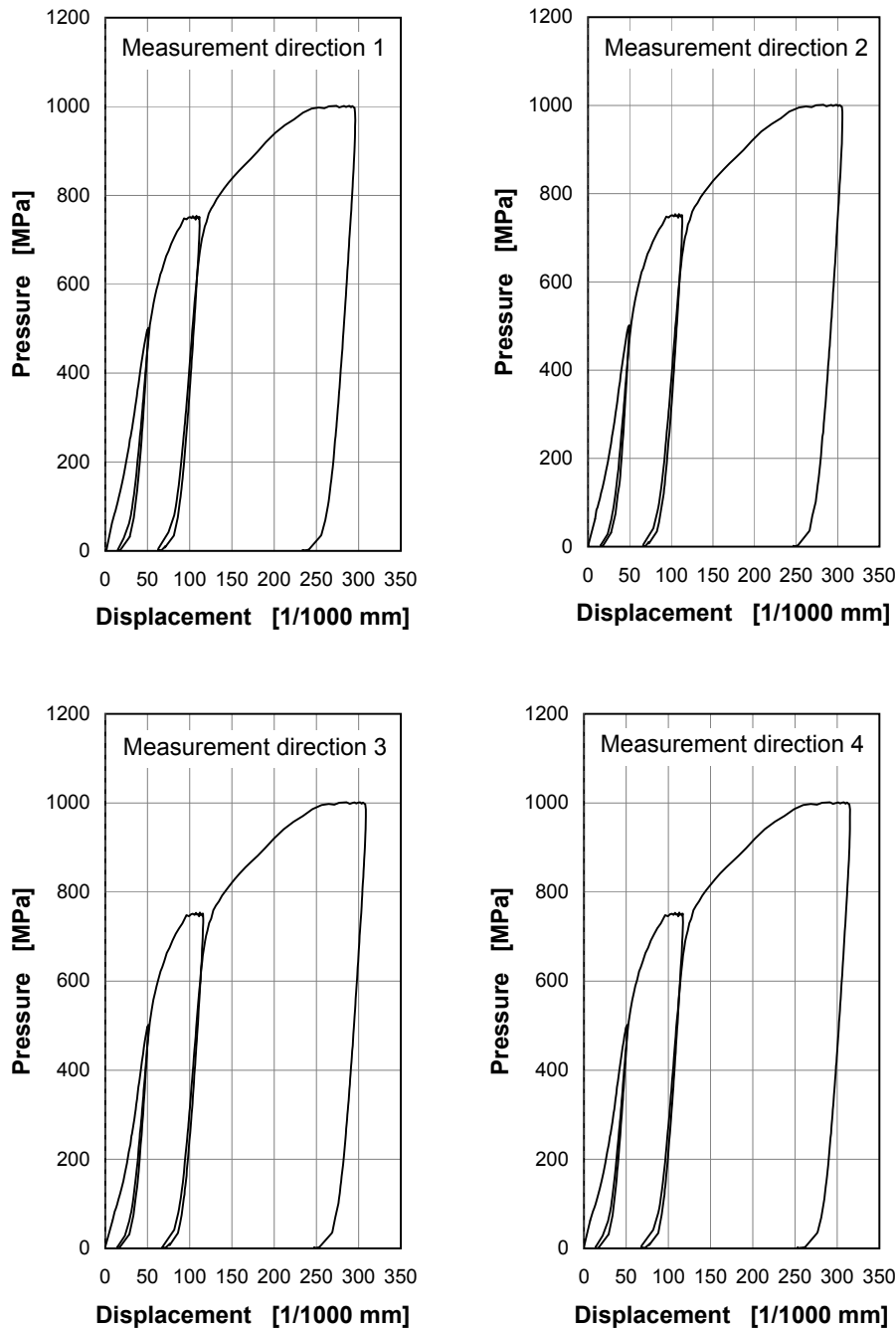


Figure 8.10: Example of a load-deformation diagram for a hollow cylindrical specimen from shaft 2

The moduli of elasticity for the specimens from the shafts, determined at different unloading steps and measurement directions in each test, are shown in Figure 8.11. The diagrams clearly show in some cases considerable differences in the moduli of elasticity in the exploration horizons in both shafts, which reflect salt layers with different degrees of stiffness.

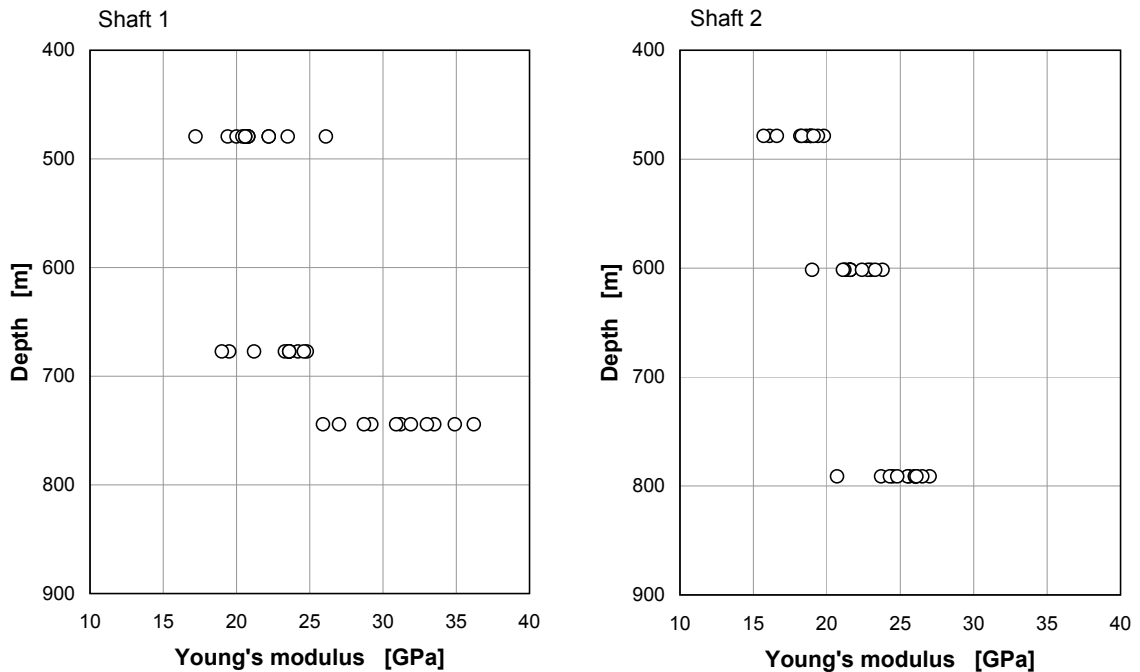


Figure 8.11: Moduli of elasticity determined in biaxial laboratory tests on cores from shaft 1 and shaft 2

Moduli of elasticity of between 17 GPa and 26 GPa were determined in biaxial tests in the overcored specimens from exploration horizons EH-450 and EH-650 in shaft 1. These are lower than the moduli of elasticity determined by the short-term tests (cf. Chapter 8.1.3.2). In contrast, the moduli of elasticity determined from the samples from exploration horizon EH-720 (shaft 1) correspond closely to the results of the short-term tests.

There appears to be a depth dependency of the moduli of elasticity in the overcored specimens from shaft 2. However, depth-dependency of this kind is not observed on solid cores which were used for short-term testing. In addition, only moduli of elasticity in samples from EH-760 in shaft 2 correspond to the results of the tests on solid cylindrical specimens. The parameters from the higher exploration horizons are smaller.

The moduli of elasticity were determined in biaxial tests on 28 cores from the overcoring tests to ascertain the rock stress in EL1 at the 840 m level. Figure 8.12 shows, as an example, the load-deformation diagrams determined from a specimen taken from EL1. The diameter changes determined in the four measurement directions, like the results of the tests on cores from the shafts, have closely corresponding curves, and therefore also confirm the isotropic deformation behaviour of the rock salt.

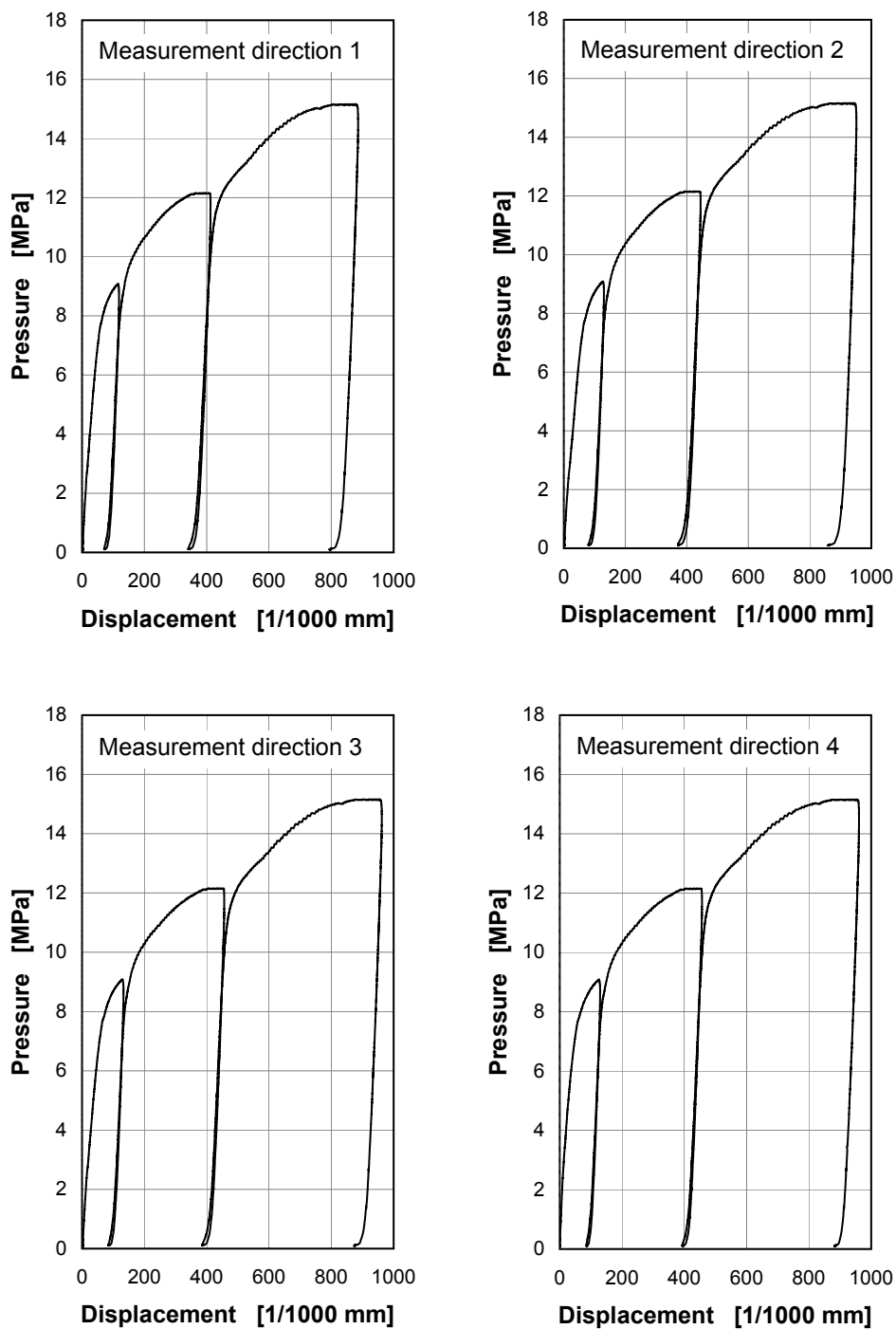


Figure 8.12: Load-deformation diagrams for a hollow-cylindrical specimen from EL1

Moduli of elasticity with an average of 21.0 GPa to 21.2 GPa were calculated from material from various boreholes drilled in the Unteres Orangesalz (z3OSU) at EL1. These values are slightly smaller than the static moduli of elasticity determined under uniaxial stress (cf. Chapter 8.1.3.3). The investigation of the Oberes Orangesalz (z3OSO) penetrated by one borehole produced, of contrast, an average modulus of elasticity of 27.0 MPa in the biaxial tests – a value which lies between the static moduli of elasticity under uniaxial and triaxial stress.

8.1.3.4 Tensile strength (Brazilian test)

The average tensile strength of the samples from shaft 1, shaft 2 and EB1 is shown in Figure 8.13. The values for the Bunter Salz (z3BT) and the Anhydritmittelsalz (z3AM) are each only represented by a single test result. Although two additional Brazilian tests were carried out for the Anhydritmittelsalz, these did not give rise to any analysable fracture and therefore did not produce any valid test.

The highest tensile strengths were measured in the specimens from the Hartsalz. The lowest tensile strength was found in the Unteres Orangesalz in shaft 2, ignoring the single test on z3BT. A pre-damage specimen is suspected in this case, as suggested by the ultrasonic measurements. The test results did not indicate any verifiable influence of material anisotropies on the magnitude of the tensile strength.

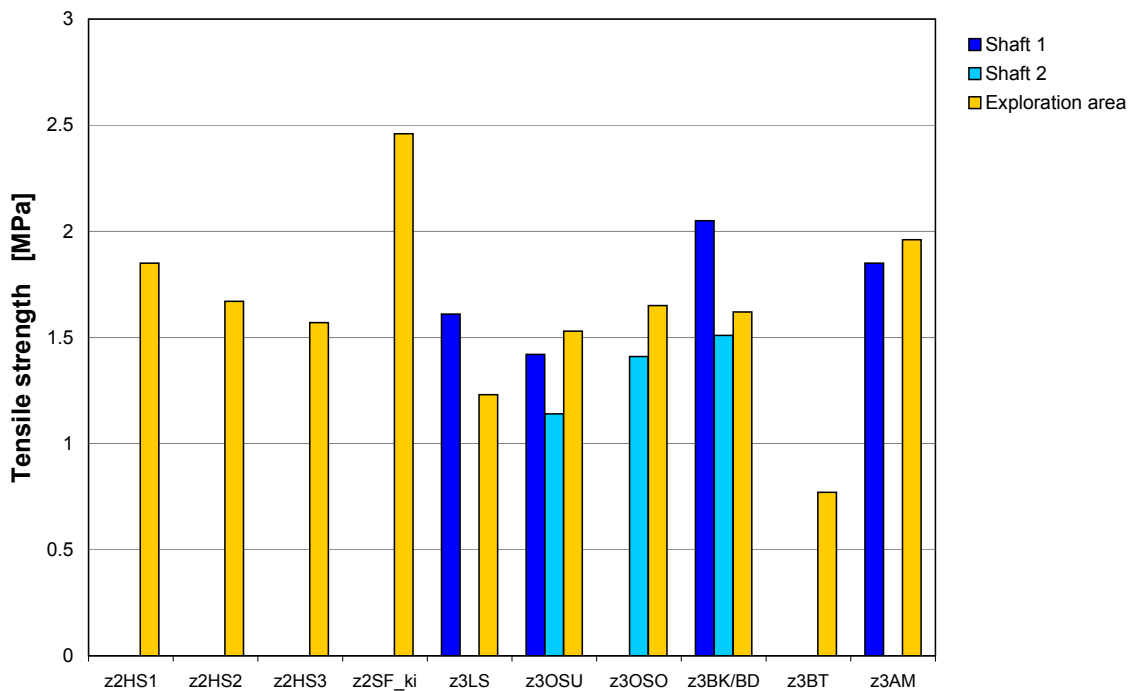


Figure 8.13: Average tensile strengths of the investigated rock samples

8.1.3.5 Uniaxial and triaxial compressive strengths

Short-term tests were carried out with different confining pressures to assess any possible differentiation of the strength behaviour in accordance with stratigraphic/petrographic criteria. In addition, the test temperature and the deformation rates were varied to ascertain the influence of temperature and loading rates on the strengths. This variation was carried out systematically in the test series on samples taken from the shafts. Variations in the loading rate were carried out on a random sample of specimens from the exploration level.

Figure 8.14 shows the uniaxial compressive strengths (failure strengths). The test results were determined at room temperature and axial deformation rates of 10^{-5} s^{-1} .

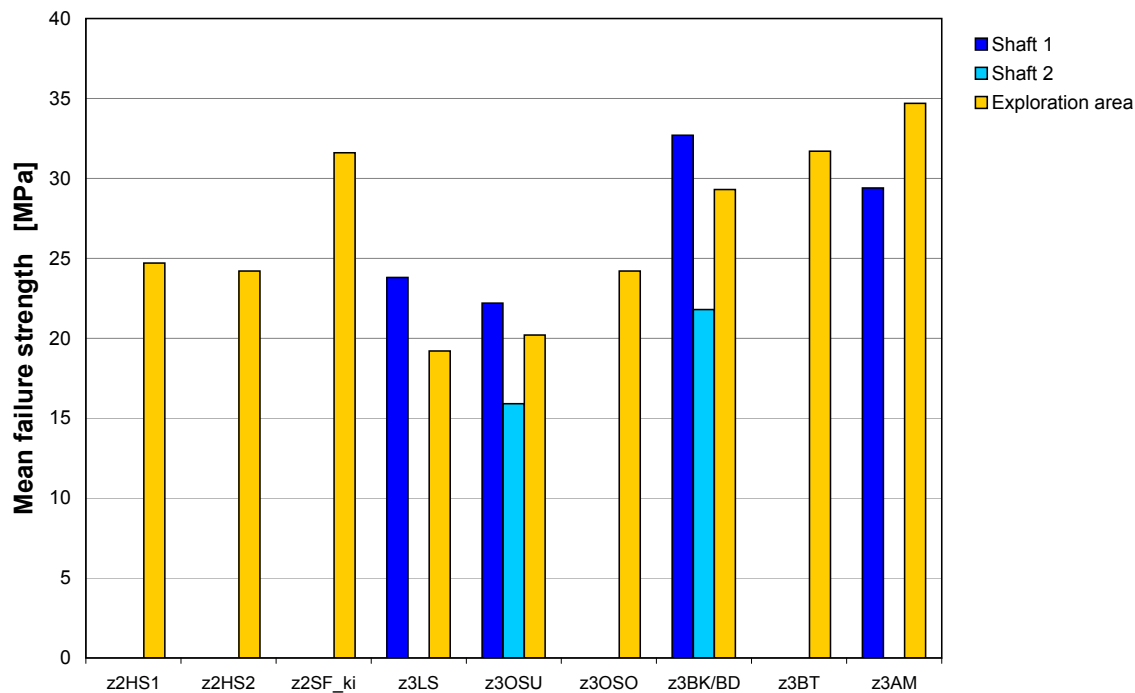


Figure 8.14: Average uniaxial failure strength of the investigated stratigraphic units

The maximum scatter of approx. 50 % is relatively high for the uniaxial compressive strengths. Noticeably low strengths were observed in the samples from stratigraphic units in the Unteres Orangesalz (z3OSU) and the Bank/Bändersalz (z3BK/BD) from shaft 2. These samples are strongly affected by fabric deconsolidation and/or foreign mineral impurity content, and the presence of gas inclusions.

Figure 8.15 shows the uniaxial and triaxial failure strength in the octahedral stress plane for all of the rock samples from the shafts. Tests were carried out at room temperature and with deformation rates of 10^{-5} s^{-1} . This clearly shows that the strengths rise with increasing minimal stress (confining pressure). With the exception of the strengths of the Bank/Bändersalz (z3BK/BD) from shaft 2, the relative scatter of maximum 20 % for the individual tests is low.

Parabolic regressions were carried out for the individual tests of the stratigraphic units and separate locations (HESSER & SCHNIER 2002). These regressions are based on the functional integration of octahedral shear stress and octahedral normal stress – as also used in the reference curve after HUNSCHKE (1995). The reference curve represents a lower envelope of the compressive strengths for more than 90 % of the separate tests on rock salt. The regression curves reveal a ranking of the strengths: with z3BK/BD from shaft 2 at the base, rising through z3OSO, z3LS, z3OSU from shaft 1 and then to z3AM and z3BK/BD from shaft 1.

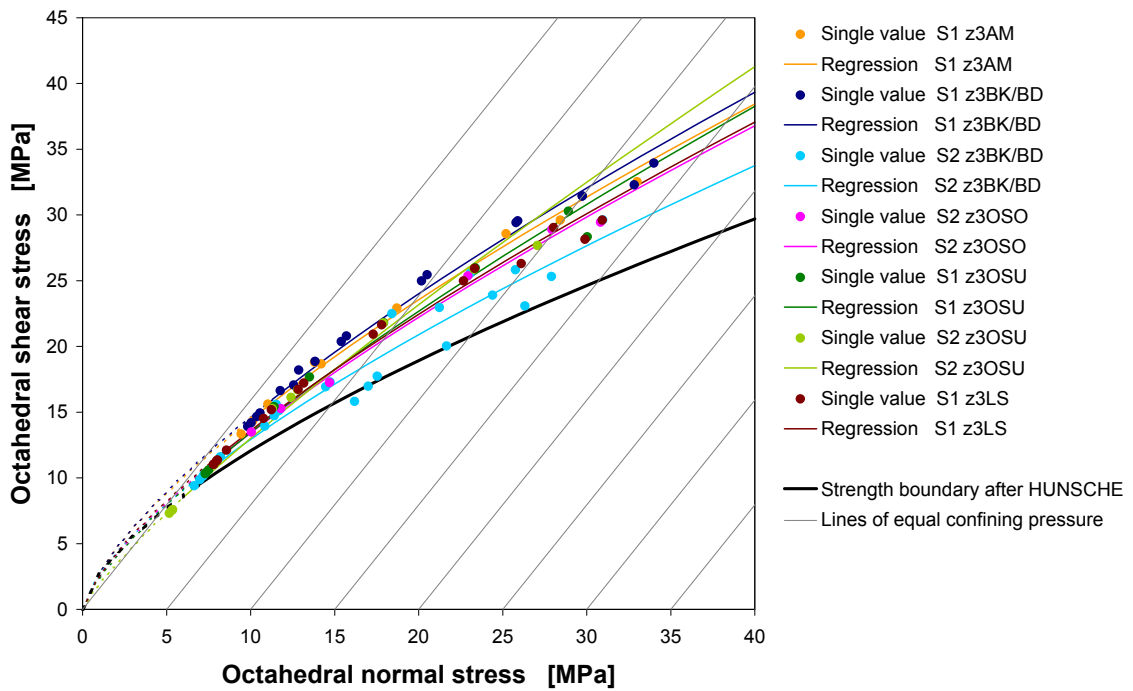


Figure 8.15: Uniaxial and triaxial failure strengths in rock samples from the shafts

Figure 8.16 shows the failure strengths of the stratigraphic units encountered at the exploration level. To improve comprehensibility, this graph does not show the separate tests but only the regression curves.

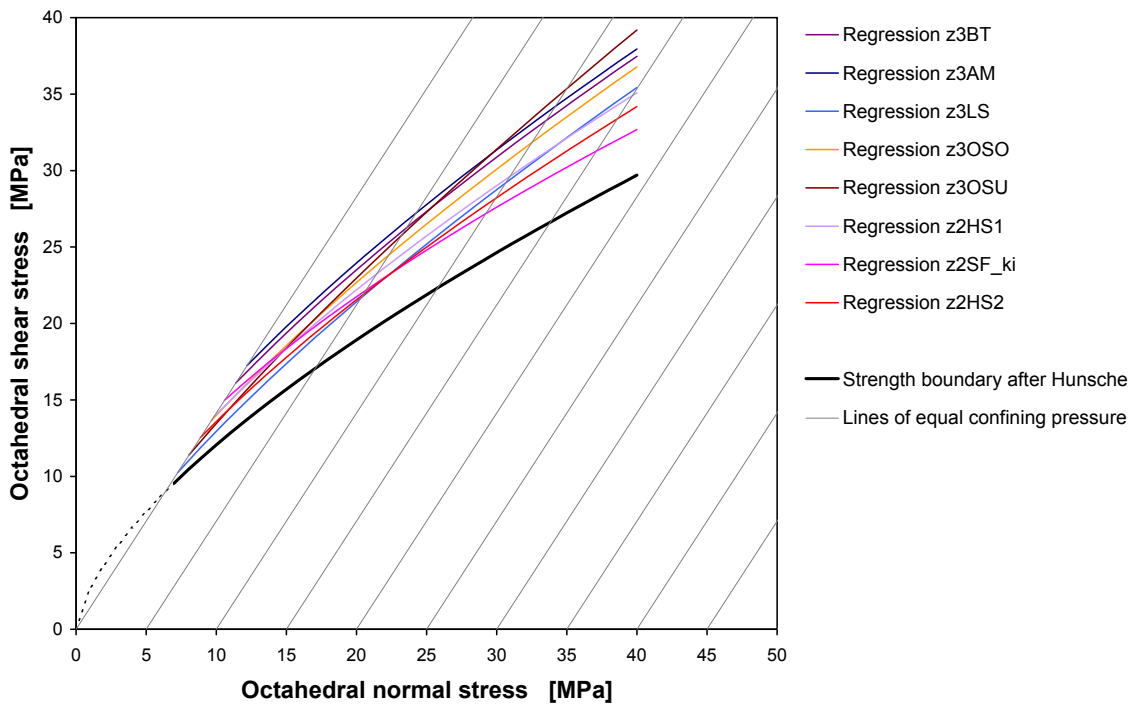


Figure 8.16: Uniaxial and triaxial failure strengths in rock samples from the exploration level

The relative scatter here is 15 %. All of the failure strengths in the separate tests lie above the reference curve after HUNSCHÉ (1995), even those of the Hartsalz from z2SF. Compared to the halite-dominated units, the Hartsalz tests at low confining pressures yielded average failure strengths. The lowest failure strengths are measured, however, if the confining pressures are higher. Contrasting behaviour is observed in the Unteres Orangesalz (z3OSU), where only low strengths were recorded under low confining pressures. However, the failure strength increased disproportionately with rising confining pressures. The other stratigraphic units can be ranked from low to high failure strength in the following order: z2HS2, z3LS, z2HS1, z3OSO, z3BT to z3AM.

Tests were carried out at temperatures of 80 °C, 120 °C and 180 °C to evaluate the influence of temperature on the failure strength. These temperature ranges reflect the temperatures expected in a geologic repository in a rock salt formation. The tests revealed a decrease in the average failure strength with increasing temperature. At a test temperature of 180 °C, the failure strengths obtained in the tests are around 50 % lower than at room temperature. The greatest changes in failure strengths with rising test temperatures are seen in the samples of the Knäuelsalz (z2HS1) and the Hartsalz (z2SF). The Anhydritmittelsalz (z3AM) shows a lower dependency of failure strength on the test temperature.

Slightly higher failure strengths with changes of 5 % to 8 % are observed when varying the deformation rate to a higher rate of 10^{-4} s^{-1} . At lower deformation rates of 10^{-6} s^{-1} , the failure strengths were 4 % to 11 % lower. No significant sensitivity of specific stratigraphic units to changes in deformation rate could be confirmed by the data.

8.1.3.6 Post-failure strength

The post-failure strengths were mainly influenced by the formation of the fracture surfaces and the magnitude of the confining pressure because they determine the friction on the fracture surface and therefore the magnitude of the shear stresses that can be withstood.

The post-failure strengths rise with increasing confining pressure and approach those of the failure strength. The dependency of post-failure strength on the confining pressure is aptly described by a linear correlation in the test range up to 20 MPa – as shown in Figure 8.17 for the post-failure strengths of specimens from shaft 1 and shaft 2.

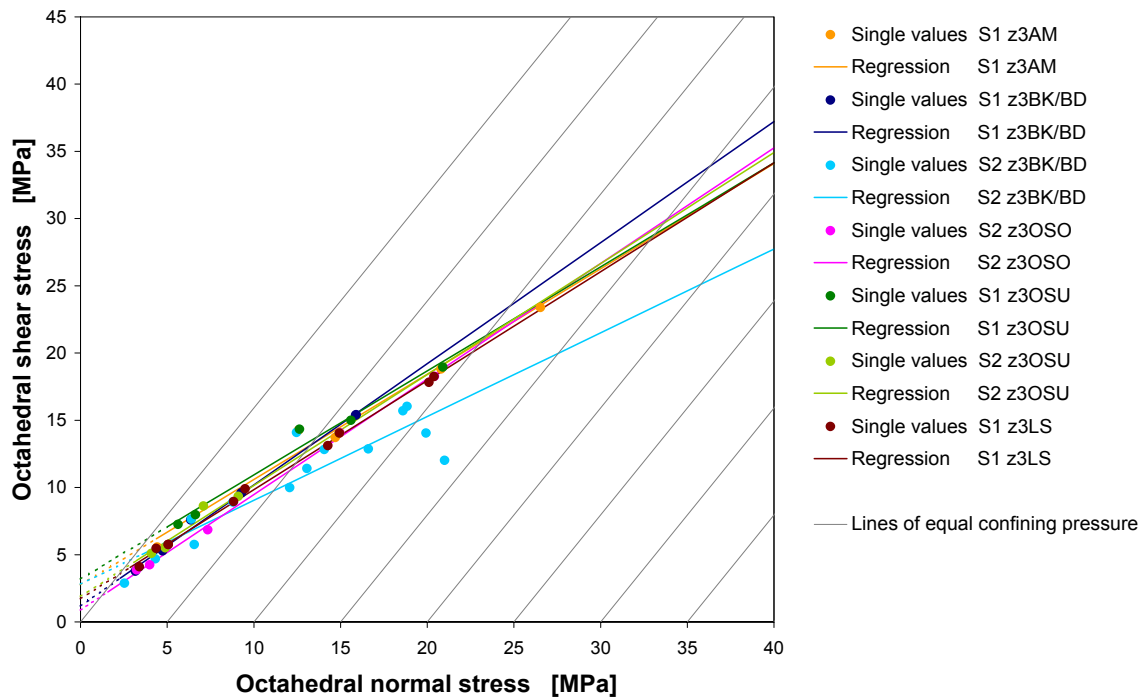


Figure 8.17: Post-failure strength of rock specimens from the shafts

The results indicate no clear ranking – even the samples from shaft 2 taken from the exposed Unteres Orangesalz (z3OSU) show good alignment with the post-failure strengths of the other locations and stratigraphic units. Only the Bank/Bändersalz (z3BK/BD) from shaft 2, containing carnallite impurities and gas inclusions, lies at the lower boundary of the scatter of all the tests.

8.1.3.7 Failure strain

The compression of the specimens until they fail in the compression tests is dependent on the confining pressure, temperature and loading rate. The failure strain increases with increasing confining pressure and increasing temperature. On the other hand, the failure strain decreases with increasing loading rate. Figure 8.18 shows the changes in failure strain dependent on temperature at an confining pressure of 1 MPa and a deformation rate of 10^{-5} s^{-1} . This example contains the tests on samples from the exploration level.

The Knäuelsalz and Streifensalz of the Staßfurt-Folge revealed a significant sensitivity between failure strain and rising temperature. This contrasts with the samples from the Anhydritmittelsalz and the Hartsalz where temperature rises had the least influence on the failure strain.

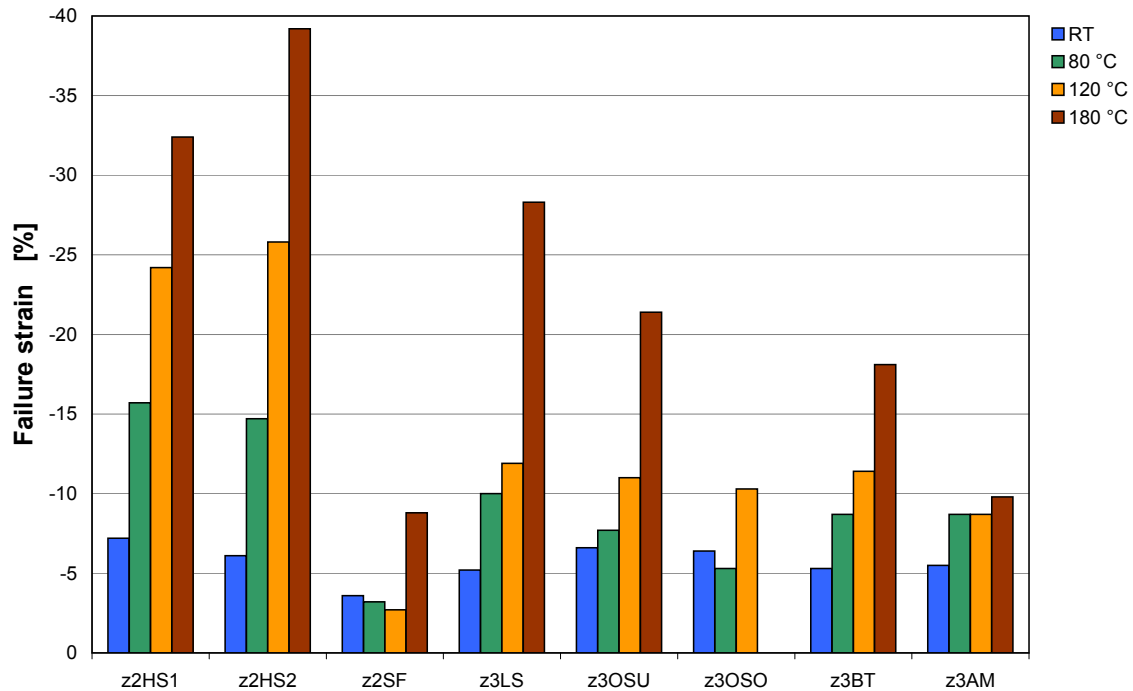


Figure 8.18: Failure strains dependent on temperature at a confining pressure of 1 MPa and a deformation rate of 10^{-5} s^{-1}

8.1.3.8 Creep behaviour

The rock samples tested to ascertain their creep behaviour were taken from a range of stratigraphic units at the exploration level and in the exploration horizons in the shafts. The creep classes (cf. Chapter 8.1.1) determined from the numerous creep tests, as well as their fluctuation ranges, are shown separately in Tables 8.2 to 8.5 for each location. No creep behaviour tests were carried out on z3OSM (Gorleben Bank).

The fluctuation range to be taken into consideration in a homogenous zone (cf. Chapter 8.3) is determined on the basis of the creep class range shown in the table (cf. Table 8.1). This means for instance that a fluctuation range from class 3 to 6 represents a range in values of the pre-factor (parameter of the creep capacity for material laws BGRa and BGRb, cf. Chapter 8.2) of $2^3/32 = 1/4$ to $2^6/32 = 2$.

Additional information in the tables includes details on the accessory constituents to help in identifying dependencies and trends. These form the basis for defining the creep classes in areas which have not yet been tested. The derived creep classes and the associated fluctuation ranges are based on geo-statistical analysis (PLISCHKE 2002).

Table 8.2: Recommended creep classes for the steady-state creep of different stratigraphic units in the evaporitic sequence of shaft 1

Stratigraphy	Accessories	Depth * [m]	Number of sub-tests.	Rec. creep class	Fluctuation range (classes)
z3LS	A3	279.7 – 312.2	18	5	5 - 7
z3OSU	A3	312.2 – 327.5	13	5	4 - 6
z3OSO	Mostly A3	327.5 – 359.1	36	3	2 - 5
z3BK/BD	Frequently A3	359.1 – 391.8	24	0	-1 - 3
z3OSO		391.8 – 433.8	0	3	□
z3OSU	None	435.2 – 456.2	2	5	□
z3LS		456.2 – 484.5	0	5	□
z3OSU	Mostly none	484.5 – 578.3	9	4	3 - 5
z3LS	A3	578.3 – 706.4	10	6	3 - 7
z3OSU	A6	706.4 – 714.9	5	3	2 - 4
z3OSO		715.8 – 732.3	0	3	□
z3BK/BD	A6, S8	732.3 – 742.9	10	2	2 - 5
z3BT		742.9 – 750.8	0	2	□
z3AM		750.8 – 804.8	0	1	□
z3BT		804.8 – 817.9	0	2	□
z3BK/BD	A6, S8	817.9 – 833.6	4	2	1 - 2
z3OSO		833.6 – 860.8	0	3	□
z3OSU	None or A3	861.2 – 888.2	16	3	1 - 5
z3OSO	A3	888.4 – 933.0	2	3	□

* Depths refer to ground level

□ No fluctuation ranges are given here because no creep tests were carried out in these zones.

Recommended creep classes are based on analogies.

Table 8.3: Recommended creep classes for the steady-state creep of the different stratigraphic units in the evaporitic sequence in shaft 2

Stratigraphy	Accessories	Depth * [m]	Number of sub-tests.	Rec. creep class	Fluctuation range (classes)
z3OSO	A1	258.2 – 303.5	0	3	□
z3OSU	None	303.9 – 335.5	2	4	□
z3OSO	A2/3	336.2 – 370.5	29	3	2 - 5
z3BK/BD	A/P Occasionally K and F	370.5 – 434.8	35	4	2 - 6
z3OSO	In parts A2	434.8 – 461.5	4	5	4 - 5
z3OSU	Mostly none	461.7 – 566.0	23	6	4 - 7
z3OSO		567.6 – 601.8	0	4	□
z3OSU	A3	602.5 – 626,8	8	5	3 - 6
z3LS		626.8 – 641.5	0	4	□
z3OSU	Occasionally P3, A3, C8	641.5 – 691.8	16	4	2 - 4
z3OSO		692.3 – 765.5	0	4	□
z3OSU	Occasionally A3, P3, C8	766.5 – 795.3	8	5	2 - 5
z3OSO	A2, C8, S8	796.0 – 834.5	6	3	2 - 4
z3BK/BD		834.5 – 843.3	0	2	□

* Depths refer to ground level

□ No fluctuation ranges are given here because no creep tests were carried out in these zones.

Recommended creep classes are based on analogies.

Table 8.4: Recommended creep classes for steady-state creep in the parts of EB1 in Gorleben investigated to date

Stratigraphy	Accessories	Borehole	Number of sub-tests.	Rec. creep class	Fluctuation range (classes)
z2HS2 + z2HS	A3	RB210	29	6	3-6
z2HS3	A3	RB210	23	2	1-4
z2HS1	A4 In parts A5	RB341/342	59	6	5-8
z2HS2	A3	RB213	23	5	4-6
z2HS2	A3/9	RB427	2	4	3-4
z2HS3	A8/9	RB427	26	5	3-6
z2HG	A5	RB427	5	4	4-6
z2HS3	A mixed	RB119	8	4	3-5
z2HS3	A3	RB120	10	5	4-6

Table 8.5: Recommended creep classes for steady-state creep in the stratigraphic units in the infrastructure area of EB1 investigated to date

Stratigraphy	Accessories	Number of sub-tests.	Rec. creep class	Fluctuation range (classes)
z3LS	A8	21	4	3 – 6
z3OSU	None and A3/6	12	3	2 – 4
z3OSO	Mostly none	10	3	1 – 5
z3BK/BD	Mostly none	23	2	0 – 3
z3BT	None and A3	15	2	0 – 4
z3AM	A1/3/6/9	27	1	0 - 3

The following dependencies on petrography, stratigraphy and tectonics were derived from the results of the numerous creep tests and the creep classes shown in Tables 8.2 to 8.5:

- The upper geological units (younger stratigraphic units) usually creep much more slowly than the lower units (older).
- Tectonically condensed zones creep faster than strongly thinned or internally strongly folded zones.
- Rocks with finely distributed impurities usually creep slower than other rocks.
- Coarse crystalline (recrystallised) salt usually creeps faster than fine crystalline salt.

The grain size cannot have any direct influence on the creep behaviour. But when coarse-crystalline rock salt is formed by recrystallisation, particle coagulation must also lead to an enlargement of the distances between the particles, the factor determining ductility. Grain sizes, therefore, are only an indirect but quite useful indicator for classifying the creep capacity.

8.2 *Material laws governing thermo-mechanical behaviour*

In connection with the use of salt deposits for final disposal of waste or caverns for storage of crude oil, gas etc., BGR has developed calculation methods over the last 30 years for stability and long-term safety analysis to enable the relevant processes to be modelled, taking into consideration the geomechanical properties of salt. This meant that it was also necessary to develop material laws which realistically describe the behaviour of rock salt as a possible host for a geologic repository, taking into consideration the effective thermo-mechanical load.

The physical basis of the material laws developed for salt is derived from those developed for crystalline materials in solid-state and metal physics. Drawing on salt mechanics, these material laws were broadened to incorporate specific processes involved in the material behaviour of rock salt. Their development and verification at BGR is based on the material properties of the so-called "Speisesalz". This specific type of rock salt was chosen as reference salt because it is very homogenous and only has a small proportion of foreign minerals. This guarantees the reproducibility of the results in test series. Adjustments were then made for the material properties of other rock salt types reflecting the different stratigraphic units, or when required, to the material properties of rock salt from a specified homogenous zone within the Gorleben salt dome.

The creep behaviour of rocks has already been described in material laws for a long time (e.g. GRIGGS 1939). In general, these feature phenomenological mathematical formulations which take into consideration the marked non-linearity of the deformation rate dependent on the stress deviator and the temperature. One of the first summaries of creep laws covering the steady-state and transient creep of rock salt was published in ALBRECHT & HUNSCHE (1980).

This formed the basis for the development and use of the BGR's different creep laws – BGRa and BGRb – to describe the temperature-dependent and stress-dependent steady-state creep behaviour of salt rocks. These material laws are well suited to predict the long-term temporal and spatial development of creep-related deformations and stresses in underground workings, and form the basis for the stability and integrity verifications carried out so far with the help of model calculations.

More complex material laws are described in detail in Hunsche & Schulze (1994). The monograph by CRISTESCU & HUNSCHE (1998) extends the law to include development of dilatancy and damage. The material laws of CRISTESCU & HUNSCHE (1998), AUBERTIN et al. (1996), and HOU & LUX (2002) are comparable in their level of development. Numerous separate reports by national working groups involved in the development of material laws are compiled in the BMBF synthesis report (HAMPEL et al. 2007). The current status of the development of material laws at BGR is characterised by the Composite Dilatancy Model (CDM) (HAMPEL & SCHULZE 2007).

Most of the material law modules describing creep incorporate an exponential term for the temperature-dependency, and a power term for dependency on the stress deviator. The CDM material law also includes all of the previously identified relevant processes affecting the thermo-mechanical behaviour of rock salt.

Creep laws to describe the steady-state creep

The BGRa and BGRb creep laws are primarily used for model calculations which take into consideration the different steady-state creep behaviour of rock salt under different temperature and pressure conditions. They also form the basis for the homogenous zone determination (Chapter 8.3).

The BGRa material law contains the pre-factor V which takes into consideration the different creep capacities of different salt types. It is determined by the creep under uniaxial load, i.e. by adjusting BGRa to the steady-state creep rates determined in experiments under relative air humidities of approx. 45 % and temperatures of up to 30 °C.

The BGRb creep law consists of two modules and takes into consideration the temperature dependency of two deformation mechanisms acting alongside each other. It is used for temperatures above 30 °C at which humidity-induced creep is no longer involved. This also applies to conditions with relatively low air humidity (< 45 %). In tests with stress applied to all sides, humidity-induced creep is basically suppressed as long as a stress state in the dilatance range is not reached. In this case, the BGRb material law forms the basis for modelling the steady-state long-term creep with a pre-factor V determined in the same way.

The equations (8.1) for BGRa and (8.2) for BGRb describe the temperature dependency and stress dependency of the steady-state creep in a form used to determine the homogenous zones.

Reference creep law BGRa for rock salt:

$$\dot{\varepsilon}_s = V \cdot A \cdot \exp\left(\frac{-Q}{R \cdot T}\right) \cdot \left(\frac{\sigma}{\sigma^*}\right)^n \quad V = \frac{2^K}{32} \quad (8.1)$$

$$A = 0.18 \text{ d}^{-1}$$

$$Q = 54 \text{ kJ/mol}$$

$$R = 8.314 \cdot 10^{-3} \text{ kJ/(mol} \cdot \text{K)}$$

$$n = 5$$

$$\sigma^* = 1 \text{ MPa (standardisation)}$$

$$T = \text{temperature in K}$$

$$K = \text{creep class of the homogenous zone}$$

Reference creep law BGRb for rock salt:

$$\dot{\varepsilon}_s = V \cdot \left[A_1 \cdot \exp\left(\frac{-Q_1}{R \cdot T}\right) + A_2 \cdot \exp\left(\frac{-Q_2}{R \cdot T}\right) \right] \cdot \left(\frac{\sigma}{\sigma^*}\right)^n \quad V = \frac{2^K}{32} \quad (8.2)$$

$$A_1 = 2.3 \cdot 10^{-4} \text{ d}^{-1}$$

$$A_2 = 2.1 \cdot 10^6 \text{ d}^{-1}$$

$$Q_1 = 42 \text{ kJ/mol}$$

$$Q_2 = 113 \text{ kJ/mol}$$

8.3 Identification of homogenous zones

Homogenous zones are identified in principle from the different material properties of the investigated rocks. The exploration work carried out to date at the Gorleben site has identified homogenous zones within the salt dome on the basis of their creep behaviour, which is derived from the creep classes determined by creep tests as described in Chapter 8.1.3.8. This takes into consideration a significant dependency of creep behaviour on petrography, stratigraphy and tectonics. The differences in creep behaviour encountered in parts of the rock salt can therefore be attributed to fabric properties which are measurable and correlate with stratigraphic units. Details of this aspect are described in Chapter 8.1.3.8 as well as in PLISCHKE (2002) and PLISCHKE & HUNSCHE (2002).

It is important to note in this context that a stratigraphic unit can consist of several different homogenous zones. Moreover, different stratigraphic units can be incorporated within one homogenous zone.

The geological model (BORNEMANN et al. 2003) summarised in Chapter 3 is an important basis for identifying homogenous zones.

A homogenous zones model was elaborated according to these principles with the help of the results of the creep behaviour tests. Figures 8.19 to 8.21 show the homogenous zone mapping of the shafts, the infrastructure area and EB1 in the Gorleben salt dome.

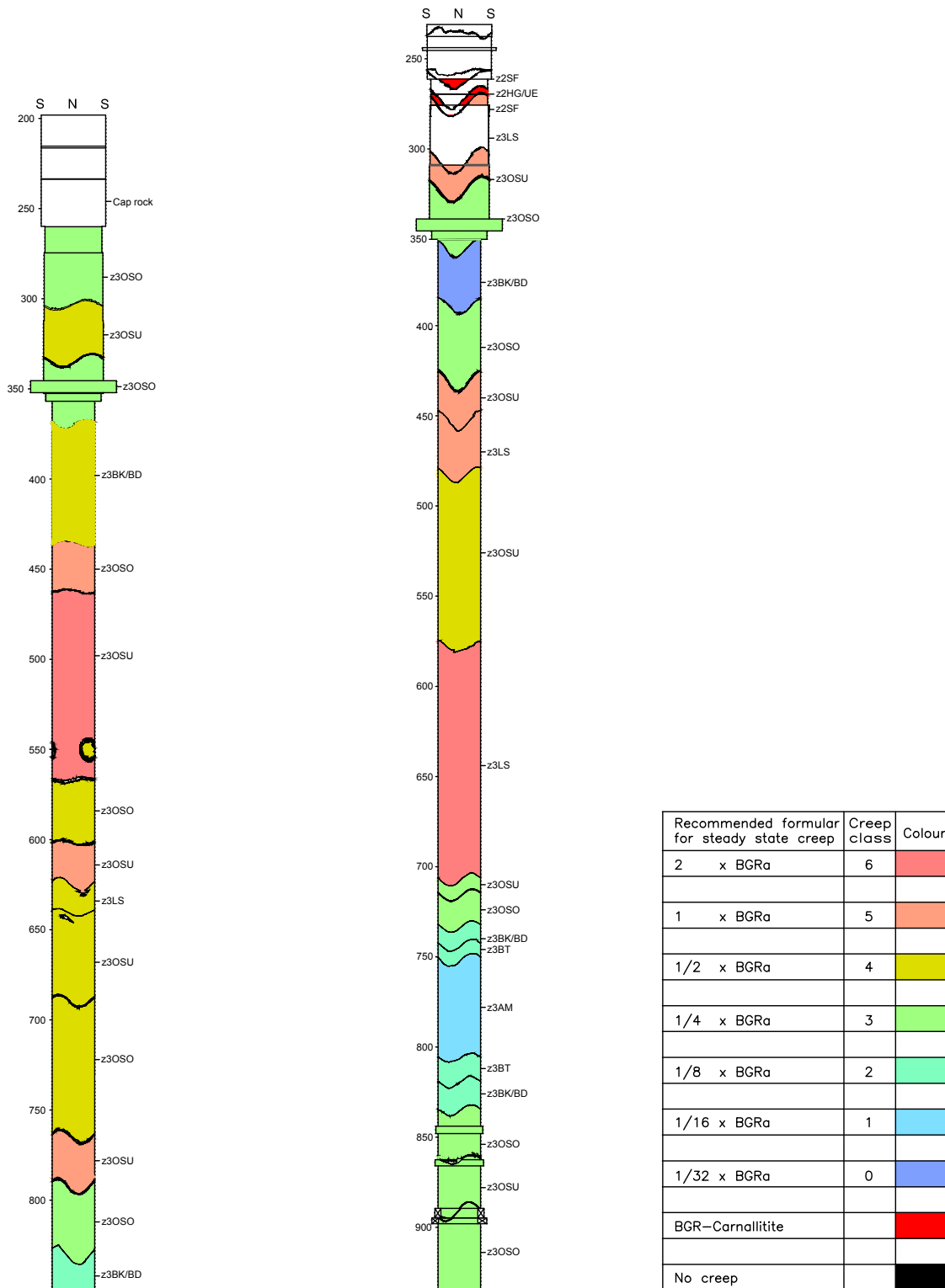


Figure 8.19: Assignment of homogenous zones in the shafts 1 and 2

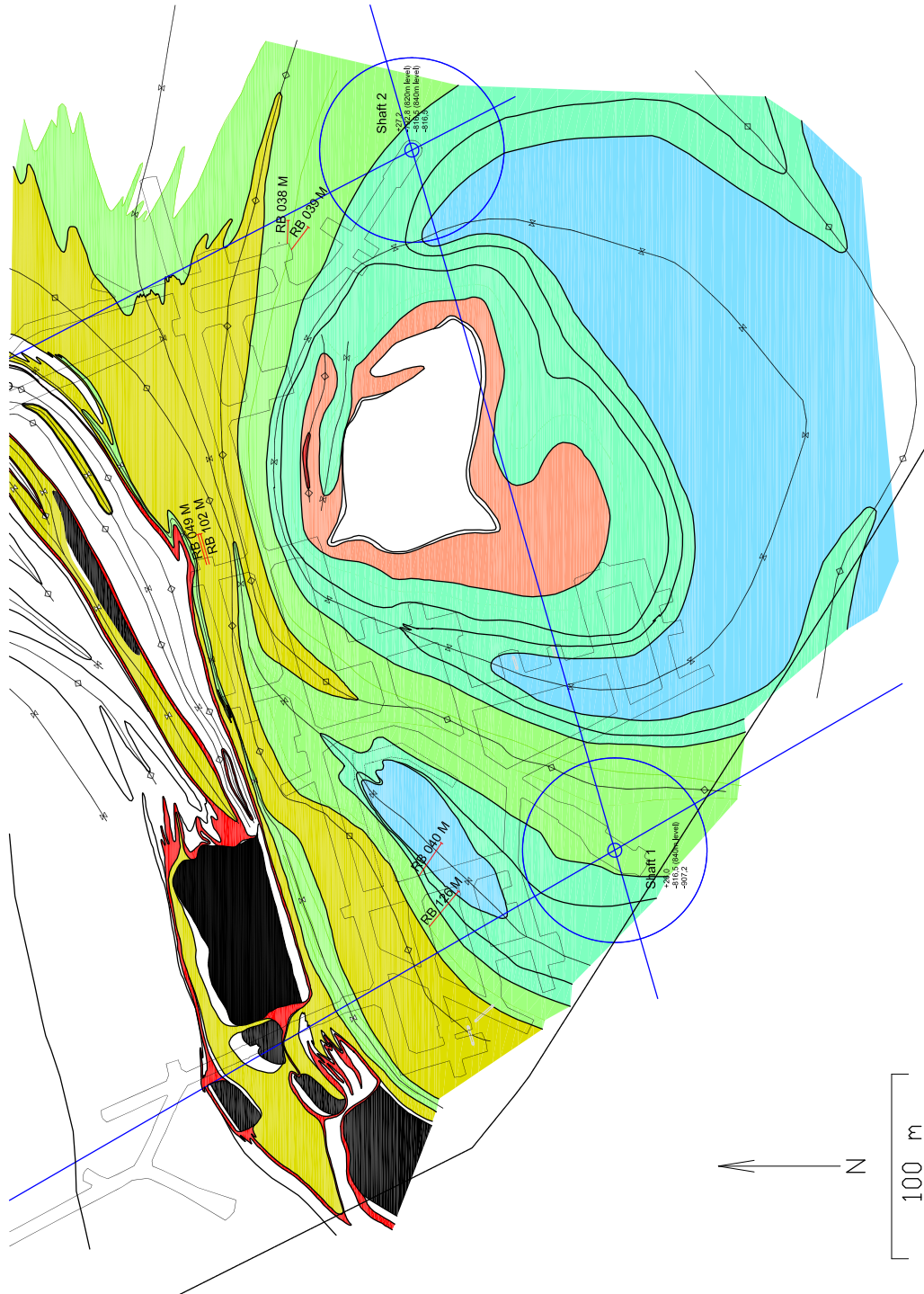


Figure 8.20: Homogeneous zones in the infrastructure area of EB1 at the 840 m level (legend see Figure 8.19)



Figure 8.21: Homogenous zones in the exploration area (EB1) at the 840 m level (legend see Figure 8.19)

9 Model calculations

Location-specific model calculations of the thermal and thermo-mechanical stresses affecting the load-bearing elements of the underground load-bearing system in specific parts of the mine (e.g. shafts, drifts) and the salt barrier were carried out as part of the exploration of the Gorleben salt dome. Modelling was also used to interpret the in-situ measurements and local observations, as well as to optimise the layout of the mine as the exploration proceeded. These calculations encompassed the following work in particular, prior to the onset of the moratorium:

- Thermo-mechanical calculations for the geologic repository in the Gorleben salt dome based on the information available from 1984 to 1986 (NIPP 1988).
- Large-scale thermo-mechanical model calculations for the technical geologic repository concept 1 (borehole emplacement BSK3) for the rock-mechanical assessment of the integrity of the salt barrier at exploration area EB1 (NIPP & HEUSERMANN 2000).
- Thermo-mechanical model calculations to analyse and interpret shaft convergence and rock mass deformation measurements in shaft 1 (NIPP et al. 2003).
- Thermo-mechanical model calculations to analyse thermally induced fractures observed in the outer surface of shaft 1 as a result of the circulatory mine ventilation and the associated cooling down in autumn 1996 and winter 1996/1997 (NIPP et al. 2003).
- Large-scale thermo-mechanical model calculations to determine the distance from the Hauptanhydrit to the northern cross-measure drift at exploration area EB1 (NIPP et al. 2003).
- Special model calculations for numeric simulation and analysis of overcoring tests in the salt dome (HEUSERMANN et al. 2003a).

Originally planned more detailed geomechanical and thermo-mechanical model calculations were not carried out due to the moratorium, and the associated suspension of work on the Gorleben site starting in 2000.

The calculations described here only deal with the issues relevant to geotechnical exploration, such as the evaluation and interpretation of geotechnical measurement results, the interpretation of local observations, and the layout of exploration drifts. Not dealt with in this report are the results of thermo-mechanical model calculations to predict the effects of the emplacement of heat-generating waste on the stability of geologic repository

components during the operational phase, and the integrity of the geological barriers in the post-operational phase.

All of the model calculations presented here were carried out according to the finite-element method using a quality-certified release version of the BGR program system ANSALT I (Analysis of Nonlinear Thermo-mechanical Response of Rock Salt) (NIPP 1991).

9.1 *Thermal and mechanical rock mass parameters*

The material properties of the stratigraphic units to be analysed in the geomechanical modelling must be modelled as realistically as possible by using suitable material models and parameters.

Thermal properties

The principles described in Chapter 5.2 were used for the thermal and thermo-mechanical calculations. The thermal rock mass properties are taken into consideration using the location-specific material parameters for specific thermal capacity and thermal conductivity of the modelled rock mass layers.

Mechanical properties

The mechanical behaviour of the rock layers present was described by material models which, in addition to the time-independent elastic shape changes, also take into consideration time-dependent deformation, and in particular the steady-state creep of the rock salt. In addition, dilatant deformations resulting from plastic flow conditions or failure conditions were also taken into consideration via a visco-plastic material model.

The effective steady-state creep rate is determined dependent on the temperature T and the effective stress σ_{eff} by material law BGRa using equation (8.1). For the different creep properties of the different stratigraphic units, the structure factor A (8.1) is replaced by the relevant pre-factor V , which is dependent on the applicable creep class.

For some issues the dilatant deformation of rock salt had to be taken into consideration. This was described by a visco-plastic material law incorporating an associated flow rule:

$$\dot{\varepsilon}_{ij}^{vp} = \frac{1}{\eta} \cdot \langle F \rangle \cdot \frac{\partial Q}{\partial \sigma_{ij}}; \quad Q = F \quad (9.1)$$

where η = viscosity in MPa·d
 Q = stress potential in MPa
 $\langle F \rangle = \begin{cases} 0, & \text{when } F < 0 \\ F, & \text{when } F \geq 0 \end{cases}$ in MPa

The flow described by equation (9.1) comes into effect above a yield limit F which is defined by a modified Drucker-Prager criterion and adapted in the model calculations to the modelled stratigraphic units with the parameters α and k :

$$F = 0 = \alpha \cdot J_1 + \sqrt{J_2^D} - k \quad (9.2)$$

where J_1 = first invariant of the stress tensor in MPa
 J_2^D = second invariant of the stress deviator in MPa²

The parameters in equation 9.2 are defined such as to produce an adequately correspondence between the yield limit used here and the dilatancy boundary after CRISTESCU & HUNSCHE (1998).

The following parameters were used:

$$\alpha = \frac{1}{2\sqrt{3}} \approx 0.2887$$

$$k = 0.0$$

The visco-plastic material model used allows the dilatant material behaviour occurring above the dilatancy boundary to be taken into consideration. The additional strain which arises here causes stress relocations and thus large deviator stresses are absorbed. After an appropriately long period of time, the stress states at all material points are essentially at or below the dilatancy boundary. The zone in which the stress conditions exceed the dilatancy boundary at one point over the course of the calculation is referred to as a deconsolidation zone or dilatant zone. The stress on the material is limited as a consequence to the zone beneath the dilatancy boundary and the maximum possible size

of a deconsolidation zone is thus determined as a conservative assessment. The viscosity in the visco-plastic model is selected to ensure that the stress states of all of the material points at the point in time being evaluated are virtually on or below the dilatancy boundary.

9.2 Interpretation of the deformation measurements

Once the establishment of circulating mine ventilation in the Gorleben exploration mine from the downcast shaft 1 to the upcast shaft 2 began in October 1996, temperatures developed at the perimeter of shaft 1 which are even today still subject to considerable seasonal fluctuations. Whilst the initial temperature differences between summer and winter were more than 20 °C, the measured temperatures in the most recent measuring period only indicate fluctuations in the range of approx. 10 °C (cf. Chapter 6.3.1.1). The seasonal temperature fluctuations also influenced, however, the convergence in the shafts, which is affected by temperature-dependent creep processes, as revealed by the deformation measurements. These showed immediate or delayed effects caused by the seasonal temperature changes. Thermo-mechanical model calculations were carried out to analyse and interpret in detail the shaft convergence measurements and the rock mass deformation measurements in shaft 1 (cf. Chapter 6.3.1.5).

Rock-mechanical modelling

Exploration horizon 4 (EH-650) was selected for the modelling of shaft 1 because, unlike in the other exploration horizons, only one stratigraphic unit – Liniensalz (z3LS) – crops out at this measurement location. The stratigraphy around exploration horizon 4, the instruments in the measurement borehole, and the geometrical dimensions are shown in Figure 6.10.

Shaft 1 has a radius of 3.75 m in the vicinity of exploration horizon 4 (depth 652.4 m). The primary stress state was assumed to be the theoretical lithostatic overburden pressure. This yields a primary stress of 14.9 MPa if a constant density of 2.2 g/cm³ is assumed. This largely matches the results of the rock stress measurements in the shafts (Chapter 6.3.1.2 and HEUSERMANN et al. 2003a).

The parameters for thermal conductivity and specific thermal capacity reported in NIPP et al. (2003) were used to calculate the instationary temperature distribution. A linear thermal expansion coefficient of 4.0×10^{-5} 1/K was selected.

The mechanical behaviour of the rock mass was modelled by material model BGRa in equation (8.1) with the material parameters for Liniensalz (z3LS), and using the material model for visco-plastic flow incorporating the modified Drucker-Page criterion as the

yield limit (equation 9.1). The reference parameters used for the creep are based on the knowledge derived from the results of the laboratory tests as described in Chapter 8.1.3.8.

An axi-symmetrical model was selected for the geometrical idealisation of exploration horizon 4 because of the circular shape of the shaft and the homogenous Liniensalz (z3LS) surrounding the investigation zone. Because there are also no effects negatively influencing the symmetry conditions in the axial direction of the shaft, the measurement location being investigated was modelled as a 1-m-thick annular disc with a plane-strain state. The internal radius is 2.75 m, the external radius 400 m. Figure 9.1 shows a section of the FE model.

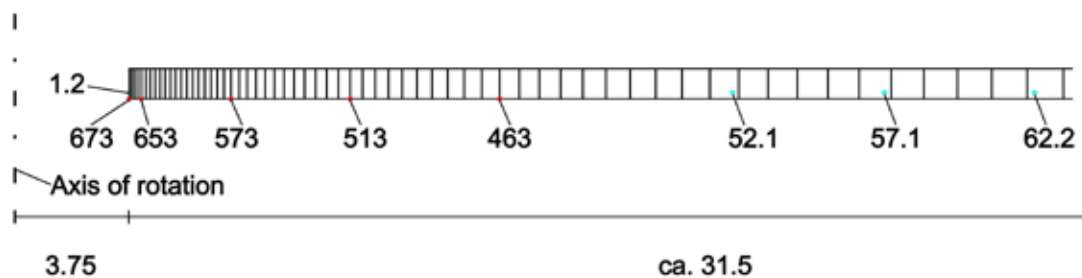


Figure 9.1: FE modelling of the shaft in the form of an axi-symmetrical annular disc (section)

The FE mesh consists of 134 isoparametric 8-node elements with 673 nodes. The upper and lower boundaries are positioned so that they cannot be distorted in the vertical direction, whilst horizontal displacements are prevented at the right hand edge of the model.

The transient temperature field over a time period of six years was modelled first, assuming an initial temperature in the rock mass of $T = 33.7 \text{ }^{\circ}\text{C}$. The temperature measured in an approx. 40 cm deep niche at the side of shaft 1 was applied as a boundary condition for the thermal analysis. The measured temperature curve was slightly smoothed for the purposes of simplification.

In the following rock-mechanical calculation, the excavation of the shaft was simulated in the first calculation step. This was followed by a six-year modelling period in which the creep of the rock salt mass was analysed taking into consideration the transient temperature distribution.

This analysis considered a reference model with best-estimate parameters and four additional model versions. The thermal boundary condition applied in the reference model was the temperature measured in situ in the vicinity of the shaft perimeter. In the alternative models, the variations included different thermal boundary conditions as well as different temperature fields and material parameters. By comparing them with the reference model, this improved the understanding of the system behaviour.

Calculation results

The results of the transient temperature calculations of the reference model are shown in Figure 9.2 for selected nodes in the FE model. The position of each of the nodes and its distance from the perimeter of the shaft can be seen in Figure 9.1.

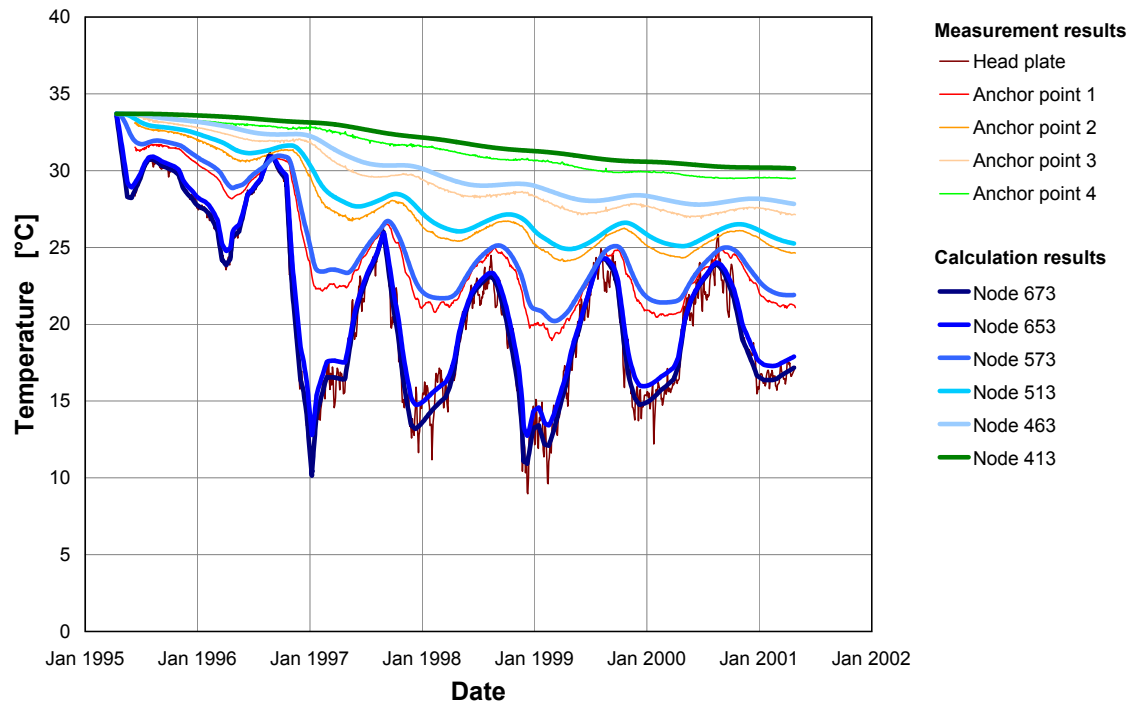


Figure 9.2: Calculated and measured temperature trends

The correlation between the calculated temperatures and the temperatures measured in the extensometer measurement boreholes is relatively good.

Figure 9.3 shows typical results of the thermo-mechanical calculations. The positions of the selected integration points and the nodes, as well as their respective distances from the perimeter of the shaft, are shown in Figure 9.1.

The upper half of the diagram in Figure 9.3 shows the change in average temperatures over time for different measuring lines (perimeter to 3 m, 3 m to 7 m, 7 m to 12 m, 12 m to 20 m). For example, the lowest temperature plot represents an average value between that of the temperature calculated for the head plate of the extensometer and the temperature determined for a point 3 m deep into the borehole. The lower half of the diagram shows the change over time of the radial stress (σ_x), the vertical stress (σ_y), and the tangential stress (σ_z).

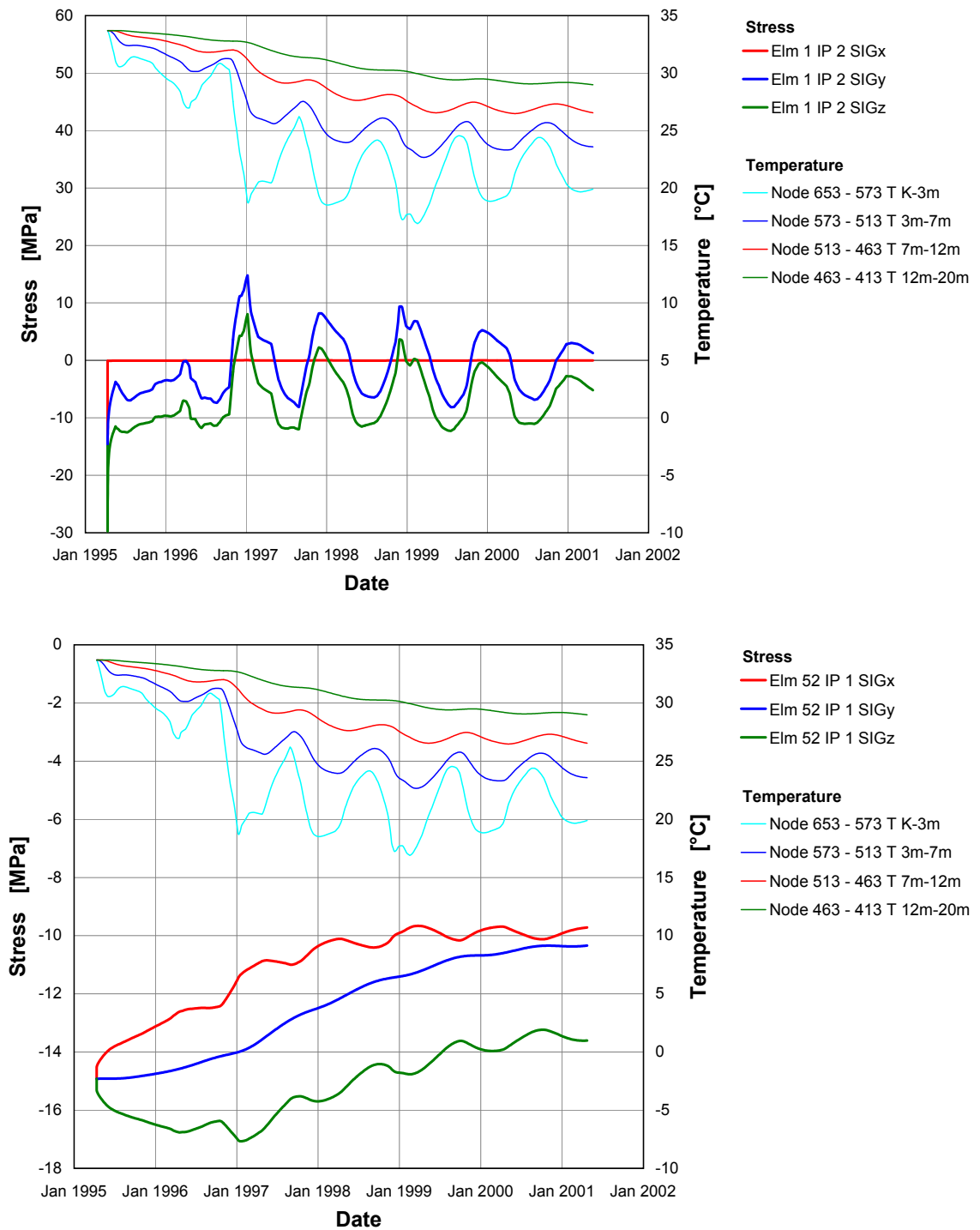


Figure 9.3: Calculated stresses for a rock mass point close to the perimeter (upper diagram) and for a rock mass point 20 m from the shaft perimeter (lower diagram).

The upper graphic in Figure 9.3 shows the stresses calculated for an element integration point located 1.7 cm from the perimeter of the shaft. This shows that the vertical and tangential stresses in particular react directly to the temperature changes in the zone proximal to the shaft. Because of the selected material parameters, strong cooling in the perimeter of the shaft produces considerable calculated tensile stresses in a vertical direction.

The lower diagram in Figure 9.3 shows the change over time in three stress components at an integration point located 20.3 m from the perimeter of the shaft. The compressive stress level drops in rock mass zones located further from the shaft because of the slow spread of the cooling of the zones proximal to the shaft. The influence of the seasonal temperature fluctuations can still be seen here in the oscillations of the stress curve.

Figure 9.4 shows a typical example of the comparison of the calculated and the measured rock mass deformations. This shows the relative displacements over time between the head plate of an extensometer and a rock mass point located 20 m from the perimeter of the shaft (lower part of the diagram). In addition, the measured and calculated changes in temperature over time are shown as average values of the temperatures determined for the two positions considered (upper half of the diagram). Calculated values have to be corrected with an offset to allow a meaningful comparison of the calculated and measured rock mass deformations. The offset ensures that the calculated deformations are zero for the time of the reference measurement.

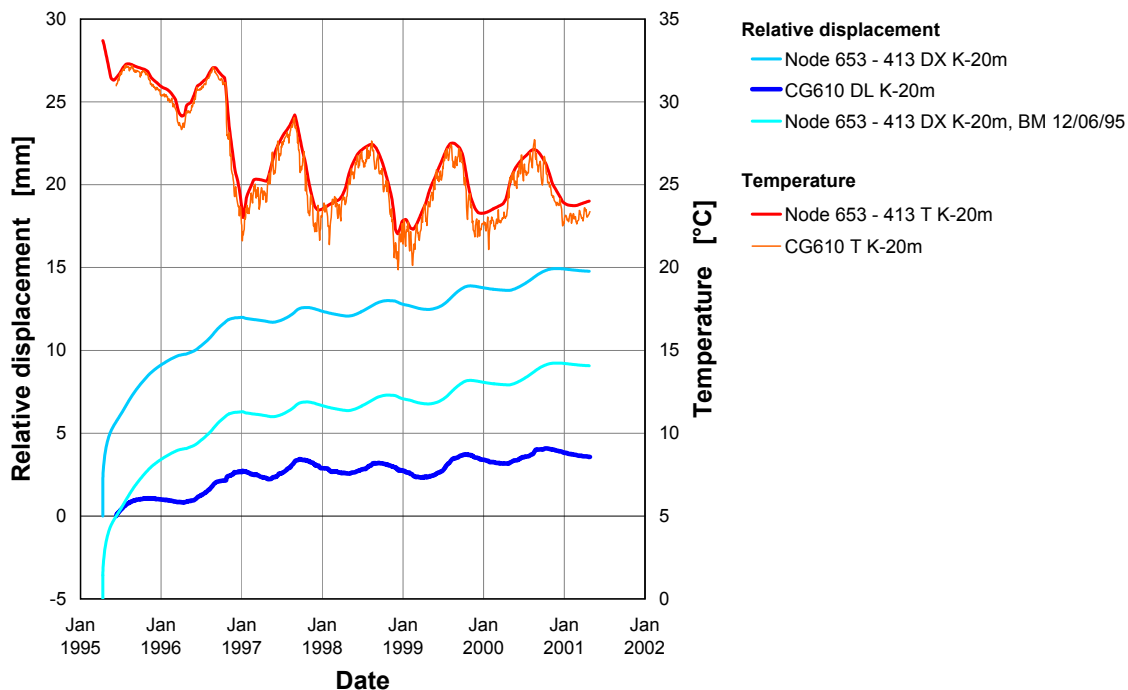


Figure 9.4: Relative displacements calculated and measured with an extensometer between the head plate and a point in the rock mass located 20 m from the perimeter of the shaft

Figure 9.4 reveals that the calculated values corrected in this way are much higher than the measured values. However, the long-term rising trend of the plot is very similar, particularly from the time when circulating ventilation began in October 1996. From this point in time, the measured and the calculated curves run almost parallel until the end of the investigation period in April 2001.

Figure 9.5 shows the calculated shaft convergence compared to the measured values. As in the procedure described above, the calculated values here are also corrected with an offset. The results produce a satisfactory correspondence between the calculated and the measured curves, with calculated values slightly higher than the measured values.

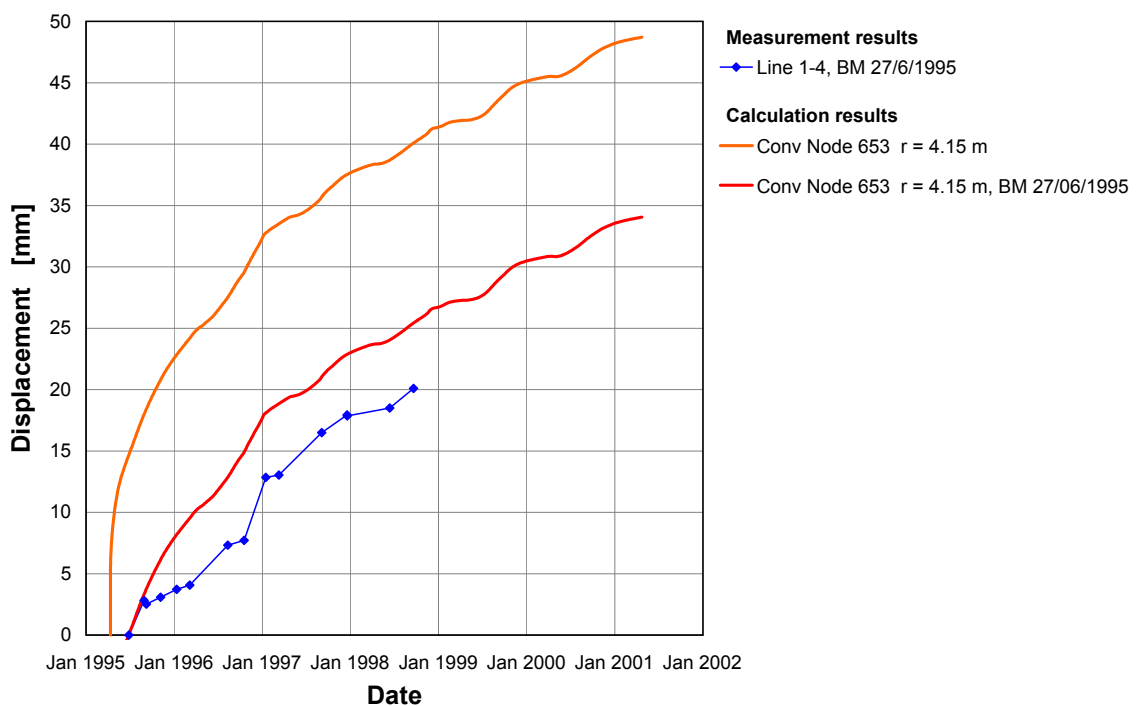


Figure 9.5: Measured and calculated shaft convergence values

Assessment

The calculation results generated by the reference model show that the calculated temperatures and displacements correlate well with the values measured in shaft 1. In terms of the stresses, if only creep is considered, high tensile stress components are calculated after a cooling phase in the perimeter zone of the shaft. These are considered to be unrealistic because they are impossible due to the low tensile strength of the rock salt. The tensile stress portion is reduced by using a visco-plastic material model for the approximate model calculation of the fractured deconsolidated zones.

In addition, the model calculations reveal that the displacement of an extensometer anchor point located around 20 m from the perimeter of the shaft accounts for approximately 40 % of the displacement of the shaft perimeter. If the anchor point is assumed to be a fixed point, it is possible that the extensometer measurements will be wrongly interpreted, particularly with respect to a comparison with the shaft convergence measurements. This confirms the findings from the in-situ measurements with reference to the extensometer measurements (cf. Chapter 6.3.1.5).

9.3 *Thermally induced fissures in shaft 1*

Once the circulation of the mine ventilation in shaft 1 and shaft 2 became established in mid-October 1996, the temperatures at the perimeter of shaft 1 dropped by more than 20 °C below the initial rock temperature because of the seasonal cold weather period. At the beginning of January 1997, approx. 40 horizontal fissures with apertures between 1 and 3 mm were observed in the perimeter of shaft 1. BGR carried out model calculations to find out the cause of these fissures. These calculations were particularly aimed at determining whether the fissures observed in situ could be simulated by seasonal weather-related cooling down.

Rock-mechanical modelling

The portion of the shaft sunk in the salt dome was simplified as a single homogenous zone so that an axisymmetrical annular disc with a plane-strain state could be used to model the shaft (Figure 9.6). The internal radius (shaft perimeter) is 3.75 m, the outer radius of the numerical model 200 m, and the height 12.5 m. From the shaft perimeter to a distance of 5 m into the rock, contact elements (gap elements) were positioned along the centre line of the finite-element model. These only allow transfer of the compressive stresses orthogonal to the contact surface and simulate a potential, horizontally-oriented fissure surface. These elements open as soon as tensile stresses develop.

The model calculations were carried out using two different material models. Firstly, the rock salt mass was described by a model with ideal elastic behaviour and steady-state creep. Secondly, the failure behaviour of the evaporite was taken into consideration in the model calculation. This made use of a Drucker-Prager criterion which limited the tensile stresses to 1 MPa. This enabled rock mass zones to be identified in the model where the failure criterion is violated and homogeneously distributed deconsolidation occurs. This allowed the estimation of the influence of this dilatancy zone on the apertures of discrete fissures in the zone proximal to the shaft, and the estimation of the stress distribution.



Figure 9.6: FE modelling of the shaft by an axi-symmetrical annular disc (above: total model; below: detail)

The temperatures measured on the perimeter of the shaft at the various exploration horizons form the basis for calculating the transient temperature field, and were input into the model calculations as traverse-type positioned temperature boundary conditions. In addition, the sinking of the shaft over time was also taken into consideration.

The model calculations were carried out using exploration horizon 3 (EH-550) and exploration horizon 5 (EH-720) as examples, to also be able to assess the depth dependency of the calculated fissures, apertures, rock mass deformations, and rock stresses. The theoretical lithostatic overburden pressure was assumed for the primary stress state. Assuming a constant density of 2.2 g/cm^3 , this gives a primary stress of approx. 12.8 MPa for EH-550 and approx. 16.4 MPa for EH-720. This largely matches the results of the rock stress measurements in the shafts (Chapter 6.3.1.2 and HEUSERMANN et al. 2003a). The time periods considered in the calculations were 837 days for exploration horizon 3 and 661 days for exploration horizon 5.

Calculation results

The change over time of the calculated and measured temperatures for several rock mass points located at different distances from the perimeter of the shaft is shown for exploration horizon 3 as an example in Figure 9.7. The traverse-type approximated theoretical temperature plot at the perimeter of the shaft clearly reproduces the marked oscillation of the measured values. There is a remarkably good correspondence between the measured and calculated temperatures at the points lying a greater distance from the perimeter of the shaft. Chapter 6.3.1.1 discusses the temperatures measured in the proximal zone to the shafts.

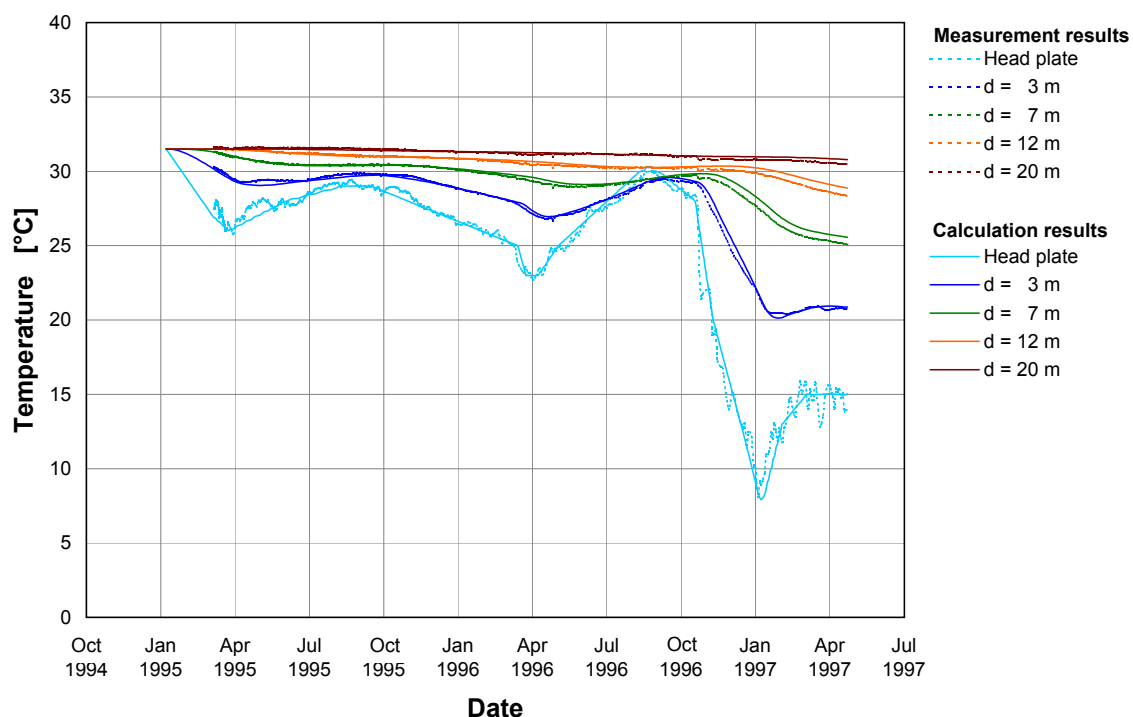


Figure 9.7: Measured and calculated temperature development in exploration horizon 3 in shaft 1

Figure 9.8 presents an example from exploration horizon 3 of the deformed FE model with the distribution of the main tensile stresses at time 734 d (without taking into consideration the failure criterion).

The largest fissure apertures determined by the model occur at this time. Cooling gives rise to tensile stresses in the zone close to the perimeter of the shaft gives rise to tensile stresses the contact elements to open. The fissure opens to a depth of approximately 4.7 m into the rock mass. Because of the constraints of the model, it is not possible for fissures to develop in the upper and lower edges of the model. This is why higher tensile stress values of up to 13 MPa are calculated in these areas – which are actually impossible because of the lower tensile strength of rock salt. An adjusted model taking

into consideration the Drucker-Prager failure criterion with a tensile strength of 1 MPa only gives lower tensile stresses. The length of the fissures is then somewhat shorter and has a slightly smaller aperture.

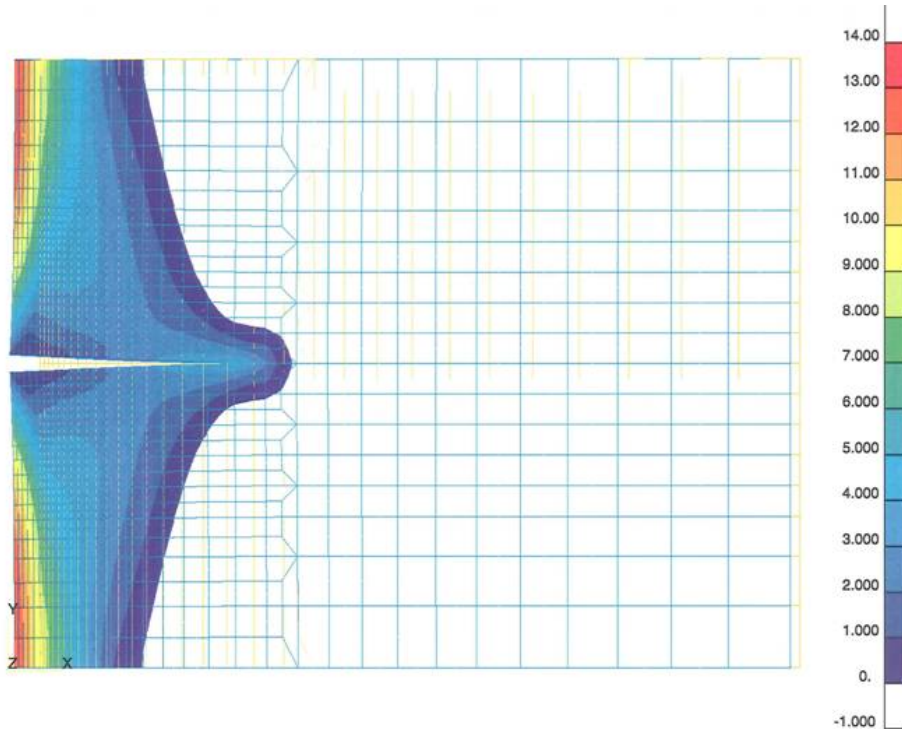


Figure 9.8: Calculated deformation and tensile stresses in the shaft perimeter at EH-550 for $t = 734$ d

The change in fissures aperture over time directly on the perimeter of the shaft is shown in Figure 9.9 using exploration horizon 3 as an example – in this case with and without taking into consideration the Drucker-Prager failure criterion. This reveals that when the failure behaviour is not taken into consideration by ignoring the dilatant distortions, the fissure apertures are considerably larger. The time at which the fissures occur is largely independent of the selected material law.

The maximum fissure apertures for exploration horizon 3 are approx. 4.4 mm (with failure criterion) or 7.2 mm (without failure criterion). The maximum fissure apertures calculated for exploration horizon 5 are around 2.1 mm (with failure criterion) or 5.2 mm (without failure criterion).

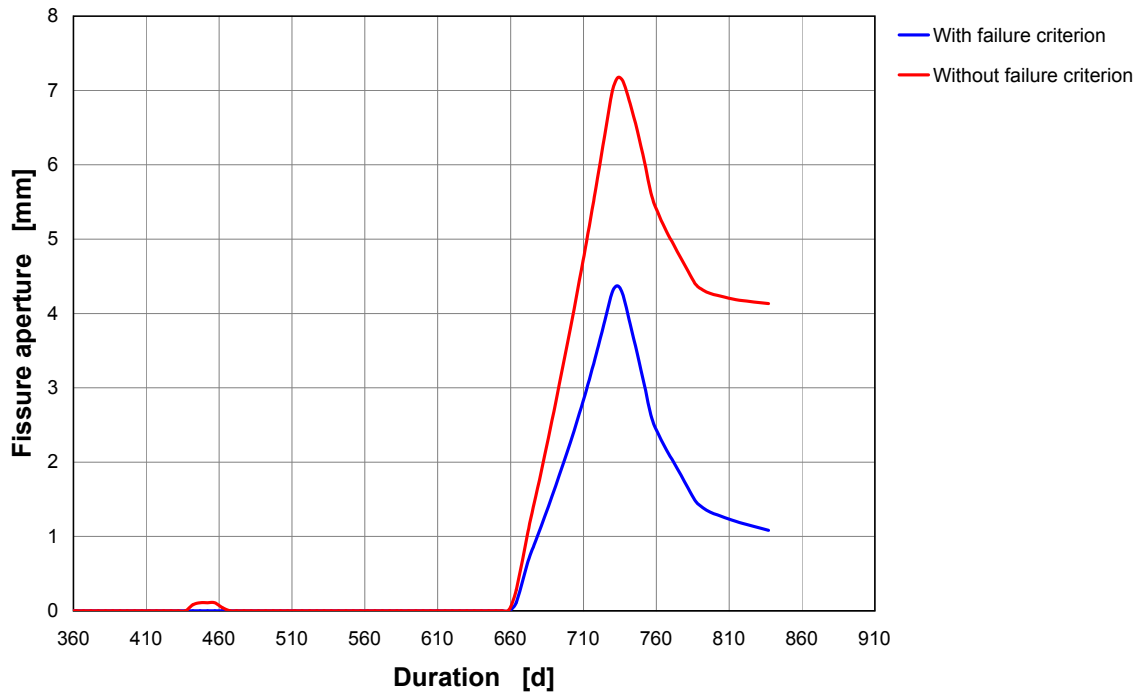


Figure 9.9: Development of fissures aperture over time for exploration horizon 3

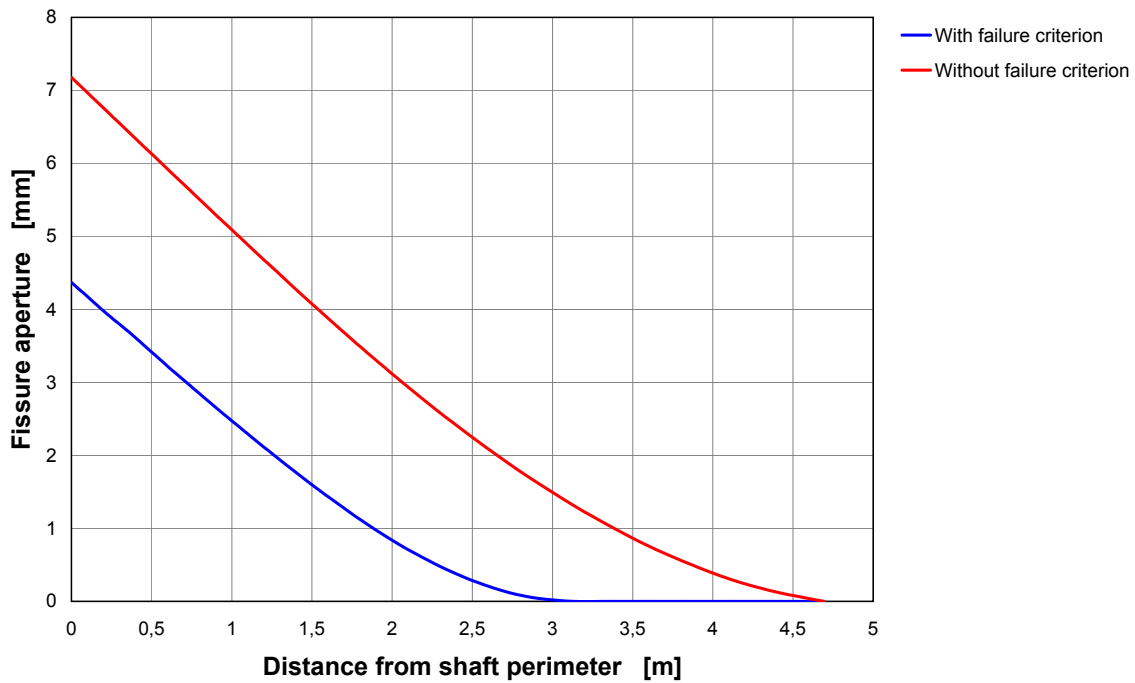


Figure 9.10: Fissure apertures in the shaft perimeter of exploration horizon 3 at time $t = 734$ d

Figure 9.10 shows the fissure apertures against distance from the perimeter of the shaft (corresponds to fissure depth) for exploration horizon 3. The point in time selected is that at which the aforementioned maximum fissure aperture occur in each model variant. Accordingly, the maximum fissure depth in exploration horizon 3 is approx. 3.2 m (with failure criterion) or approx. 4.7 m (without failure criterion). The maximum fissure depths in exploration horizon 5 are 1.9 m (with failure criterion) or 3.8 m (without failure criterion).

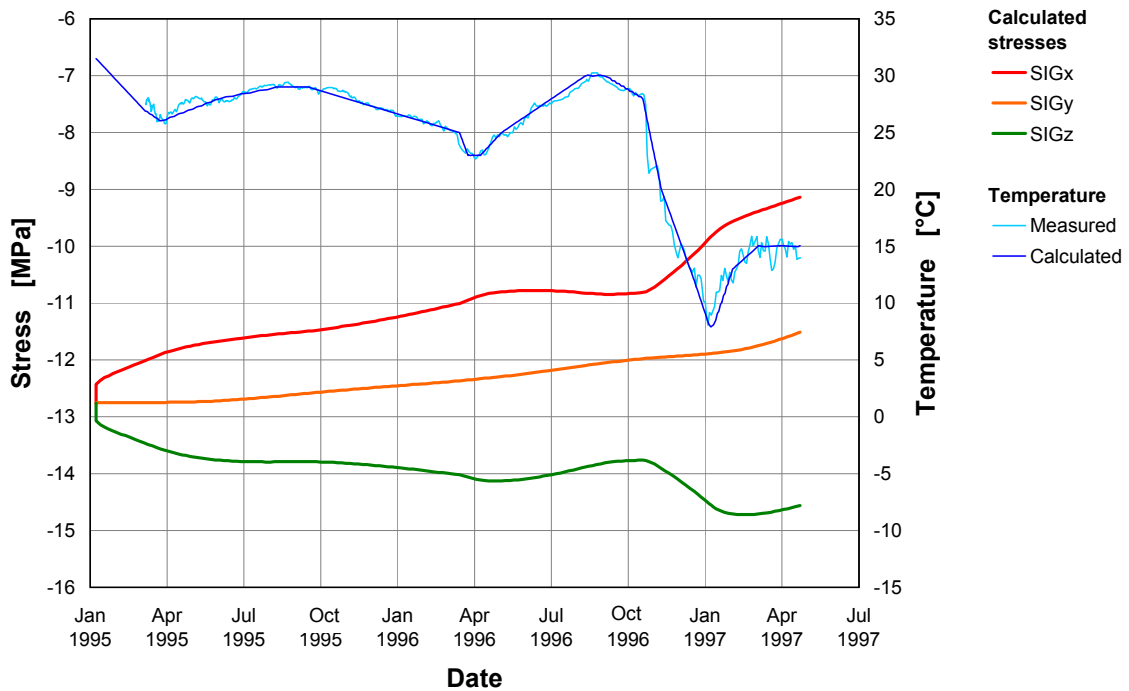


Figure 9.11: Calculated changes in principal stresses over time at a distance of 20 m from the perimeter of the shaft at exploration horizon 3

Figure 9.11 shows the calculated radial, tangential and vertical stresses against time at a rock mass point in exploration horizon 3 located 20 m from the perimeter of the shaft without incorporating the failure criterion. The figure also shows the change over time of the measured and calculated temperatures at the perimeter of the shaft. The temperature changes occurring at the perimeter of the shaft also have a significant effect on the stress developments at a distance of 20 m from the perimeter.

Evaluation

In addition to the model calculations, the overall evaluation of the fissures observed in shaft 1. As well as temperature measurements (Chapter 6.3.1.1), data particularly from the long-term stress measurements in the rock salt mass (Chapter 6.3.1.3) and the shaft convergence measurements (Chapter 6.3.1.5) were analysed.

The comparison of the calculated and measured shaft convergence rates revealed a good qualitative and quantitative correlation for exploration horizon 3. The measured data at exploration horizon 5, however, indicate much lower convergence than the model calculations. This is mainly attributed to the fact that while the calculations assumed the presence of a uniform stratigraphic unit consisting of Liniensalz (z3LS), actual in situ rock salt beds (z3BK/BD, z3AM) have much lower ductility.

The model calculations presented here are highly appropriate to theoretically clarify the causes for the thermally-induced fissures observed in shaft 1, despite the aforementioned limitations with respect to the selected rock-mechanical model. The results of the model calculations reveal that the presence of the fissures in the perimeter of the shaft can be unequivocally attributed to the seasonal weather-related cooling down of the rock mass at the perimeters of the shaft and the associated development of tensile stresses. The radial fissures determined in the model calculations do not jeopardise the stability of the shaft perimeter as long as fissure patterns with other orientations do not develop, e.g. with fissure surfaces parallel to the perimeter of the shaft because this could lead to spalling. A favourable effect for the stability of the shaft is that the fissures close again during the warming up phase following the cooling down phase.

9.4 Northern cross-measure drift in the exploration area

The drifting in EB1 during 1998 required the line of the northern cross-measure drift to be defined, particularly with respect to the distance from the northern Hauptanhydrit. BGR carried out the relevant investigations to define the safety distance required and/or to verify the selected distance, particularly with respect to the future thermal stress affecting the rock mass as a result of the emplacement of heat-generating waste. These investigations involved a range of model calculations taking into consideration the lithological and geo-technical understanding of the Gorleben salt dome available at the time.

Rock-mechanical modelling

The idealised geological model used in the rock-mechanical modelling is shown in Figure 9.12. It comprises the undifferentiated overburden with Quaternary (q) and Tertiary (t); the cap rock (cr); the undifferentiated adjoining rock mass with Cretaceous (kr), Jurassic/Keuper (j/k) and Bunter Sandstone (so-su); the basement with the Rotliegendes (r) as well as the rock salt mass with the Hauptsalz (z2HS, undifferentiated), the Hangendsalz to Übergangssalz (z2HG-UE), the Kaliflöz Staßfurt (z2SF, Trümmer-Carnallit); Liniensalz (z3LS), Unteres Orangesalz (z3OSU), Oberes Orangesalz (z3OSO), Bank/Bändersalz (z3BK/BD), Buntessalz (z3BT), Leine-Steinsalz to Aller-Steinsalz (z3-z4, undifferentiated), and the Hauptanhydrit (z3HA).

In addition to the homogenous zones, the diagram also shows the shaft axes and the three possible positions of the northern cross-measure drift with the distances of the perimeters of the drift to the Hauptsalz/Hangendsalz boundary of 10 m, 30 m and 50 m. The calculations only take into consideration the distance of 10 m because this distance is already adequate according to the integrity criteria (LANGER & HEUSERMANN 2001).

In addition, the diagram also shows the position of the emplacement level and the planned emplacement field. The northern cross-measure drift was assumed to have a height of 3.8 m, a floor with a width of 6.2 m and a maximum width (at a height of 1.8 m) of 7.0 m.

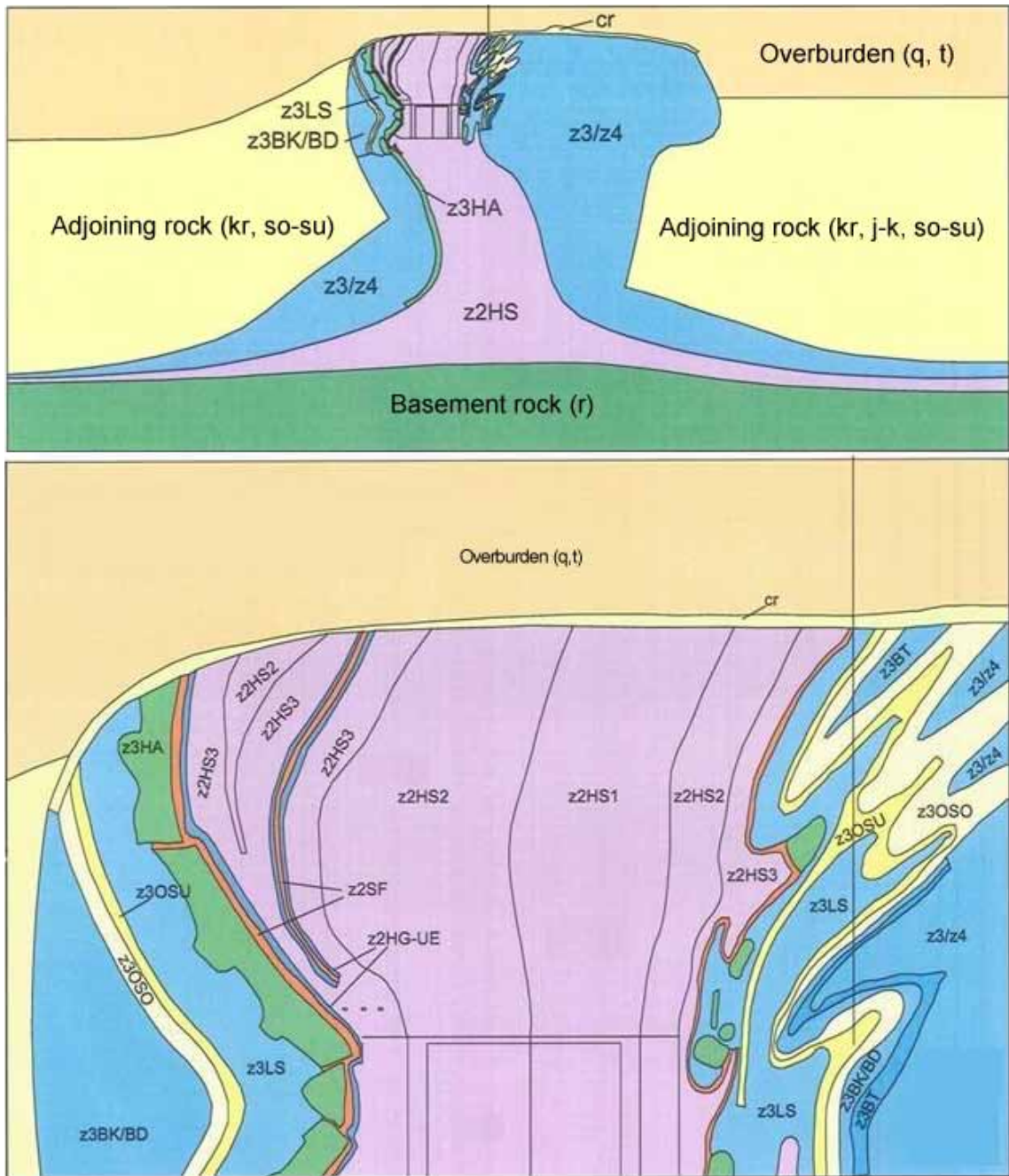


Figure 9.12: Idealised geological model

For the temperature field calculations, the thermal material parameters (thermal conductivity, specific thermal capacity) were assumed to be temperature-dependent for the rock salt layers, and partially temperature-dependent and partially temperature-independent for the other formations. Values used for the rock salt depend on the stratigraphy (NIPP et al. 2003).

The mechanical behaviour of the strata in the overburden, adjoining rock and basement, as well as the Hauptanhydrit close to the exploration area were exclusively simulated with a linear-elastic material model. The mechanical behaviour of the plastic rock salt was simulated by material models which, in addition to elastic deformation, also reflect steady-state creep in accordance with equation (8.1). Elastic parameters (modulus of elasticity, Poisson's ratio, linear thermal expansion coefficient and density), as well as the material model and its parameters for the steady-state creep of rock salt are specified in NIPP et al. (2003).

Because of the marked unidirectional strike of the geological structure, and the similarly oriented northern cross-measure drift, a two-dimensional FE model was generated for the calculations. A vertical section running centrally through the exploration area, and close to the geological section in cross-cut 1 West (BORNEMANN & BRÄUER 1999) was selected for the calculation plane. The calculation profile selected for the modelling extends 9000 m horizontally and 4000 m vertically.

The discretisation of the FE model generated 13673 isoparametric 8-node elements and 41168 nodes. The nodes at the two vertical edges of the model can shift vertically but are fixed in a horizontal direction. The nodes of the lower boundary of the model can shift horizontally but are fixed in a vertical direction.

Two model variants were looked at. Variant 1 is based on a constant temperature field over time so that the rock stress in the area of the northern cross-measure drift could be determined in an isothermal calculation without incorporating the influence of emplaced heat-generating waste. The calculation time period was 100 years. Variant 2 investigated the influence on the stress and deformation states of the spread of thermal energy generated by the emplacement of heat-producing waste. To calculate the transient temperature field, it was assumed that each final disposal canister contained 3 fuel rods (BSK3 concept with 10-year interim storage period). This gave rise to thermal outputs which were uniformly spread over the emplacement field in the numerical model. The calculation period for this variant was 1000 years assuming a 10-year "cold phase" before the start of emplacement.

Calculation results

In addition to the thermal and mechanical state values, the model calculations also determined the dilatant and hypothetical frac-risk rock mass zones. These calculation results are required to assess the mechanical integrity of the rock salt mass (LANGER & HEUSERMANN 2001, HEUSERMANN 2001).

Because the calculations in this case exclusively assumed elastic material behaviour and creep for the salt beds, the dilatant zones had to be determined in a subsequent calculation. This involved calculating the overstepping and undercutting of the dilatancy boundary after CRISTESCU & HUNSCHE (1998). The zones where the dilatancy boundary is exceeded are highlighted by colours.

The following presents the results of the model variant that takes into consideration the spread of heat after the emplacement of heat-generating waste, because there are only very minor differences compared to the reference case. The dilatant zones in the rock salt mass after 40 years are shown in Figure 9.13. The only dilatant zones which failed to satisfy the dilatancy criterion are in the contour of the drifts. The spatial extent of these zones changes only slightly over time. An approx. 10 m wide intact barrier remains in the z2HS between the northern cross-measure drift and the critical boundary between z2HS and z2HG-UE.

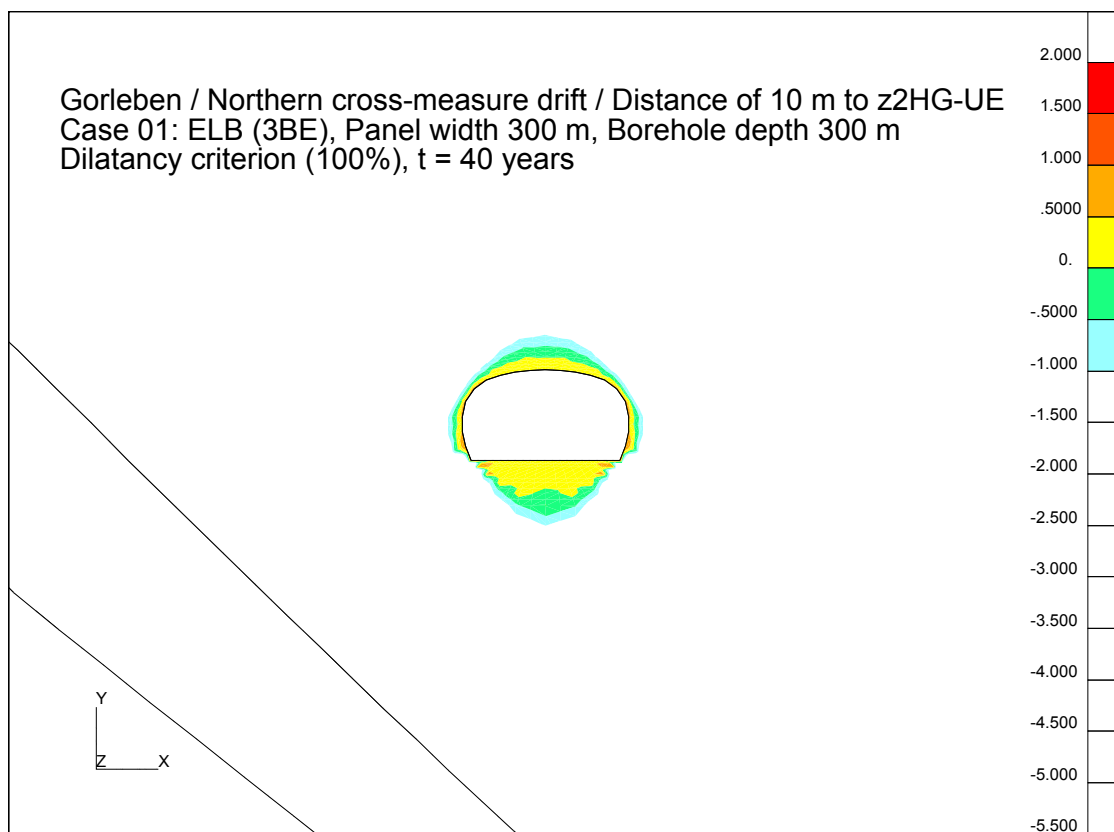


Figure 9.13: Dilatant rock mass zones after thermal input (t = 40 years)

The hypothetical frac-risk zones are shown in Figure 9.14 after 40 years. A comparison with the reference model shows that the zones marked in yellow and red are very localised at this point in time. The zones which failed to satisfy the frac criterion become even smaller over time. This is caused by the superimposition of thermally-induced compressive stresses due to heating, which have a favourable effect on the frac criterion.

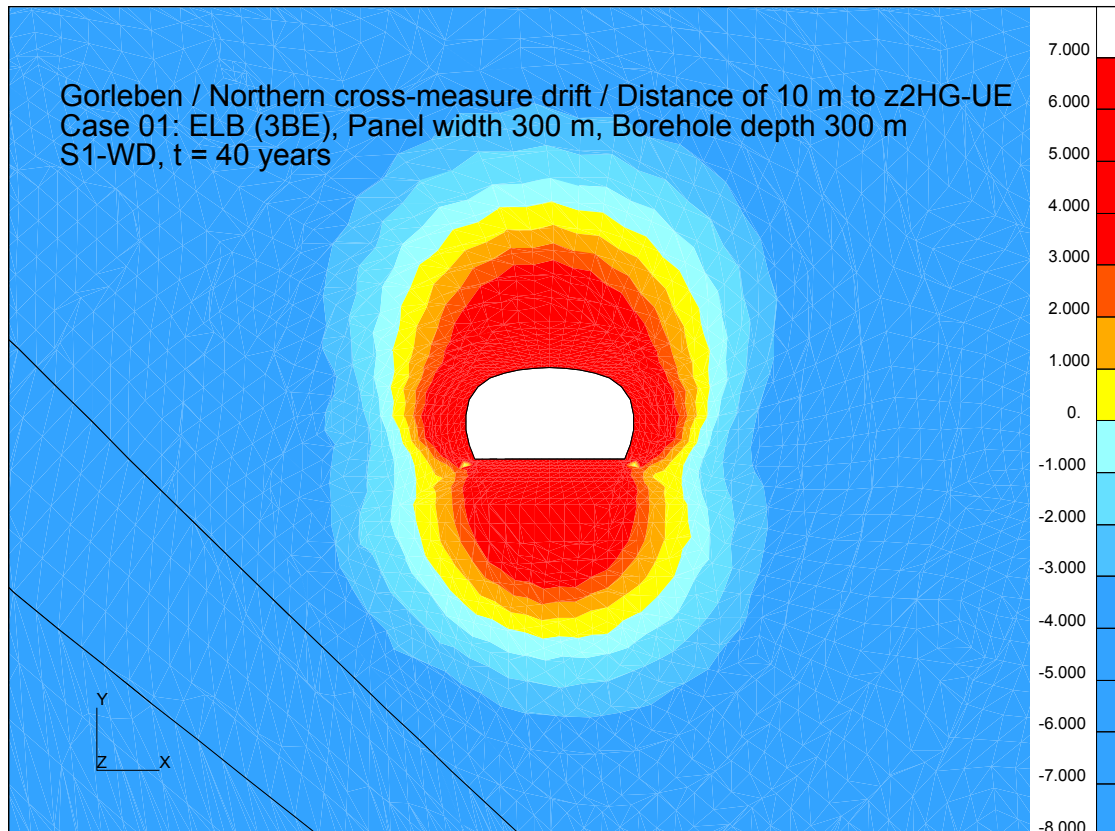


Figure 9.14: Hypothetical frac-risk zones after heating up (t = 40 years)

Evaluation

The calculation results confirm that deconsolidation caused by dilatant deformation only occurs close to the driftwall in the northern cross-measure drift. This dilatancy zone is not expected to broaden as a result of the thermal effects arising from the emplacement of heat-generating waste. In fact, the effect of the heat is to reduce the extent of the dilatant rock mass zone. Even over the longer term, an adequately large intact rock zone remains in the z2HS between the drift and the critical boundary z2HS/z2HG-UE.

The evaluation in accordance with the frac criterion reveals that the zones which fail to satisfy the frac criterion are limited to an area close to the northern cross-measure drift. Even in the long term, the critical boundary between z2HS and z2HG-UE remains in a rock mass zone which mathematically satisfies the frac criterion.

The recommendation derived from the calculation results is that a safety distance of 10 m be maintained from the z2HS/z2HG-UE boundary. This safety distance must also be observed in drift niches and drilling locations excavated from the northern cross-measure drift.

9.5 Evaluation of the overcoring tests

The evaluation of the stress measurements carried out using the overcoring method requires the numerical determination of the depth-dependent and stress-dependent evaluation factors κ because of the non-linear time-dependent deformation behaviour of rock salt (cf. Chapters 6.1.1., 6.3.1.2 and 6.3.2.2). This should give consideration to all of the boundary conditions which influence the deformations of the pilot borehole measured in the overcoring test. These include in particular after HEUSERMANN et al. (2003a):

- Elastic parameters (modulus of elasticity, Poisson's ratio)
- Creep behaviour (ductility)
- Installation depth of the overcoring displacement sensor (distance from the mouth of the pilot borehole)
- Rock stress level (the target parameter to be determined; initially only estimated as a depth-dependent value)
- Large-scale influence of large cavities (e.g. shafts) on the rock stress state

Because some of these influencing parameters cannot be determined precisely, only a range can be estimated for the evaluation factor κ , which means that the rock stresses determined from the in-situ measurement also have an associated range.

Numerical model

In addition to the elastic material behaviour (modulus of elasticity $E = 25$ GPa, Poisson's ratio $\nu = 0.27$), the model calculations are also based on the steady-state creep according to equation (8.1). The overcoring usually took around 30 minutes, and took place approximately one hour after drilling the pilot borehole. This means that a steady-state creep law is not adequate to simulate the overcoring process because the much higher creep rates occurring during the initial phase of the transient creep must be taken into consideration. In the calculations, the simulation of the transient creep used higher steady-state creep rates as a simplification by incorporating appropriate pre-factors of 500 and 1000 (cf. Table 8.1 and Chapter 8.3). These raised creep rates can be derived from the creep rates measured

in the laboratory during the transient creep phase. During the first hour after the beginning of the creep test, they are approx. 500 times to 1000 times the steady-state creep rates.

An axisymmetrical finite-element model is used for the model calculation of the overcoring test. Figure 9.15 shows an extract of this FE model and focuses on an investigation zone with a width of 10 m in the radial direction and a length of more than 15.5 m in the axial direction (borehole direction). The 500 mm long pilot borehole with a radius of 23 mm starts from the end of the vertically aligned wide borehole with a length of 5 m. The elements of the overcoring path were removed step-by-step from the FE model to simulate the overcoring process. Figure 9.15 shows the phase after the end of the overcoring activity, i.e. all of the elements along the overcoring path have been removed. The deformation of the pilot borehole occurring during the overcoring procedure was evaluated halfway down the length of the pilot borehole (red-marked position in the FE model).

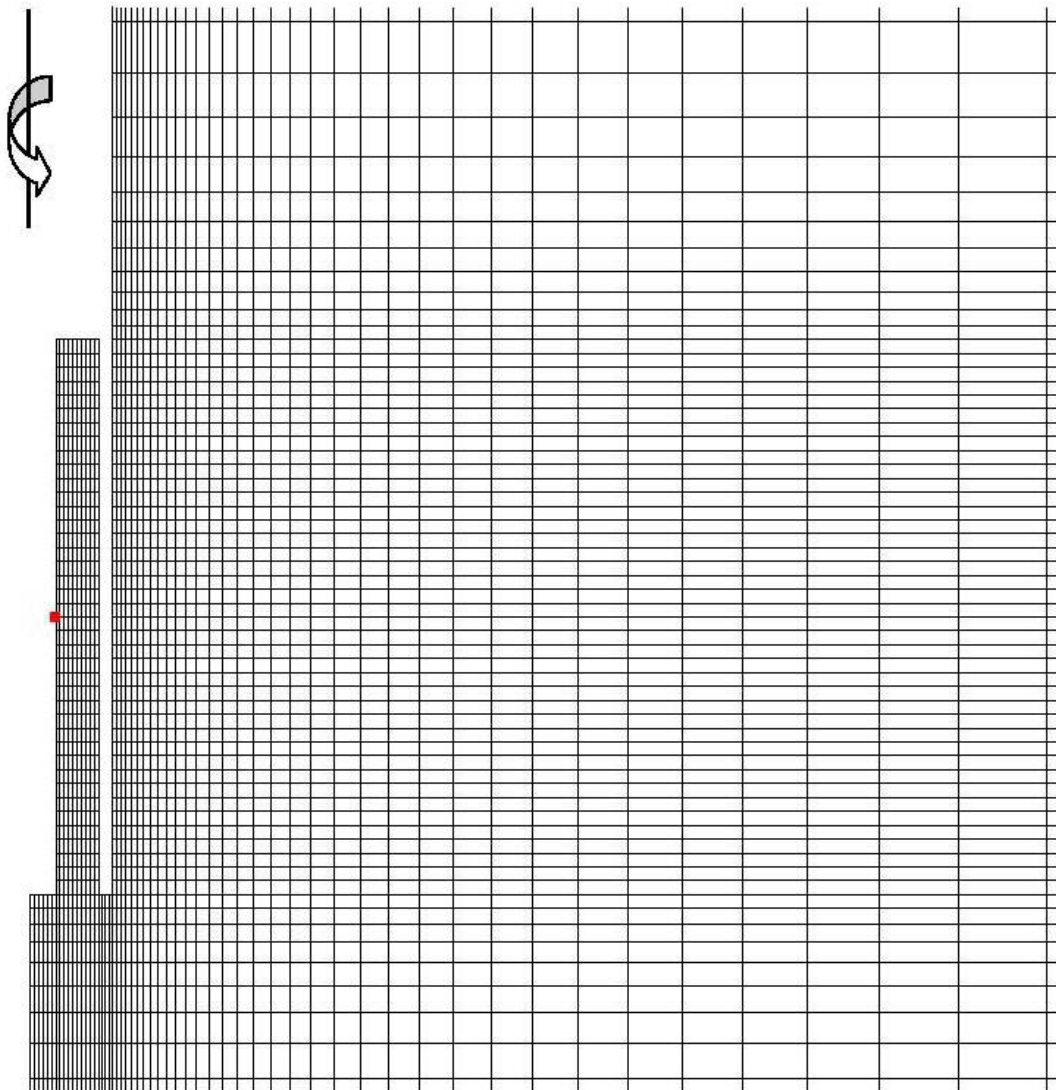


Figure 9.15: Axi-symmetrical finite-element model (extract) for the numerical calculation of an overcoring test

Calculation results

The calculated overcoring curves for a depth of 1000 m are shown in Figure 9.16 as examples of different creep behaviours in rock salt. A plot is shown for comparison derived exclusively from elastic material behaviour. If the creep is taken into consideration, larger radial deformations occur at the beginning of the overcoring process than in the case with elastic material behaviour. Roughly halfway through the overcoring process, maximum negative radial deformations occur at the evaluation point lying halfway down the pilot borehole because of the temporarily occurring stress concentrations. These are clearly visible as minimum points in the calculated overcoring plots in Figure 9.16.

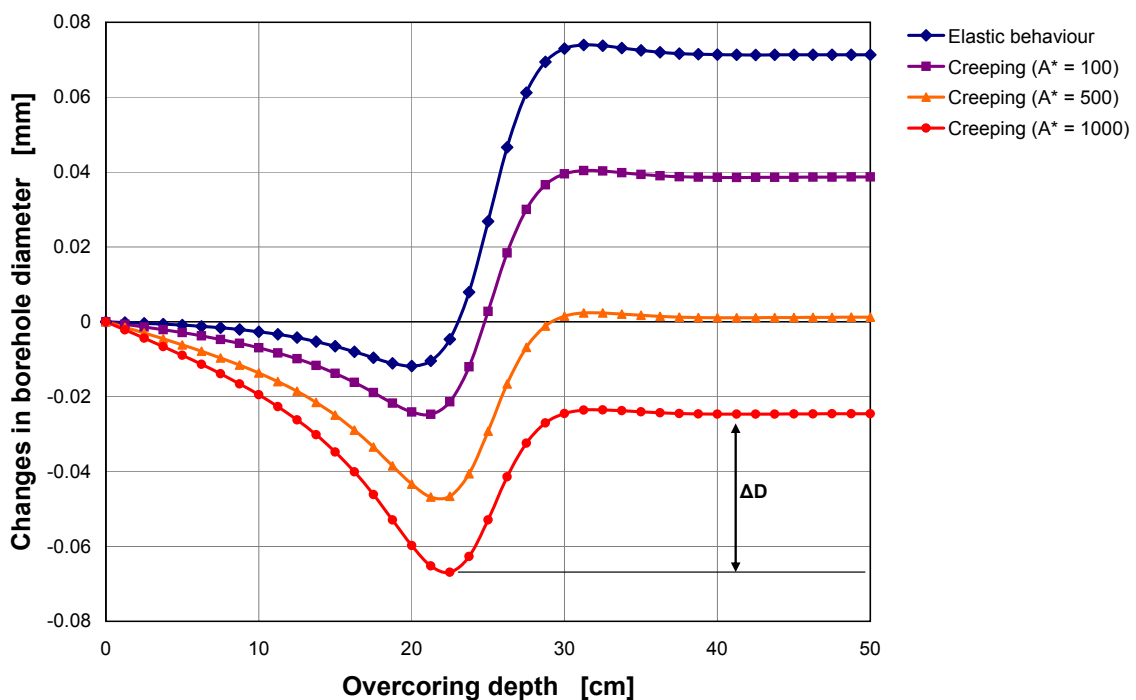


Figure 9.16: Theoretical overcoring plots at 1000 m dependent on the ductility of the rock salt

As coring continues from this point on, the load is released in the hollow cylinder created by the overcoring and reveals a major expansion of the pilot borehole. The overcoring is simulated with a constant overcoring speed of around 16.7 mm/min – this corresponds to an overcoring duration of 30 min. An elasticity-theory-based evaluation of the diameter changes of the pilot borehole calculated here, usually underestimates the rock mass stresses.

Numerical determination of correction factors

Because the rock stresses are already specified for each variant of the model calculations, an evaluation factor $\kappa = \sigma_{\text{rock mass}} / \sigma_{\text{evaluation}}$ can be determined. This factor is dependent on the primary stress state and therefore also on the depth of the investigation, as shown

in Figure 9.17. A lower value of the evaluation factors of κ_u for a pre-factor of 500, and an upper value of κ_o for a pre-factor of 1000 were determined from the FE calculations with different stress levels (11.0 MPa, 16.5 MPa, and 22.0 MPa) and the corresponding formation depths (500 m, 750 m and 1000 m). An average evaluation factor κ_m is used as the basis for evaluating the overcoring tests, and is derived by averaging for the lower and upper limits.

The evaluation factors determined from the model calculations are shown against the depth and ductility in Table 9.1 for shaft 1, in Table 9.2 for shaft 2, and in Table 9.3 for EB1. The average evaluation factors κ_m were used to evaluate the overcoring tests (cf. Chapter 6.3.1.2).

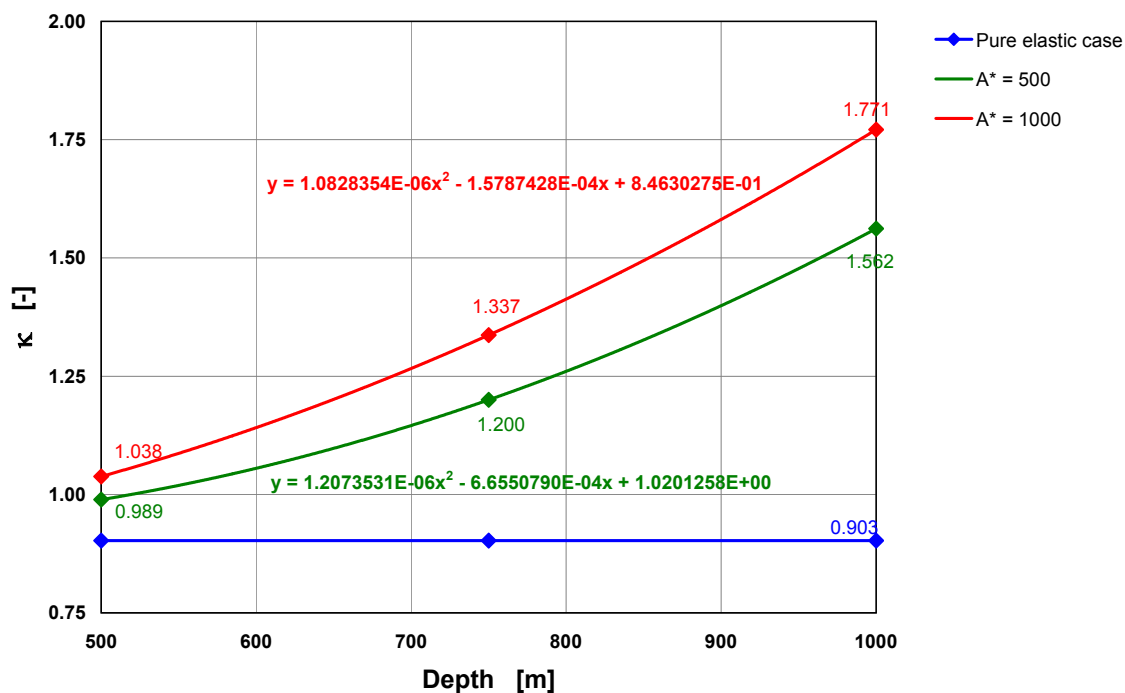


Figure 9.17: Evaluation factor κ against the investigated depth

Table 9.1: Gorleben, shaft 1, evaluation factor κ for overcoring tests

Gorleben	Shaft 1			
	Depth [m]	κ_u [-]	κ_m [-]	κ_o [-]
EH1	---	---	---	---
EH2	479.4	0.98	1.00	1.02
EH3	---	---	---	---
EH4	677.2	1.12	1.18	1.24
EH5	744.2	1.19	1.26	1.33

Table 9.2: Gorleben, shaft 2, evaluation factor κ for overcoring tests

Gorleben	Shaft 2			
	Depth [m]	κ_u [-]	κ_m [-]	κ_o [-]
EH1	---	---	---	---
EH2	478.6	0.98	1.00	1.02
EH3	601.6	1.06	1.10	1.14
EH4	---	---	---	---
EH5	791.2	1.25	1.325	1.40

 Table 9.3: Gorleben, exploration level, evaluation factor κ for overcoring tests

Gorleben	Exploration level			
	Depth [m]	κ_u [-]	κ_m [-]	κ_o [-]
EB1	840.0	1.31	1.40	1.48

10 Summary

The exploration of the Gorleben salt dome located in the Lüchow-Dannenberg rural district in Lower Saxony, began in 1979 and continued until the start of the moratorium on 1 October 2000. At the start of the moratorium, all of the investigations were suspended with the exception of the measurements to monitor underground workings. This report describes the investigation methods and the results of the underground geotechnical exploration of the Gorleben salt dome, as well as the associated laboratory tests and model calculations. Because the underground exploration had to be suspended, and the work at EB1 had therefore not been finished, this report cannot be considered complete with regard to an overall geotechnical evaluation of the salt dome.

The geotechnical exploration of the salt dome is founded on the findings from geological exploration activity with the aim of understanding the behaviour of the evaporite beds around the underground workings after they have been affected by excavation activity, as well as to record their physical properties. To achieve these aims, exploration locations and measurement profiles for the geomechanical monitoring were set up and in-situ tests were carried out. The characterisation of the rock also involved determining the lithological parameters in laboratory tests. These results are used as the basis for stability calculations and long-term safety analysis. This report documents the status of the geotechnical exploration of the Gorleben salt dome. The main findings are summarised below.

Findings from the seismological monitoring

The Gorleben site can be categorised seismologically as a quiet area from the results of the seismological monitoring of the Gorleben salt dome, which has taken place permanently since 1986, and taking into consideration historical findings. This “seismological quiescence” does not just refer to stronger earthquakes with macroseismic effects, but also microseismic events. From a seismological point of view there is no evidence of safety-relevant displacements or fracturing processes.

Findings from the geothermal investigations

For determination of the initial temperature field at EB1, laboratory tests to quantify the thermo-physical properties of the host rock and in-situ temperature measurements in boreholes were implemented, in addition to geothermal model calculations.

The laboratory tests revealed that the investigated rock salt has a very low porosity. The thermal conductivity dependent on temperature and pressure, as well as the temperature-dependent thermal capacity of the analysed halites, correspond to the standard figures reported in the literature, whilst the thermal expansion coefficients determined by the testing are slightly lower than the standard values because of the presence of natural material inhomogeneities.

Geothermal in-situ measurements were used as the basis for determining the primary three-dimensional temperature distribution in the salt dome, which corresponds to the temperature field postulated by the model calculations. The primary rock temperature at a reference point at the 840 m level is thus 37.85 °C, and the average geothermal gradient is 2.35 K/100 m depth increase. The asymmetry of the salt flanks means that the temperatures orthogonal to the axis of the main anticline decline slightly from north-west to south-east. In a horizontal direction at the depth of the exploration level, an increase in the primary rock temperature of around 1.3 K was determined from the southernmost underground workings to the intersection of the northern cross-measure drift with cross-cut 1 East in the north.

Findings from the geomechanical in-situ measurements

Together with BfS, BGR designed and implemented a comprehensive geomechanical exploration programme which incorporated short-term tests as well as long-term observations in a range of locations throughout the underground workings. The short-term tests were provisionally concluded at the beginning of the moratorium, whilst the long-term observations to monitor the underground workings and the rock mass were continued.

The measurement of the primary rock stresses around the shafts and at the exploration level revealed that it is correct to assume an isotropic primary stress state in the salt dome and a linear increase in primary rock stresses with a density of 2.1 t/m³.

The results of the long-term stress measurements are significantly influenced by temperature effects. On the one hand, there is an oscillation in the measured stress changes which clearly correlates with seasonal fluctuations in the temperature of the ventilation air in the mine. On the other hand, the cooling down and the associated contraction of the rock mass is currently causing the measured stress changes to decline. However, when a stationary temperature distribution has been established, a renewed increase in the stress is expected up to the level of the primary rock stresses.

The deformation measurements are affected by the ventilation air temperatures in a similar way, resulting in significant seasonality in the measurement results. The size of the deformations is largely determined by the density of the underground workings and the geological conditions existing at the measurement locations. Single underground cavities are usually affected by greater levels of deformation than underground workings in more intensely mined zones. In terms of the dependency of deformation on geology, observations revealed that the deformations are highest in geologically older stratigraphic units (Hauptsalz of the Staßfurt-Folge), and decrease towards the geologically younger beds (Bank/Bändersalz of the Leine-Folge). This finding is verified by the results of the laboratory investigations. The only exception is the Anhydritmittelsalz (z3AM) which laboratory tests proved to have only a low level of ductility. This contrasts with the in-situ measurements which revealed a much higher deformation capacity. The causes of these findings need to be investigated further on the basis of additional in-situ and laboratory analysis.

Much of the observed deformation is a result of rock mass deformation close to the perimeters of underground workings, probably caused by excavation-related damage to the rock. Rock mass zones at a greater distance from the underground workings, however, also contribute to the deformation of the underground workings as a result of the lithologically-dependent creep behaviour. The deepest measurement points of the installed extensometers and inclinometers can therefore not be considered as fixed points. This means that the deformation measurement data must be supplemented by determining absolute position changes (e.g. levelling measurements) to allow the unequivocal identification of uplift and subsidence, as well as compression, extension and potential changes in the inclinations of the shafts.

The instrumental monitoring of the Gorleben Bank has so far not shown any displacements indicating an opening of this fabric horizon. However, the measurement results do reveal

shear deformation at the level of the Gorleben Bank mostly aligned into the underground workings. This shear deformation was probably initiated by the excavation of the underground workings and will gradually approach a final value determined by the specific geological and geometrical conditions existing at each measurement location.

Findings of the rock-hydraulic investigations

Amongst other analysis, the existence of a containing rock zone has to be investigated in order to verify the long-term safety of a planned geologic repository. The hydraulic characterisation of the Gorleben salt dome therefore has to take into consideration the spatial distribution of tight rock salt, dilatant zones in the rock salt, jointed anhydrite, and isolated occurrences of fluids in order to identify potential transport path for radionuclides in the salt structure.

In Exploration Area 1 permeability measurements were carried out in one exploration borehole until the start of the moratorium. All of the test intervals were within the Streifensalz (z2HS2) of the Staßfurt-Folge (z2). A disposal of heat generating radioactive waste will take place in the Hauptsalz in the case that the Gorleben salt dome is found to be suitable for this purpose. The upper limits for the permeability of the rock mass calculated from the test of borehole intervals with nitrogen lay between $2 \cdot 10^{-21} \text{ m}^2$ and $5 \cdot 10^{-22} \text{ m}^2$. Because of the moratorium on further exploration work, no tests were carried out in the Kristallbrockensalz (z2HS3) or in the Knäuelsalz (z2HS1). Additional investigations are required because the data produced to date are inadequate to characterise the hydraulic properties of the stratigraphic units in EB1.

The permeability measurements carried out in the salt dome identified no significant excavation-damaged zone in the rock salt mass beyond 30 cm from the perimeters of the cavities.

All occurrences of fluids which were encountered up to the start of the moratorium were proven to be isolated without any connection to an aquifer outside of the salt dome. On the basis of the geological understanding acquired so far, the occurrences of fluids penetrated by exploration boreholes can be assigned to specific stratigraphic units within the salt dome. Brines and gases are stored, for example, in joints within the Hauptanhydrit. The calculated sizes of the occurrences of fluids are consistent with the geological model of the Gorleben salt structure. The maximum amount of brine that flowed into an exploration borehole from an occurrence of fluids was 165.7 m^3 . This occurrence of fluids was outside the potential area for waste emplacement, which is located in the Hauptsalz of the Staßfurt-Folge (z2).

Findings from the laboratory investigations

A comprehensive laboratory analysis programme was planned for the geomechanical characterisation of the evaporite beds encountered in the Gorleben exploration mine. Only part of this laboratory programme was implemented before the beginning of the moratorium.

The results of the tests carried out to date permit a reliable determination of the elastic material parameters to describe the deformation behaviour of the investigated rock salt. No significant dependency of the calculated moduli of elasticity on the stratigraphic units was found. In terms of strength behaviour, only a minor scatter in the failure strength the individual rock salt units has been determined so far. Natural differences in the failure strength and the deformation behaviour are due to the nature and extent of mineral inclusions and the fabric properties of the samples. As an overall trend, there is an increase in the strength (with a simultaneous decrease in deformability until failure) with a decrease in the age of the rock salt.

The comprehensive creep tests which were carried out reveal a significant dependency on the age of the stratigraphic units: geological hanging beds (younger stratigraphic units) usually creep much more slowly than the geological underlying beds (older stratigraphic units). In addition, the creep could be shown to increase in tectonically strongly condensed zones and internally strongly folded zones. However, creep decreases with the presence of finely distributed impurities, whilst coarse-crystalline salt usually creeps faster than fine-crystalline salt.

The test results provided the basis for identifying homogenous zones by definition of creep classes, which are input into the model calculations to verify the stability of the underground workings and the integrity of the salt barrier, as well as to forecast the long-term thermo-mechanical behaviour of the underground workings and the host rock.

Because of the moratorium, it has so far not been possible to adequately investigate the beds of Kristallbrockensalz, Bank/Bändersalz and part of the Bunter Salz. There has also been no sampling at all of the beds of Hauptanhydrit and the carnallitic Kaliflöz Staßfurt. To address specific issues, it may be necessary to include the beds of Grauer Salzton and thin beds such as the transition layers from the Hauptsalz to the Grauer Salzton or the Gorleben Bank in a subsequent investigation programme. As the in-situ measurements showed, more detailed investigations are also required on the mechanical behaviour of the Anhydritmittelsalz (z3AM). It is not yet possible to assess whether the thinner or peripheral rock types with respect to the underground workings also need to be investigated in detail to provide an adequately complete geomechanical model.

Findings from the model calculations

The exploration of the Gorleben salt dome included implementation of location-specific model calculations to evaluate and interpret the geotechnical in-situ measurements and local observations, as well as to define the positions of exploration drifts. The calculations were carried out using the finite-element method, incorporating suitable material models and location-specific material parameters for the thermo-mechanical rock mass behaviour.

A numerical model was developed to interpret the deformation measurements which was used to analyse how the sinking of the shafts and the instationary temperature spread arising from the mine ventilation influence the deformation behaviour of the rock salt mass. The calculation results revealed a good correlation between the temperatures calculated for different distances from the shaft and the temperatures measured at relevant extensometer anchor points. There was also a satisfactory correspondence between the calculation results and the measurement data with respect to the relative displacement of extensometer anchor points and convergence measurement data. In addition, the calculations also confirmed the finding of the in-situ measurements that the deepest measurement points of the extensometers and inclinometers cannot be taken as fixed points.

Other model calculations have the objective of analysing the causes of the radial fissures observed in shaft 1 after establishment of a circulatory mine ventilation system. The calculations clearly showed that the fissures were caused by the cooling down of the perimeter of the shaft and the associated tensile stresses developing in the proximal perimeter zone. However, the model calculations also indicated that the radial fissures do not have any negative impact on the stability. This mathematical finding concerning the stability is supported by the observation that the subsequent warming up of the perimeter of the shaft after the cooling down caused the fissures to close again.

BGR carried out model calculations to provide planning data for investigation and definition of the safety distance required between the northern cross-measure drift and the northern Hauptanhydrit bed with regard to future thermal stress arising from the emplacement of heat-generating waste. These model calculations confirmed that an excavation-damaged zone is limited to the narrow halo around the perimeter of the northern cross-measure drift. Instead of becoming wider as a result of additional thermal stress, this excavation-damaged zone actually shrinks as a consequence. The findings thus confirmed that the planned safety distance between the northern cross-measure drift and the Hauptanhydrit is adequate.

Despite the fact that the exploration of the Gorleben salt dome has not yet been concluded, the results of the investigations of the salt dome so far show no findings which diminish the potential suitability of the Gorleben salt dome from a geotechnical point of view.

References

- ALBRECHT, H., BOEHME, J., BORNEMANN, O., DELISLE, G., EISENBURGER, D., FABER, E., FIELITZ, K., FISCHBECK, R., FRITSCH, J., GERLING, P., GIESEL, W., HOLLMANN (BfS), A., HUNSCH, U., JARITZ, W., KOPIETZ, J., LEYDECKER, G., LUDWIG, R., NICKEL, H., NIPP, H.-K., PLISCHKE, I., SCHELKES, K., SCHMIDT, G., SCHULZE, O., STREBEL, O., TITTEL (BfS), G. & ZIRNGAST, M. (1991): Übertägige geowissenschaftliche Erkundung des Standortes Gorleben.-- BGR, unpublished report, archive no. 108 880: 369 pp., 118 figures, 62 tables, 39 appendices; Hannover.
- ALBRECHT, H. & HUNSCH, U. (1980): Gebirgsmechanische Aspekte bei der Endlagerung radioaktiver Abfälle in Salzdiapiren unter besonderer Berücksichtigung des Fließverhaltens von Steinsalz. (Geomechanical aspects of radioactive waste disposal in salt domes with emphasis on the flow of rock salt).-- Fortschr. Miner., Vol. 58(2): pp. 212 - 247; Stuttgart.
- AUBERTIN, M., GILL, D.E. & SERVANT, S. (1996): Preliminary determination of constants for an updated version of the SUVIC Model. – (In: GHOREYCHI, M., BEREST, P., HARDY JR., H.R. & LANGER, M. [Eds.]: The mechanical behavior of salt.)-- Proceedings of the Conference on Mechanical Behavior of Salt 3 (MECASALT III), 1993, Palaiseau, Frankreich: pp. 19 - 30; Clausthal (Trans Tech Publ.) - ISBN 0-87849-100-7.
- BALDSCHUHN, R., FRISCH, U. & KOCKEL, F. (1996): Die Strukturen im Untergrund NW-Deutschlands 1 : 500 000.-- BGR; Hannover.
- BÄUERLE, G., MENGEL, K. & BORNEMANN, O. (2000): Lösungs- und Gasführung Gorleben-Bank.-- BGR, unpublished report, archive no. 0120601: 255 pp., 34 figures, 24 tables, 27 appendices; Hannover.
- BORNEMANN, O., BEHLAU, J. & MINGERZAHN, G. (2002): Endlagerprojekt Gorleben – Geologische Bearbeitung der Erkundungssohle. 2. Geologischer Fachbericht (Geologische Schnitte zur untertägigen Erkundung).-- BGR, unpublished report, archive no. 0122249: 19 pp., 32 appendices; Hannover.
- BORNEMANN, O., BEHLAU, J., FISCHBECK, R., HAMMER, J., JARITZ, W., KELLER, S., MINGERZAHN, G. & SCHRAMM, M. (2008): Standortbeschreibung Gorleben, Teil 3: Ergebnisse der über- und untertägigen Erkundung des Salinars.-- Geol. Jb., C 73: 211 pp., 49 figures, 7 tables, 5 appendices; Hannover.

- BORNEMANN, O., BEHLAU, J., FISCHBECK, R., HAMMER, J., JARITZ, W., KELLER, S., MINGERZAHN, G. & SCHRAMM, M. (2008): Description of the Gorleben Site Part 3. Results of the geological surface and underground exploration of the salt formation.-- BGR: 223 pp., 50 figures, 7 tables, 5 appendices; Hannover - ISBN 978-3-9813373-6-5.
- BORNEMANN, O., BEHLAU, J., KELLER, S., MINGERZAHN, G. & SCHRAMM, M. (2003): Projekt Gorleben – Standortbeschreibung Gorleben – Teil III, Ergebnisse der Erkundung des Salinars.-- BGR, unpublished report, archive no. 0124403: 222 pp., 6 tables, 30 figures, 4 appendices, 1 inclosure; Hannover.
- BORNEMANN, O. & BRÄUER, V. (1999): Results of Geological Investigations at the Gorleben Salt Dome, the Potential Repository Site for Radioactive Waste in Germany.-- In: The 7th Intern. Conf. Proc. on Rad. Waste Management and Environmental Remediation (ICEM '99), Nagoya, Sept. 26 - 30., ICEM '99, CD-ROM: 4 figures, 1 table; Nagoya, Japan - ISBN 0-7918-1966-3.
- BRÄUNER, G. (1991): Gebirgsdruck und Gebirgsschläge, Fragen der Standsicherheit von Grubenbauen.-- 137 pp., 103 figures, 7 tables; Essen (Glückauf).
- CRISTESCU, N. & HUNSCH, U. (1998): Time Effects in Rock Mechanics.-- John Wiley & Sons: 343 pp.; Chichester.
- DELISLE, G. (1980): Berechnungen zur raumzeitlichen Entwicklung des Temperaturfeldes um ein Endlager für mittel- und hochradioaktive Abfälle in einer Salzformation.-- Z. dt. geol. Ges., 131: pp. 461-482, 12 figures, 1 table; Hannover.
- DGGT (2008): Indirekter Zugversuch an Gesteinsproben – Spaltzugversuch. Empfehlung Nr. 10 des Arbeitskreises 3.3 „Versuchstechnik Fels“ der Deutschen Gesellschaft für Geotechnik.-- Bautechnik 85, issue 9: pp. 623 – 627.
- DUNNICLIFF, J. (1993): Geotechnical Instrumentation for monitoring field performance.-- John Wiley & Sons: 577 pp.; New York - ISBN 0-471-00546-0.
- EILERS, G. & PREUSS, J. (1997): Geotechnische Untersuchungen bei der untertägigen Erkundung des Salzstockes Gorleben.-- Internal report, BfS ET-IB-93: 29 pp.; Salzgitter.
- EISENBURGER, D. & GRISSEMANN, C. (2003): Projekt Gorleben – Laboruntersuchungen zur Bestimmung der thermophysikalischen und elektrischen Gesteinsparameter.-- BGR, unpublished report, archive no. 0124313: 373 pp., 219 appendices; Hannover.

- FRANZ, G. (1958): Unmittelbare Spannungsmessung in Beton und Baugrund.-- Bauingenieur 5/1958.
- GARTUNG, E. (1985): Empfehlung Nr. 10 des Arbeitskreises 19 – Versuchstechnik Fels – der Deutschen Gesellschaft für Erd- und Grundbau e. V.: Indirekter Zugversuch an Gesteinsproben - Spaltzugversuch.-- Bautechnik 6: pp. 197 – 199, 3 figures, 2 tables; Berlin.
- GLÄSS, F. & SCHNIER, H. (1996): Bewertung der Verformungsmessungen in den Schächten Gorleben 1 und 2 (Salinar).-- BGR, unpublished report 1994/95, daybook no. 10657/96; Hannover.
- GRIGGS, D. T. (1939): Creep of Rocks.-- Jour. Geology, 47: pp. 225 - 251; Chicago.
- GRISSEMANN, C. & CZORA, C. (2003): Projekt Gorleben – Temperaturmessungen von der Erkundungssohle – Das natürliche Temperaturfeld im Erkundungsbereich.-- BGR, unpublished report, archive no. 0123780: 49 pp., 10 figures, 4 tables, 15 appendices, 1 appendix; Hannover.
- GRISSEMANN, C., CZORA, C. & KOSS, G. (2000): Untertägige Temperaturmessungen im Rahmen der geowissenschaftlichen Standorterkundung des Endlagers für radioaktive Abfälle in Morsleben.-- BGR, unpublished report, archive no. 116704 : 63 pp., 23 figures, 7 tables, 53 appendices; Hannover.
- GRÜNTAL, G., STROMEYER, D., WYLEGALLA, K., KIND, R., WAHLSTRÖM, R., YUAN, X. & BOCK, G. (2007): Die Erdbeben mit Momentmagnituden von 3,1 - 4,7 in Mecklenburg-Vorpommern und im Kaliningrader Gebiet in den Jahren 2000, 2001 und 2004.-- Z. geol. Wiss., 35: 1-2, pp. 63-86.
- HAMPEL, A. & SCHULZE O. (2007): The Composite Dilatancy Model: A constitutive model for the mechanical behaviour of rock salt. (In: M. WALLNER, K-H. LUX, W. MINKLEY & H.R. HARDY Jr. [Eds.]: The Mechanical Behaviour of Salt. Understanding of THMC Processes in Salt.)-- Proceedings of the 6th conference of the Mechanical Behavior of Salt (Saltmech 6), Germany, 22 - 24 May 2007, Balkema; Hannover 2007.-- Taylor & Francis: pp. 99-107; London - ISBN 978-0-415-44398-2.
- HAMPEL, A., SCHULZE, O., HEEMANN, U., ZETSCHKE, F., GÜNTER, R.-M., SALZER, K., MINKLEY, W., HOU, Z., WOLTERS, R., DÜSTERLOH, U., ZAPF, D., ROKAHR, R. & PUDEWILLS, A. (2007): BMBF-Verbundprojekt: Die Modellierung des mechanischen Verhaltens von Steinsalz: Vergleich aktueller Stoffgesetze und Vorgehensweisen – synthesis report.-- Forschungszentrum Karlsruhe: 167 pp., 100 figures, 6 tables; Karlsruhe.

- HÄNEL, R. (1998): Atlas of Subsurface Temperatures in the European Communities.-- Commission of the European Communities, Directorate for Research, Sciences and Education: 36 pp., 43 plates; Hannover.
- HÄNSEL, W. & PREUSS, J. (1991): Geotechnische Untersuchungen bei der untertägigen Erkundung des Salzstockes Gorleben.-- Internal report BfS ET-IB-39: 30 pp., 3 tables; Salzgitter.
- HENGER, M., LEYDECKER, G., SCHLOTE-MEISSNER, H. & STORCK, B. (1988): Überwachung der Seismizität im Bereich des Salzstockes Gorleben zur Bewertung des Gefährdungspotentials eines zukünftigen Endlagers durch tektonische Bewegungen.-- BMFT Forschungsvorhaben KWA 8503, 8. final report, archive no. 103917, daybook no. 12.264/88, BGR; Hannover.
- HESSER, J. & SCHNIER, H. (2002): Projekt Gorleben - Ergebnisse festigkeitsmechanischer Laboruntersuchungen an Bohrkernen aus den Schächten Gorleben 1 und 2.-- BGR, unpublished report, archive no. 0122532: 144 pp., 1 volume of appendices; Hannover.
- HEUSERMANN, S. (1984): Aspects of Overcoring Stress Measurements in Rock Salt. (In: HARDY, H.R. & LANGER, M. [Eds.]: The Mechanical Behavior of Salt.)-- Proc. 2nd Conf. Mech. Behavior of Salt: pp. 272-289; Clausthal-Zellerfeld (Trans Tech Publ.).
- HEUSERMANN, S. (1993): Measurement of Initial Rock Stress at the Asse Salt Mine. (In GHOREYCHI, M., BEREST, P., HARDY, H.R. & LANGER, M. [Eds.]: The mechanical behavior of salt.)-- Proceedings of the Conference on Mechanical Behavior of Salt 3 (MECASALT III), 1993, Palaiseau, Frankreich: pp. 101-114; Clausthal-Zellerfeld (Trans Tech Publ.) - ISBN 0-87849-100-7.
- HEUSERMANN, S. (1995): Analysis of Initial Rock Stress Measurements in Salt.-- 5th Int. Symp. on Numerical Models in Geomechanics, Sept. 6 – 8; Davos, Switzerland.
- HEUSERMANN, S. (2001): Beurteilung der geomechanischen Stabilität und Integrität von Endlagerbergwerken im Salzgebirge auf der Grundlage geologischer und ingenieurgeologischer Untersuchungen.-- Geologische Beiträge Hannover, 2: pp. 159-174.
- HEUSERMANN, S. & EICKEMEIER, R. (2004): Finite-Elemente-Analysen zur Ermittlung der Steifigkeit hydraulischer Gebirgsspannungsgeber.-- Messen in der Geotechnik 2004, Mitteilung des Instituts für Grundbau und Bodenmechanik, TU Braunschweig, issue 77: pp. 281-292; Braunschweig.

- HEUSERMANN, S., EICKEMEIER, R., HANISCH, J., SPRADO, K.-H., KUNZ, H., HOPPE, F.-J. & KÜCHEMANN, W. (2003a): Projekt Gorleben – Gebirgsspannungsuntersuchungen in den Schächten 1 und 2. – Abschlussbericht.-- BGR, unpublished report, archive no. 0122843: 50 pp.; Hannover.
- HEUSERMANN, S., EICKEMEIER, R., SPRADO, K.-H. & HOPPE, F.-J. (2003b): Initial rock stress in the Gorleben salt dome measured during shaft sinking.(In: O. NATAU, E. FECKER & E. PIMENTEL [Eds.]: Geotechnical Measurements and Modelling.)-- Swets & Zeitlinger, pp. 139-144; Lisse, Netherlands.
- HEUSERMANN, S., EICKEMEIER, R., SPRADO, K.-H., HOPPE, F.-J., KUNZ, H. & KÜCHEMANN, W. (2003c): Projekt Gorleben - Gebirgsspannungsuntersuchungen im Erkundungsbereich EB.-- BGR, unpublished report, archive no. 0123785: 32 pp.; Hannover.
- Hou, Z. & K.-H. LUX, (2002): A material model for rock salt including structural damages as well as practice-oriented applications. (In: N. D. CRISTESCU, H.R. HARDY JR., R. O. SIMIONESCU [Eds.] - Basic and Applied Salt Mechanics.)-- Proc. 5th Conf. on the Mech. Beh. of Salt, Mecasalt V : pp. 151 – 169.
- HUND, W., STIER-FRIEDLAND, G., GREVE, D. & JARITZ, W. (1991): Geowissenschaftliche Untersuchungen bei der Erkundung des Salzstockes Gorleben von unter Tage.-- Interner Arbeitsbericht ET-IB-48-REV-1: 42 pp., 2 appendices; Salzgitter.
- HUNSCH, U. (1995): Salzmechanische Laboruntersuchungen an Steinsalz aus den Schächten Gorleben. (In: JESSBERGER, H.L. [Ed.]: Gefrierschächte Gorleben 94.)-- Proc. Symposium Gefrierschächte Gorleben, Bochum, Germany, 21 - 22 September 1994: pp. 251 – 262, 11 figures, 1 table; Rotterdam (Balkema) - ISBN 90-5410-525-9.
- HUNSCH, U. & SCHULZE, O. (1994): Das Kriechverhalten von Steinsalz.-- Kali und Steinsalz, Vol. 11 (8/9): pp. 238 - 255.
- JARITZ, W. (1993): Die geowissenschaftliche Untersuchung des Salzstocks Gorleben auf seine Eignung für ein Endlager für radioaktive Abfälle.-- Geol. Jb., A 142: pp. 295 - 304, 1 figure; Hannover.

- JUNG, R., OCHMANN, N., THIELEMANN, T., RÖHLING, S., SCHELLSCHMIDT, R., SCHULZ, R. & ROGGE, S. (2002): Geothermische Potenziale zur Stromerzeugung – Ressourcen in Deutschland. (In BMU [Ed.]: Geothermische Stromerzeugung.)-- Pro. of symposium „Geothermische Stromerzeugung – eine Investition in die Zukunft“, 20-21/06/2002 in Landau/Pfalz: pp. 21-31; Berlin.
- KAISER, D., LEYDECKER, G. & SCHLOTE, H. (2004): Überwachung der Seismizität im Bereich des Salzstockes Gorleben, annual report 2003.-- BGR, daybook no. 10549/04.; 29 pp., 9 figures, 8 tables; Hannover.
- KAISER, D. & SCHLOTE, H. (2008): Überwachung der Seismizität im Bereich des Salzstockes Gorleben - annual report 2007.-- BGR, daybook no. 10753/08; Hannover.
- KAPPELMEYER, O. & HÄNEL, R. (1974): Geothermics with Special Reference to Application.-- Geoexploration Monographs, Gebrüder Bornträger, Series 1 – No. 4: 238 pp.; Berlin-Stuttgart .
- KLINGE, H., BÖHME, J., GRISSEMANN, C., HOUBEN, G., LUDWIG, R. R., RÜBEL, A., SCHELKES, K. & SCHILDKNECHT, F. & SUCKOW, A. (2007): Standortbeschreibung Gorleben, Teil I. Die Hydrogeologie des Deckgebirges des Salzstocks Gorleben.-- Geol. Jb., C 71: 147 pp., 59 figures, 4 tables, 1 appendix; Stuttgart (Schweizerbart) - ISBN 978-3-510-95962-4.
- KLINGE, H., BÖHME, J., GRISSEMANN, C., HOUBEN, G., LUDWIG, R. R., RÜBEL, A., SCHELKES, K. & SCHILDKNECHT, F. & SUCKOW, A. (2007): Description of the Gorleben site, Part 1. Hydrogeology of the overburden of the Gorleben salt dome.-- BGR: 145 pp., 59 figures, 4 tables, 1 appendix; Hannover - ISBN 978-3-9813373-4-1.
- KÖTHE, A., HOFFMANN, N., KRULL, P., ZIRNGAST, M. & ZWIRNER, R. (2007): Standortbeschreibung Gorleben, Teil 2. Die Geologie des Deck- und Nebengebirges des Salzstocks Gorleben.-- Geol. Jb., C 72: 201 pp., 42 figures, 19 tables; Stuttgart (Schweizerbart) - ISBN 978-3-510-95963-1.
- KÖTHE, A., HOFFMANN, N., KRULL, P., ZIRNGAST, M. & ZWIRNER, R. (2007): Description of the Gorleben site, Part 2. Geology of the overburden and adjoining rock of the Gorleben salt dome.-- BGR: 201 pp., 42 figures, 19 tables; BGR Hannover - ISBN 978-3-9813373-5-8.
- KOPIETZ, J. (1983): Temperaturfelderkundung Gorleben. Abschlussbericht zum BMFT-Forschungsvorhaben KWA 206000.-- BGR, unpublished report, archive no. 0094954: 13 pp., 11 figures, 3 appendices; Hannover.

- LANGER, M. & HEUSERMANN, S. (2001): Geomechanical Stability and Integrity of Waste Disposal Mines in Salt Structures.-- Eng. Geol., 61: pp. 155 - 161; Elsevier.
- LEYDECKER, G. (2007): Erdbebenkatalog für die Bundesrepublik Deutschland mit Randgebieten für die Jahre 800 - 2005.-- <http://www.bgr.de/quakecat> BGR; Hannover.
- MUTSCHLER, T. (2004): Einaxiale Druckversuche an zylindrischen Gesteinsprüfkörpern. Neufassung der Empfehlung Nr. 1 des Arbeitskreises „Versuchstechnik Fels“ der Deutschen Gesellschaft für Geotechnik e. V.-- Bautechnik, 81: 20 pp., 8 figures, 5 tables; Berlin.
- NIPP, H.-K. (1988): Thermomechanische Berechnungen zum Endlager im Salzstock Gorleben (Berechnungsmodell 1986).-- BGR, unpublished report, archive no. 103379; Hannover.
- NIPP, H.-K. (1991): Testbericht und Freigabemitteilung für das Programmsystem ANSALT I (Release 1991-1).-- BGR, unpublished report, archive no. 108586; Hannover.
- NIPP, H.-K., EICKEMEIER, R. & HEUSERMANN, S. (2003): Projekt Gorleben – Erkundungsbegleitende großräumige gebirgsmechanische Berechnungen.-- BGR, unpublished report, archive no. 0123803; Hannover.
- NIPP, H.-K. & HEUSERMANN, S. (2000): Erkundungsbergwerk Gorleben – Gebirgsmechanische Beurteilung der Integrität der Salzbarriere im Erkundungsbereich EB1 für das technische Endlagerkonzept 1 (Bohrlochlagerung BSK3).-- BGR, unpublished report, archive no. 0120209; Hannover.
- NOWAK, T. & WEBER, J. (2002): Projekt Gorleben – Hydraulische Charakterisierung der Salzbarriere Gorleben.-- BGR, unpublished report, archive no. 0123070: 122 pp., 57 figures, 16 tables; Hannover.
- PAHL, A. & HEUSERMANN, S. (1991): In-situ-Untersuchungen zur Ermittlung von Gebirgsspannungen - Methoden, ausgewählte Meßergebnisse und deren Interpretation.-- Mitteilungen des Instituts für Grundbau, Bodenmechanik, Felsmechanik und Verkehrswasserbau der RWTH Aachen [Ed.: W. WITTKÉ], issue 21: pp. 81 - 110; Aachen.
- PAUL, A. & GARTUNG, E. (1991): Empfehlung Nr. 15 des Arbeitskreises 19 – Versuchstechnik Fels – der Deutschen Gesellschaft für Erd- und Grundbau e. V.: Verschiebungsmessungen längs der Bohrlochachse - Extensometermessungen.-- Bautechnik, 68: pp. 41 – 48, 13 figures, 1 table; Berlin.

- PLISCHKE, I. (2002): Projekt Gorleben, Ingenieurgeologische Erkundung der Homogenbereiche.-- BGR, unpublished report, archive no. 0122147: 28 pp., 16 figures, 4 tables, 2 appendices; Hannover.
- PLISCHKE, I. & HUNSCHKE, U. (2002): Projekt Gorleben, Laboruntersuchungen an Proben aus dem Salinarteil der Schächte.-- BGR, unpublished report, archive no. 0121812: 95 pp., 29 figures, 10 tables, 3 appendices; Hannover.
- RISSELER, P. (1979): Empfehlungen für die Versuchstechnik im Fels – Empfehlung Nr. 2: Dreiaxiale Druckversuche an Gesteinsproben.-- Die Bautechnik, 56, issue 7: pp. 221 – 224, 9 figures, 2 tables; Berlin.
- SCHNIER, H. (2003): Bewertung der Verformungsmessungen in den Schächten Gorleben 1 und 2 (Salinar).-- BGR, unpublished report, archive no. 0123688: 112 pp.; Hannover.
- SCHUSTER, K. (1968): Methodische und apparative Entwicklungen geothermischer Verfahren für Anwendungen im Bergbau und in der Tiefenerkundung.-- Dt. Verl. f. Grundstoffind. FFH, Reihe C, 232: 65 pp.; Leipzig.
- STIER-FRIEDLAND, G., RANFT, M. & BORNEMANN, O. (1997): Geowissenschaftliche Untersuchungen bei der Erkundung des Salzstockes Gorleben von unter Tage – Erkundungssohle.-- Internal report BfS ET-IB-96: 54 pp., 1 figure, 2 tables, 8 appendices; Salzgitter.
- STÜHRENBURG, D. (2002): Kompaktion und Permeabilität von Salzgrus.-- BGR, unpublished report, archive no. 0122321; Hannover.
- STÜHRENBURG, D. (2004): Compaction and Permeability Behaviour of Crushed Salt and Mixtures of Crushed Salt and Bentonite.-- Conference Proceedings of DisTec2004, International Conference on Radioactive Waste Disposal; Berlin.
- STÜHRENBURG, D. & ZHANG, C. L. (1998): Projekt Gorleben: Kompaktion und Permeabilität von Salzgrus.-- BGR, unpublished report, archive no. 116922; Hannover.
- STORMONT, J. C. (1997): In Situ Gas Permeability Measurements to Delineate Damage in Rock Salt.-- Int. J. Rock Mech. Min. Sci. 34, 7: pp. 1055 - 1064; Oxford, Elsevier.
- WORCH, G. (1967): Elastische Scheiben.-- In: Betonkalender 1967, 2nd part, W. Ernst & Sohn: pp. 1-128; Berlin.

Abbreviations

BfS	Bundesamt für Strahlenschutz (Federal Office for Radiation Protection)
BGR	Bundesanstalt für Geowissenschaften und Rohstoffe (Federal Institute for Geosciences and Natural Resources)
BMU	Bundesministerium für Umwelt, Naturschutz und Reaktorsicherheit (Federal Ministry for the Environment, Nature Conservation and Nuclear Safety)
bsl	below sea level
CDM	Composite Dilatancy Model
DBE	Deutsche Gesellschaft zum Bau und Betrieb von Endlagern für Abfallstoffe mbH (German Company for the Construction and Operation of Waste Repositories)
EB1	Exploration Area 1
EDZ	Excavation-damaged zone
EL1	Exploration location 1 (location of measurement points for geomechanical investigations)
EL2	Exploration location 2 (location of measurement points for geomechanical investigations)
EL4	Exploration location 4 (location of measurement points for geomechanical investigations)
FE	Finite Element
ML	Local magnitude (logarithmic scale of seismic energy of an earthquake, "Richter scale")
S1	Shaft 1
S2	Shaft 2
WIPP	Waste Isolation Pilot Plant

List of tables	Page
Table 3.1: Simplified stratigraphic table of the Zechstein beds around the underground workings in Gorleben, showing the average thicknesses	15
Table 4.1: Earthquakes within a radius of approx. 100 km from the Gorleben site detected by the Gorleben seismometer network	20
Table 5.1: Temperature data from deep boreholes Go 1003, Go 5001 and Go 5002 at depths ranging from - 700 m bsl to - 900 m bsl	27
Table 7.1: Material balance for the maximum value in an exploration borehole	90
Table 7.2: Material balance for the minimum value in an exploration borehole	91
Table 8.1: Pre-factors associated with the creep classes	102
Table 8.2: Recommended creep classes for the steady-state creep of different stratigraphic units in the evaporitic sequence of shaft 1	121
Table 8.3: Recommended creep classes for the steady-state creep of the different stratigraphic units in the evaporitic sequence in shaft 2	122
Table 8.4: Recommended creep classes for steady-state creep in the parts of EB1 in Gorleben investigated to date	123
Table 8.5: Recommended creep classes for steady-state creep in the stratigraphic units in the infrastructure area of EB1 investigated to date	123
Table 9.1: Gorleben, shaft 1, evaluation factor κ for overcoring tests	154
Table 9.2: Gorleben, shaft 2, evaluation factor κ for overcoring tests	155
Table 9.3: Gorleben, exploration level, evaluation factor κ for overcoring tests	155

List of figures

Figure 3.1:	Underground workings of the Gorleben exploration mine (source: DBE)	16
Figure 4.1:	Seismometer station network around Gorleben and the epicentres of the seismic events (excluding blasting events) recorded and localised by this station network within a radius of approx. 50 km from the Gorleben site.	18
Figure 5.1:	Geothermal field in the Gorleben salt dome based on a 2D modelling (DELISLE 1980)	22
Figure 5.2:	Temperature measuring apparatus in an ex-proof housing	25
Figure 5.3:	Location map of the geothermally-logged boreholes	25
Figure 5.4:	Temperature distribution in shaft exploratory borehole Go 5001	26
Figure 5.5:	Temperature distribution in borehole RB032	28
Figure 5.6:	Temperature distribution in borehole RB120	29
Figure 5.7:	Vertical geological cross section A-A' of boreholes Go 1003, RB032 and Go 5001 (from BORNEMANN et al. 2003) with isotherms of the natural temperature field for the depth zone surrounding the exploration level	30
Figure 5.8:	Initial temperature field at the depth of the 840 m level	32
Figure 5.9:	Horizontal geological cross section at the 840 m level after BORNEMANN et al. (2003) with natural temperature field isotherms, legend in Figure 5.7	33
Figure 6.1:	Overcoring test principle following the BGR method	36
Figure 6.2:	BGR overcoring probe type Mk14 in a rock salt core	36
Figure 6.3:	Principle of the Rock stress measurements using the hydro-frac method (BRÄUNER 1991)	38
Figure 6.4:	Stress monitoring stations with Glötzl pressure cells	39
Figure 6.5:	BGR dilatometer type Mk III	40
Figure 6.6:	Principle of the dilatometer test carried out using a BGR probe	41
Figure 6.7:	Principle behind convergence measurements in a drift	42
Figure 6.8:	Principle behind extensometer measurements using a triple extensometer as an example (after PAUL & GARTUNG 1991).	43
Figure 6.9:	Principle behind inclinometer measurements	45
Figure 6.10:	Example of the instrumentation installed in an exploration horizon in the shafts (after: DBE)	48
Figure 6.11:	Measuring instruments installed in exploration location EL1 (source: DBE)	50
Figure 6.12:	Measuring instruments installed in exploration location EL2 (source: DBE)	51
Figure 6.13:	Measuring instruments installed in exploration location EL4 (source: DBE)	51

Figure 6.14: Development of temperature at the temperature sensors of extensometer CG410E installed in exploration horizon EH-450 in shaft 1	52
Figure 6.15: Development of temperature at the temperature sensors in extensometer CG420E installed in exploration horizon EH-450 in shaft 2	53
Figure 6.16: Measured changes in diameter of the pilot boreholes during overcoring tests at various depths in shaft 2	55
Figure 6.17: Summary of the primary stresses determined by overcoring tests	56
Figure 6.18: Influence of ventilation air temperatures on the measured stress values in exploration horizon EH-450 in shaft 1	58
Figure 6.19: Change in convergence at convergence measuring station CG310K at a depth of -652 m bsl in shaft 1	60
Figure 6.20: Average convergence rates from the beginning of 2003 to the end of 2005 for the main measuring lines of the convergence measurement profiles in shaft 1	61
Figure 6.21: Average convergence rates during the period from the beginning of 2003 to the end of 2005 for the main measuring lines of the convergence measurement profiles in shaft 2	62
Figure 6.22: Measured relative displacements and temperatures at the CG410E extensometer in exploration horizon EH-450 in shaft 1	63
Figure 6.23: Calculated section deformations and measured temperatures at extensometer CG410E in exploration horizon EH-450 in shaft 1	64
Figure 6.24: Relative displacements at the deepest measuring points of extensometers installed diametrically in the exploration horizons in shaft 1	66
Figure 6.25: Relative displacements of the deepest measuring points of extensometers installed diametrically in the exploration horizons in shaft 2	67
Figure 6.26: Vertical displacements determined from the changes in inclination at the starting points and end points of inclinometer sections in shaft 1	67
Figure 6.27: Vertical displacements determined from the inclination changes at the starting points and end points of the inclinometer sections in shaft 2	68
Figure 6.28: Results of the fissurometer measurements in measuring horizon MH-785 in shaft 2	69
Figure 6.29: Change in temperatures at the measurement points of the floor extensometers installed in the exploration locations	71
Figure 6.30: Example of an overcoring test in EL1	72
Figure 6.31: Comparison of the minimum stresses derived from the overcoring tests and the hydro-frac measurements	73
Figure 6.32: Stress changes in the floor of EL1	75
Figure 6.33: Qualitative stress change beneath EL1	76
Figure 6.34: Stress changes in the walls of EL1	77
Figure 6.35: Vertical convergence rates in the exploration area drifts	78

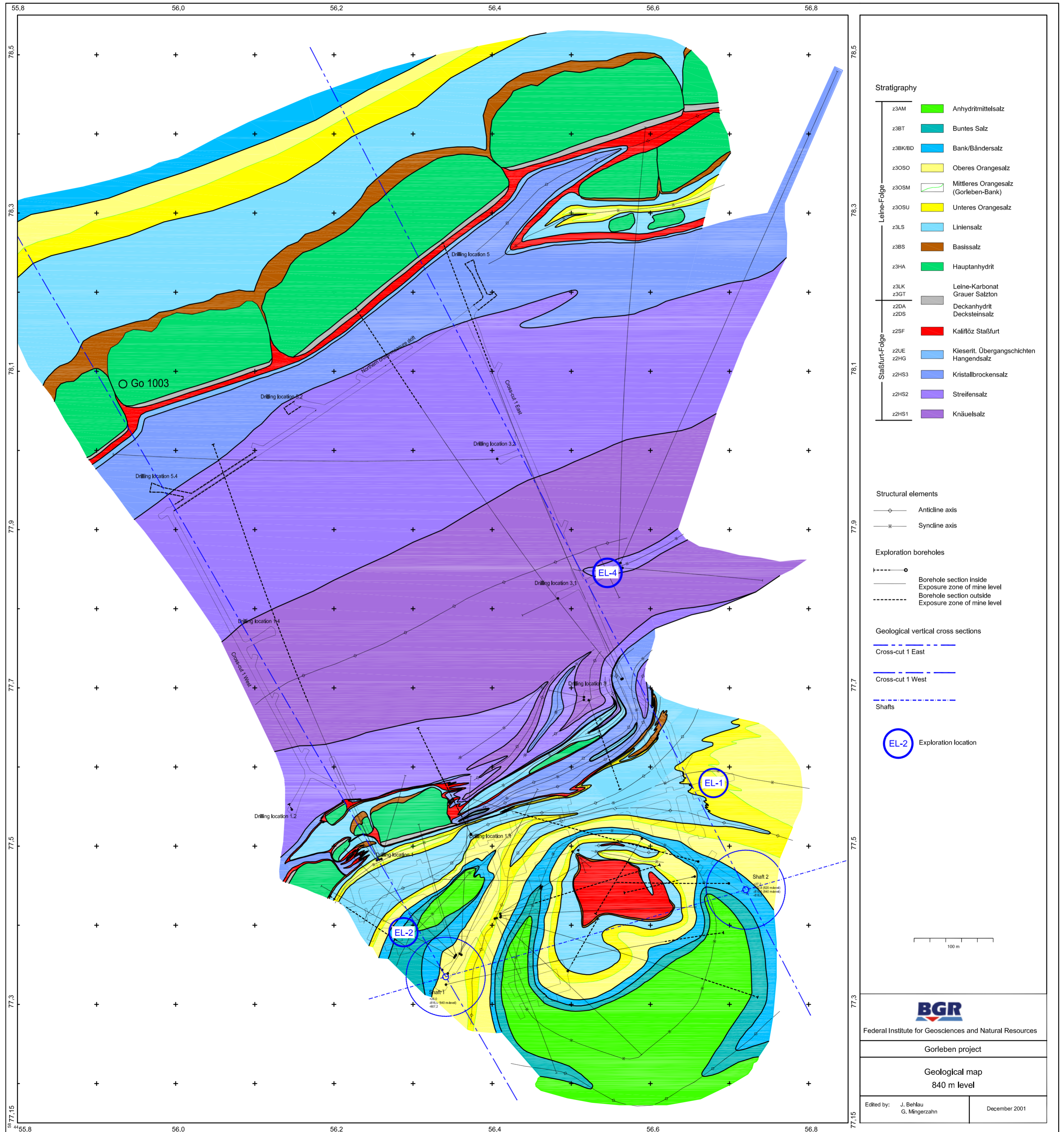
Figure 6.36: Vertical Convergence rates in the infrastructure area drifts	78
Figure 6.37: Section deformations at extensometer CG011E in EL2	79
Figure 6.38: Section deformations of extensometer CG104E in EL4	80
Figure 6.39: Resulting displacement directions of the Gorleben Bank (z3OSM)	82
Figure 7.1: Test evaluation example	84
Figure 7.2: Permeability testing equipment (probe – data station – wireline cable)	85
Figure 7.3: Permeability measurements in the excavation-damaged zone in the Gorleben exploration mine and in the WIPP site	88
Figure 7.4: Example of the measurement procedure carried out in an exploration borehole	89
Figure 7.5: Isolated and non-isolated occurrence of fluids	91
Figure 7.6: Stabilised pressure measurement plot against real time and against the Horner time function	92
Figure 7.7: Brine outflow rates and cumulative brine outflow in an exploration borehole	93
Figure 7.8: Core with healed joints in the Hauptanhydrit	95
Figure 8.1: Sketch of the principle behind a Brazilian test (GARTUNG 1985 and DGGT 2008)	98
Figure 8.2: Structure of a triaxial test apparatus for mechanical strength investigations	99
Figure 8.3: Determining the failure stresses in uniaxial and triaxial strength tests	100
Figure 8.4: Uniaxial and triaxial creep test apparatus	102
Figure 8.5: Laboratory test apparatus for carrying out biaxial tests on hollow cylindrical specimens	103
Figure 8.6: Average densities of the investigated rock specimens from different stratigraphic units in shaft 1, shaft 2, and the exploration area	106
Figure 8.7: Average ultrasonic wave velocities of the specimens from the shafts and the exploration area	108
Figure 8.8: Dynamic moduli of elasticity E_{dyn} and dynamic Poisson's ratios ν_{dyn} of the investigated stratigraphic units	109
Figure 8.9: Average static moduli of elasticity of the exploration level for uniaxial stresses E_{UC} and triaxial stresses E_{TC}	110
Figure 8.10: Example of a load-deformation diagram for a hollow cylindrical specimen from shaft 2	112
Figure 8.11: Moduli of elasticity determined in biaxial laboratory tests on cores from shaft 1 and shaft 2	113
Figure 8.12: Load-deformation diagrams for a hollow-cylindrical specimen from EL1	114
Figure 8.13: Average tensile strengths of the investigated rock samples	115
Figure 8.14: Average uniaxial failure strength of the investigated stratigraphic units	116

Figure 8.15: Uniaxial and triaxial failure strengths in rock samples from the shafts	117
Figure 8.16: Uniaxial and triaxial failure strengths in rock samples from the exploration level	117
Figure 8.17: Post-failure strength of rock specimens from the shafts	119
Figure 8.18: Failure strains dependent on temperature at a confining pressure of 1 MPa and a deformation rate of 10^{-5} s^{-1}	120
Figure 8.19: Assignment of homogenous zones in the shafts 1 and 2	128
Figure 8.20: Homogenous zones in the infrastructure area of EB1 at the 840 m level (legend see Figure 8.19)	129
Figure 8.21: Homogenous zones in the exploration area (EB1) at the 840 m level (legend see Figure 8.19)	130
Figure 9.1: FE modelling of the shaft in the form of an axi-symmetrical annular disc (section)	135
Figure 9.2: Calculated and measured temperature trends	136
Figure 9.3: Calculated stresses for a rock mass point close to the perimeter (upper diagram) and for a rock mass point 20 m from the shaft perimeter (lower diagram).	137
Figure 9.4: Relative displacements calculated and measured with an extensometer between the head plate and a point in the rock mass located 20 m from the perimeter of the shaft	138
Figure 9.5: Measured and calculated shaft convergence values	139
Figure 9.6: FE modelling of the shaft by an axi-symmetrical annular disc (above: total model; below: detail)	141
Figure 9.7: Measured and calculated temperature development in exploration horizon 3 in shaft 1	142
Figure 9.8: Calculated deformation and tensile stresses in the shaft perimeter at EH-550 for $t = 734 \text{ d}$	143
Figure 9.9: Development of fissures aperture over time for exploration horizon 3	144
Figure 9.10: Fissure apertures in the shaft perimeter of exploration horizon 3 at time $t = 734 \text{ d}$	144
Figure 9.11: Calculated changes in principal stresses over time at a distance of 20 m from the perimeter of the shaft at exploration horizon 3	145
Figure 9.12: Idealised geological model	147
Figure 9.13: Dilatant rock mass zones after thermal input ($t = 40 \text{ years}$)	149
Figure 9.14: Hypothetical frac-risk zones after heating up ($t = 40 \text{ years}$)	150
Figure 9.15: Axi-symmetrical finite-element model (extract) for the numerical calculation of an overcoring test	152
Figure 9.16: Theoretical overcoring plots at 1000 m dependent on the ductility of the rock salt	153
Figure 9.17: Evaluation factor κ against the investigated depth	154

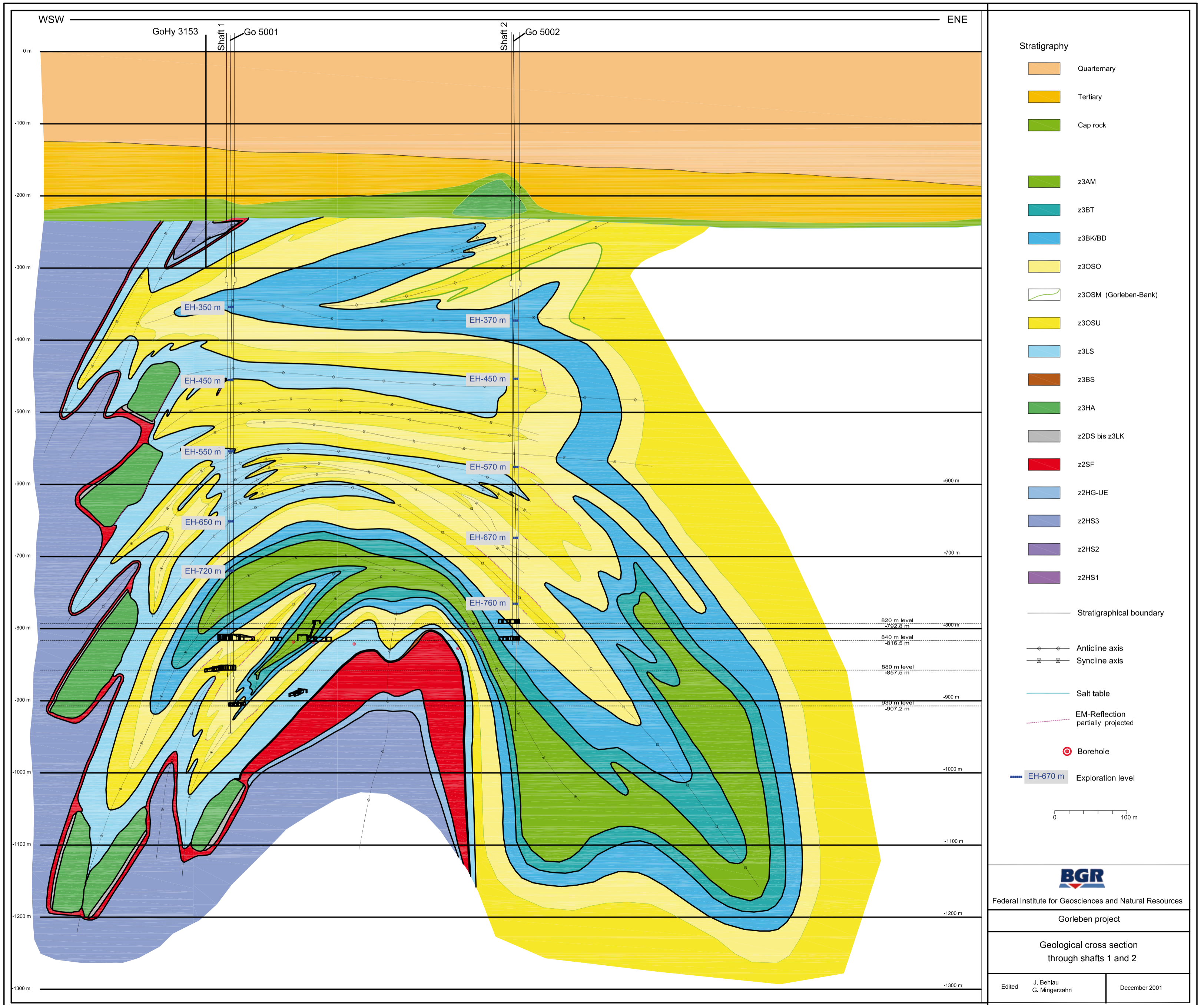
List of appendices

- Appendix 1: Geological base map of the 840 m level after BORNEMANN et al. (2002)
- Appendix 2: Vertical geological cross-section through shafts 1 and 2 after BORNEMANN et al. (2002)

Appendix 1: Geological base map of the 840 m level after BORNEMANN et al. (2002)



Appendix 2: Vertical geological cross-section through shafts 1 and 2 after BORNEMANN et al. (2002)



Bundesanstalt für Geowissenschaften und Rohstoffe (BGR)
Geozentrum Hannover
Stilleweg 2
30655 Hannover
Germany

www.bgr.bund.de

ISBN 978-3-9814108-0-8